

# Imaging structure and dynamics using controlled molecules

## Dissertation

zur Erlangung des Doktorgrades  
an der Fakultät für Mathematik, Informatik und Naturwissenschaften,  
Fachbereich Physik  
der Universität Hamburg

vorgelegt von

THOMAS KIERSPEL

aus Bergisch Gladbach

Hamburg

2017

Gutachter der Dissertation:	Prof. Dr. Jochen Küpper Dr. Oriol Vendrell
Zusammensetzung der Prüfungskommission:	Prof. Dr. Jochen Küpper Dr. Oriol Vendrell Prof. Dr. Henry N. Chapman Dr. Oliver D. Mücke Prof. Dr. Caren Hagner
Datum der Disputation:	3. März 2017
Vorsitzender des Prüfungsausschusses:	Prof. Dr. Caren Hagner
Vorsitzender des Promotionsausschusses:	Prof. Dr. Wolfgang Hansen
Dekan der Fakultät für Mathematik, Informatik und Naturwissenschaften:	Prof. Dr. Heinrich Graener

## **Eidesstattliche Versicherung**

Hiermit versichere ich an Eides statt, dass ich die Inanspruchnahme fremder Hilfen aufgeführt habe, sowie, dass ich die wörtlich oder inhaltlich aus anderen Quellen entnommenen Stellen als solche kenntlich gemacht habe. Weiterhin versichere ich an Eides statt, dass ich die Dissertation selbst verfasst und keine anderen als die angegebenen Hilfsmittel benutzt habe.

---

Thomas Kierspel



## Abstract

Folding, isomerization, and dissociation of molecules, i. e., bond breaking and bond formation, is happening on ultrafast time scales. Femtoseconds ( $1 \text{ fs} = 10^{-15} \text{ s}$ ) are the time scale on which atoms move. Hence, the observation of a chemical process on that time scale allows not only to measure the reactants and products of a chemical reaction, but also allows to observe the systems far from equilibrium. Within this dissertation several complementary measurements are presented, which are designed to measure chemical reactions of controlled gas-phase molecules at synchrotrons, high-harmonic generation based radiation sources, and the 4th generation x-ray light sources, x-ray free-electron lasers.

Gas-phase molecular ensembles are cooled in molecular beams and purified by either spatial separation of different rotational isomers, or size-selection of molecular clusters to provide a clean sample for the experiments. Furthermore, control is gained by the alignment of the initially isotropically distributed molecular sample to the laboratory frame. The controlled molecular samples, or their fragments, are imaged by several techniques, ranging from one-dimensional ion time-of-flight measurements, over two-dimensional velocity-map imaging of electrons and ions, to the measurement of scattered x-ray photons by an x-ray camera.

At first it is demonstrated that the *cis*- and *trans*-conformer of 3-fluorophenol can be purified in the interaction region to more than 90 % via spatial separation, and thus providing an ideal sample to study isomerization dynamics (chapter 3). The sample was chosen such that it is possible measure the ultrafast isomerization dynamics via photoelectron diffraction by using a free-electron laser.

In addition to the spatial control of the molecular beam, the alignment of the gas-phase molecular sample is demonstrated at the full repetition rate of a free-electron laser by the use of an in-house Ti:Sapphire laser system (chapter 4). Since most facilities have synchronized Ti:Sapphire laser systems at their corresponding end stations, this approach is demonstrating an alignment technique which can be easily implemented in most experiments.

The controlled gas-phase molecules were probed by hard x-ray photons to determine their structure via diffractive imaging (chapter 5). Diffractive imaging of gas-phase molecules at free-electron lasers is a highly promising approach to image ultrafast molecular dynamics of gas-phase molecules. The alignment of the molecular sample does have the advantage that, providing the molecules are perfectly aligned (or more general perfectly oriented), its diffraction pattern is equal to the diffraction pattern of a single molecule, which allows for the reconstruction of bond distances and bond angles of the molecule.

Furthermore, the x-ray photophysics of indole and indole-water clusters measured at a synchrotron are presented in chapter 6 and chapter 7. Indole and microsolvated indole-water clusters were spatially separated and both locally ionized by soft x-ray radiation. The ionic fragments as well as emitted electrons were recorded in coincidence. The fragmentation patterns of both species are compared to learn about the influence of the hydrogen-bonded water on the fragmentation of indole. This experiment was aiming at

the difference between isolated molecules and molecules in solvation, and also to study hydrogen bonds which are of universal importance in chemistry and biochemistry.

The potential use of a high-harmonic generation based radiation as a further source—next to the established accelerator-based facilities—for extreme ultraviolet photons is demonstrated in section 8.1 to study ultrafast dynamics of gas-phase molecules. Moreover, the sample preparation of the amino acid glycine is shown in section 8.2 for future studies of ultrafast charge migration in conformer-selected molecular samples by the use of attosecond pulses generated by higher harmonics.

## Zusammenfassung

Faltung, Isomerisierung oder die Dissoziation von Molekülen findet auf der Zeitskala von Femtosekunden ( $1 \text{ fs} = 10^{-15} \text{ s}$ ) statt. Experimente mit einer Zeitauflösung im Bereich von fs machen es somit möglich, nicht nur den Anfangs- und Endzustand einer chemischen Reaktion zu beobachten, sondern erlauben es auch ein Bild von der Chemie weit entfernt vom Gleichgewichtszustand des jeweiligen System zu bekommen. In dieser Arbeit werden mehrere Experimente präsentiert, welche konzipiert sind um zukünftig verschiedenen ultraschnelle chemische Prozesse in kontrollierten Molekülen in der Gasphase mit verschiedenen Strahlungsquellen (Laser oder höhere harmonische eines Lasers, Synchrotron, Freie-Elektronen-Laser) zu messen.

Die Kontrolle der Moleküle wurde auf zwei unterschiedliche Weisen realisiert. Zum einen wurden verschiedene molekulare Spezies (Isomere und molekulare Cluster) durch inhomogene statische elektrische Felder räumlich voneinander getrennt. Zum anderen wurde die räumliche Ausrichtung der Moleküle durch Laserpulse kontrolliert. Die kontrollierten Moleküle wurden anschließend mit verschiedenen Strahlungen (Infrarot-Laser, Ultraviolett-Laser, weiche und harte Röntgenstrahlung) vermessen. Die Resultate der Interaktion wurden durch Ionen-Flugzeitmassenspektrometer, "Velocity-Map Imaging"-Spektrometer, oder einer Röntgenkamera abgebildet.

Im ersten gezeigten Experiment wird die räumliche Trennung des *cis* und *trans*-Konformer von 3-Fluorphenol demonstriert (Kapitel 3). Hierbei wird gezeigt, dass es möglich ist eine nahezu reine Probe von beiden Konformeren zu erhalten, welche dazu genutzt werden können Isomerisierungsdynamiken in der Gasphase zu untersuchen.

Anschließend wird die räumliche Ausrichtung von Molekülen in der Gasphase bei voller Repetitionsrate von einem Freie-Elektronen-Laser demonstriert (Kapitel 4). Dies ist eine wichtige Demonstration, da die eingesetzten Laser an nahezu jeder Messstation von Freie-Elektronen-Lasern vorhanden sind, wodurch es vielen Experimentatoren ermöglicht wird ohne großen experimentellen Aufwand Moleküle in der Gasphase auszurichten.

Die ausgerichteten Moleküle wurden genutzt um mittels Röntgenbeugung die atomare Struktur des einzelnen Moleküls zu bestimmen (Kapitel 5). Durch die ultrakurzen Röntgenblitze von Freie-Elektronen-Lasern ist es nämlich möglich Strukturen sowie Strukturänderungen mit einer Zeitauflösung von Femtosekunden zu messen und somit einen direkten Einblick in the Femtochemie zu bekommen. Das Ausrichten der Molekülen erlaubt es dabei viele einzelne Bilder aufzunehmen, deren Summe dann–im Fall von perfekt ausgerichteten Molekülen (oder allgemeiner perfekt orientieren Molekülen)–gleich dem Bild des einzelnen Moleküls ist.

Anschließend wird die Photophysik von Indol sowie Indol-Wasser-Clustern untersucht (Kapitel 6, Kapitel 7). Dabei wurden beide Spezies räumlich voneinander getrennt und lokal am Indol-Molekül ionisiert.

Die ionischen Fragmente und Elektronen wurden in Koinzidenz gemessen. Die unterschiedlichen Fragmentationskanäle wurden verglichen um den Einfluss des gebundenen Wassers auf die Fragmentation vom Indol-Monomer zu untersuchen.

Zusätzlich wurde eine laborbasierte Laserquelle genutzt um die Fragmentation von Iodmethan durch lokalisierte Innerschalenionisation zu messen (Abschnitt 8.1). Dafür wurden höhere Harmonische des Lasers erzeugt, welche Iodmethan lokal ionisiert haben. Auch hier wurden die emittierten Elektronen und die ionischen Fragmente in Koinzidenz gemessen. Das Experiment wird in den Zusammenhang mit ähnlichen Experimenten gesetzt, welche an beschleunigerbasierten Photonenquellen durchgeführt wurden, um das Potential laborbasierter Messung im Bereich der extrem ultravioletten Strahlung zu demonstrieren. Anschließend wird die mögliche Separation der Konformere von Glycin in einem Molekülstrahl diskutiert. Ziel des Experiments ist es konformerenabhängige Ladungsmigration in Glycin mittels höherer harmonischer eines Laser zu messen (Abschnitt 8.2).

# Contents

<b>1</b>	<b>Introduction</b>	<b>1</b>
1.1	Sample preparation . . . . .	2
1.2	X-ray diffractive imaging . . . . .	3
1.3	X-ray photophysics and coincident measurements . . . . .	4
1.4	Outline of the thesis . . . . .	5
<b>2</b>	<b>Fundamental concepts</b>	<b>7</b>
2.1	Performed experiments . . . . .	7
2.2	Molecules in electric fields . . . . .	10
2.3	Adiabatic alignment of molecules . . . . .	12
2.4	X-ray matter interaction . . . . .	14
2.4.1	X-ray absorption and relaxation . . . . .	15
2.4.2	X-ray diffraction . . . . .	17
<b>3</b>	<b>Conformer separation of gas-phase molecules</b>	<b>21</b>
3.1	Introduction . . . . .	21
3.2	Experimental details . . . . .	22
3.3	Results and discussions . . . . .	23
3.4	Conclusions . . . . .	25
<b>4</b>	<b>Alignment at 4<sup>th</sup> generation light source</b>	<b>27</b>
4.1	Introduction . . . . .	27
4.2	Experimental Setup . . . . .	28
4.3	Results from experiments at LCLS . . . . .	31
4.4	Results from experiments at CFEL . . . . .	32
4.5	Discussion . . . . .	33
4.6	Summary . . . . .	36
<b>5</b>	<b>X-ray diffractive imaging of controlled molecules</b>	<b>39</b>
5.1	Introduction . . . . .	39
5.2	Experimental setup . . . . .	41
5.3	Simulations . . . . .	42
5.4	CSPAD data handling . . . . .	48
5.5	Experimental results . . . . .	50
5.6	Discussion . . . . .	57
5.7	Conclusion and outlook . . . . .	60

<b>6</b>	<b>X-ray photophysics of indole</b>	<b>63</b>
6.1	Introduction . . . . .	63
6.2	Experimental setup . . . . .	64
6.3	Coincidence spectra . . . . .	66
6.4	Photoelectron spectrum . . . . .	72
6.5	Discussion . . . . .	73
6.6	Conclusion . . . . .	76
<b>7</b>	<b>X-ray photophysics of indole-water clusters</b>	<b>79</b>
7.1	Introduction . . . . .	79
7.2	Experimental setup . . . . .	80
7.3	Ion coincidence spectra . . . . .	81
7.4	Electrons . . . . .	86
7.5	Discussion . . . . .	88
7.6	Summary and outlook . . . . .	89
<b>8</b>	<b>Applications of HHG photon sources</b>	<b>91</b>
8.1	HHG source for coincidence ion imaging of gas-phase molecules . . . . .	91
8.1.1	Introduction . . . . .	92
8.1.2	High-repetition-rate and high-photon-flux XUV source . . . . .	93
8.1.3	Coherently combined femtosecond fiber chirped pulse amplifier . . . . .	93
8.1.4	Nonlinear compression . . . . .	94
8.1.5	High photon flux source at 68.6 eV . . . . .	96
8.1.6	Coincidence detection of CH <sub>3</sub> I ionization fragments . . . . .	99
8.1.7	Photon flux estimate . . . . .	102
8.1.8	Conclusion and outlook . . . . .	103
8.2	Toward charge migration in conformer-selected molecular samples . . . . .	104
8.2.1	Simulations: Stark curves and deflection profile . . . . .	105
8.2.2	Experiment . . . . .	108
8.2.3	Conclusion and outlook . . . . .	110
<b>9</b>	<b>Summary</b>	<b>111</b>
9.1	Sample preparation . . . . .	111
9.2	X-ray diffractive imaging . . . . .	112
9.3	X-ray photophysics and coincident measurements . . . . .	112
<b>10</b>	<b>Conclusion and outlook</b>	<b>115</b>
	<b>Bibliography</b>	<b>117</b>

<b>Appendix</b>	<b>135</b>
<b>A Supplementary information chapter 5</b>	<b>135</b>
A.1 Molecular properties of 2,5-diiodothiophene . . . . .	135
A.2 Diffractive imaging – ADU gate optimization . . . . .	136
<b>B Supplementary information chapter 6 and 7</b>	<b>139</b>
B.1 Molecular beam reconstruction . . . . .	139
B.2 Coincidence spectrum (PIPICO) . . . . .	140
B.3 Mass spectrum calibration . . . . .	141
B.4 Ion VMI calibration . . . . .	141
B.5 Electron VMI calibration . . . . .	145
<b>Acknowledgment</b>	<b>149</b>
<b>List of Publications</b>	<b>151</b>



# 1 Introduction

Images of nature, animals, humans, or the night sky can not only look really nice but they can also be intellectually appealing. Consider, for example, images of Antarctica. Most people have not yet visited Antarctica but thanks to the images most people have an image in their mind about Antarctica and the animals that live there. Additionally, the images provide us, at least those of us who have not yet been there, a glimpse on what living in Antarctica would be like: very cold, half of the year pretty dark, no big supermarkets or bars. At least the beer won't get warm. The point is, images can tell us something about a place or a person even though we might never have seen or experienced the place or have never talked to the person. The experiments presented in this dissertation show the imaging of controlled molecules in the gas-phase. Images were recorded to study their structure as well as to learn about the response of gas-phase molecules and molecular clusters to localized ionization. Unlike the cameras which were used to make photos of Antarctica, the applied scientific cameras are optimized to image tiny molecules in the gas-phase. Imaging is here also not only restricted to the detection of photons, but it is also covering the imaging of electrons and ions with techniques like an ion-time-of-flight (TOF, 1D image) [1], or velocity-map imaging (VMI, 2D image) [2–5] of electrons and ions. Additionally, the images were taken of controlled cold molecular samples. Control encompasses the spatial separation of different molecular species, such as isomers or size-selection of molecular clusters, as if one would first sort the penguins in Antarctica by hand according to species, or by the size of their family before the pictures are shot. Furthermore, control is gained by aligning the controlled molecules in the gas-phase, which would otherwise typically have a random orientation in space, i. e., making sure that the penguins are all standing on their feet or head, instead of sitting or lying.

The presented experiments can be divided into three sections, namely sample preparation, x-ray diffraction imaging and the x-ray photophysics of gas-phase molecules and clusters. The common (future) goal of these experiments is to study structural changes of the molecules on femtosecond timescales, i. e., to get a closer insight into the femtochemistry (1 femtosecond = 1 fs =  $10^{-15}$  s) of gas-phase molecules. In general, femtosecond(s) is the timescale of atomic motion within a molecule. Femtochemistry allows the study of not only the educts and products, but also the evolution between them, i. e., the structure and properties of the systems far from an equilibrium point. The field covers, for instance, bond breaking, bond formation, folding and isomerization dynamics, as well as proton transfer or dissociation dynamics. A pioneer in this field was Ahmed H. Zewail whom was awarded the Nobel Prize in 1999 for his studies of the transition states of chemical reactions using femtosecond spectroscopy [6]. The presented experiments image the static structure of molecules/molecular clusters as well as their product states. This was partly due to the fact that most experiments were designed such that ultrashort x-ray laser pulses delivered by x-ray free-electron lasers (FEL) are required to probe the femtochemistry, and hence beamtime has to be approved.

## 1. Introduction

### 1.1 Sample preparation

Molecules in the gas-phase have the advantage that they can be treated as isolated systems, whereby the intrinsic properties can be studied without influence from the environment. The focus of this dissertation is to probe various aspects of controlled gas-phase molecules and to image their structure or fragmentation pattern. To maximize the control over the molecules it is necessary to start with a cold (few Kelvin) molecular beam, which was achieved by a supersonic expansion [7]. The control of the molecules covered the spatial separation of different species present in the molecular beam as well as the alignment of the isotropic distributed molecules in space.

The different species in the molecular beam are due to different conformers of the gas-phase molecule or due to different molecular clusters. In general, different conformers of complex molecules often exist in a molecular beam even at low temperatures [8]. The number of different conformers, the relative population of these conformers, and the experimental observables can lead to a much higher complexity in the extracted data or can make it simply impossible to interpret the experimental findings correctly. In experiments focussing on molecular clusters, a similar problem arises. The cluster formation relies on the collision between the various species present in the molecular beam in the early phase of the supersonic expansion. The overall size and cluster distribution can be controlled by the relative amount of sample present in the gas-phase prior the supersonic expansion. However, there will always be various clusters present in the molecular beam in addition to the desired cluster size to study. Spatial separation of the different clusters helps to reduce the complexity and ensures that the desired cluster size dominates or is at least enhanced. Thus, spatial separation is important to have a well defined starting point for the imaging of structural dynamics in the molecules. The spatial separation was achieved by a device called the deflector [9–13], which consists of two closely spaced electrodes generating a strong inhomogeneous direct current (DC) electric field. In analogy to the Stern-Gerlach deflector [14], where inhomogeneous magnetic fields were used to deflect silver atoms, the strong inhomogeneous DC electric fields were used to spatially separate molecular species according to their effective dipole moments. Thus, the spatial separation of conformers works best if they have a large difference in their effective dipole moment. For clusters, the effective dipole moment to mass ratio is the important factor.

In addition to the control of molecules via spatial separation, the control of the alignment of a molecular ensemble in space was utilized in the presented experiments. The orientation of molecules in the gas-phase is typically isotropic. Experiments, which aim at the study of molecular frame dependent properties such as the molecular frame photo-angular distribution (MFPAD) [15], or experiments, which aim at structure determination by MFPAD [16–20], recoil-frame photo angular distributions (RFPAD) [19, 21–23], or structure determination via diffractive imaging with x-rays as well as electrons (chapter 5) [24–32], require the alignment of the gas-phase molecules or it can be highly advantageous. For example, MFPAD as well as RFPAD experiments simply require access to the molecular frame to measure molecular-frame dependent properties. For x-ray and electron diffraction experiments, the alignment of the molecular

ensemble has practical and scientific advantages. Due to the low density in a molecular beam the scattering signal is typically very weak (for x-ray diffraction less than one photon per FEL pulse [25], chapter 5). The practical advantage is that the alignment of the molecules can locally increase the signal to noise ratio on the detector. Scientifically, the alignment has the advantage that it ensures to always diffract from molecules in the same orientation. Thus, it is possible to integrate the diffraction images and be able to reconstruct an image as if the photons have been scattered from a single object. This allows reconstructing bond lengths and bond angles from the diffraction image, where the latter one is typically hidden for an isotropically distributed molecular sample. The alignment can be done in several ways, ranging from DC electric fields by so-called brute force orientation [33, 34], by laser alignment [35–38], or a combination of both called mixed-field orientation [38, 39]. The difference between alignment and orientation is that aligned molecules can still have an up-down symmetry (penguins standing on their feet or their head), which is broken in the case of orientation. Laser alignment is sensitive to the polarization anisotropy in the molecule, which leads to an alignment of the most-polarizable axis of the molecule along the major axis of the alignment laser polarization ellipse [38]. It can be separated into adiabatic, non-adiabatic, and intermediate regime, which are quantified by the rising (falling) times of the envelope of the laser pulse and the rotational period of the molecule [35, 37]. For the presented experiments, the laser alignment was conducted in the intermediate regime. An alternative to brute force orientation or laser alignment is the reconstruction of the molecular axis *a posteriori*. This can be achieved if the probe pulse induces a Coulomb explosion in the molecule, the recoil of the ions is well defined in the molecular frame, and all momenta of the ions are measured in coincidence [19, 21–23].

## 1.2 X-ray diffractive imaging

Within the context of the dissertation, x-ray diffraction was applied to aligned gas-phase molecules to image their structure. But why does one need x-rays to image small structures? Considering a standard camera first, the reason why it (or the human eye) can make an image of something is also related to the wavelength  $\lambda$  of visible light ( $\lambda \approx 400\text{--}800$  nm), which is orders of magnitude smaller than the size of the object typically imaged. In 1873 Ernst Karl Abbe formulated that the resolution limit of a microscope is in the order of the wavelength used to illuminate the sample [40]. Considering that criteria, the imaging of viruses ( $\approx 100$  nm), proteins ( $\approx 10$  nm), or molecules ( $\approx 1$  nm) with atomic resolution ( $\approx 0.1$  nm) is not possible with visible light. In 1895 Wilhelm Conrad Röntgen discovered a type new type of radiation, which he gave the german name X-strahlen (Röntgen’sche Strahlen, Röntgenstrahlen) [41], or in english x-rays. X-rays are a form of electromagnetic radiation and, depending on the definition, cover a wavelength region ranging from a few nm to a few pm [42–44]. Consequently, x-rays fulfill the Abbe criteria to image structure with atomic resolution. X-ray diffractive imaging in crystalline samples is still today a really successful approach to probe structures of, e. g., bacteria, viruses, or proteins. It led to the discovery of the structure of the benzene ring [45] and the structure of the DNAs’ double-helix [46]. The structure determination of viruses of bacteria lead, among many other things, to the development

## 1. Introduction

of structural based drug design [47]. Also, several Nobel prizes have already been awarded to structural biology, with the most recent one in 2009 for unraveling the structure of the ribosome [48]. Most of the experiments were conducted at synchrotrons, which provided until the year 2009 the most powerful x-ray photon sources. In 2009 the era of x-ray free-electron lasers (FELs) started with the Linac Coherent Light Source (LCLS) at the SLAC National Accelerator Laboratory being the first to go in user mode. FELs are nowadays the brightest x-ray sources in the world and provide coherent x-ray pulses with pulse durations in the order of femtoseconds. The short pulses of the free-electron lasers have the advantage that they can outrun the radiation damage induced by the x-rays in the sample [49, 50], i. e., the photons diffract off the sample before the structure of interest is destroyed. Additionally, they provide the time-resolution to study ultrafast dynamics in gas-phase molecular samples. Thus, FELs are a highly promising photon source to image the structure of gas-phase molecules and, more importantly, to image structural changes of the molecule on ultrafast timescales. In a scattering and diffraction type of experiment this has already been demonstrated for gas-phase molecules in a gas-cell [51, 52]. In the environment of a cold molecular beam only static diffraction images have been recorded so far [24–26]. This is due to the orders of magnitude lower density of molecules in a molecular beam compared to the density achievable in a gas-cell. The experiment conducted in the scope of this dissertation was performed at a much shorter wavelength compared to [24–26], which allowed consequently for a higher spatial resolution.

### 1.3 X-ray photophysics and coincident measurements

X-rays are not only very suitable for diffraction experiments but can also be used for localized ionization of a molecular sample due to their element selectivity [42, 43]. Site-specific ionization within a molecule as a starting point for controlled dynamics is a key to gain even more control about the triggered dynamics or the probe pulse. Site-specific ionization is typically not achievable with femtosecond lasers since, in that case, the ionization process relies on multiphoton or tunnel ionization, where the exact knowledge of where the ionization in the molecule has happened is hidden from the experimentalist. Ionization by soft x-ray photons has been used in a variety of experiments to observe, for instance, charge rearrangement in dissociating molecules [53, 54], relaxation of highly excited states by observation of Auger electrons [55–57], or fragmentation of the molecule following (site) specific ionization [22, 58–61] with the common goal to get a closer insight into the world of femtochemistry.

Within the context of the dissertation, soft x-ray radiation was used to study the photofragmentation of gas-phase molecules and molecular clusters upon localized core-shell ionization. The experiments were aiming at two goals. First, the photofragmentation of indole and indole-water clusters was studied in detail to understand the influence of the hydrogen-bonded water on the fragmentation of indole. The localized ionization at the indoles' nitrogen using soft x-ray radiation played a key role to guarantee that the fragmentation was always triggered in the same way. These molecular systems allowed thus to study hydrogen bonding, which is of universal importance in chemistry and biochemistry. In the second case, the photon source was a laboratory-based high-harmonic generation (HHG) source, which was used for

site-specific ionization of iodomethane molecule. The experiment was conducted to put HHG sources in the realm of accelerator-based light sources, and to demonstrate the potential of the laboratory based studies. In all cases the measurements were performed in a coincident mode, meaning that the ionic fragments as well as electrons were recorded in coincidence. This allowed in all cases a 3D momentum reconstruction of the ionic fragment and a 2D momentum reconstruction of the photo- and Auger electrons. Coincidence measurements do have the strength that they help to understand the fragmentation of the molecule upon inner-shell ionization [17, 21–23, 58, 59, 61, 62]. Also, the coincidence measurements do allow to measure RFPADs of the molecules [19, 21–23] with the possibility to image the molecules upon fragmentation, and to get thus an even closer insight into the femtochemical reaction.

## 1.4 Outline of the thesis

In chapter 2 the fundamental concepts of the dissertation are described, covering the generation of a molecular beam, the fundamentals to spatially separate different conformers/clusters (possibly) present in the molecular beam, and the alignment of gas-phase molecules. Also, the fundamental concepts of x-ray matter interaction are shortly described, ranging from the relaxation following core-shell ionization to an insight into x-ray diffraction.

In chapter 3 the spatial separation of the *cis* and *trans* conformer 3-fluorophenol is demonstrated by making use of the strong inhomogeneous electric fields generated within the deflector. It demonstrates for the first time that it is possible to purify (> 90%) the conformer with the lower effective dipole moment, which was additionally less populated in the molecular beam. The aim was to provide a pure molecular sample to study isomerization dynamics.

In chapter 4 the alignment of molecules in the gas-phase at the full FEL repetition rate is shown. It demonstrates a universal preparation of molecules tightly fixed in space by the use of the available in-house laser system at the coherent x-ray imaging (CXI) beamline at the Linac Coherent Light Source. The molecules were aligned for structure determination via diffractive imaging.

Chapter 5 shows the diffractive imaging part of chapter 4. The results show evidence for the measurement of a 1D diffraction image. The 2D diffractive imaging data cannot confirm the experimental findings in the 1D diffraction image, also due to the experimental background, which was much higher than the diffraction signal of the molecules. This chapter gives an outline for diffractive imaging of controlled gas-phase molecules and discusses about improvements for future experiments.

Chapter 6 shows a detailed photofragmentation study of indole—the chromophore of the amino acid tryptophan—triggered by inner-shell ionization. Photo- and Auger electrons as well as ionic fragments have been measured in coincidence. The results show that indole is primarily fragmenting in three fragments, where only two of them are ionized. The data also show coincidences, which are primarily present if the indole monomer is localized ionized at its nitrogen atom. This experiment was conducted to understand the photofragmentation of indole and provide thus a foundation for the photofragmentation study of indole-water cluster.

## 1. Introduction

Chapter 7 shows the photofragmentation of indole-water clusters upon localized ionization at the indole-part of the cluster. The indole-water clusters have been spatially separated from the indole monomer and higher clusters. The spatial separation allowed to determine the fragmentation signature of indole-water, which primarily showed a charge and proton transfer to the hydrogen-bonded water. Furthermore, it showed that the generation of, in total, three ionic fragments is much more likely in the case of indole-water compared to the indole monomer.

Chapter 8 is divided into two experiments. Section 8.1 shows the potential use of a HHG source to measure the photophysics upon localized ionization by a table-top laser system. The experiment compares the outcome with comparable experiments conducted at FELs and synchrotrons. Section 8.2 shows an early stage of sample preparation of glycine for a conformer-selected attosecond pump-probe experiment to measure conformer-specific charge migration. It provides simulations that show the possibility to spatially separate/purify different conformers. Additionally, it shows that a molecular beam of glycine could not be generated by the use of the pulsed Even-Lavie valve. Alternative evaporation sources like laser-desorption or laser-induced acoustic desorption were used to demonstrate the measurement on an ion-TOF spectra of glycine in the gas-phase.

## 2 Fundamental concepts

This chapter provides at first a general step-by-step overview, starting with the generation of a molecular beam, followed by the control of molecules in the gas-phase using DC and alternating current (AC) electric fields. Finally, the different probing schemes and detection techniques, which were applied in the context of the dissertation, are described. A more detailed description of some of the fundamental concepts is given in the sections of this chapter following the general description. A generalized\* experimental setup is shown in Figure 2.1, and an overview of the conducted experiments and their corresponding experimental setups, as well as ionization and detection schemes, is given in Table 1.

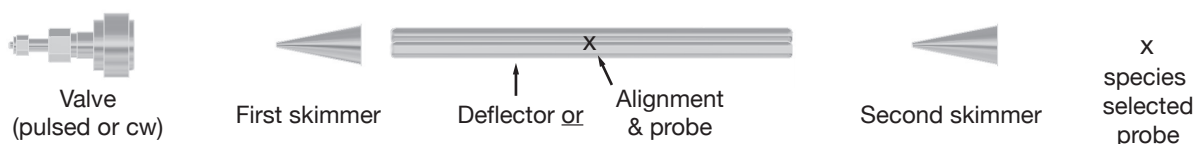


Figure 2.1: Drawing of a generalized\* experimental setup showing the pulsed valve [63], two skimmers, and the deflector. X is indicating two different probing positions. The left X is showing the location where molecules have been aligned and subsequently probed by a laser, and the right X is showing the probe position of a conformer/cluster selected molecular beam.

### 2.1 Performed experiments

The aim of the conducted experiments was to probe various aspects of controlled molecules in the gas-phase. Therefore, the molecules had to be introduced into the gas-phase and the molecules had to be cooled. The studied molecules were either in the liquid (3-fluorophenol, iodomethane) or solid (2,5-diiodothiophene, indole, glycine) phase at room temperature. For the described experiments the liquids' vapor pressure was high enough such that the molecules could be used without further modification. Solids, on the other hand, were heated close to, or above, their melting point to promote enough molecules into the gas-phase for the generation of a molecular beam. The promotion of molecules into the gas-phase via heating is only possible for thermally stable molecules. Glycine, for instance, could only be successfully detected by alternative evaporation methods like laser desorption (LD [64]) or laser induced acoustic desorption (LIAD [65]). Once the molecules were evaporated they were mixed with an inert gas (helium or neon) called seeding or carrier gas. The mixture of molecules and seeding gas was expanded into

---

\*The experimental setups varied between the different experiments. Therefore, in each chapter the corresponding setup is shown separately.

## 2. Fundamental concepts

vacuum either via a pulsed valve [63] (valve shown in Figure 2.1) or a continuous nozzle to generate a supersonic expansion. Due to collisions between the seeding gas and molecules in the early phase of the expansion a cooling of the molecules' vibrational and rotational states is achieved such that only the vibrational ground state and the lowest rotational states were significantly populated afterwards [7]. The cold molecular beam was subsequently skimmed by the first skimmer (Figure 2.1). The skimmer was used for differential pumping between the valve and the deflector/interaction chamber, to select the coldest part of the molecular beam, and to reduce the size of the beam such that fewer collisions between the beam and the deflector (Figure 2.1) occur, which lead to a warmer molecular beam.

The control of the cold molecular beam was achieved either by spatial separation of the different species present in the molecular beam [9–11], or by alignment of the isotropically distributed molecules in space [35]. The spatial separation of the different molecular species was achieved by the deflector (Figure 2.1), and performed to probe primarily the species of interest, i. e., a certain conformer or a certain cluster size. In short, the deflector consists of two closely spaced electrodes (a cross section is shown in Figure 2.2 c)) generating a strong inhomogeneous electric DC field. The inhomogeneous electric field is required to exert a force on the different molecular species, which is proportional to the effective dipole moment of the molecules. Due to the effective dipole moment, which is dependent on the molecules rovibronic state, and which is also typically dependent on the species, different states and species will experience a different force which leads to a spatial separation after the deflector. A second skimmer (Figure 2.1) after the deflector was used as differential pumping stage before the molecular beam was entering the probe section of the experimental setup. A more detailed description of the concept of molecular deflection is given in section 2.2.

In addition to the control of molecules via spatial separation, the control of the molecules was achieved by laser-alignment of the isotropically orientated molecules in space [35]. The alignment was performed to measure the structure of molecules via x-ray diffraction. The alignment of the molecular ensemble has the experimental advantage of a local increase of the signal-to-noise ratio on the detector [24–26]. Scientifically its advantage is that the diffraction image of a perfectly aligned (or more general oriented) molecular ensemble is equal to the diffraction image of a single molecule [24–26]. In these experiments, alignment and probing was conducted after the first skimmer, as it is indicated in Figure 2.1. In short, a linear polarized laser pulse induces a dipole moment in the molecule which is dependent on the molecular-frame polarizability. The molecular axis with the highest polarizability will align along the alignment laser polarization. A more detailed description is given in section 2.3.

The probe pulses applied for the presented experiments are ranging from infrared to hard x-ray photons. Sorted by increasing photon energy, an infrared (IR) femtosecond (fs) laser pulse was applied to probe the molecules via strong-field ionization. Probing molecules by a fs-laser pulse is a general approach applicable to a large range of molecules and observation parameters. It was used to measure an ion TOF spectrum, and it was used to trigger a Coulomb explosion of the molecules to measure their degree of alignment via velocity map imaging. An ultraviolet (UV) laser was used to probe different conformers of a molecule by

resonant enhanced multi-photon ionization (REMPI). Among others, REMPI has the advantage of being conformer specific, i. e., it can be used to probe different structural isomers of the same molecule. This was done to prove that different conformers could be spatially separated. Not all molecules do have suitable REMPI transitions and hence it is only applicable to a limited amount of molecules. XUV and soft x-ray radiation was used for localized ionization of the molecule from inner-shell orbitals. Localized ionization has the advantage that it is a much cleaner probe pulse compared to, for instance, strong field ionization since the ionization will primarily happen at the same/at a few known positions within the molecule. Finally, hard x-ray photons were primarily used to image the structure of molecules.

In most of the experiments molecular ions as well as their ionic fragments were used as observables. The simplest form of imaging was measuring a 1 dimensional (1D) TOF spectrum in a Wiley-McLaren [1] type of spectrometer. It was used to determine the mass spectrum of the probed molecules, and thus to measure the molecular species present in the molecular beam. 2 dimensional (2D) imaging of electrons and ions was performed by a VMI spectrometer [2–5]. Velocity-map imaging is an imaging technique which allows to determine the velocity components of the ions or electrons parallel to the detector surface. For the case of aligned molecules, VMI was used to determine the degree of alignment of these molecules. Furthermore, it was used to measure kinetic energies of electrons and ionic fragments to get an insight into the dissociation processes of a molecule. In addition to electron and ion imaging, an x-ray camera was used to detect scattered photons from the molecular sample which contain information about the molecular structure.

Table 1: Overview of the experimental setups

Chapter	Molecule	Valve	Deflector	Alignment	Probe	Detector
chapter 3	3-fluorophenol	pulsed	conformer	–	REMPI	TOF
chapter 4	2,5-diiodothiophene	pulsed	–	laser	fs, x-ray	VMI
chapter 5	2,5-diiodothiophene	pulsed	–	laser	x-ray	x-ray camera
chapter 6	indole	pulsed	–	–	x-ray	TOF and VMI
chapter 7	indole-Water	pulsed	cluster	–	x-ray	TOF, VMI
section 8.1	iodomethane	cont.	–	–	XUV (HHG)	TOF, VMI
section 8.2	glycine	pulsed	—	—	fs	TOF

## 2. Fundamental concepts

### 2.2 Molecules in electric fields

The deflector was used to spatially separate different conformers as well as different molecular clusters according to their effective dipole moment [9–11]. In the following it is described how the molecular Hamiltonian is modified in the presence of an external electric field, what the effective dipole moment is, and how it that can be used to spatially separate the different species.

The energy  $W$  of a molecule in quantum mechanics can be obtained by solving the Schödinger equation  $W\Psi = H\Psi$ , where  $\Psi$  are the wavefunctions, and  $H$  is the molecular Hamiltonian [66–69]. If the molecules are in the presence of an external electric field the Hamiltonian can be modified by

$$H_{\text{rot},\epsilon} = H_{\text{rot}} + H_{\text{Stark}}, \quad (1)$$

where  $H_{\text{rot},\epsilon}$  is the Hamiltonian of the molecule in the external electric field,  $H_{\text{rot}}$  is a simplified molecular Hamiltonian<sup>†</sup>, and  $H_{\text{Stark}}$  is the Hamiltonian describing the interaction between the molecule and the electric DC field, which is also known as the Stark effect [71].  $H_{\text{rot}}$  is given by

$$H_{\text{rot}} = H_{\text{Rigid}} + H_{\text{d}} \quad (2)$$

, where  $H_{\text{Rigid}}$  is the simplified Hamiltonian<sup>†</sup> of the rigid rotor molecule, and  $H_{\text{d}}$  compensates for the centrifugal distortions of the molecule<sup>†</sup>.  $H_{\text{Stark}}$  is given by

$$H_{\text{Stark}} = -\boldsymbol{\mu} \cdot \boldsymbol{\epsilon} = -\epsilon_Z \sum_{g=a,b,c} \mu_g \phi_{Z_g} \quad (3)$$

where  $\boldsymbol{\mu}$  is the permanent dipole moment, and  $\boldsymbol{\epsilon}$  is the electric field vector in the laboratory frame. Commonly  $Z$  is chosen for the electric field direction in the laboratory frame.  $\mu_g$  is the dipole moment along the molecules principal inertial axes, and  $\phi_{Z_g}$  is projection of different molecular axis (direction cosine) onto the field direction  $Z$ . This formula gives thus directly the connection between the molecular dipole moment and the change of the molecular Hamiltonian in the presence of the electric field. The eigenvalues of the Hamiltonian are found by matrix diagonalization in the basis of the symmetric-top wavefunctions and were calculated throughout the presented work by the CMISTark code [70].

Figure 2.2 a) shows exemplarily the calculated Stark curves (energy  $W$  of a rotational state in dependence of the electric field strength  $\epsilon$ ) for the two lowest rotational states of the first two conformers (red and black) of glycine (section 8.2). All presented states do change their energy in the presence of the electric field, with a global trend towards lower energy for an increased field strength. Conformer II shows a bigger change in energy than conformer I due to its higher dipole moments (Equation 3, section 8.2). The effective dipole moment  $\mu_{\text{eff}}$  from a single molecular state can be derived by

$$\mu_{\text{eff}} = -\partial W / \partial \epsilon, \quad (4)$$

---

<sup>†</sup>The Hamiltonian and the energies of the molecules in the external field were calculated throughout the dissertation by using the CMISTark code [70] which also specifies the simplifications taken into account.

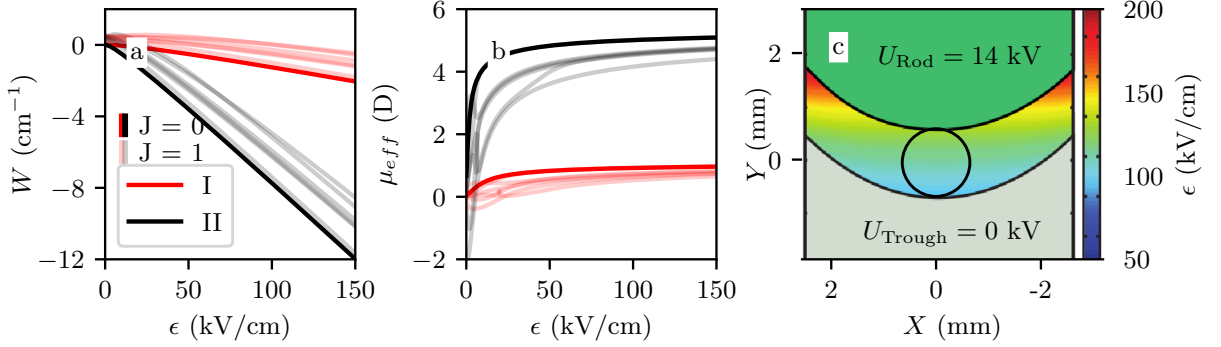


Figure 2.2: a) and b): Stark energies and effective dipole moments for the first two conformers of glycine (section 8.2). c) Cross section through the deflector electrodes. The color code is given for the gap between the electrodes and indicates the generated field strength between those. The circle is indicating the molecular beam. Its propagation direction is perpendicular to the plane of the page.

and is shown in Figure 2.2 b) for the corresponding states and conformers of glycine. Some of the molecular states in Figure 2.2 b) do show a local minima at a field strength below 50 kV/cm. These states are called low-field seeking (lfs) states since they lower their energy with decreasing field strength. Due to avoided crossings of the different states, the lfs states turn into high-field seeking (hfs) states at a certain field strength. The lowest rotational state ( $J = 0$ ) of both conformers has the highest effective dipole moment which is, at the given electric field strength, continuously increasing with increasing electric field strength. In the presence of very high electric fields the effective dipole moment  $\mu_{\text{eff}}$  is converging to the permanent dipole moment of the molecule. In an inhomogeneous electric field, the molecules experience a force  $\mathbf{F}$  which is described by

$$\mathbf{F} = \mu_{\text{eff}}(\epsilon) \cdot \nabla \epsilon, \quad (5)$$

and which is the force causing the spatial separation of the different species in the molecular beam. The force exerted on the molecules is linear dependent on the effective dipole moment and the gradient of the electric field. The electric field between the deflector electrodes is shown in Figure 2.2 c). The electrodes are displayed here in the top (rod) and bottom (trough) part of the image. The electric field strength in the gap between the electrodes is indicated by the color code. It is given for an applied voltage  $U$  of 14 kV at the rod electrode, and a grounded trough electrode. The molecular beam is shown by the circle in the center of the electrodes, and its propagation direction is perpendicular to the plane of the page. The electric field gradient in the gap is nearly constant along the  $X$ -axis, but changes significantly along the  $Y$ -axis. Taking Equation 5 into account, the molecules will experience a force in the  $Y$ -direction and will be deflected towards higher  $Y$  if they are in a hfs state. Since  $\mathbf{F}$  is also linear dependent on  $\mu_{\text{eff}}$ , and considering the significantly higher effective dipole moment of the second conformer of glycine (Figure 2.2 b)), a spatial separation of the different conformers can be achieved.

The deflector has already been used to spatially separate different quantum states of small molecules like

## 2. Fundamental concepts

OCS [72], nuclear-spin isomers [73], conformers (chapter 3) [10, 11, 13], or to spatially separate molecular clusters (chapter 7) [12, 13].

### 2.3 Adiabatic alignment of molecules

Laser alignment of molecules was used to measure diffraction images of an aligned gas-phase molecular ensemble. The alignment of the molecules was important for two reasons. First, the diffraction pattern of an aligned molecular ensemble gives a local increase of the signal-to-noise ratio on the detector [24–26, 29]. Also, the diffraction pattern of a perfectly aligned (or more general oriented) molecular ensemble is equal to the diffraction pattern from a single molecule<sup>‡</sup> which allows to determine bond length as well as bond angles [24–26, 29].

Figure 2.3 a) shows an ensemble of isotropically oriented iodomethane molecules ( $\text{CH}_3\text{I}$ , section 8.1) in space which is a typical distribution of gas-phase molecules if they are not manipulated further. An example of aligned gas-phase molecules is shown in Figure 2.3 b). In this example the molecules have been aligned by a vertically linear polarized laser  $\epsilon$ , resulting in an alignment of the molecules most polarizable axis along the alignment laser polarization. The iodine-carbon axis, which is the most polarizable axis in iodomethane, is still pointing in opposite directions, and the molecules can still freely rotate around that axis. Breaking the up-down symmetry of the dipole moment vector leads to orientation of the molecules in

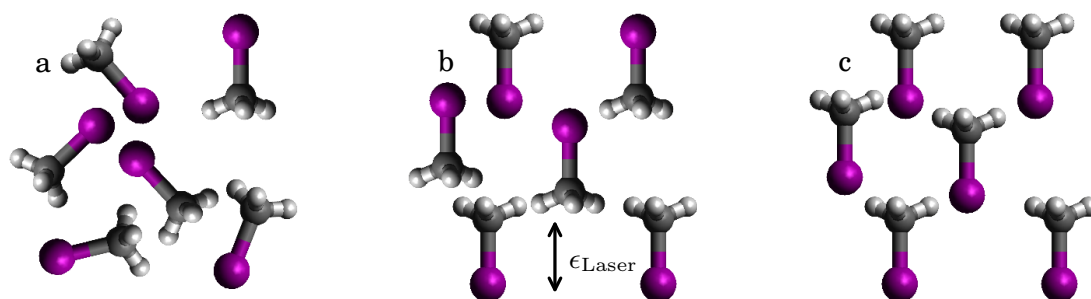


Figure 2.3: a) Isotropic, b) aligned, and c) oriented ensemble of iodomethane (section 8.1)

space, as it is shown in Figure 2.3 c). Orientation can be achieved by strong DC electric fields (brute-force orientation [33, 74]) or by mixed-field orientation [39], i. e., a combination of strong laser fields and a DC electric field which can be used to increase the degree of orientation. The orientation of molecules is mentioned here for completeness and will not be discussed further.

The alignment of molecules with non-resonant lasers is applicable to all polar and non-polar molecules, as

---

<sup>‡</sup>Depending on the symmetry of the molecular structure, alignment or orientation is required to achieve the same diffraction pattern as from a single molecule

long as they do have a polarizability anisotropy. It is typically separated into three different cases [35], quantified by the rising and falling times of the laser pulse intensity  $\tau_{\text{Laser}}$ , and the rotational period  $\tau_{\text{Rot}}$  of the molecule.

If  $\tau_{\text{Laser}} \gg \tau_{\text{Rot}}$  the molecules are adiabatically aligned, i. e., the population of states in the molecule is equal before and after the laser pulse; the eigenstates of the field-free molecular Hamiltonian will be transferred to field-dressed pendular states in the presence of the slowly rising laser field intensity. If  $\tau_{\text{Laser}} \ll \tau_{\text{Rot}}$  rotational states are coherently coupled and the molecule experiences a periodic field-free alignment after the laser pulse. If  $\tau_{\text{Laser}} \approx \tau_{\text{Rot}}$ , the molecules are aligned in the presence of the laser field (similar to adiabatic alignment), and do experience a periodic field-free alignment after the laser pulse (similar to non-adiabatic alignment). The experiments presented in chapter 4 and chapter 5 were conducted in this intermediate regime; the molecules were probed at the peak of the alignment laser pulse and no focus was put on the field free alignment after the laser pulse. Hence, the following discussion is focussing on adiabatic alignment of molecules in the gas-phase. A more detailed description can be found for instance in [35, 36, 75].

The period of the electric field of a laser with a central wavelength of 800 nm is (in vacuum) 2.7 fs, which is orders of magnitude shorter than the rotational period of molecules. The comparable fast oscillations of the laser field lead to a suppression of the Stark effect (section 2.2), because the molecules effective dipole moment cannot follow the fast oscillations within the laser field. But the laser field can induce a dipole moment  $\mu_{\text{Ind}}$  within the molecule. In simple words, the laser field induces electron oscillations within the molecule on the frequency of the laser field; the heavy nuclei cannot follow the field that fast, leading to a relative charge displacement, i. e., an induced dipole moment. The induced dipole moment does depend on the polarizability tensor  $\alpha_{ij}$  of the molecule, the electric field strength  $\epsilon$ , and the angle between  $\alpha_{ij}$  and the polarization of the laser field. For an asymmetric top molecule the induced potential by a linear polarized laser can be described by

$$V_{\text{Ind}}(t) = -\frac{(E_0\epsilon(t))^2}{4}(\sin^2\theta(\alpha_{xx}\cos^2\chi + \alpha_{yy}\sin^2\chi) + \alpha_{zz}\cos^2\theta) \quad (6)$$

where  $E_0$  is the electric field strength and  $\epsilon(t)$  is the laser pulse envelope.  $\alpha_{xx}$ ,  $\alpha_{yy}$ , and  $\alpha_{zz}$  are the polarizability tensor components with respect to the molecular frame,  $\theta$  is polar Euler angle between the laser field polarization and the molecular axis, and  $\chi$  is the azimuthal Euler angle about the molecules  $z$ -axis.

The experimental realization of the measurement of the degree of alignment is shown in Figure 2.4. A molecule is aligned along the alignment laser polarization  $\epsilon_{\text{Laser}}$  (Figure 2.4 a)). The angle between  $\epsilon_{\text{Laser}}$  and the molecular axis is  $\theta$ . In the presented experiments (chapter 4, chapter 5) the degree of alignment was probed via a second laser pulse which triggered a Coulomb explosion of the molecule. This is illustrated by the broken bond between the iodine<sup>+</sup> and the CH<sub>3</sub><sup>+</sup> part of the molecule. Ideally, the ionic fragments recoil along the intramolecular axis. The angle  $\theta$  can be measured for an ensemble of molecules and can be used to quantify the degree of alignment  $\langle \cos^2\theta \rangle$ . Depending on how well the

## 2. Fundamental concepts

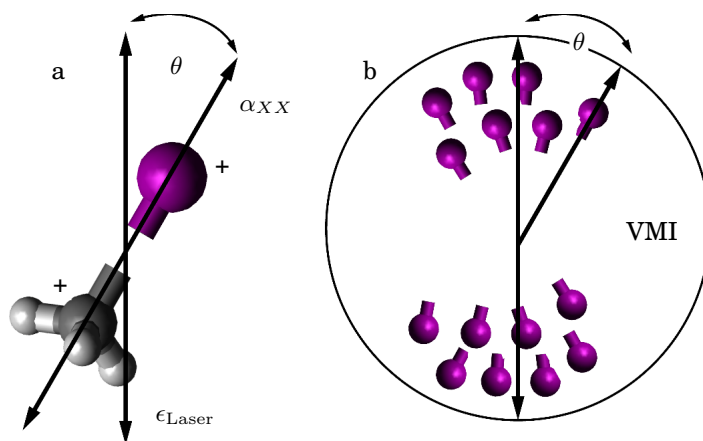


Figure 2.4: a) A single molecule aligned along the laser polarization axis. The broken bond indicates the Coulomb explosion of the fragmenting molecule. b) Drawing of a possible VMI image of aligned molecules gated on a specific fragment.

molecules are aligned,  $\langle \cos^2\theta \rangle$  can take values between  $1/3$  and  $1$  for an isotropically and a perfectly aligned molecular ensemble respectively. In the presented experiment the degree of alignment is measured by mapping the 3 dimensional (3D) velocity distribution of a certain ionic fragment of the molecule onto the detector via velocity-map imaging [2-5] (Figure 2.4 b)). However, velocity-map imaging allows only to determine the velocity components parallel to the detector surface. Thus, only the 2D projection of the polar Euler angle  $\theta$  is measured.  $\langle \cos^2\theta_{2D} \rangle$  can be between  $0.5$  and  $1$  for an isotropically and a perfectly aligned molecular ensemble respectively. Among others,  $\langle \cos^2\theta \rangle$  can be reconstructed by a rotation of the laser polarization, such that it is perpendicular to the detector surface and measuring again  $\langle \cos^2\theta_{2D} \rangle$  from that second angle.

### 2.4 X-ray matter interaction

In the presented experiments x-ray radiation was used to image the structure of controlled gas-phase molecules. Also, x-rays have been used for localized ionization of controlled gas-phase molecules and molecular cluster, to learn about their photophysics and charge-rearrangement upon core-shell ionization. The x-ray spectrum can be classified into the regime of soft and hard x-ray photons for low and high energetic photons respectively [42, 43]. The photon energies are not strictly defined. Here, the definition given in [44] is used, which puts the soft x-ray photons between the electron  $1s$  binding energies of a carbon and an argon atom, i. e., the spectrum is ranging from  $284$  eV to  $3.2$  keV. Photon energies on the order of several keV are considered as hard x-rays, and photon energies in the region of MeV are considered as gamma rays.

In the experiments presented in chapter 6 and chapter 7 soft x-ray radiation ( $420$  eV) was used for

side-specific ionization in the molecular sample. Additionally, the experiment shown in section 8.1 was conducted in the XUV region, i. e., at a photon energy of 70 eV, also for side-specific ionization in the molecular sample. Side-specific ionization is achieved by tuning the photon energy on, or slightly above, the core-resonances of the atom(s) within the molecule, and increasing thus the probability of photoabsorption in that atom(s). If the photon energy is higher than the binding energy of electron in the core, the sample can be core-shell ionized. The excited atoms or molecules can relax via, for instance, emission of a further electron (Auger decay, chapter 4, chapter 6, chapter 7, section 8.1) or emission of a photon (x-ray fluorescence, chapter 5). The x-ray photoabsorption and the following relaxation mechanisms are shortly described in subsection 2.4.1.

In addition to photoabsorption, the x-ray radiation can also scatter off the atoms/molecules which can be used for structure determination (chapter 5). To achieve atomic resolution hard x-ray photons are required, since their wavelength is short enough to image small structures, i. e., shorter than the intramolecular distances. The scattering process can be coherent (elastic) or incoherent (inelastic), where the coherent part of the scattering process is containing the structure information of the molecular sample. The incoherent part is considered as background radiation in diffractive imaging experiments. Both processes are described in more detail in subsection 2.4.2.

A collection of cross sections for the different interactions can be found in [76–78]. A good overview about the theoretical treatment of the x-ray matter interaction is given in [42, 43] as well as by the tutorial [44] and references therein.

### 2.4.1 X-ray absorption and relaxation

Figure 2.5 a) show a schematic drawing of the lowest energy states of an atom. The incident x-ray photon  $h\nu$  is absorbed by a K-shell electron and ionizes the sample. The kinetic energy of the photoelectron  $E_{\text{kin}}$  is given by the difference of incident photon energy and the binding energy. The absorption cross section scales approximately with the atomic number  $Z^4$  [43]. For a constant  $Z$ , the photoabsorption cross section scales with the photon energy  $E_{\text{ph}}^{-3}$ . The total absorption cross sections  $\sigma_{\text{Tot}}$  for a carbon and a nitrogen atom are exemplarily shown in Figure 2.6 [76]. The cross section for nitrogen is generally higher than the carbon cross section ( $Z_{\text{N}} > Z_{\text{C}}$ ) and both decrease with increasing photon energy. At a photon energy of  $\approx 284$  and 410 eV the cross sections for carbon and nitrogen do increase by more than one order of magnitude. The sudden increase of the cross section is here due to the photon energy which is exceeding the ionization potentials for the 1s orbitals [78].

After ionization the atom is left in a highly core-excited state. Relaxation can happen via, for instance, an Auger decay (non-radiative decay) (Figure 2.5 b)) or via fluorescence (Figure 2.5 c)). The Auger decay is the dominant relaxation process for  $\approx Z < 18$  [44]. In this example, the created K-hole is filled from an electron of the L-shell, and an electron is emitted from the L-shell, leaving the atom in a dicationic state.

## 2. Fundamental concepts

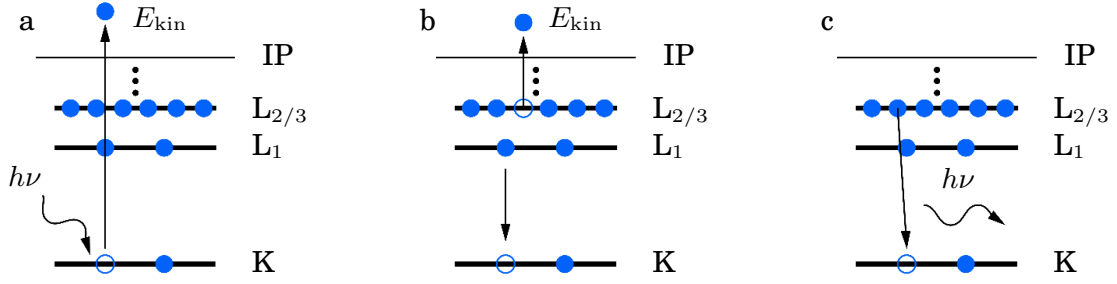


Figure 2.5: Illustration of a) x-ray photoionization, b) the Auger decay, and c) decay via x-ray fluorescence in an atom. K, L<sub>1</sub>, L<sub>2/3</sub> are illustrating the corresponding atomic levels, which are occupied by electrons (blue dots). The blue circles indicate the generated core-hole by the x-ray photon  $h\nu$  and IP is illustrating the ionization potential of the atom.

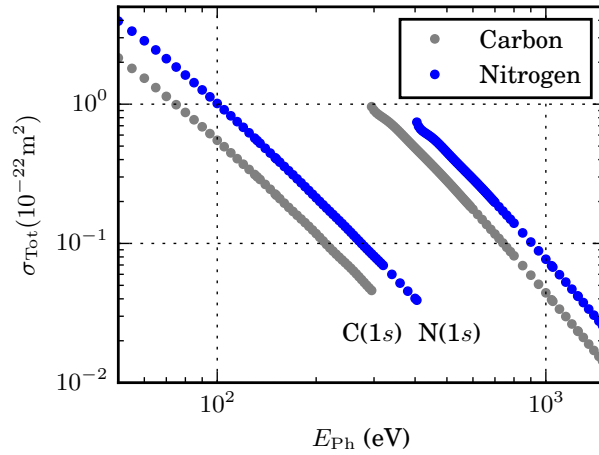


Figure 2.6: Absorption cross sections for carbon and nitrogen in dependence of the photon energy [76]

The kinetic energy of the Auger electrons energy  $E_{Aug}$  is given by [79]

$$E_{Aug} \approx E_A - E_B - E'_C \approx E_A - E_B - E_C(Z + 1), \quad (7)$$

where  $E_A$  and  $E_B$  are the ionization energies of the shells from the generated vacancy and from the less tightly bound electron which is filling the vacancy.  $E'_C$  is the ionization energy of the emitted electron for the case of a singly ionized atom.  $E'_C$  can be approximated by  $E'_C = E_C(Z + 1)$  where  $E_C$  is the ionization energy of the neutral atom from which the Auger electron is emitted. The Auger electrons are typically labeled according to their involved transitions. The Auger electron shown in Figure 2.5 would thus be labeled as KL<sub>1</sub>L<sub>2,3</sub>. In molecules the Auger electrons can originate from valence orbitals V,

which would be labeled as, for example, KLV or KVV Auger electron. In molecules and especially atomic or molecular clusters, similar relaxation processes (relaxation and electron emission) like intermolecular Coulombic decay (ICD) [80, 81] or electron-transfer mediated decay (ETMD) [82] play an important role. In ICD a core hole is created which is filled by an electron from a higher state, but the electron is emitted from a neighboring atom. In ETMD a created core hole is filled by an electron from a neighboring atom, the electron is emitted from a third atom. X-ray fluorescence (Figure 2.5 c)) is the dominant relaxation process for heavier atoms. The inner-shell vacancy is filled by an electron from a higher shell accompanied by the emission of a x-ray photon. The photon energy is equivalent to the energy difference between the two orbitals and is element specific. The transitions are labeled as, for example,  $K_\alpha$  or  $K_\beta$  if the electron relaxes from a 2p or 3p orbital, respectively, into a K-shell vacancy. The fluorescence yield scales approximately with  $Z^4$  [44] and a good overview of the different emission lines for the different atoms is given in [78].

### 2.4.2 X-ray diffraction

The following chapter is based on [43] and describes the scattering processes of coherent and incoherent scattering which are also called elastic or inelastic scattering. The coherent part of the scattering contains the structure information of the scattering object and will be treated first. Incoherent scattering does not contain structure information and is considered here as background radiation. It is assumed that the x-rays are a plane wave, have a very low interaction probability with the sample (first Born approximation), are off-resonant from any transitions in the sample, and that scattering signal comes exclusively from the electrons.

In short, coherent x-ray diffraction can be used to image the structure of small atoms or molecules. The incident x-rays induce a quiver motion in the electrons which emit dipole radiation. The dipole radiation from the individual electrons within the atom or molecule is coherently added. The coherent sum contains the structure information which is measured by the detector. The detector only measures the intensity  $I$ , i. e., the phase information is lost (phase problem). Phase retrieval algorithms can be used to iteratively reconstruct the phase and thus reconstruct the imaged object [43, 83].

Starting from a free electron, Figure 2.7 a) shows a free electron (blue) in space which is in the field of plane wave of x-ray radiation. The wavevector  $\mathbf{k}_z$  is chosen along the  $z$ -direction; the x-rays are linear polarized along the  $x$ -coordinate. The electron will respond to the incident electric field via a quiver motion along the  $x$ -direction—as indicated by the attenuated color of the electron—at a frequency equivalent to the incident plane wave. The electron acts in that case like charges in an antenna and is emitting dipole-radiation. The electric field at a point  $D$  in space can be described by

$$\begin{aligned} \frac{E_{rad}(\mathbf{R}, t)}{E_{in}} &= -r_0 \frac{e^{i\mathbf{k}\mathbf{R}}}{\mathbf{R}} \cos(\psi) \\ \frac{E_{rad}(\mathbf{R}, t)}{E_{in}} &= -r_0 \frac{e^{i\mathbf{k}\mathbf{R}}}{\mathbf{R}} P^{1/2}, \end{aligned} \quad (8)$$

where  $E_{rad}$  is the radiated electric field,  $r_0$  is the Thomson scattering length (classical electron radius),

## 2. Fundamental concepts

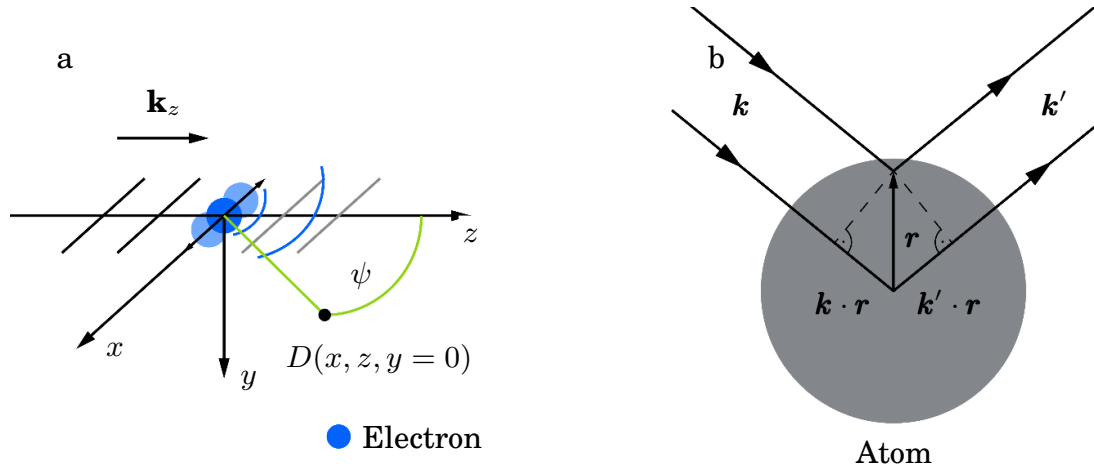


Figure 2.7: a) Scattering of an x-ray photon by an electron, where  $\mathbf{k}_z$  is the wavevector of the incident x-ray radiation and  $D$  is an observation point in the  $x - z$  plane. b) Scattering of x-rays from an atom.  $\mathbf{k}$  is incident x-ray wavevector,  $\mathbf{k}'$  is the scattered wavevector,  $|\mathbf{k}| = |\mathbf{k}'|$ , and  $\mathbf{r}$  is the difference between a wave scattered at the origin and a wave scattered at a position  $\mathbf{r}$ . The images are adapted from [43].

$\mathbf{R}$  is the distance between the observation point  $D$  and the electron,  $\psi$  is the angle with respect the incident beam, and  $E_{in}$  is the incident radiating field.  $\cos(\psi)$  is describing the angular dependency due to the linear motion of the electron within the linear polarized incident electric field. Thus, the radiated electric field is maximized at  $\psi = 0^\circ$  and minimized at  $\psi = 90^\circ$ . This polarization dependency is also commonly known as polarization factor  $P$ , which is for the given case  $\cos^2(\psi)$ , and  $1/2(1 + \cos^2(\psi))$  for an unpolarized light source.

Figure 2.7 b) shows the scattering of x-rays from an individual atom where  $\mathbf{k}$  is defined here as the incident plane wave,  $\mathbf{k}'$  is the scattered wave. For the case of elastic (coherent) scattering  $|\mathbf{k}| = |\mathbf{k}'|$ . All the electrons within the atom respond to the electric field via a quiver motion. Thus, the contribution of the individual electrons have to be added up coherently if electron-electron correlations are neglected. The atom can be divided therefore into small sections which do have a certain charge density  $\rho(r)$ .  $r$  is the distance between a certain volume element and the origin of the atom, as it is indicated in Figure 2.7 b). The phase difference  $\Delta\phi$  between the emitted wave of a volume element in the origin and at a point  $r$  can be described by

$$\begin{aligned}
 \Delta\phi &= \mathbf{k} \cdot \mathbf{r} - \mathbf{k}' \cdot \mathbf{r} \\
 &= (\mathbf{k} - \mathbf{k}') \cdot \mathbf{r} \\
 &= \mathbf{Q} \cdot \mathbf{r},
 \end{aligned} \tag{9}$$

where  $\mathbf{Q}$  is the wavevector transfer. The integration over the different volume elements gives the atomic

scattering, which is also known as the atomic form factor  $f^0(Q)$  with

$$-r_0 f^0(Q) = -r_0 \int \rho(\mathbf{r}) e^{i\mathbf{Q}\mathbf{r}} d\mathbf{r}. \quad (10)$$

The integral over the different electron charge densities  $\rho(\mathbf{r})$  is equal to the number of electrons in the atom. The atomic form factor is recognizable as a Fourier transformation connecting the density distribution  $\rho(\mathbf{r})$  in real space with the momentum space or also known as reciprocal space<sup>§</sup>. Not taken into account are the different energy levels in the atom. K-shell atoms are much stronger bounded to the nucleus than L or M-shell electrons. If, for instance, the incident photon energy is much smaller than the binding energy of the K-shell atoms, the quiver-motion of the electrons on this shell can be neglected and hence the total scattering amplitude is reduced. The total atomic form factor can then be described by

$$f(\mathbf{Q}, \hbar\omega) = f^0(\mathbf{Q}) + f'(\hbar\omega) + if''(\hbar\omega) \quad (11)$$

, where  $f'(\hbar\omega)$  is a damping factor and  $if''(\hbar\omega)$  is giving a phase correction between the electrons quiver motion and the driving field.<sup>¶</sup>

The connection between the molecular form factor  $F^{mol}(\mathbf{Q})$  and atomic form factor is given by the summation of the individual atomic form factors of the atoms within the molecule. It is important to keep track of the distances  $\mathbf{r}$  between the different atoms such that those are coherently added. Thus, the molecular form factor can be written as

$$F^{mol}(\mathbf{Q}) = \sum_{r_j} f_j(\mathbf{Q}) e^{i\mathbf{Q}\cdot\mathbf{r}_j}. \quad (12)$$

Taking Equation 8 into account, the scattering of the molecules can be described by

$$\frac{E_{rad}(\mathbf{R}, \mathbf{Q})}{E_{in}} = -r_0 F^{mol}(\mathbf{Q}) \frac{e^{ikR}}{R} P^{1/2} \quad (13)$$

For an experimentalist it is desirable to measure  $F^{mol}(\mathbf{Q})$  for sufficient  $\mathbf{Q}$ -values to be able to reconstruct, via fitting algorithms, the molecular structure.

In addition to elastic (coherent) scattering, x-rays can also inelastically (incoherent) scatter of the sample. An inelastic scattering process is schematically shown in Figure 2.8. The incident x-ray photon has a momentum  $\mathbf{p}$  and is scattered off the electron at an angle  $\theta$ . The momentum of the scattered photon is  $\mathbf{p}'$ . In the case of an inelastic scattering process  $|\mathbf{k}| \neq |\mathbf{k}'|$ ; the momentum difference is transferred to the electron. The energy of the incoherent scattered photon  $E'_{inc}$  can be described by

$$E'_{inc} = \frac{1}{1 + k(1 - \cos(\theta))} E \quad (14)$$

where  $k = E/(m_e \cdot c^2)$ , i. e., it is the incident photon energy  $E$  in units of the electron rest mass energy, and  $\theta$  the angle between incident and the scattered photon. The scattering of x-rays on a free-electron

<sup>§</sup>The atomic form factors can be parameterized. In [84] the parametrization consists of a sum of five weighted Gaussians plus a constant which are listed for a large number of neutral and ionic atoms.

<sup>¶</sup>[85] gives tabulated values for this correction.

## 2. Fundamental concepts

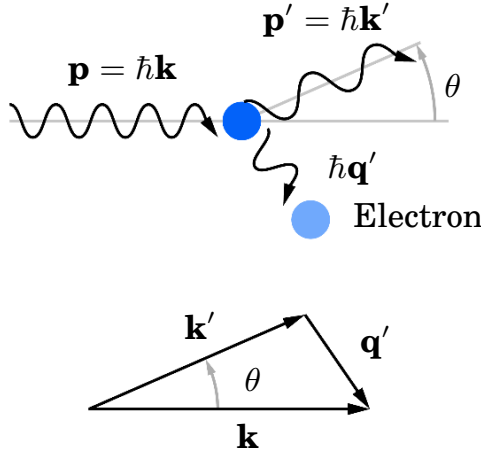


Figure 2.8: Inelastic scattering of an x-ray by an electron, where  $\mathbf{p}$  and  $\mathbf{p}'$  are the momenta of the incident and scattered photons,  $\theta$  is the angle between the incident and the scattered photons, and  $\hbar\mathbf{q}'$  is the momentum transferred to the electron.

in relativistic quantum mechanics can be described by the Klein-Nishina formula [86]. Below a photon energy of 100 keV, the Klein-Nishina formula can be approximated by [78]

$$\begin{aligned} \frac{d\sigma_{KN}}{d\Omega} &= \frac{r_e^2 P}{(1 + k(1 - \cos(\theta)))^2} \\ &= r_e^2 P \left| \frac{\mathbf{E}'_{inc}}{\mathbf{E}} \right|^2 \end{aligned} \quad (15)$$

where  $P$  is the polarization factor. The Klein-Nishina formula is here expressed as the differential cross section<sup>‡</sup> where  $\sigma_{KN}$  is the Klein-Nishina cross section per solid angle  $\Omega$  of the detector. The Klein-Nishina formula can be multiplied by the incoherent scattering function  $S(\mathbf{Q}, Z)$  to make the transformation from a single electron to a single atom.  $S(\mathbf{Q}, Z)$  is thus comparable to the atomic form factor and tabulated values can be found in [87]. The incoherent scattering can then be described by

$$P(\mathbf{k}, \mathbf{Q}) = \frac{d\sigma_{KN}}{d\Omega} \cdot S(\mathbf{Q}, Z) \quad (16)$$

where  $P(\mathbf{k}, \mathbf{Q})$  is the angular and energy distribution of the scattered photon. During the course of the dissertation the incoherent scattering was implemented within the CMIDiffract code [24, 25, 29] which is used to simulated diffraction pattern of molecules.

---

<sup>‡</sup>Differential cross sections are derived by normalization of the scattered intensity by the incident photon flux and the solid angle of the detector  $\Delta\Omega$

### 3 Conformer separation of gas-phase molecules\*

The following chapter is based on the publication [11] and demonstrates the spatial separation of the *cis*-, and *trans* conformer of 3-fluorophenol ( $C_6H_5OF$ , 3FP) utilizing their individual effective dipole moments. It starts with an introduction (section 3.1), which puts the spatial separation of conformer into context with novel, upcoming experiments and highlights the importance of conformer-separated molecular samples. The experimental setup and results are shown in section 3.2 and section 3.3. The experiment shows the first demonstration of the spatial separation of the least polar conformer, which is additionally less populated in the molecular beam.

#### 3.1 Introduction

Complex molecules often exhibit different structural isomers (conformers), even under the conditions of a cold molecular beam [8]. For a variety of upcoming novel experiments like photoelectron [16, 18], electron [32, 88], and x-ray diffraction [25, 27] imaging of gas-phase molecules, for conformer-specific chemical reaction studies [89], or for mixed-field orientation experiments [35, 38, 90], pure species-selected molecular samples with all molecules in the lowest-energy rotational states are highly advantageous or simply necessary. Using strong inhomogeneous electric fields it is possible to spatially separate individual conformers [10, 91], specific molecular clusters [12], as well as the individual quantum states of neutral polar molecules [92–94]. While the electric deflector was exploited for the spatial separation of individual conformers [10] and for the generation of highly polar samples of single-conformer molecules [38], it was not *a priori* clear whether it would be possible to create pure samples of the most polar low-rotational-energy states of any conformer but the most polar one.

Here, we demonstrate the generation of conformer-selected and very polar ensembles of both conformers of 3FP. 3FP is a prototypical large molecule with two stable conformers that differ by their orientation of the OH functional group. Conformer-selected and three-dimensionally oriented [97] ensembles of 3FP are good candidates for the investigation of conformer-interconversion reactions in an ultrafast laser pump, x-ray probe experiment, in which structural information would be accessible through photoelectron holography following  $F(1s)$  ionization [16, 18].

The structures of *cis* and *trans* 3FP are shown in Figure 3.1, together with calculated energies of their lowest rotational states in an electric field [70]. At relevant electric field strengths, all states are high-field

---

\*This chapter is based on the paper *Spatially separated polar samples of the cis and trans conformers of 3-fluorophenol*, T. Kierspel, D. Horke, Y.-P. Chang, and J. Küpper, *Chemical Physics Letters* **591**, 130–132 (2014).

I conducted the measurements together with D. Horke. I conducted the data analysis and the simulations. Together with the other authors, I discussed the results and I wrote the published article.

### 3. Conformer separation of gas-phase molecules

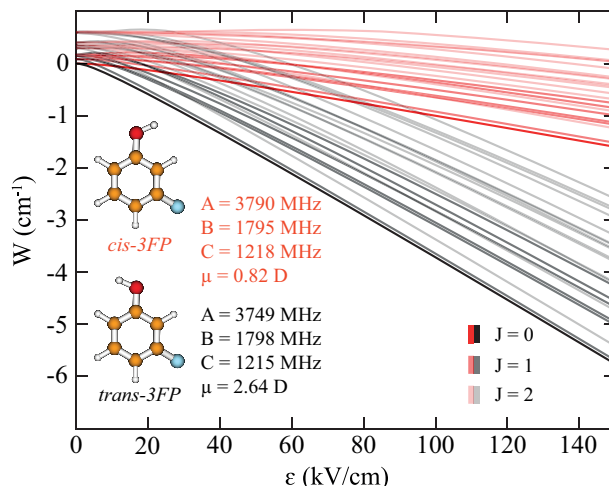


Figure 3.1: Stark-energies for the lowest rovibronic quantum states ( $J < 3$ ) of the *cis*- (red) and *trans*-conformer (black) of 3FP as a function of the electric field strength. The inset shows the molecular structures, the rotational constants [95, 96], and the calculated dipole moments of these conformers.

seeking.<sup>†</sup> Due to the different electric dipole moments of  $\mu = 0.82$  D and 2.64 D for *cis* and *trans*, respectively, the energy dependence of the molecular eigenstates as a function of electric field strength is quite different for the two conformers. The projection of the molecule-fixed dipole moment onto the electric field axis is the effective dipole moment  $\mu_{\text{eff}} = -\partial W/\partial \epsilon$ . The force exerted by an electric field on a polar molecule is  $\vec{F} = \mu_{\text{eff}}(\epsilon) \cdot \vec{\nabla} \epsilon$ <sup>‡</sup>. Thus, for a given inhomogeneous electric field *trans*-3FP is deflected more than *cis*-3FP. Moreover, the lowest energy rotational states are generally more polar, i. e., have a larger effective dipole moment  $\mu_{\text{eff}}$ , than higher-energy rotational states [38] and, therefore, are deflected more.

## 3.2 Experimental details

Figure 3.2 shows a schematic of the experimental setup [93]. In brief, 3FP was placed in a room-temperature Even-Lavie valve [63]. The molecules are coexpanded into the vacuum chamber at a repetition rate of 20 Hz in 50 bar of helium or 25 bar of neon, resulting in a supersonic expansion with a rotational temperature of the molecules of 1.5 K and 1 K, respectively. The molecular beam was collimated by two skimmers with diameters of 2 mm and 1 mm that were placed 5.5 cm and 21.5 cm downstream of the valve. Behind the second skimmer the molecular beam entered the electric deflector that provided an inhomogeneous electric field to disperse the molecular beam. A third skimmer with 1.5 mm diameter was placed directly behind the deflector. A time-of-flight mass-spectrometer was placed 30 cm downstream the

<sup>†</sup>Molecules in high-field seeking states have a negative Stark energy shift, i. e., their potential energy decreases with electric field strength. Thus, they have positive effective dipole moments (*vide infra*). Therefore, they orient along the electric field and they are attracted to regions of stronger electric field in order to minimize their energy.

<sup>‡</sup>The formula was mistakenly published with a wrong algebraic sign which has been corrected for.

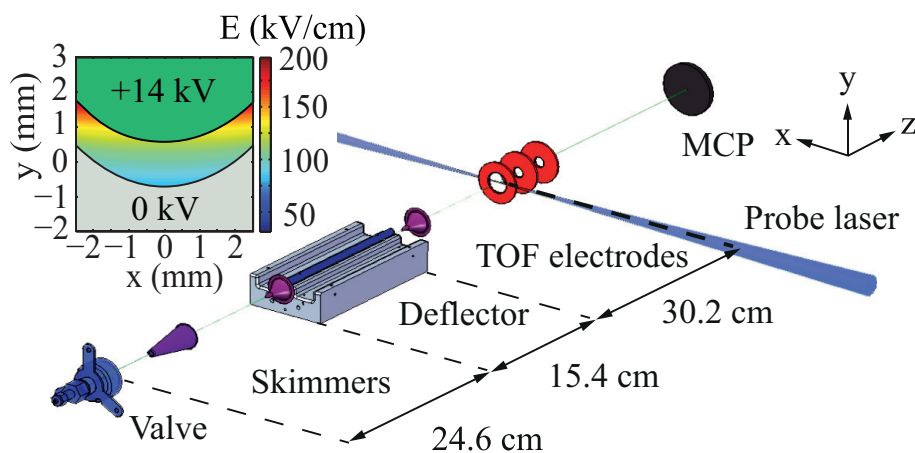


Figure 3.2: Schematic of the experimental setup consisting of a pulsed molecular beam source, a deflector, and a time-of-flight mass spectrometer. The inset shows a cut through the deflector and depicts the generated electric field.

deflector. A tunable pulsed dye laser (Fine Adjustment Pulsare Pro) provided approximately 400  $\mu\text{J}$  per pulse in a soft focus at the electronic origin transitions of  $36623\text{ cm}^{-1}$  and  $36830\text{ cm}^{-1}$  for *cis* and *trans*, respectively [98]. Individual conformers were selectively detected through resonance-enhanced two-photon ionization (R2PI) mass spectrometry. For the measurements of spatial molecular beam profiles the laser is sampled by moving the focusing lens in steps of 200  $\mu\text{m}$  in the *y*-direction.

*Ab initio* calculations (B3LYP/aug-cc-pVTZ) predict the *trans* conformer to be about  $55\text{ cm}^{-1}$  more stable than the *cis* conformer, in agreement with the  $85\text{ cm}^{-1}$  energy difference derived from a one-dimensionally torsional potential based on far-infrared spectroscopy [99]. The corresponding expected relative abundances of the *trans* and *cis* conformers in the molecular beam of approximately 2:1 agree with the experimentally obtained R2PI signal levels.

### 3.3 Results and discussions

Figure 3.3 shows the vertical molecular beam profile for *trans*-3FP seeded in helium for different voltages applied to the deflector. The height of the undeflected molecular beam (0 kV) is 2 mm, defined by the mechanical apertures of the deflector and the skimmers. When a voltage of 5 kV is applied to the deflector the beam is deflected upwards by approximately 0.4 mm for the *trans*-conformer. Increasing the voltage to 10 kV and 14 kV, the deflection increases to 0.8 mm and 1.4 mm, respectively. Solid lines show simulated spatial profiles obtained using the libcolmol package [93]. Only a single free parameter, the peak intensity of the undeflected beam, was adjusted to the experiment.

Figure 3.4 a) shows the deflection profiles of both conformers of 3FP seeded in helium for applied voltages of 0 V and 14 kV to the deflector. The *cis*-conformer was deflected significantly less than the *trans*-conformer. This leads to a spatial separation of the *trans*-conformer from the *cis*-conformer and from the original beam, e. g., the seed gas. The purity of the *trans* sample at various heights is shown in Figure 3.4 b).

### 3. Conformer separation of gas-phase molecules

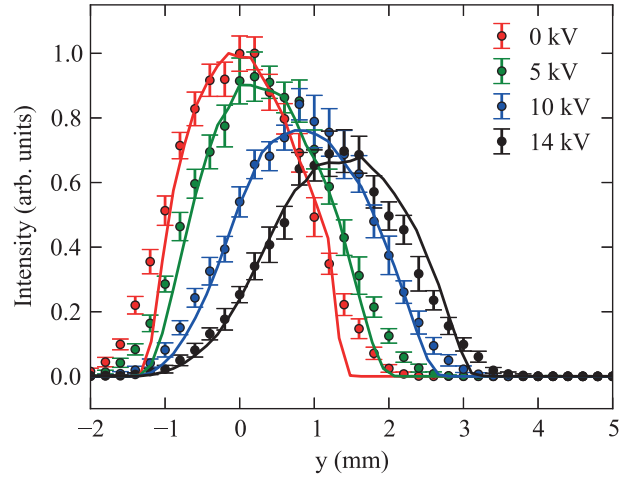


Figure 3.3: Spatial profiles for *trans*-3FP seeded in helium for different voltages applied to the deflector. The solid lines indicate simulated deflection profiles, the symbols are experimental values and the depicted ranges are their  $1\sigma$  standard deviation.

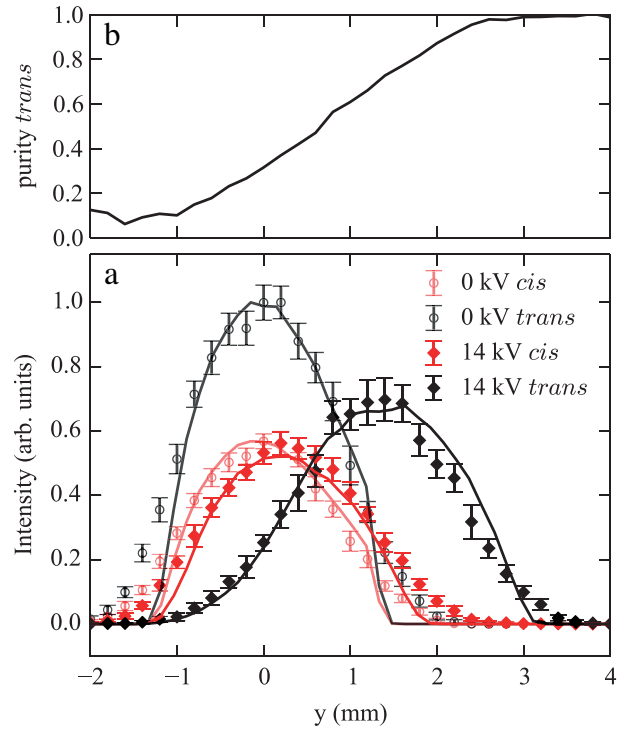


Figure 3.4: a) Field-free (0 kV) and deflected (14 kV) spatial beam profiles for the *cis* and the *trans* conformers of 3FP seeded in helium. b) The fractional population of the *trans* isomer in the beam.

Assuming similar excitation and ionization cross-sections for the two conformers, a beam of *trans*-3FP with a purity  $>95\%$  was obtained in the range of 2.5 mm to 3.5 mm. Around  $y = -0.8$  mm a nearly pure beam of *cis*-3FP was obtained, similar to previous measurements [10]. However, these samples correspond to high-energy rotational states that are not suited for the envisioned novel orientation and imaging

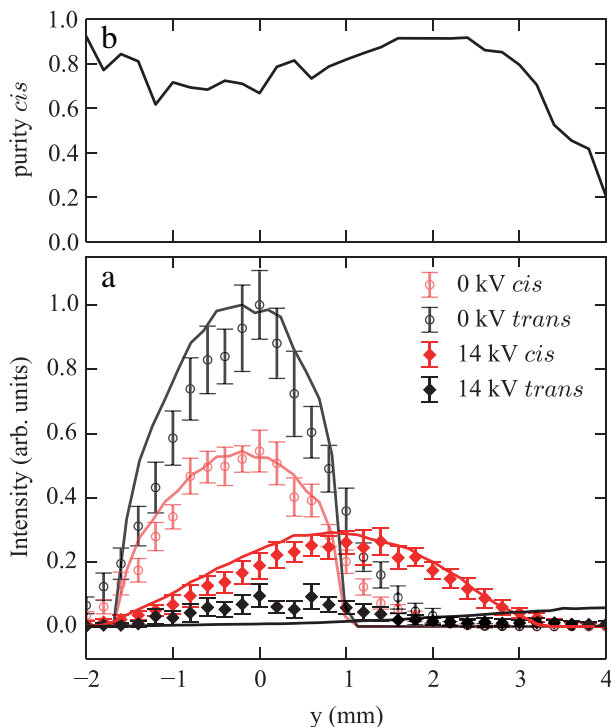


Figure 3.5: a) Field-free (0 kV) and deflected (14 kV) spatial beam profiles for the *cis* and the *trans* conformers of 3FP seeded in neon. b) The fractional population of the *cis* isomer in the beam.

experiments. Moreover, these molecules were still immersed in the atomic seed gas. In order to create a pure beam of low-energy rotational states of *cis*-3FP we increased the deflection by seeding the molecules in neon, resulting in a molecular beam with a speed of 900 m/s, half the speed of the helium expansion. The doubled interaction time resulted in a stronger deflection, as shown in Figure 3.5 a. For an applied voltage of 14 kV both conformers were strongly deflected. For the originally very cold molecular beam the deflection of *trans*-3FP was so strong that most molecules crash into the rod electrode and are lost from the beam. For the *cis* conformer, however, a strong deflection out of the seed gas beam was observed. For  $y = 1.5\text{--}2.5$  mm a beam of *cis*-3FP with a purity  $>90\%$  with all molecules in the lowest-energy rotational states was obtained, see Figure 3.5 b, even though this conformer was less abundant in the original beam (*vide supra*). The remaining signal strength at position 1.5 mm was 40 % of the maximum of the field-free case. The amplitudes for each conformer are normalized to the laser intensity. The remaining contribution from *trans*-3FP for  $y < 2$  mm is attributed to warm molecules that diffuse into the detection region after colliding with the deflector rod.

### 3.4 Conclusions

In summary, we have demonstrated the spatial separation of the *cis* and *trans* conformers of 3FP and the generation of cold, low-energy rotational state samples of both conformers of 3FP. These results demonstrate the feasibility to create pure samples of both conformers of this prototypical large

### 3. Conformer separation of gas-phase molecules

molecule using the electric deflector, allowing for strong three-dimensional alignment and mixed-field orientation [97]. These samples will allow direct molecular-frame imaging experiments on all structural isomers to disentangle the structure-function relationship for the conformer interconversion. This could be investigated through molecular frame photoelectron angular distributions and electron or x-ray diffraction experiments [15, 18, 25, 27, 28, 32].

## 4 Alignment at 4<sup>th</sup> generation light source\*

The following chapter is based on the publication [100] and shows the preparation of aligned molecular samples at the full repetition rate of free-electron lasers (FELs) utilizing a commercial Ti:Sapphire laser (TSL) system. The chapter starts with the introduction, putting the experiment into context with other experiments and motivates why alignment at high repetition rates is important for FEL experiments, followed by a short description of the experimental setup section 4.2. The results of laser-alignment at the FEL and laboratory based results are presented in section 4.3 and section 4.4, showing an measured degree of alignment of  $\langle \cos^2\theta_{2D} \rangle = 0.85$  respectively  $\langle \cos^2\theta_{2D} \rangle = 0.94$ . Both experiments were performed under similar alignment laser conditions but with different experimental setups concerning the molecular beam, leading to a warmer beam in the former case, which is discussed in section 4.5. A summary and outlook for future experiments is presented in section 4.6.

### 4.1 Introduction

Imaging the structural dynamics of gas-phase molecules using approaches such as photoelectron imaging in the molecular frame [15, 18, 101], high-harmonic-generation spectroscopy [102, 103], laser-induced electron diffraction [104, 105], electron diffraction [32, 88], or x-ray diffraction [25, 27, 106] is much improved or is only possible by fixing the molecules in space [25, 27, 28, 32, 35, 106]. Various approaches to align or orient molecules have been demonstrated, ranging from state-selection [92] over brute-force orientation [107] to laser alignment [35]. Generally, laser alignment has been implemented in two different regimes, namely, using short laser pulses to “impulsively” create coherent rotational wavepackets that generate alignment some time after the laser pulse [108, 109] or using long laser pulses to “adiabatically” create pendular states that are strongly aligned during the laser pulse [110]. In the former approach, pulses from standard commercial TSL systems can be utilized at repetition rates up to several kilohertz, whereas in the latter approach, traditionally, injection seeded Nd:YAG lasers were employed, with hundreds of millijoules of pulse energy, limited to a few 10 Hz. Through the addition of weak dc electric fields, strong orientation can be achieved in both scenarios [38, 90, 93]. Three-Dimensional (3D) alignment or orientation was also demonstrated [38, 93, 111–114]. It was shown that the degree of alignment necessary for molecular-frame diffractive imaging is very high [27, 28, 115] and, for complex molecules, could not be achieved with impulsive alignment approaches. Generally, the degree of alignment can be improved through higher

---

\*This chapter is based on the paper *Strongly aligned gas-phase molecules at free-electron lasers*, T. Kierspel, J. Wiese, T. Mullins, J. Robinson, A. Aquila, A. Barty, R. Bean, R. Boll, S. Boutet, P. Bucksbaum, H. Chapman, L. Christensen, A. Fry, M. Hunter, J. Koglin, M. Liang, V. Mariani, A. Morgan, A. Natan, V. Petrovic, D. Rolles, A. Rudenko, K. Schnorr, H. Stapelfeldt, S. Stern, J. Thøgersen, C. Yoon, F. Wang, S. Trippel, J. Küpper, *Journal Of Physics B-Atomic Molecular And Optical Physics* **48**, 204002 (2015).

I was conducting the experiments jointly with the other authors, and was primarily responsible for the molecular beam. I discussed the results with the other authors together, and I wrote the published article.

#### 4. Alignment at 4<sup>th</sup> generation light source

laser-field intensities, limited by the onset of ionization, or colder samples [116], possibly achieved through state selection [38, 90, 93].

The intermediate-pulse-duration regime, for which the alignment laser pulse duration is shorter than the lowest rotational period of the molecule, but cannot be considered impulsive anymore, had previously been analyzed theoretically [37, 117, 118]. While the laser pulse is still on, the molecules act similar to the adiabatic alignment case, whereas after the pulse periodic revivals can be observed [37]. Recently, this mesobatic regime was explored experimentally and it was realized that degrees of alignment comparable to the adiabatic limit can be achieved with much shorter and weaker laser pulses, e. g., from commercial chirped-pulse-amplified (CPA) TSL systems [119, 120]. While the nonadiabatic interaction creates interesting dynamic phenomena such as the observation of pendular motion [120], this approach does provide strongly aligned samples of complex molecules [119]. Moreover, it requires only moderately long pulses on the order of 100 ps with moderate pulse energies, i. e., a few mJ, which are available as output from the standard laser systems available at x-ray laser facilities.

Here, we demonstrate the successful implementation of intermediate-pulse-duration regime, strong alignment of the prototypical asymmetric rotor molecule 2,5-diiodothiophene ( $C_4H_2I_2S$ ) in a molecular beam at the Coherent X-ray Imaging (CXI) [121, 122] endstation of the Linac Coherent Light Source (LCLS) at the SLAC National Accelerator Laboratory (SLAC). Previous experiments with fixed-in-space molecules at FELs have exploited both, impulsive and adiabatic alignment, for instance, in ion imaging [52, 123], electron imaging [17, 18, 20, 124], or x-ray diffraction experiments [25, 26]. Our approach allows one to combine the strong alignment achieved in adiabatic alignment approaches [17, 18, 20, 25, 26] with the utilization of x-ray pulses at the full repetition rate of the LCLS [52, 124]. This allowed to perform experiments at 120 Hz, comparable to previously demonstrated intermediate regime alignment at 1 kHz in table-top experiments [119]. For comparison, we also provide measurements for the degree of alignment from experiments conducted in our laboratory at the Center for Free-Electron Laser Science (CFEL) [119] during the beam time preparation.

## 4.2 Experimental Setup

Figure 4.1 shows a sketch of the experimental setup at LCLS. A trace of 2,5-diiodothiophene was coexpanded in 80 bar helium into the vacuum by a pulsed valve [63], operated at and at a repetition rate of 120 Hz synchronized to the LCLS. The molecular beam was skimmed 8 cm downstream the nozzle using a 3-mm-diameter skimmer. This resulted in a 5.2 mm molecular beam (full width at half maximum, FWHM) in the interaction zone.

Near-infrared (IR) laser pulses were produced in a CPA TSL system (Coherent) with a central wavelength of 800 nm. The laser system is operated at and synchronized to the repetition rate of LCLS. The chirped pulses out of the regenerative amplifier were split using a beam splitter with a reflectivity of 90 %. The reflected pulses, which were used to align the molecules [119, 120], had a pulse energy of 3.3 mJ and a

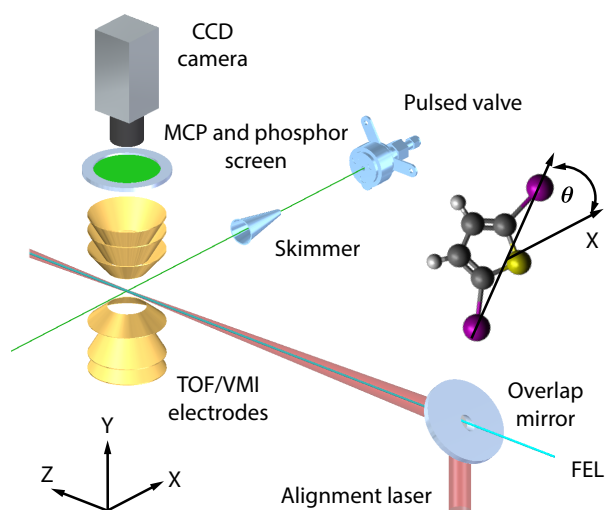


Figure 4.1: Sketch of the experimental setup showing the pulsed molecular beam valve, the laser beam path of the alignment laser (red) and the free-electron laser (cyan), and a holey mirror to collinearly overlap both beams. The detection system consists of an ion-imaging setup for time-of-flight measurements and velocity-map imaging onto a micro-channel plate, phosphor screen, and a CCD camera. In the inset the definition of  $\theta$  is depicted, it is the angle between the laser polarization, i. e., the  $X$  axis, and the most polarizable axis of the molecule, i. e., the iodine-iodine axis.

pulse duration of 94 ps (FWHM). The transmitted pulses were compressed using a standard grating-based compressor to a pulse duration of 55 fs (FWHM) at a pulse energy of 250  $\mu$ J. The compressed pulses multiply ionize the molecules through strong-field ionization, resulting in Coulomb explosion; in all experiments these compressed pulses were linearly polarized, with the polarization perpendicular to the long axis of polarization of the alignment laser pulses (*vide infra*). Both arms were spatially and temporally recombined before entering the vacuum system. This, in combination with ion imaging (*vide infra*), allows to characterize and optimize the degree of alignment without the FEL beam.

The short pulses were also utilized to measure the pulse duration of the alignment laser pulses through spectral interference. The frequency components of the chirped pulse arrive sequentially, whereas all frequencies in the compressed pulse are temporally overlapped. At finite spectrometer resolution, interference in the combined spectrum is only visible at those wavelength components of the alignment pulse that are temporally overlapped, or nearly overlapped, with the compressed pulse. The strongest interference is visible at the wavelength that temporally coincides with the compressed pulse. A delay line was used to change the relative timing between the chirped alignment and the compressed pulses. Thus, monitoring the spectrum in dependence of the delay between these two pulses provided information on the pulse duration of the chirped pulse.

To reach sufficiently high intensities to align the molecules, a telescope was used to expand both beams by a factor of three before being focused into the chamber with a 1-m-focal-length lens. A holey mirror was

#### 4. Alignment at 4<sup>th</sup> generation light source

used to spatially overlap the TSL pulses with the FEL beam path, losing 20 % of the near-infrared laser power. The hole had a diameter of 2 mm and the FEL beam was guided through the hole to achieve a collinear propagation of both beams. The alignment laser focus size was 45  $\mu\text{m}$  (FWHM) leading to an estimated peak intensity at the focus on the order of  $1 \cdot 10^{12}$  W/cm<sup>2</sup>. The FEL beam size was estimated to 12  $\mu\text{m}$  in the horizontal and 3  $\mu\text{m}$  in the vertical axis. The different beam diameters made the setup more stable against beam pointing imperfections and ensured that only well aligned molecules were probed with the FEL. The alignment laser pulse and the FEL/TSL pulses were spatially and temporally overlapped in order to maximize the degree of alignment; the exact timing was not critical [119].

The alignment laser beam was elliptically polarized with an aspect ratio of 3:1 in order to obtain 3D alignment. The major axis was parallel to the micro-channel plate (MCP) and phosphor screen surface. That way the most polarizable axis of 2,5-diiodothiophene, i. e., the iodine-iodine axis, was confined to the  $X$  axis as can be seen in Figure 4.1. The degree of alignment was probed using x-ray pulses with a pulse duration of approximately 70 fs (FWHM), a photon energy of 9.5 keV, and a pulse energy of approximately 0.64 mJ ( $4.2 \cdot 10^{11}$  photons, beam line transmission 80 %, focussing mirror transmission 40 %) in the interaction zone. X-ray absorption is largely localized at one of the iodine atoms, followed by Auger cascades and intramolecular charge redistribution leading to Coulomb explosion of the molecule. The ions were accelerated by the electric field of the spectrometer (Figure 4.1) towards a position sensitive detector consisting of a MCP and a phosphor screen (Photonis). A CCD camera (Adimec Opal), operating at the FEL repetition rate, recorded single-shot ion distributions visible as light spots on the phosphor screen. A real time online monitoring software, implementing a peak finding [125] and centroiding [126, 127] algorithm, was used to identify and localize single ion hits on the detector. By measuring the transverse velocity distribution of the iodine cations, the degree of alignment is evaluated by determining  $\langle \cos^2 \theta_{2D} \rangle^\dagger$ , where  $\theta$  is defined as indicated in Figure 4.1 and  $\theta_{2D}$  is defined as indicated in Figure 4.3.

The detection system allowed to switch between a time-of-flight (TOF) [1] mode to determine the various fragment masses and a velocity map imaging (VMI) [2] mode to determine the ion angular distribution. In the VMI mode, a fast high-voltage switch (Behlke) was used to gate the phosphor screen on a single iodine charge state determined from the TOF mass spectrum (MS).

The experimental details for the comparison measurement performed at the CFEL are described in reference 119. In short, the molecular beam was triply skimmed before it entered a VMI spectrometer where it was crossed by the alignment and probe laser pulses. The distance from the valve to the interaction zone was approximately a factor of 3.5 longer than at the LCLS. The sample reservoir was heated to 40 °C and a stagnation pressure of 90 bar helium was applied. The alignment and probe laser pulses were provided by splitting the output of an amplified femtosecond TSL system into two parts. The alignment pulses were stretched, or, more accurately, overcompressed. This resulted in negatively chirped pulses with a duration of 485 ps (FWHM) and focused to a beam waist of 36  $\mu\text{m}$  times 39  $\mu\text{m}$  (FWHM). At

---

<sup>†</sup>The two-dimensional degree of alignment is defined as  $\langle \cos^2 \theta_{2D} \rangle = \int_0^\pi \int_{v_{min}}^{v_{max}} \cos^2(\theta_{2D}) f(\theta_{2D}, v_{2D}) dv_{2D} d\theta_{2D}$ , where  $f(\theta_{2D}, v_{2D})$  is the normalized 2D projection of the probability density.

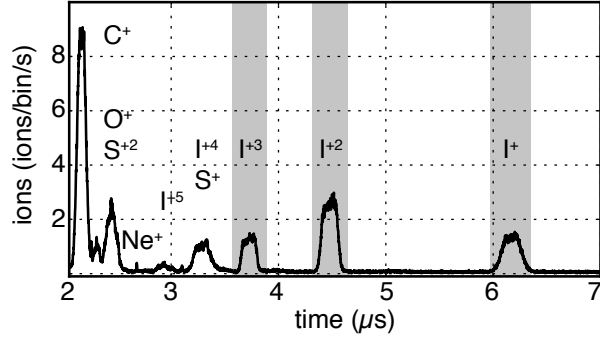


Figure 4.2: Time-of-flight mass spectrum of the ionic fragments produced in the Coulomb explosion of 2,5-diiodothiophene following absorption of a 9.5 keV x-ray photon. The gray areas indicate the gating windows for the VMI spectrometer used to determine the angular distribution for each fragment in Figure 4.3.

a maximum pulse energy of 7.4 mJ a focus peak intensity of  $9.6 \cdot 10^{11}$  W/cm<sup>2</sup> can be estimated. The temporal profile of the alignment pulse had a trapezoid-like shape, i. e., fast rising time (100 ps), longer plateau (400 ps), and fast falling time (100 ps). The alignment laser was elliptically polarized with an aspect ratio of 3:1. The probe pulses were compressed to 30 fs and focused to  $27 \times 28$  μm<sup>2</sup> (FWHM).

### 4.3 Results from experiments at LCLS

Following the absorption of a 9.5 keV x-ray photon the 2,5-diiodothiophene molecules charge up and fragment through Coulomb explosion. Figure 4.2 shows a time-of-flight (TOF) mass spectrum (MS) build up as a histogram of events from several thousand single-shot mass spectra. Clearly separated peaks for singly to triply charged iodine ions are visible, while the peaks for higher charge states of iodine ions overlap with other fragments. Based on this TOF spectrum, we have recorded angular distributions of the I<sup>+</sup>, I<sup>+2</sup>, and I<sup>+3</sup> fragments with the VMI spectrometer by gating the detector for the appropriate arrival times, as indicated by the gray areas in Figure 4.2.

In Figure 4.3 a sum of several thousand individually-processed VMI images for several iodine cation fragments of 2,5-diiodothiophene upon ionization with a 9.5 keV x-ray photon are shown. When the alignment laser was blocked, the image, Figure 4.3 a, shows a practically isotropic velocity distribution for triply charged iodine ions obtained from Coulomb explosion of randomly oriented molecules. As expected for the isotropic sample the measured degree of alignment is  $\langle \cos^2 \theta_{2D} \rangle = 0.50$ . Figure 4.3 b–d show the corresponding velocity distributions for triply, singly and doubly charged iodine fragments received from aligned molecules. The majority of detected ions is located at two distinct spots around  $\theta_{2D} = 0$  and  $\pi$ . The non-isotropic ion fragment distribution is a clear indication that the molecules are aligned along the *X* axis, the major axis of the polarization ellipse of the alignment laser. The velocity distributions show additional structure due to different fragmentation channels of 2,5-diiodothiophene upon x-ray ionization, but only the areas between the inner and outer white circles were used to determine the degree of alignment.

#### 4. Alignment at 4<sup>th</sup> generation light source

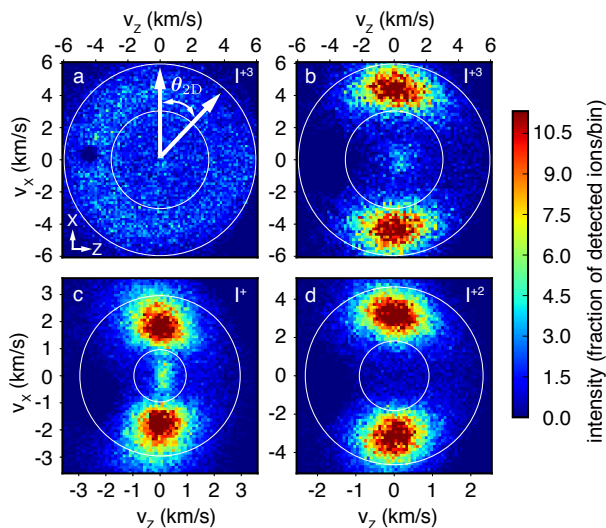


Figure 4.3: VMI images for (a) isotropic and (b–d) aligned iodine cations. The area between the inner and outer circle was used to determine the degree of alignment. The laboratory framework and the definition of the angle  $\theta_{2D}$  is shown in a). The dark spot in the left middle is due to a damaged area on the MCP, but it has no significant influence on our results; see text for details.

This corresponds to the fastest observed ion fragment for each iodine charge state. These fragments are a good measure of the degree of alignment since they are produced from molecules undergoing the fastest fragmentation, thus exhibiting the most-axial recoil. We point out that non-axial recoil would result in a smaller measured degree of alignment than actually exists and, therefore, that the measurements provide a lower limit for the actual degree of alignment. The resulting degrees of alignment for triply, doubly, and singly charged iodine cations are  $\langle \cos^2 \theta_{2D} \rangle = 0.85$ ,  $\langle \cos^2 \theta_{2D} \rangle = 0.84$ , and  $\langle \cos^2 \theta_{2D} \rangle = 0.82$ , respectively. The dark spot in the left part of the images, best visible in Figure 4.3 a), is due to a damaged area on the MCP. It has no significant influence on the measured degree of alignment as the velocity distribution of the ions, from aligned molecules, is peaked at  $\theta_{2D} = 0$  and  $\pi$ . The tilt of the  $I^{+n}$  ion distributions in the VMIs is attributed to imperfect imaging due to a off-center ionization.

#### 4.4 Results from experiments at CFEL

Figure 4.4 shows 2D momentum distributions for singly charged iodine (side view, vertical plane) and sulfur fragments (top view, horizontal plane) upon near-infrared (NIR) strong-field ionization (SFI) of 3D aligned molecules. The major (minor) axis of the alignment laser polarization ellipse was set along the X axis (Y axis). The corresponding spatial orientation of 3D aligned 2,5-diiodothiophene is indicated by the two molecules. For singly charged iodine ions three major Coulomb fragmentation channels are visible by the three maxima in the transverse velocity. The velocity distribution of the fragmentation channel with the highest kinetic energy (indicated by the white circles) was used to determine the degree

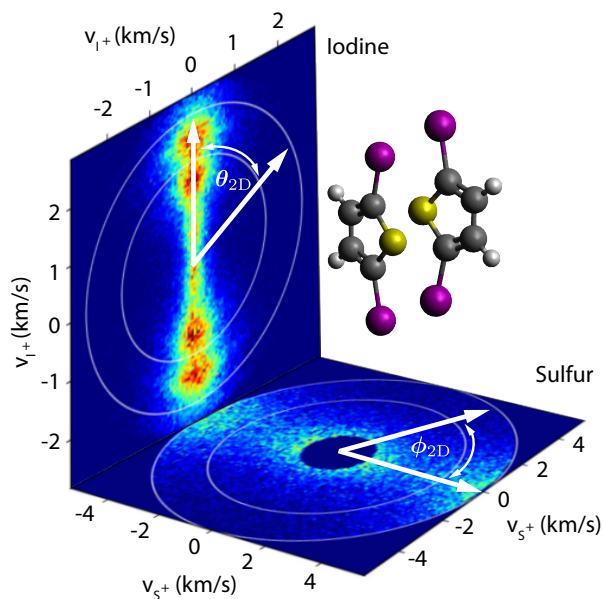


Figure 4.4: VMI images for singly charged iodine (side view, vertical plane) and sulfur (top view, horizontal plane) measured upon near-infrared strong field ionization. The two molecules sketch the 3D alignment. The area between the inner and outer white circles was used to determine the degree of alignment. Background from low-energy fragmentation channels were removed in the sulfur VMI. The color scale is the same as for Figure 4.3. The white arrows in the images depict the angles  $\theta_{2D}$  and  $\phi_{2D}$ .

of alignment as  $\langle \cos^2 \theta_{2D} \rangle = 0.94$ , reflecting the very strong alignment of the iodine-iodine axis. For the sulfur ions, two major fragmentation channels are observed. The slow channel, located in the center of the image, is significantly stronger in signal and has been removed to increase the contrast for the fast channel. The degree of alignment obtained from the velocity distribution of the fast sulfur ions is  $\langle \cos^2 \phi_{2D} \rangle = 0.79$ , reflecting the additional strong alignment of the molecular plane to the plane of polarization of the alignment laser.

In Figure 4.5 the degree of alignment of the iodine-iodine axis is shown as a function of the laser pulse energy, obtained from  $I^+$  momentum images. The typical power dependence of the degree of alignment for a cold beam is observed. The highest degree of alignment of  $\langle \cos^2 \theta_{2D} \rangle = 0.94$  is obtained at a peak intensity of  $9.6 \cdot 10^{11} \text{ W/cm}^2$ , but above  $7 \cdot 10^{11} \text{ W/cm}^2$  no significant change of the degree of alignment can be seen, indicating the saturation of the degree of alignment.

## 4.5 Discussion

The principal aim of the experiment performed at LCLS was to record the x-ray diffraction patterns of isolated gas phase molecules, similar to previous experiments [25, 26], which will be reported elsewhere. The experiments at CFEL were performed in preparation of that beamtime. Since in the diffractive

#### 4. Alignment at 4<sup>th</sup> generation light source

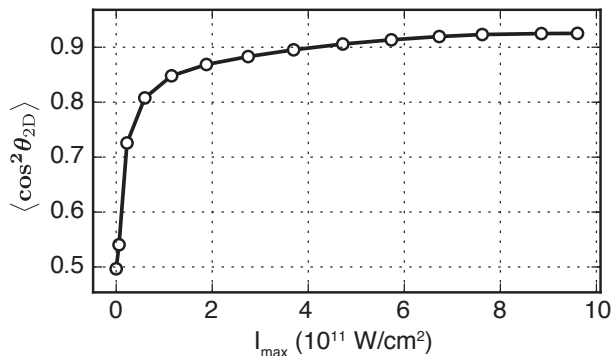


Figure 4.5: The degree of alignment for singly charged iodine as a function of the peak intensity of the alignment laser using a pulse duration of 485 ps (FWHM). This experiment was conducted at CFEL.

imaging experiment the amount of scattered photons scales linearly with the density of the molecules in the molecular beam, the experimental setup was designed such that the pulsed valve was located as close as possible to the interaction region for a collimated, dense, cold molecular beam. A density estimation of the molecular beam can be derived from the mass spectrum, Figure 4.2. To obtain a lower boundary for the molecular beam density it was assumed that all ionized molecules show two ionic iodine fragments and that the total ion-detection efficiency is 50 %. This led to an average of 8.6 ionized molecules per x-ray pulse. X-ray photons mainly interact with inner shells electrons and therefore the total molecular photo-absorption cross section is approximated by the sum of the individual atomic photo-absorption cross sections. At a photon energy of 9.5 keV the atomic photo-absorption cross sections are  $3.86 \cdot 10^{-20} \text{ cm}^2$  for iodine,  $3.05 \cdot 10^{-21} \text{ cm}^2$  for sulfur, and  $4.88 \cdot 10^{-23} \text{ cm}^2$  for carbon [24, 128]. The interaction length is given by the FWHM of the molecular beam. This results in a molecular beam density of  $1 \cdot 10^9$  molecules per  $\text{cm}^{-3}$ .

To determine the degree of alignment it was assumed that the iodine ions recoil along the most polarizable axis of the molecules, which is parallel to the iodine-iodine axis. This lead to an underestimation of the degree of alignment since positive charges can also be created at different locations in the molecule, for instance at the sulfur atom, leading to a non-axial recoil of the iodine ions. The difference in the degree of alignment between  $\text{I}^+$ ,  $\text{I}^{+2}$ ,  $\text{I}^{+3}$  can be explained by the stronger Coulomb repulsion for higher charge states, resulting in faster fragmentation. This provided a more instantaneous mapping of the molecular orientation. Thus a more accurate, less underestimated, value for the degree of alignment is measured for higher charged states.

For the 3D alignment measurement conducted at CFEL, the difference in alignment of the two different molecular axes ( $\langle \cos^2 \theta_{2D} \rangle$  vs.  $\langle \cos^2 \phi_{2D} \rangle$ ) is due to the fact that the most polarizable axis, the iodine-iodine axis, aligns along the long axis of the laser polarization, resulting in the strongest interaction. The second-most polarizable axis of the molecule aligns along the short axis of laser polarization, resulting in a somewhat weaker interaction. For the rigid molecule investigated here, the third axis can safely be

assume to be fixed with respect to the two others, and thus shows the same degree of alignment as the secondary axis. We note that all degrees of alignment are specified as projections on the experimental screen, as is typically done in experiments on comparably large and complex molecules [38, 119, 129, 130]. The difference between the measured degree of alignment at LCLS and CFEL can be understood as follows: The major factors that affect the achievable degree of alignment are the peak intensity of the alignment laser pulse, the rise time of the alignment laser pulse, and the rotational temperature of the molecules. Moreover, different probing schemes can influence the observed degree of alignment. Here, the alignment laser pulses, at LCLS and CFEL, are not expected to cause this big discrepancy. Generally, for a given laser peak intensity, the degree of alignment decreases with decreasing adiabaticity. To account for the non-adiabaticity of the molecular alignment, the rise time of the laser pulses and the peak intensities have to be examined. Both laser pulses had a comparable peak intensities in the focus. The rise times at LCLS and CFEL were 70 and 100 ps, respectively. Considering that the largest classical rotation period of the molecule is about 2 ns, it is expected that the alignment dynamics during the rising edges of the laser pulses at both experiments are similar. This is supported by the observed saturation of the degree of alignment for a cold molecular beam, at CFEL, for the investigated peak intensities.

An analysis of the degree of alignment of (complex) molecules in dependence of the pulse duration has not yet been performed, but from other experiments we have learned that the degree of alignment is nearly independent of the pulse duration for a given pulse energy, over a wide range of intermediate-regime durations, as long as ionization is avoided [120]. Generally, for complex molecules it will be most practical to obtain the optimal pulse duration, for maximum alignment, experimentally and corresponding experiments are forthcoming, especially in preparation of future campaigns at FELs.

The different probing schemes, i. e., single photon x-ray probe at LCLS and IR strong field ionization at CFEL, should both be reliable probing schemes and not cause the discrepancy in the measured degree of alignment. This was confirmed by NIR strong field ionization experiments at LCLS to probe the degree of alignment while no x-rays were available. Here, no significant changes in the degree of alignment compared to the one obtained by the single photon x-ray probe were observed under otherwise identical experimental conditions. Therefore, we conclude that the rotational temperature of the molecular ensemble causes the significant difference in the measured degree of alignment, an effect that was described in detail elsewhere [38, 116]. The temperature of the pulsed valve was approximately 35 °C higher at LCLS than at CFEL, which leads to a somewhat higher initial rotational temperature in the supersonic expansion. In addition the stagnation pressure of the helium seed gas was lower at LCLS than at CFEL, leading to a less efficient cooling in the expansion. Moreover, at LCLS the pulsed valve was only 18 cm away from the interaction zone, which is likely too short a distance to get a molecular beam without any collisions between the contained atoms and molecules [131], i. e., the molecular beam could not have reached its terminal temperature.

The achieved degree of alignment is slightly lower than the  $\langle \cos^2 \theta_{2D} \rangle = 0.89$  previously obtained at LCLS for a molecule with a similar polarizability anisotropy [25]. This can be attributed to the colder molecular

#### 4. Alignment at 4<sup>th</sup> generation light source

beam achieved in that experiment and the fully adiabatic alignment in the 10-ns-duration pulses provided by a 30 Hz Nd:YAG laser system. However, while the Nd:YAG laser system needed to be user supplied and required a special setup with significant technical challenges and safety implications, TSLs are generally available at FEL facilities for pump-probe experiments and typically support the full XFEL repetition rates.

Furthermore, the elliptically polarized laser pulses were expected to 3D align the molecules. The 3D alignment was not independently measured by ion-imaging at LCLS, but demonstrated by the experiments at CFEL using the same alignment laser polarization ellipticity. However, due to the warmer molecular beam at LCLS, the molecules are also expected to be less confined in 3D. The final analysis of the x-ray diffraction data will provide more details on this.

The described experiment should be directly extensible to larger (bio)molecules, such as the building blocks of life or small model peptides. These systems often have a polarizability anisotropy comparable to, or even larger than, the current sample and scalar polarizabilities that essentially scale with mass. The main obstacle for the molecular-frame investigation of such systems at FELs is the generation of cold ensembles with sufficient density. Related resolution limits of diffraction experiments had previously been discussed [132].

## 4.6 Summary

We have shown that it is possible to use the direct output from the regenerative amplifier of the in-house TSL at the CXI beamline at LCLS to strongly align molecules at the full LCLS repetition rate. We have measured a degree of alignment of  $\langle \cos^2\theta_{2D} \rangle = 0.85$ . We reasoned that the degree of alignment was limited by the intrinsic temperature of the molecular beam, which was optimized for increased diffraction signal, rather than by the alignment-laser parameters. We have presented evidence for 3D-alignment of our molecular sample. This allows to directly observe bond length and angles in the molecule in an x-ray diffraction experiment.

The demonstrated technique is advantageous to, for instance, Nd:YAG-laser-based alignment as it allows to utilize the full repetition rate of current FELs. Experiments at those facilities are expensive and by adapting this approach one makes optimal use of the limited beam time. Current FEL facilities already have synchronized TSL systems making the implementation of our setup fast, convenient, and, arguably, easy. Moreover, considering more complex experiments in a fs-laser-pump x-ray-probe scheme, or *vice versa*, it is possible to use different beams of the same optical laser source as alignment, pump, and probe pulses. This reduces the amount of lasers to be synchronized, the amount of possible sources of errors, and, therefore, makes the experiment overall more stable. Our approach will also allow to utilize a very large fraction, if not all, of the nearly 27 000 pulses per second at the upcoming European XFEL or the one million pulses of LCLS-II, solely depending on the availability of a synchronized high-repetition-rate millijoule-level near-infrared laser system at these facilities. We point out that our method does not rely on the presence of a well-defined molecular recoil-frame and, thus, has advantages over coincidence

techniques [133] for molecular-frame investigations of complex molecules, even at high repetition rates. Furthermore, the alignment approach allows for multiple isolated molecules in the interaction volume. Providing stretched pulses of high-power amplified TSL systems, for instance, with pulse energies on the order of 10 mJ and durations of  $\sim 1$  ns, would allow for investigations of strongly-aligned very large molecules, for instance, through coherent diffractive imaging.



## 5 X-ray diffractive imaging of controlled molecules

The following chapter describes an experiment where an ensemble of aligned gas-phase molecules was probed by hard x-ray photons, aiming at the structure determination of the molecules via x-ray diffraction. The experiment was conducted at the Coherent X-ray Imaging (CXI) [121, 122] endstation of the Linac Coherent Light Source (LCLS) at the SLAC National Accelerator Laboratory. The first part of the experiment, i. e., the long-pulse alignment of molecules at the full Free-Electron Laser (FEL) repetition rate is described in detail in chapter 4. The current chapter focusses on the diffraction signal recorded from that experiment. It starts with the motivation (section 5.1) and puts the concept of x-ray diffraction of isolated aligned gas-phase molecules into the context of other experiments. The experimental setup is briefly described section 5.2 with a focus on measurement of the diffraction signal, building up on chapter 4. Next, the simulated diffraction pattern of the molecules and the seeding gas is described in section 5.3, followed by an explanation of the data processing of the diffraction images recorded by the Cornell-SLAC pixel array detector (CSPAD) [134] (section 5.4). The recorded diffraction images are shown in section 5.5 and the results are discussed in section 5.6. The chapter closes in section 5.7 with a discussion of the current state of diffractive imaging of controlled gas-phase molecules and provides an outlook of the possibilities to study structural dynamics of controlled gas-phase molecules as well as the potential of using x-ray diffractive imaging to probe the structure of small biomolecules.

### 5.1 Introduction

Diffractive imaging of gas-phase molecules is a promising tool to unravel the intrinsic structural dynamics of gas-phase molecules on ultrafast timescales [27, 28]. Approaches like photoelectron imaging in the molecular frame [15, 18, 101], high-harmonic-generation spectroscopy [102, 103], laser-induced electron diffraction [104, 105], electron diffraction [32, 88], or x-ray diffraction [24, 25, 27, 51] are nowadays applied to probe the dynamics of dilute gas-phase molecular samples.

The development of ultrashort and intense hard x-ray laser pulses generated by FELs opens the possibility to conduct x-ray diffraction experiments on gas-phase molecules [25, 51, 135]. The pulse durations in the femtoseconds range allow one to study ultrafast structural dynamics and can outrun the radiation damage caused by the probing x-rays in the sample [49]. Radiation damage is induced in the sample via absorption of the x-ray photons, which lead to a destruction of the sample while it is still being probed by the x-ray pulse. If the fragmentation of the structure of interest within the sample is slower than the FEL pulse duration, the diffraction pattern still contains the structure of interest, which is termed ‘diffraction before destruction’ [49, 50].

In contrast to diffractive imaging of crystalline samples [50], gas phase molecules have a much lower density, are isotropically oriented in space and do have no fixed distances among each other. Thus, Bragg

## 5. X-ray diffractive imaging of controlled molecules

peaks, which do locally strongly increase the coherent part of the diffraction signal in crystallography, are not measurable. Instead, the signal measured by the detector is an incoherent sum of the molecule's individual diffraction pattern. Measuring or controlling the molecules orientation in space while the diffraction pattern is recorded is highly advantageous or simply necessary to retrieve the three-dimensional structure of the molecule. Ideally, the orientation of each molecule and their individual contribution to the diffraction image is known. In principle this could be done by probing single molecules [49] and subsequently determining their orientation from the diffraction pattern [136–139] or, if their diffraction signal is too weak, by a simultaneously measurement of the ions' time-of-flight and velocity distribution in space. In the latter case it is possible to reconstruct the molecules' 3D orientation in their recoil frame as shown in chapter 6. This knowledge could be used to sum up the individual diffraction images by taking the molecules orientation into account. However, it is ultimately limited by the signal to noise ratio, and becomes impractical for small gas-phase molecules since their diffraction signal is too weak. Alternatively, measuring the molecules diffraction pattern can be achieved by probing an aligned ensemble of molecules [25, 26]. In that case the diffraction patterns of the individual molecules are incoherently added in a common alignment. The signal is thus amplified due to the many particles in the beam (as in crystallography), but without the interference between Bragg peaks, which leads to the measurement of the entire reciprocal space of the molecule [140].

Electron diffractive imaging is conceptually very close to x-ray diffraction. Utilizing electrons instead of x-rays for a diffraction experiment has the advantage of orders of magnitude higher coherent scattering cross sections at a comparable spatial resolution. Also, the generation of electrons with a short de Broglie wavelength is comparatively easy, considering that electrons with an energy of 150 eV already have a de Broglie wavelength of 0.1 nm (equivalent to an x-ray photon energy of 12.4 keV). This lead to the development of small laboratory based electron diffraction setups, such as those developed within the CMI group [141]. The drawbacks of electron diffractive imaging are the Coulomb forces between the electrons, which lead to a temporal and spatial broadening of the electron pulse, and therefore limit the number of electrons per pulse [142]. Further, a velocity mismatch between an electron and a laser pulse in a pump-probe experimental scheme does limit the temporal resolution due to the electrons velocity, which is always slower than the speed of light [143]. Both problems can be partially suppressed by the use of relativistic electrons, which are now available at larger electron facilities [144, 145]. In general, electron diffractive imaging is sensitive to full Coulomb potential within a molecule, whilst x-ray diffraction is sensitive mostly to the electron density within a molecule. Both are thus complementary experimental approaches.

In the presented experiment 2,5-diiodothiophene ( $C_4H_2I_2S$ ) molecules were seeded in 80 bar helium and expanded into vacuum. The molecules were aligned by an uncompressed laser pulse generated by an Ti:Sapphire laser system. The molecular degree of alignment was probed by velocity map imaging [2–5], which is in detail explained in chapter 4 [100]. The aligned ensemble of molecules and the carrier gas were probed by hard x-ray photons at a photon energy of 9.5 keV ( $\lambda = 130$  pm) and diffraction images were

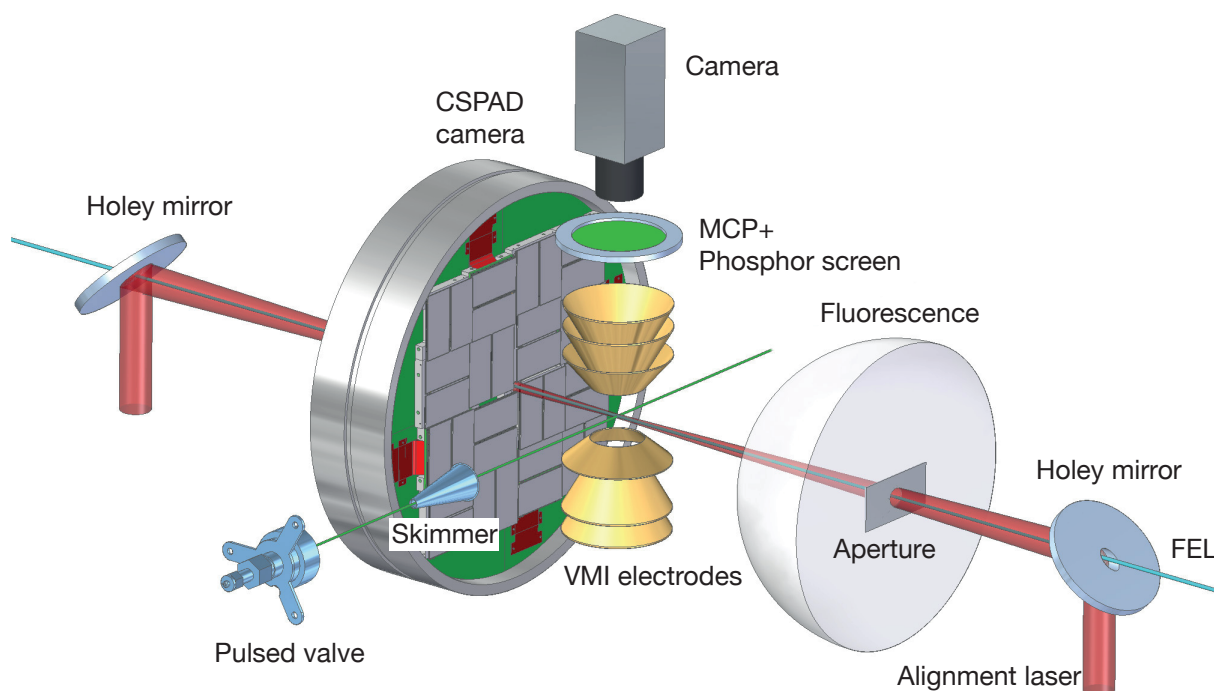


Figure 5.1: Sketch of the experimental setup showing the pulsed valve, skimmer and the molecular beam axis indicated by the green line, which is crossed by the FEL (cyan) and the alignment laser (red). The FEL and alignment lasers were spatially overlapped by a holey mirror and transmitted through a hole in the CSPAD camera, which was used to record the diffraction pattern of the molecules. The ion detection system consisting of VMI electrodes, an MCP and phosphor screen and a camera were used to measure the degree of alignment of the molecules. Fluorescence photons, indicated by the half-sphere, were induced in the aperture by photons from the beamline.

recorded by the Cornell-SLAC pixel array detector (CSPAD) [134]. The diffraction image consists of an incoherent sum of the molecules' and the helium diffraction pattern, where the latter one is considered as background. The goal of the experiment was to measure 2D slices through the diffraction volume of 2,5-diiodothiophene.

## 5.2 Experimental setup

The experimental setup is shown in Figure 5.1 [100]. It is the same setup as described in detail in section 4.2, but it shows additional elements such as the aperture, the Cornell-SLAC pixel array detector (CSPAD) [134] and the out-coupling mirror.

A trace of 2,5-diiodothiophene molecules was placed within the sample reservoir of a pulsed valve [63] and heated to a temperature of 75 °C. The molecules were seeded in 80 bar helium and expanded into vacuum at a repetition rate of 120 Hz, matched to the repetition rate of the FEL. The molecular beam was singly skimmed at a distance of 8 cm from the pulsed valve with a 3-mm-diameter skimmer, which resulted in a

## 5. X-ray diffractive imaging of controlled molecules

5.2 mm molecular beam (FWHM) in the interaction zone.

The FEL was operating at a photon energy of 9.5 keV ( $\lambda = 130$  pm) with a pulse energy of approximately 0.64 mJ ( $4.2 \cdot 10^{11}$  photons, beamline transmission 80%, focussing mirror transmission 40%), a pulse duration of approximately 70 fs (FWHM), and a repetition rate of 120 Hz. It was transmitted through the hole of a holey mirror, which was used to spatially overlap the FEL with the alignment laser (Coherent CPA TSL system, pulse energy 3.3 mJ, pulse duration 94 ps (FWHM), Figure 5.1 [100] ) and, thus, to collinearly propagate both beams toward the interaction zone. The FEL was placed temporally in the center of the alignment laser pulse. An iron aperture with a central hole was placed before the interaction zone to reduce background photons from the beamline on the detector. The background photons induced unwanted fluorescence in the iron aperture. These fluorescence photons were emitted at a photon energy of 7 keV and are indicated by the spherical wave originating from the aperture. After passing the aperture, the molecules were aligned by the 94 ps long alignment laser pulse and their structure was probed by the FEL. The alignment of the molecules was probed via velocity map imaging [136–139] of certain fragments of the molecule, corresponding details can be found in chapter 4 [100]. Diffracted photons were recorded with the CSPAD camera, which was placed  $\approx 8$  cm downstream of the interaction zone. The detector consisted of 2.3 megapixel in total, is built up of 64 application-specific integrated circuits (ASICs) with a resolution of  $185 \cdot 194$  pixel each, and has a read-out speed of 120 frames per second. The FEL beam was transmitted through a hole in the center of the detector and was guided toward a beam dump. The alignment laser was guided through the same hole of the detector and sent outside of the vacuum chamber via a holey mirror to reduce the number of back-scattered photons on the detector.

### 5.3 Simulations

The simulations for this experiment were carried out using the CMIDiffract code, which was developed within the CMI group to simulate the diffraction of x-rays/electrons off gas-phase molecules [24–26, 29]. The molecular cross section can be approximated by the sum of the atomic cross sections [24–26, 43]. Hence, the cross sections for all relevant atoms in this experiment are shown in Table 2 [128] for a photon energy of 9.5 keV. The incoherent scattering cross section ( $\sigma_{\text{inc}}$ ) for hydrogen as well as helium is bigger than the coherent scattering cross section ( $\sigma_{\text{coh}}$ ), and comparable in the case of carbon. For heavier atoms like sulfur or iodine coherent scattering is the dominant process. The photoelectric absorption cross sections ( $\sigma_{\text{abs}}$ ) are shown here for comparison and will be discussed again in section 5.6. From Table 2 it is evident, that the photoelectric absorption is the dominant process for heavier atoms. In the case of 2,5-diiodothiophene, the total ratio of coherent and incoherent cross section is 31, i. e., scattering is dominated by the coherent scattering. In contrast, the ratio for helium is only 0.4. Since helium was the seeding gas of the molecules, and no deflector was used to separate molecules and helium [28], it was much more abundant in the interaction zone and can therefore not be neglected. Figure 5.2 shows the simulated

Table 2: Atomic and molecular cross sections at a photon energy of 9.5 keV for coherent and incoherent scattering as well as photoelectric absorption [128]

Atom/Molecule	$\sigma_{\text{coh}}(10^{-24}\text{cm}^2/\text{atom})$	$\sigma_{\text{inc}}(10^{-24}\text{cm}^2/\text{atom})$	$\sigma_{\text{abs}}(10^{-24}\text{cm}^2/\text{atom})$
Hydrogen	0.04520	0.5965	0.0054
Helium	0.4267	1.043	0.2306
Carbon	3.431	2.653	48.82
Sulfur	40.73	5.451	3045
Iodine	619.5	12.13	38560
2,5-diiodothiophene	1293.5	41.52	80360

diffraction pattern of 2,5-diiodothiophene for a) an unaligned ( $\langle \cos^2\theta_{2D} \rangle^* = 0.5$ ), b) well aligned ( $\langle \cos^2\theta_{2D} \rangle = 0.81$ ), c) a perfectly aligned ensemble of molecules ( $\langle \cos^2\theta_{2D} \rangle = 1$ ). The color code is given in photons per pixel. The degree of alignment chosen in Figure 5.2 b) is equivalent to the measured degree of alignment before and in between the diffraction measurements recorded of 2,5-diiodothiophene (section 5.5). The insets of the molecules show a sketch of the aligned molecules ensemble, neglecting the misalignment in the third dimension (perpendicular to the  $x - y$  plane), and the rotation of the molecule around the alignment laser polarization. In the experiment the molecules were 3D aligned with an elliptically polarized laser, see chapter 4 [100]. The angle  $\alpha$  (Figure 5.2 c) is defined between the polarization of the FEL and the major axis of the alignment laser polarization and was set to  $66^\circ$ .

The simulations were performed based on experimentally determined parameters (chapter 4) such as a molecular beam density of  $1 \cdot 10^9$  molecules per  $\text{cm}^{-3}$ , and a molecular beam diameter of 5.2 mm in the interaction zone. Also included is the polarization of the FEL, visible by the vertically (horizontally) stretched (squeezed) diffraction pattern in Figure 5.2 a), the  $4.2 \cdot 10^{11}$  photons per FEL pulse at a photon energy of 9.5 keV, and the geometry and distance of the CSPAD camera. Additionally, the simulations are multiplied by the number of shots acquired during the experiments (section 5.5). The structure for 2,5-diiodothiophene was calculated using the GAMESS-US MP2/6-311G\*\* level of theory, and can be found in section A.1.

The strongest contribution in the diffraction pattern is due to interference between the two iodine atoms of the molecule, as expected due to the high coherent scattering cross section for iodine (Table 2). Thus, the diffraction pattern is dominated by two-point interference, similar to diffraction from a double-slit. For unaligned molecules, this diffraction pattern expresses itself as rings of constructive and destructive interference around the center of the image. The stronger the molecules are aligned, the more pronounced will be the interference fringes. The tilt of the double-slit like interference pattern arises from the alignment

\*The two-dimensional degree of alignment is defined as  $\langle \cos^2\theta_{2D} \rangle = \int_0^\pi \int_{v_{min}}^{v_{max}} \cos^2(\theta_{2D}) f(\theta_{2D}, v_{2D}) dv_{2D} d\theta_{2D}$ , where  $f(\theta_{2D}, v_{2D})$  is the normalized 2D projection of the probability density.

5. X-ray diffractive imaging of controlled molecules

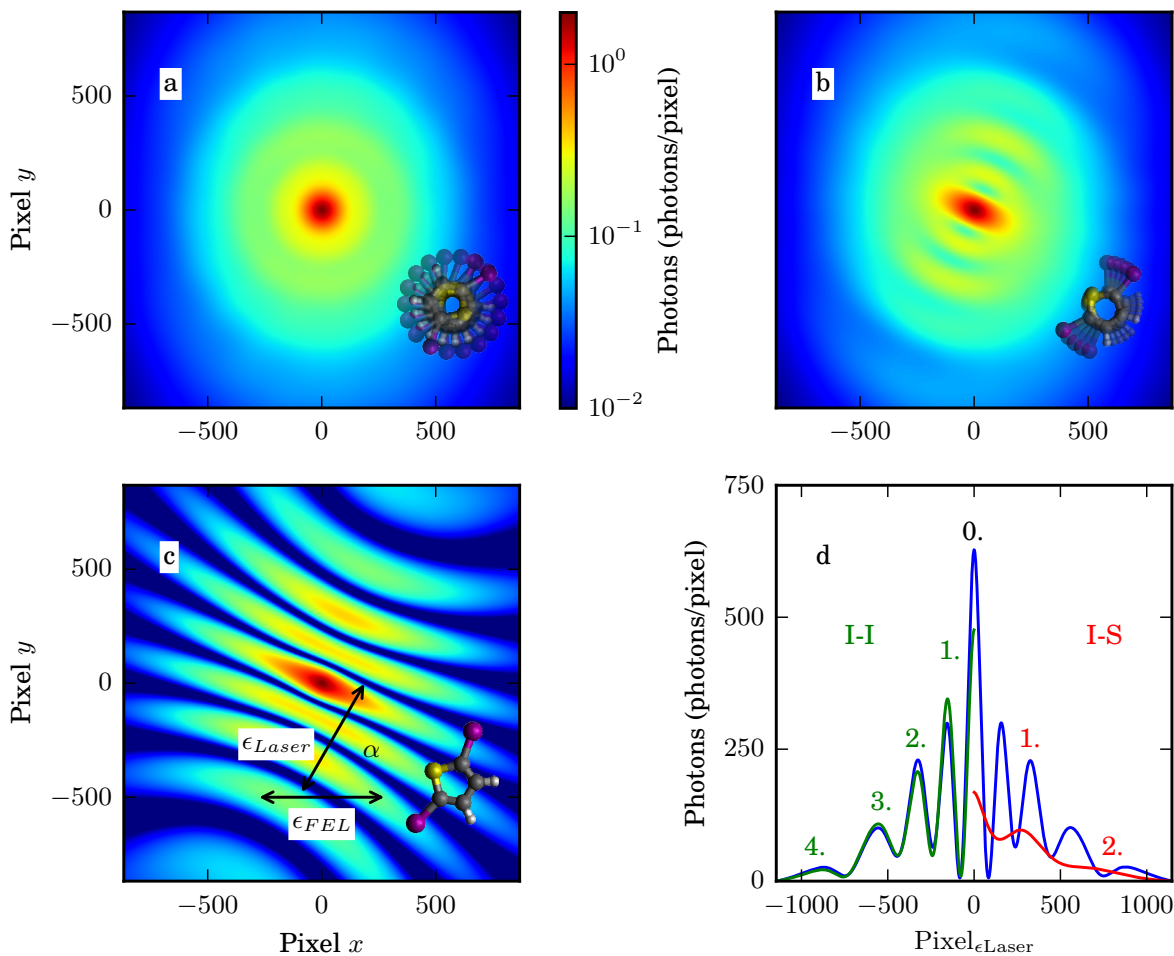


Figure 5.2: Simulated diffraction pattern of 2,5-diiodothiophene for a) an unaligned, b) strongly aligned and c) a perfectly aligned ensemble of molecules. d) A projection of c) perpendicular to the alignment axis of the molecule (blue). The green and red curve show the contribution of the iodine-iodine and iodine-sulfur interference term to the diffraction pattern.

of the molecules at  $66^\circ$  with respect to the FEL polarization. The distance between maximum/minimum is in linear relationship to the distance of the iodines within the coordinate space of the Ewald sphere. The increasing distance between the interference fringes (best visible in Figure 5.2 c) and d)) is due to the projection of the Ewald's sphere onto the flat detector. This projection explains as well the increasing bend of the interference fringes best visible in Figure 5.2 c). The color code is indicating that only the pixel in the central part do have a high probability of detecting more than one photon. Experimentally, the signal can be extracted by adding up several pixels, which reduces on one hand the resolution but, on the other hand, can drastically increase the number of photons per pixel area (section 5.5) [25, 26].

In Figure 5.2 d) a 1D diffraction pattern of Figure 5.2 c), projected onto the alignment laser polarization, is shown in blue. The iodine-iodine interference term contribution to the interference pattern is shown in the left part of the image, indicated by the green color. According to these simulations the first four

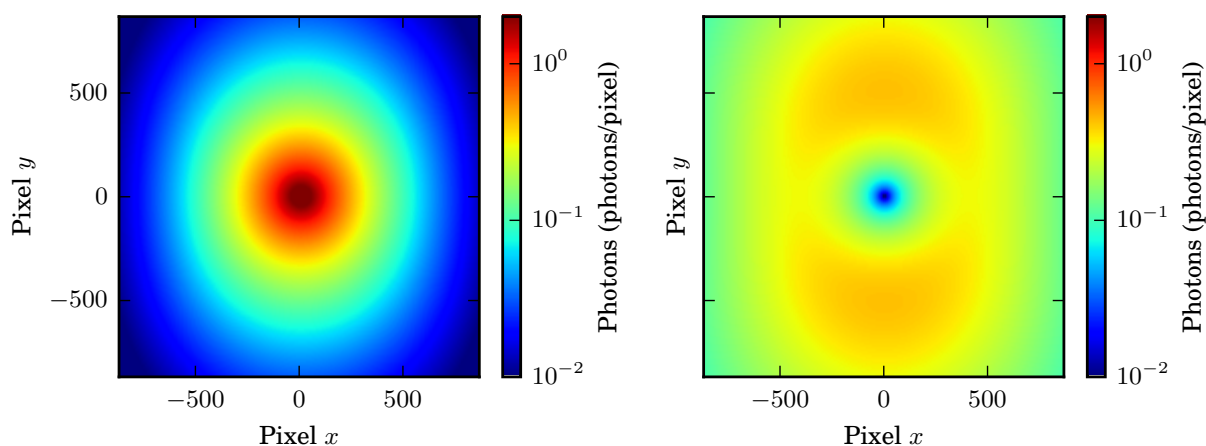


Figure 5.3: Simulated diffraction pattern of helium separated in its coherent (left) and incoherent (right) contributions to the diffraction signal.

orders of the constructive interference would be measurable with the detector under these experimental conditions. The iodine-sulfur interference pattern is the second strongest contributor to the diffraction pattern and is indicated by the red color in the right part of the graph. Their distance is roughly half of the iodine-iodine distance, and tilted by approximately 12 degrees with respect to the iodine-iodine axis (section A.1). In this case only the first two constructive interference maximum are expected to be measurable with this detector configuration.

The simulated diffraction pattern for helium, i. e., the seeding gas, is shown in Figure 5.3, separated by its coherent and incoherent contributions to the diffraction image. The simulation for the coherent (incoherent) diffraction is shown in the left (right), displayed with a logarithmic color scale. The FEL polarization dependent scattering is visible in both patterns as a modulation in the scattering intensity with the azimuthal component of the scattering angle, with a maximum along the vertical axis (at  $x = 0$ ) and a minimum along the horizontal axis (at  $y = 0$ ).

In the latter case a minimum is found in the center of the detector, i. e., in the case of forward scattering. This is a well known characteristic of inelastically scattered photons. A shift in photon energy corresponds to a shift in the momentum vector of the photon. If there is no shift in the energy of the scattered photon there will be no incoherent scattering and hence the photon is not incoherently scattered (section 2.4). The ratio between coherent and incoherent photons on the detector is approximately 0.51. It is slightly higher than the ratio for the coherent and incoherent cross section of helium (*vide supra*), which can be explained by the limited size of the detector.

The sum of the simulated diffraction patterns for helium (coherent and incoherent scattering) and for the molecular diffraction pattern, with a degree of alignment given by  $\langle \cos^2 \theta_{2D} \rangle = 0.81$  (see Figure 5.2 b)), is shown in Figure 5.4 a). The central part of the diffraction image has been suppressed to enhance the contrast in the rest of the image; the labels Q1-Q4 indicate the four different quadrants of the detector. The ratio between the number of helium and 2,5-diiodothiophene molecules was assumed to be between

## 5. X-ray diffractive imaging of controlled molecules

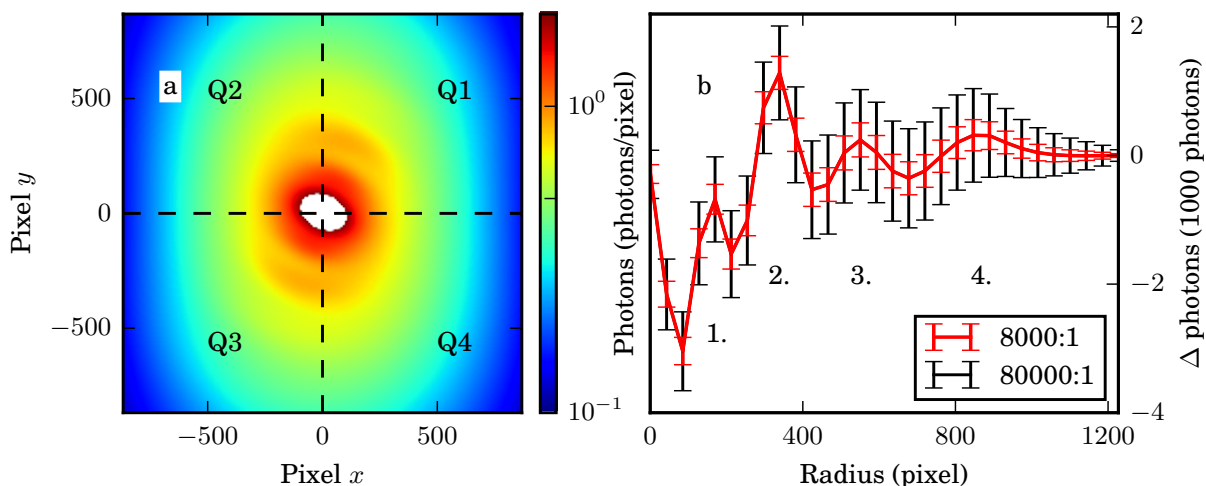


Figure 5.4: a) Sum of diffraction patterns of the molecule and the coherent and incoherent scattering of helium for a ratio of helium to molecule of 8000:1. The labels Q1-Q4 indicate the four different quadrants of the detector. b) Radial plot for  $(Q1_R + Q3_R) - (Q2_R + Q4_R)$  for two different He:Molecule ratios

8000:1 and 80000:1, with the former case shown in the simulated diffraction image. This ratio is based on the assumption, that the vapour pressure of 2,5-diiodothiophene is between 1 and 10 mbar at a temperature of 75 °C under an atmosphere of 80 bar helium. At the lower boundary, i. e., at a ratio of 8000:1, the simulations suggest that approximately  $1.2 \cdot 10^6$  scattered photons ( $\approx 0.52$  photons/FEL pulse) in the diffraction pattern originate from helium, compared to  $2.15 \cdot 10^5$  scattered photons ( $\approx 0.1$  photons/FEL pulse) from the molecule. It is evident that the molecular diffraction pattern in Figure 5.4 a) is barely visible by eye. This is a typical situation for diffraction experiments with molecular beams.

There are several ways to extract the molecular interference pattern from the 2D diffraction image. The following discussion will focus first on the 1D reconstruction of the molecular diffraction pattern, which utilizes the symmetry of the diffraction pattern, and was also the first step in the data analysis. The advantage of the 1D reconstruction is an increased signal to noise ratio per bin due to the collection of several thousand pixel into a single bin.

In Figure 5.2 it was shown that alignment of the molecular ensemble enhances the number of photons in top right (Q1) and lower left (Q3) part of the image. In contrast, the molecular scattering signal must be reduced in Q2 and Q4. The contribution of the carrier gas in the diffraction pattern is independent of the alignment laser and is thus equal in all quadrants. This can be utilized to generate differential plots between the quadrants, which is shown in Figure 5.4 b). The red curve shows the differential radial plot for  $(Q1_R + Q3_R) - (Q2_R + Q4_R)$ , where  $QX_R$  is the radial plot of a single quadrant. The error bars are given as the statistical error per bin; the line, which is connecting the different points, is simply given as visual aid. The four maxima of the iodine-iodine interference term are now clearly visible and are highlighted by the numbers 1-4. The strongest contribution to the differential radial plots of the molecular interference pattern is given by the second maximum; the first maximum is suppressed due to a strong contribution in

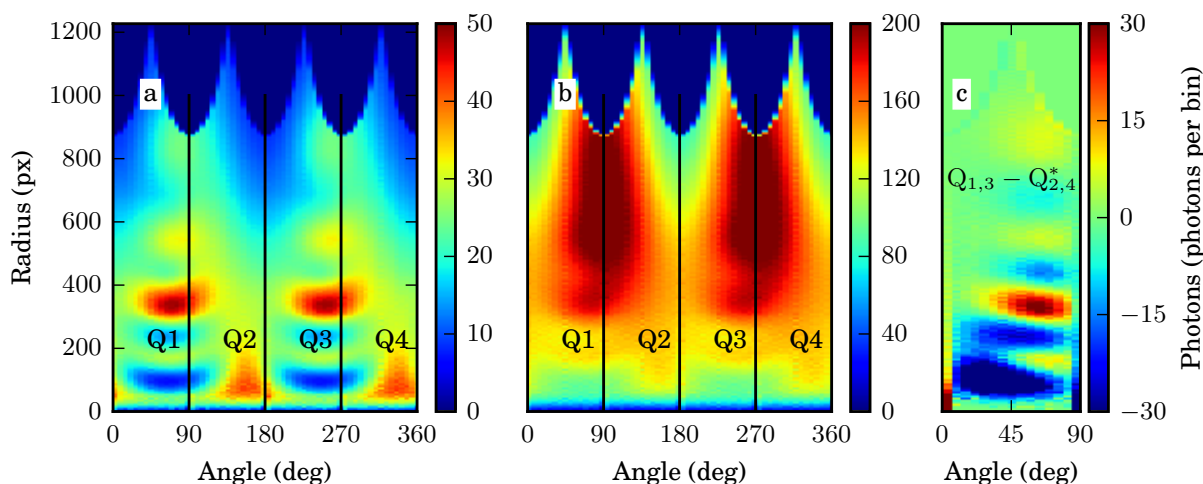


Figure 5.5: Diffraction images displayed in a polar coordinates. a) Molecular diffraction pattern for a molecular degree of alignment of  $\langle \cos^2 \theta_{2D} \rangle = 0.81$ . b) Same as a) including the coherent and incoherent contribution of the helium diffraction. c) Differential images of b), where  $(Q2+Q4)$  is added, and reversed in the  $x$ -axis before it is subtracted from  $(Q1+Q4)$

the central part of the diffraction image, which falls into quadrant one and three, visible, for instance, in Figure 5.2. The black error bars are given for a helium to molecule ratio of 80000:1. The increased amount of helium does not influence the shape of the molecular interference pattern but increases the error bars due to the higher number of background photons per pixel.

The symmetry of the diffraction image can also be utilized to extract a 2D diffraction image, which is shown in Figure 5.5. For those images the coordinate system has been changed from a Cartesian into a polar coordinate system. The angle is determined from the center of Figure 5.2 a) in a mathematical sense and different pixels were integrated, which lead to a 2D histogram with a resolution of 60 times 200. The different quadrants have been labeled, and the color code is given in photons per bin. In Figure 5.5 a) the polar plot of Figure 5.2 b) is shown, i. e., the molecular diffraction pattern for a molecular degree of alignment of  $\langle \cos^2 \theta_{2D} \rangle = 0.81$ . Similar to the 1D diffraction image in Figure 5.4 b) the second maxima shows here the strongest contribution, visible by the increased signal in Q1 and Q3 at a radius of approximately 350 pixel. The molecular diffraction pattern in Q1 and Q3, as well as in Q2 and Q4 is the same for symmetry reasons. Figure 5.5 b) shows additionally the contribution from the coherent and incoherent diffraction of helium. Visible are two strong maxima at an angle of  $90^\circ$  and  $270^\circ$  degree and a radius of approximately 500-900 pixel. These maxima are due to the polarization dependent scattering. As discussed in the case of the 1D diffraction pattern the helium contribution is symmetric around the borders of Q1/Q2 and Q3/Q4, which can be utilized to subtract the helium background. Both, Q1 and Q3 as well as Q2 and Q4 do have the same diffraction image and can thus be added up to  $Q_{1,3}$  and  $Q_{2,4}$  to increase the statistics. To cancel out the contribution of the helium diffraction pattern the  $x$ -axis (angle) has to be reversed in, for example,  $Q_{2,4}$ , which is then subtracted from  $Q_{1,3}$ . This is shown in Figure 5.5

## 5. X-ray diffractive imaging of controlled molecules

c), where  $Q_{2,4}^*$  is indicating the reversed  $x$ -axis of  $Q_{2,4}$ . The second maxima is now clearly visible at an angle of  $66^\circ$  and a radius of approximately 350 pixel.

The presented 1D and 2D reconstructions of the diffraction image are not the ideal solutions because they rely on the symmetry of the background radiation. As will be discussed in the experimental results in section 5.5, the background radiation from the beamline, and the observed fluorescence signal was asymmetric. Typically, diffraction images of aligned and unaligned molecules are recorded and their difference is displayed [25, 26, 31]. This was not possible for the presented experiment due to the lack of recorded data as discussed in section 5.5.

### 5.4 CSPAD data handling

Before the scattering signal from 2,5-diiodothiophene could be analyzed the raw data from the CSPAD camera had to be converted into x-ray photons. The signal from the CSPAD camera is provided by a so called ADU (analog-to-digital-unit) value, which is simply the electronically measured signal in each pixel per frame. Considering the 2.3 megapixel of the detector, it was providing  $2.3 \cdot 10^6$  ADU values per frame. The camera was operating at 120 frames per second, and 5.2 hours of diffraction image as well as 1.76 hours of background measurement were acquired (section 5.5). Thus, in total  $7 \cdot 10^{12}$  ADU values were analyzed for the presented experiment. To convert an ADU count into a photon, the DC offset was first subtracted from each pixel (dark field calibration), than the gain of each pixel was calibrated via a flat field measurement (white field correction). Subsequently a pixel based ADU histogram was generated, and corrected by a DC shift to correct for the relative ADU offset between the pixel, followed by a calibration for the photon energy response of the CSPAD by filtering over the desired ADU range.

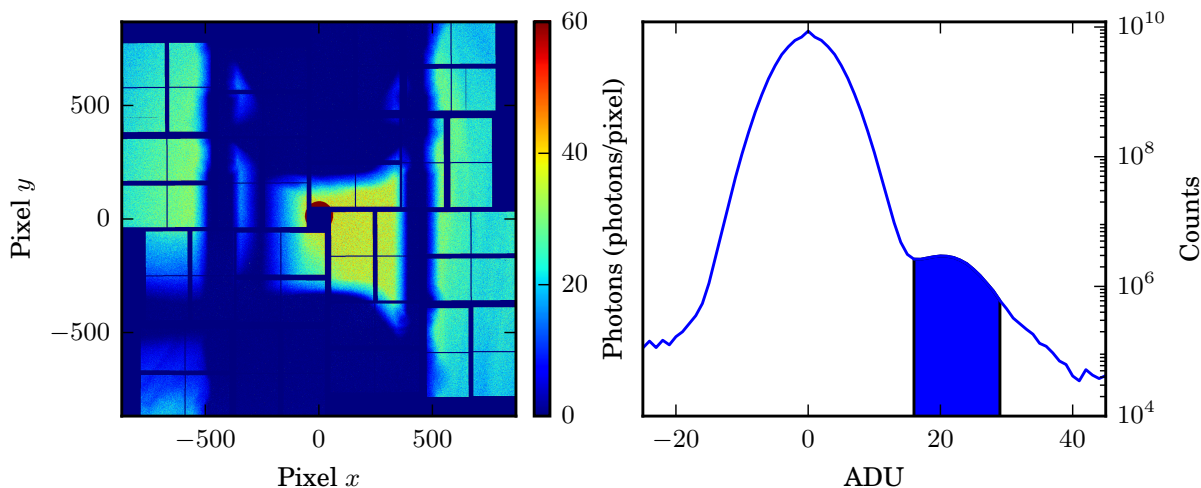


Figure 5.7: CSPAD detector image (left) and corresponding sum of corrected, pixel-based ADU histograms (right). The CSPAD image shows the shadow of the VMI electrodes and holding posts (three vertical lines) if it is gated on the fluorescence photons in the ADU range highlighted by the blue area in the right graph.

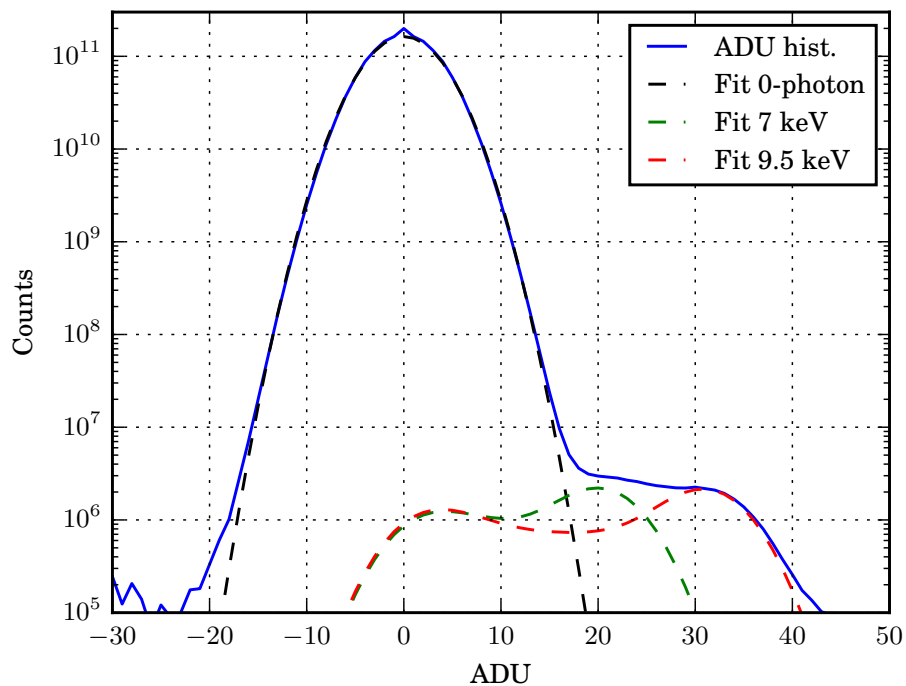


Figure 5.6: Sum of the corrected pixel-based ADU histograms for all pixels (blue). The black, green, and red plots show fits of the estimated ADU photon distribution, which were obtained according to [146].

The dark field calibration was applied to the data by recording for  $\approx 30$  minutes dark images. The averaged ADU value in each pixel was subsequently subtracted from the pixel-based ADU value. The gain correction was applied next. The gain per pixel can be explained by the amount of generated charges within a pixel upon interaction with a x-ray photon. The amount of generated charge is, to a first approximation, linearly dependent on the photon energy per pixel. To quantify the gain per pixel, a calibration measurement was used for which a copper plate was placed in the interaction zone (center of the VMI) and irradiated by the FEL. The FEL induced  $K\alpha$  fluorescence in the copper, which uniformly illuminated the detector. These monochromatic x-ray photons had a photon energy of 8 keV and allowed thus for the generation of a pixel-based gain map. In the next step the single frames for the signal and background measurement have been integrated. The integration was done by a pixel based histogram of the offset and gain corrected ADU values. The amount of entries within the histogram of a pixel was thus equal to the number of FEL shots integrated. Before the data could be used for data analysis, the maximum of the pixel based ADU histograms were shifted to a common value. Assuming that the highest peak in each pixel-based histogram corresponds to their offset value, i. e., assuming that most of the time no photon has been detected. The shift leads thus to an additional pixel based offset correction. Figure 5.6 shows a sum of all individual pixel based histograms of the CSPAD detector in the blue graph. The main peak in the histogram is at zero ADU, which corresponds to the zero-photon peak, i. e., when no photon has been measured. Two peaks are visible in the tail of the zero-photon peak at around 21.5 and 30 ADU. These two peaks correspond to photon energies of 7 and 9.5 keV, resulting from the iron

## 5. X-ray diffractive imaging of controlled molecules

fluorescence and elastic scattering respectively. Despite their separation of 8.5 ADU, both peaks strongly overlap, which can be explained by the following consideration. If a photon at a certain energy would always create the same ADU value in a pixel, its minimum ADU width would be determined by the ADU value generated by the photon and its convolution with the background measurement of that pixel. The FWHM of the background measurement is 7 ADU; the peak separation between the photon energies is 8.5 ADU. This broadening and the too close lying photon energies results in this big overlap, for which the two peaks are impossible to distinguish. The dashed black, green and red curve show a fit to the expected ADU photon distributions for a photon energy of 0, 7, and 9.5 keV [146]. One can see that the shape of the ADU distributions for 7 and 9.5 keV photons do have a double peak structure. The peak at the lower ADU value is due to the photon sharing effect. The sharing effect is due to photons, which hit in between two pixels, or close to the edge of a pixel. In that case the charge created by the photon will be shared between the pixels, resulting in the detection of two ADU values for one photon. The sum of the ADU values is corresponding again to the ADU value, which the single photon would create in a single pixel. After gating on the desired photon energy, the location of each pixel in space had to be assigned. As mentioned already in section 5.2, the CSPAD consists of 64 ASICs with a resolution of 185·194 pixel each. The images acquired by the CSPAD camera were provided in a single file with a resolution of 1480 times 1552 pixels. A so called geometry file was used to assign each ASIC to its true location and orientation in space as shown in the left part of Figure 5.7. The visible structure is a shadow image of the VMI electrodes and their holding posts, see Figure 5.1. This image was recorded in the early phase of the experiment and shows, on purpose, an example where the FEL was strongly clipped by the aperture. It thus provides a visually strong contrast that shows the geometry of the CSPAD camera and, more importantly, demonstrates the influence of the fluorescence radiation on the image, i. e., the visible shadow of the VMI electrodes and holding posts. In the right graph, the ADU histogram for that measurement is presented and the ADU range, which was accepted as signal is highlighted by the blue area under the graph. The lack of 9.5 keV photons at 30 ADU highlights again that, almost exclusively, fluorescent photons emitted from the aperture were detected.

### 5.5 Experimental results

An overview of the different diffraction and background datasets acquired is shown in Table 3. In total 5.2 hours of diffraction of aligned molecules (signal measurement), and 1.75 hours of background measurement have been acquired. Measurements are declared as signal measurements if the molecules have been aligned at an angle of 66 degree and were probed by the FEL. The background measurements can be divided into three categories and are here labelled as background 1, 2, and 3. They deviate by the presence of the molecular beam and, if the molecular beam was probed, on the relative alignment of these molecules. Background 1 contains background measurements of the FEL without molecules in the interaction zone, or with the molecular beam being temporally delayed such that it was not probed by the FEL. It thus provides a background measurement of the fluorescence photons, photons from the beamline,

Table 3: Data set overview used for the diffraction data analysis

	Molecules	Alignment laser	Acquisition time (hrs)
Signal	On	On (66 degree)	5.2
Background 1	Off or delayed	On/Off	1
Background 2	On	On (zero degree)	0.53
Background 3	On	Off	0.23

which hit the detector, and a small contribution from photon, which diffracted off the background gas within the vacuum chamber. Background 2 contains diffraction measurements of  $0^\circ$  aligned molecules and provides thus additional background from the seeding gas and signal from the molecules aligned under a angle different than the signal measurements (chapter 4). These were originally acquired to determine the

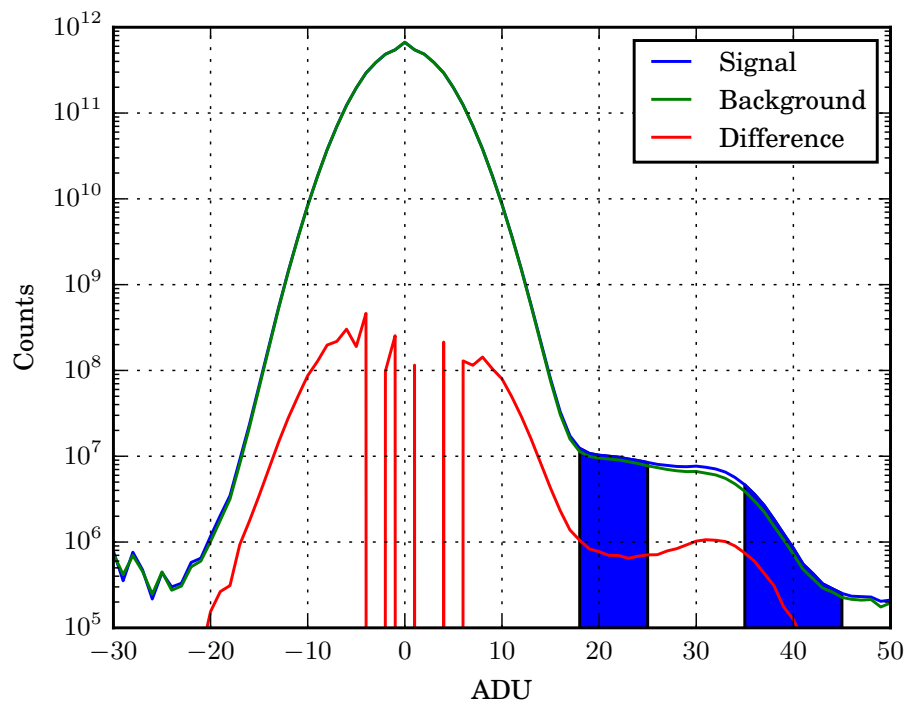


Figure 5.8: Summation of the pixel-based ADU histogram for the collected diffraction runs (blue), the scaled background (Table 3, green) and their difference (red).

degree of alignment of the molecules before and in between signal measurements. Background 3 contains diffraction measurements of unaligned molecules. Background measurement 2 and 3 were declared as background measurements to improve the statistic for the background measurement 1. For symmetry reasons, the molecular signal from an isotropic molecular sample, as well as from molecules, which are aligned along the horizontal or vertical axis of the detector do not have an influence on the differential radial plots shown in Figure 5.4. But they contribute to the size of the error bars, which is negligible here

## 5. X-ray diffractive imaging of controlled molecules

due to significantly larger other sources of background photons. A sum of the CSPAD pixel based ADU histograms for the signal and background measurements is shown in Figure 5.8 by the blue and green curve, respectively. The background measurement was scaled by the ratio of acquired FEL shots for signal and background measurement such that both contain the same number of FEL shots. The red curve shows the difference between the signal and the scaled background measurements. Before subtraction, the 7 keV photon peak at 21.5 ADU is more pronounced than the signal peak at 9.5 keV (30 ADU). After subtraction the situation is reversed. The residual counts within the area of 21.5 ADU will partially come from the non-perfect background subtraction due to a limited amount of statistics. Also, it originates partially from photons, which are detected close to the edge of a pixel or between two pixels (*vide supra*). The blue areas do highlight the ADU ranges of 18-25 and 35-45 ADU, which is assigned to fluorescence background and signal from the molecular beam. The peak at 9.5 keV (30 ADU), which should contain the strongest signal from the molecules, is still strongly contaminated by background and could thus not be used for the data analysis. This limitation is discussed in the context of Figure 5.11 and Figure 5.14. Figure 5.9 shows reconstructed CSPAD images for the two blue areas highlighted in Figure 5.8. The displayed images are binned down by a factor of 56 and the color code is given in counts per bin. Figure 5.9 a) and b) show the reconstructed CSPAD images for the signal only measurements for an ADU range of 18-25 and 35-45 ADU respectively. In both images the shadow of the VMI electrodes and its holding posts is visible. The shadow looks different compared to the detector image shown in Figure 5.7 due to a different positioning of the detector with respect to the hole of the aperture, caused by an optimization procedure to reduce the clipping of the FEL at the aperture. By comparing Figure 5.9 a) and b) a difference between the distribution of photons is visible. The fluorescence background photons (18-25 ADU) have been mainly detected in the lower part of the detector and are almost absent in its center. Photons attributed to 9.5 keV (35-45 ADU) however are mainly detected in the center of the detector. Figure 5.9 c) and d) show the background subtracted reconstruction of the CSPAD image for the same ADU range, which result from photons counted in the blue area below the red curve shown in Figure 5.8. In both background subtracted images the shadow of the VMI electrodes and posts is strongly suppressed. Also here a clear difference between both images is visible. In Figure 5.9 c) the photons are still mainly detected in the lower left part of the detector. In Figure 5.9 d) the photons are detected around the center of the detector. This photons are attributed to coherently and incoherently photons scattered off the molecular beam, i. e., the diffraction signal. A shadow, shaped like a half circle, is visible in the top part of the image but its origin is unclear.

Figure 5.10 shows the diffraction image Figure 5.9 d) in a polar coordinate system. The angle (given in degrees) increases counterclockwise from the line  $y = 0$ ; the different quadrants are labelled as Q1-Q4 and correspond to the quadrants shown in Figure 5.9 d). Figure 5.10 a) and b) do shows the radial sum and radial average of the CSPAD image. The lack of counts at a radius below 20 pixel is due to the central hole of the detector; the periodic structure above a radius of 800 pixel is due to the borders of the square shaped detector. Both plots have been corrected for the gaps of the CSPAD camera. This was done by

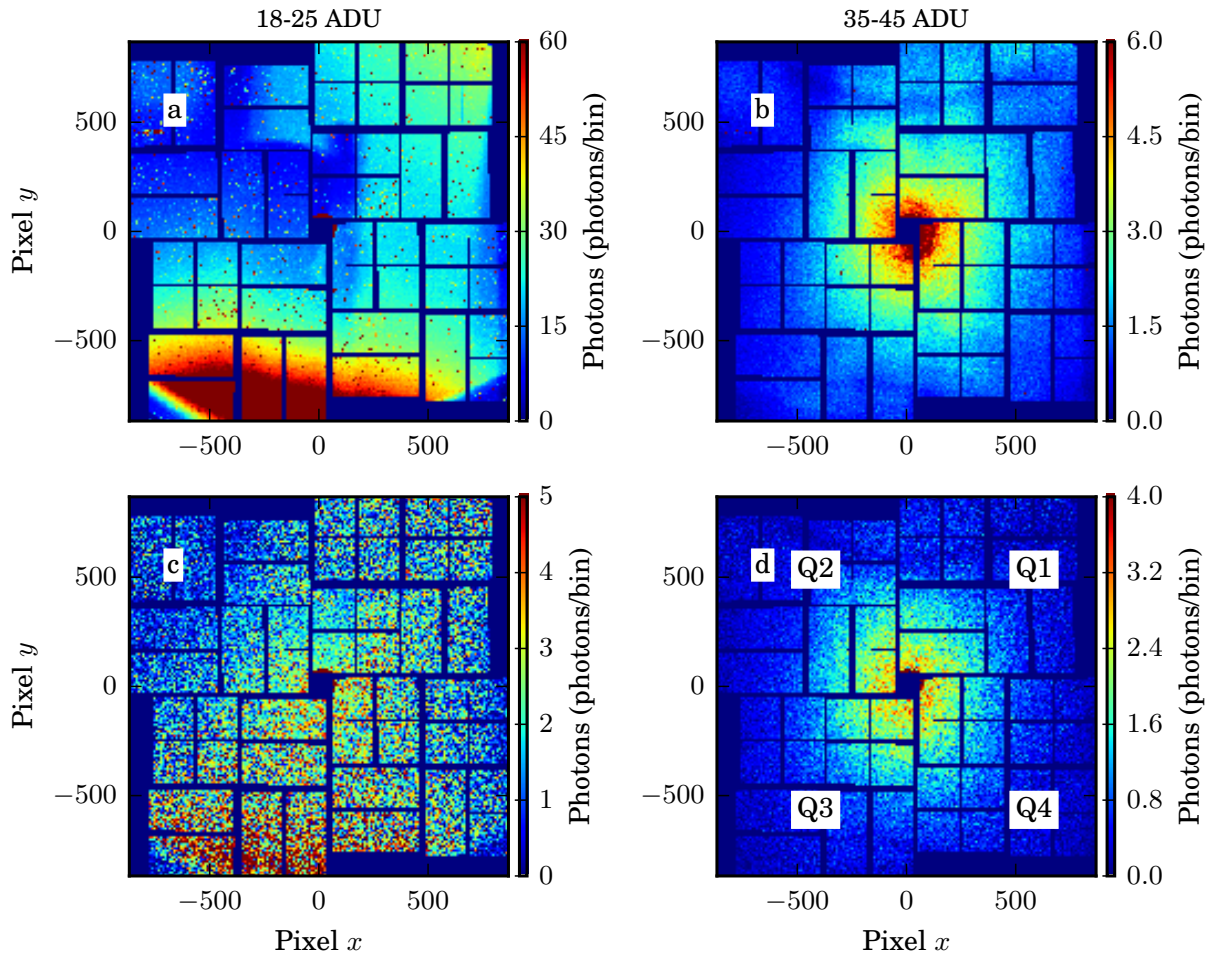


Figure 5.9: a) and b): CSPAD detector images for the signal measurements, gated on an ADU range of 18-25 (left) and 35-45 (right). Bottom: Reconstructed CSPAD detector images for the signal measurements subtracted by the scaled background measurements, gated on an ADU range of 18-25 (left) and 35-45 (right)

further reducing the image size  $36 \cdot 25$  bins, as it is shown in Figure 5.10. Subsequently the ratio of ‘pixels per bin for a gapless detector’ to ‘pixel per bin for the CSPAD camera’ was used as a scaling factor. The half circled shadow with unknown origin (*vide supra*) is visible between 45 and 120 degree at a radius of 600 to 900 pixels. Both plots show maxima at an angle of 90 and 270 degree, which is explained by the polarization dependent scattering of the linear polarized x-rays on the sample.

The diffraction signal within a single quadrant in Figure 5.10 a) can be reduced to a 1D diffraction signal by summing up the different angular contributions within a single quadrant. This leads to four 1D diffraction signals (Q1, Q2, Q3, Q4), which are the radial sums of the diffraction pattern within each quadrant. These four 1D diffraction images can be used to generate radial difference plots equivalent to the one presented in the simulations in Figure 5.4. This is shown in Figure 5.11 for three different ADU acceptance ranges, namely 35-45 ADU, 36-41 ADU, and 31-41 ADU for a), b) and c). The ADU

## 5. X-ray diffractive imaging of controlled molecules

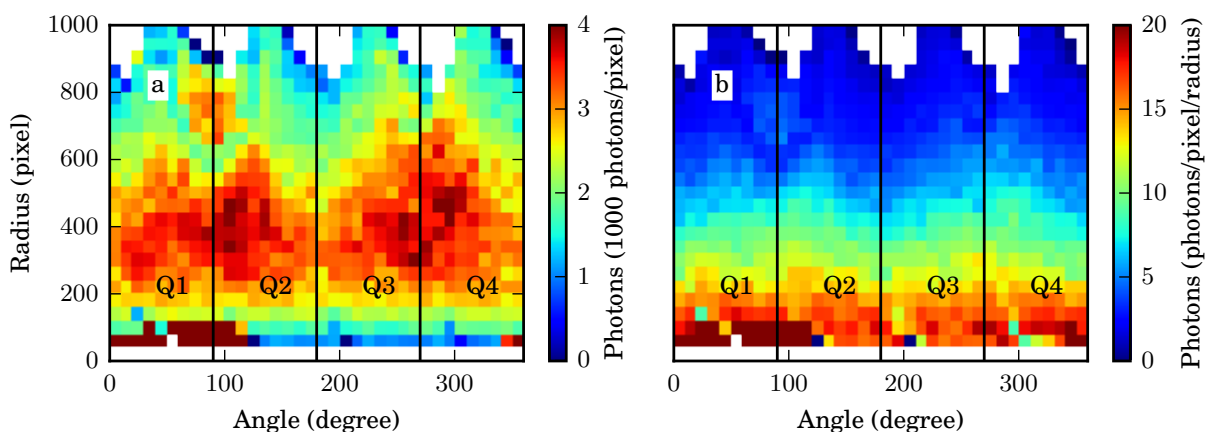


Figure 5.10: The CSPAD image of Figure 5.9 d) is illustrated here in a polar coordinate system, where the angle (given in degrees) increases counterclockwise from the line  $y = 0$  and the quadrants Q1-Q4 correspond to the quadrants shown in Figure 5.9 d) . a) and b) do show the radial sum and the radial average of the CSPAD image respectively. Both plots have been corrected by the gaps of the CSPAD camera.

range presented in a) is the one, which was used to generate the images in Figure 5.9 b) and d) as well as Figure 5.11. Due to the high background contamination it is not obvious what the optimum ADU range and ADU gate width is to retrieve the diffraction signal from the molecule. Hence, these three different ADU ranges represent (relatively speaking) a) intermediate signal to noise ratio (SNR) and intermediate number of photons, b) high SNR and low number of photons, and c) low SNR and high number of photons. The determination of the 3 ADU ranges is described in section A.2.

Figure 5.11 a) shows in black simulated differential radial plot for  $(Q1+Q3)-(Q2+Q4)$ . It is the same as presented in Figure 5.4 but modified by the pixel grid of the CSPAD camera, i.e., including the gaps of the detector. The simulated differential plot was generated by the same procedure that was used to generate the radial profiles of the experimental data. The gray areas do highlight the expected locations for the first, second and third maxima of the molecules' iodine-iodine interference term. The red curves in a), b) and c) are labeled as  $\Delta_{\text{all}}$  and show the radial difference between  $(Q1+Q3)-(Q2+Q4)$  for the experimental data (Figure 5.10 a)). The green and blue graph show the differential radial plot of  $Q1-Q2 = \Delta_{12}$  (upper half of the detector) and  $Q3-Q4 = \Delta_{34}$  (lower half of the detector) respectively. The error bars for  $\Delta_{\text{all}}$ ,  $\Delta_{12}$ , and  $\Delta_{34}$  are given as the Poisson noise per bin, the connections between the bins are given as visual aid, and  $\Delta_{12}$  and  $\Delta_{34}$  have been scaled by a factor two for an easier comparison to  $\Delta_{\text{all}}$ . In general,  $\Delta_{12}$  and  $\Delta_{34}$  have the same contribution of the diffraction pattern due to the symmetry of the diffraction pattern. But, due to the asymmetry of the background radiation their shape can differ.

From the simulations in Figure 5.4 it was expected that the strongest signal of the molecules will be visible at the location of the second maximum. In Figure 5.11 a)  $\Delta_{\text{all}}$  does show a local maximum at the location of the second maximum. Decomposing  $\Delta_{\text{all}}$  into  $\Delta_{12}$  and  $\Delta_{34}$  shows that the local maximum

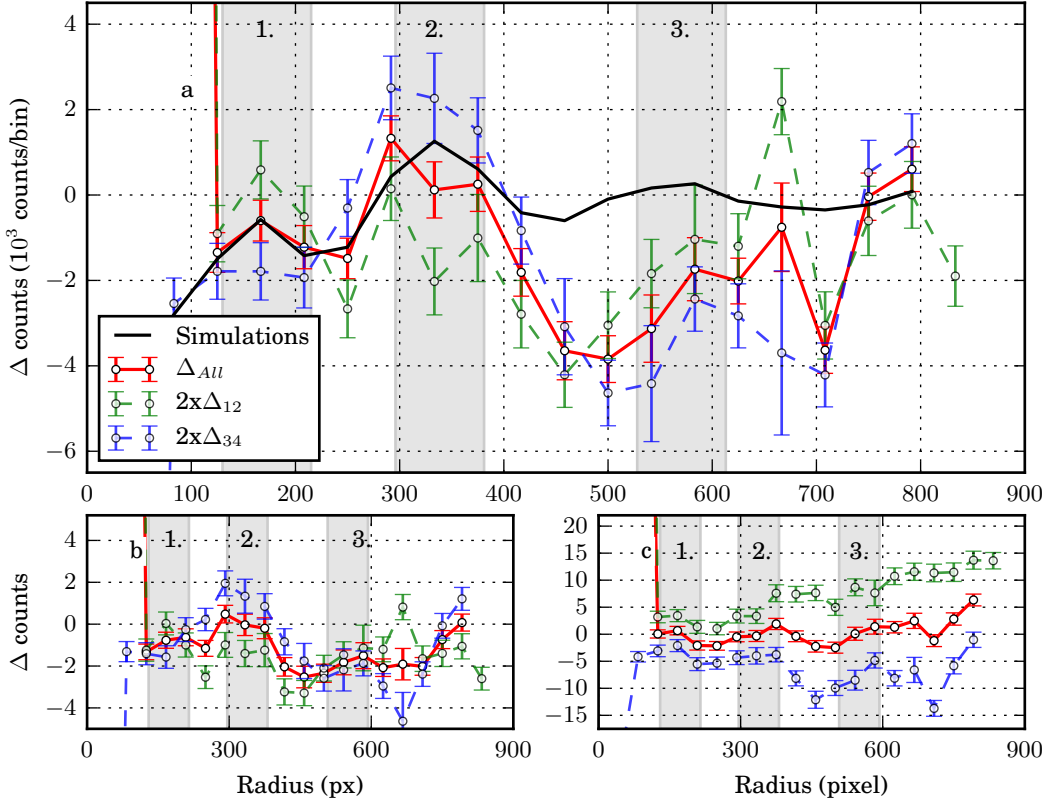


Figure 5.11: Differential radial plots (similar to the simulations in Figure 5.4) for the ADU acceptance ranges of a) 35-45 ADU, b) 36-41 ADU, and c) 31-41 ADU. The black graph in a) shows the simulated diffraction pattern for  $(Q1+Q3)-(Q2+Q4)$  which is similar to the one presented in Figure 5.4. In a), b) and c)  $\Delta_{12}$  ( $\Delta_{34}$ ) shows the experimentally determined radial difference between the quadrants Q1 and Q2 (Q3 and Q4), which is displayed in green (blue) and scaled by a factor of 2. The difference between  $(Q1+Q3)-(Q2+Q4)$  is labeled  $\Delta_{All}$  and is shown in red. The error bars per bin are given as the Poisson noise and the vertical gray areas represent the simulated locations of the first, second, and third maximum of the iodine-iodine interference term (section 5.3).

is mainly due to the contribution from  $\Delta_{34}$ , which shows a value of  $y = -2$  at the location of the first maximum, increases to  $y = +2$  at the location of the second maximum, and reduces toward higher radii to  $y = -4$ .  $\Delta_{12}$  on the other hand fluctuates around a value of  $y = -1$  at radii between 100 and 400 pixel. For higher radii no clear trend is visible. Figure 5.11 b) shows the same behavior as Figure 5.11 b).  $\Delta_{34}$  has a local maximum at the point of the second maximum and  $\Delta_{12}$  fluctuates around a  $y = -1$ . The ADU gate chosen in Figure 5.11 c) does have a smaller SNR compared to a) and b), but more photons have been accepted. For this ADU range  $\Delta_{all}$  is (on the given scale) fluctuating around a value of  $y = 0$  for all radii.  $\Delta_{12}$  increases toward higher radii at a similar slope as  $\Delta_{34}$  is decreasing. The influence of the background radiation is here the strongest of all three gates, visible by the opposing trend of  $\Delta_{12}$  and  $\Delta_{34}$

## 5. X-ray diffractive imaging of controlled molecules

and considering that the contribution from the diffraction signal of the molecules as well as the helium should be the same in  $\Delta_{12}$  and  $\Delta_{34}$ . Interesting to note is the peak at the location of the second maximum for  $\Delta_{34}$  is now strongly suppressed compared to Figure 5.11 a) and b). This would not be expected for a peak originating from the background radiation, indicating therefore a true molecular feature.

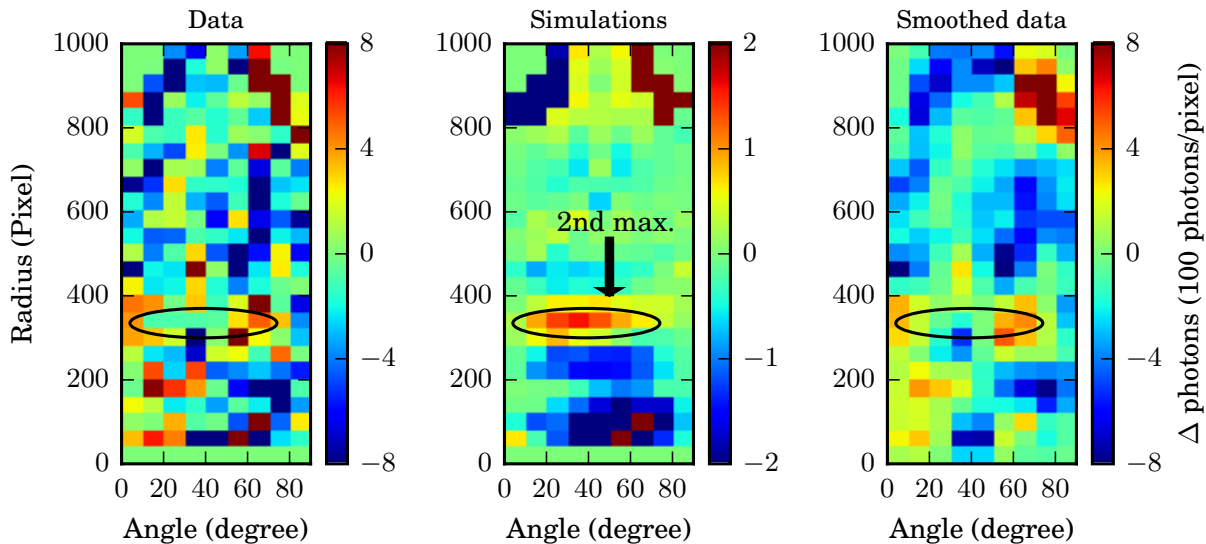


Figure 5.12: Differential images of quadrant 3 and 4 for the experimental data (left), simulations (center), and smoothed experimental data (right). The angular coordinate of quadrant 4 has been reversed prior the subtraction to compensate for the polarization dependent scattering effect. The location of the second maximum is highlighted by the oval shaped circle.

$\Delta_{34}$  in Figure 5.11 a) shows a distribution closest to the simulated data and hence it was used to generate a 2D diffraction image, which is shown in Figure 5.12. It shows the subtraction of Q4 from Q3 in the polar coordinate space as it is shown in Figure 5.10. The angular coordinates of Q4 have been reversed before subtraction such that the 2D array of Q4 was ranging from 360 to 270 degree before it was subtracted from Q3 ranging from 180-270 degree. This was done to cancel out the effect of the polarization dependent scattering. The left image shows the difference from the experimental data shown in Figure 5.10 a), the central image shows the simulations, and the right image shows again the experimental data convolved by a Gaussian function with a sigma of 1.5 bins. The location of the second maximum is highlighted in all images by the oval shaped circle. The simulation shows an area of constructive interference. The experimental data do show no clear signature of a maximum at the location of the second maximum.

Figure 5.13 shows the statistical error and the signal to noise ratio (SNR) of the 2D diffraction image shown in Figure 5.13. The statistical error is given by the square root of the contributions from the signal and scaled background measurement in each bin of Q3 and Q4. The SNR 2D histogram shows the ratio

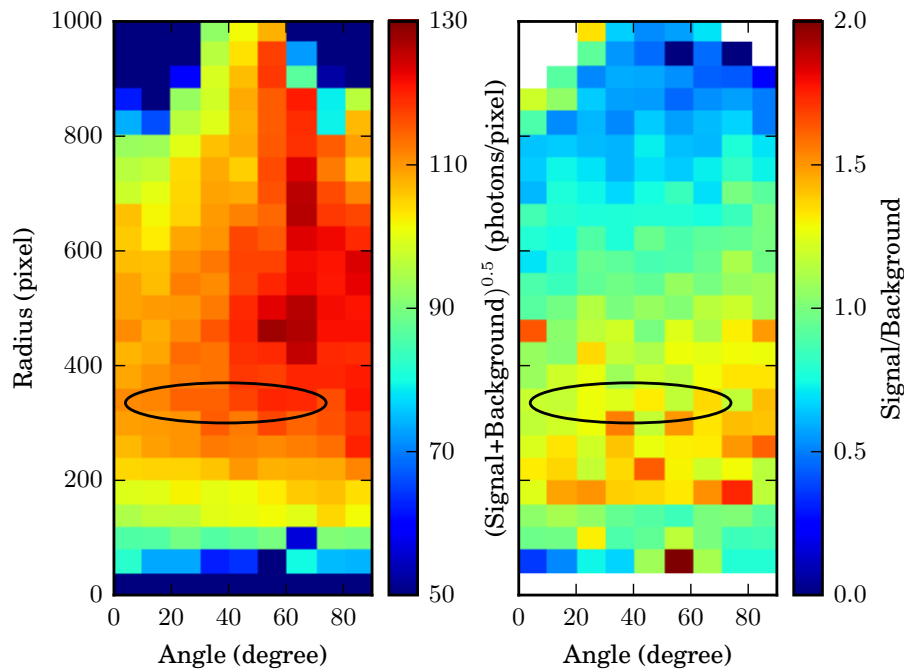


Figure 5.13: Statistical error (left) and SNR (right) for the experimental data shown in Figure 5.12. The circles show the location of the second maximum of the iodine-iodine interference term derived from the simulation in Figure 5.12

between the (scaled) background subtracted signal and (scaled) background measurements. The circle represents again the location of the second maximum derived by the simulations shown in Figure 5.12. It can be seen that the statistical error in this region of this maximum is almost constant above 110 photons per pixel. Also the SNR in this area is somewhat constant. At this statistical level the 2D representation of the diffraction signal does neither confirm nor reject the attribution of the maxima detected in the 1D diffraction diffraction pattern shown in Figure 5.11. In general it can be seen that, at radii bigger than  $\approx 450$  pixel, the SNR is getting lower, which can explain the discrepancy between data and simulations shown in Figure 5.12. The statistical error shows an increase in the central right region, which is due to the higher number of photons there, originating from the polarization dependent scattering.

## 5.6 Discussion

The recorded diffraction pattern in Figure 5.10 shows a clear signal of scattered photons, which is dependent on the polarization of the FEL. The contribution from the rest gas in the chamber were compensated by the background measurements; the fluorescence and beamline photons do have a different signature. Therefore, these photons must originate to from the molecular beam (seeding gas, molecules).

From the simulations in Figure 5.4 it was expected that the second maxima of the iodine-iodine interference is the strongest interference signal measurable in a 1D differential plot. The experimentally determined 1D differential plots shown in Figure 5.11 a) and b) do show a maximum at the location of the second maxima

## 5. X-ray diffractive imaging of controlled molecules

for the differential plots of the quadrants Q3-Q4, i. e., the lower part of the CSPAD camera. On the other hand, this maxima is not visible for the different plots of the quadrants Q2-Q1, which are located on the upper half of the detector. The overall influence of the background radiation is visible in Figure 5.11 c), which shows a general trend for Q2-Q1 (Q3-Q4) too higher (lower)  $y$ -values at an increased distance from the center of the detector. The overall trend also show that earlier assigned second maximum in the lower half of the detector (Q3-Q4) did not increase. This could be explained by a molecular signals, which is, at these given ADU gates, much more dominated by the background peak. The 2D diffraction images shown in Figure 5.12 do neither confirm nor reject the possible detection of the second maxima in the 1D diffraction images. The Poisson noise of the 2D diffraction images and the signal to noise level shown in Figure 5.13 do simply show a lack of statistics for this analysis.

The source of x-ray background photons has two origins. Fluorescence photons induced by the FEL in the iron aperture were mainly detected in the lower part of the detector (Figure 5.9 a)). Photons origin from the beamline are mainly found in the right part of the detector, which is shown in Figure 5.14. This image was acquired by gating on an ADU range of 29-31 ADU for the signal measurement (Figure 5.8), i. e., a photon energy of 9.5 keV. Both sources of background photons could be partially suppressed by accepting only relatively high ADU values as signal photons (35-45 ADU for the discussed data in Figure 5.10), with the cost of fewer photons being part of the diffraction image. Though visually the diffraction pattern in Figure 5.10 looks background corrected, the radial plots in Figure 5.10 show that this is not the case. First, there is significant difference in the signal between the different radial plots for the upper part of the detector ( $\Delta_{12}$ ) and the lower part of the detector ( $\Delta_{34}$ ). Second, a change in the ADU acceptance range leads to a change of the overall shape of the radial difference plots, which is explained by a change in background signature for different ADU ranges (Figure 5.9, Figure 5.14). The CSPAD gap correction can be excluded as a cause of such differences because it is independent of the ADU range and has been applied to the simulations as well (Figure 5.11 and Figure 5.12), and ,in any case, does not lead to significant deviations from the gapless radial plots. A contradicting result to the 1D diffraction images is discussed in the following. As shown in the simulations in Figure 5.4, the ratio of helium to molecules in the molecular beam is important to determine the absolute error of the radial plots. This ratio can be estimated by examination of the ion TOF spectrum, as shown in Figure 5.15. The spectrum is similar to the spectrum shown in Figure 4.2, but with an extended TOF window to include the contribution from the helium ions. Above a TOF of 1950 ns, the spectrum has been multiplied by 20 to visually enhance ions originating from the molecule. To determine the ratio of helium to molecule in the molecular beam, the area under the different peaks, proportional to the number of detected ions, can be integrated. To do so it has to be assumed that the ion signal measured is independent of the mass of the ion. To determine the molecular contribution, the charge states of  $I^+$  to  $I^{+5}$  have been added.  $I^{+4}$  cannot be distinguished in this TOF from a singly charged sulfur atom. Hence, this area under the peak has been scaled by 0.66 to compensate for the higher number of iodines in the molecule. For helium, only singly charged ions have been considered. Under this condition the area under the helium peak is 2.36 times larger than the

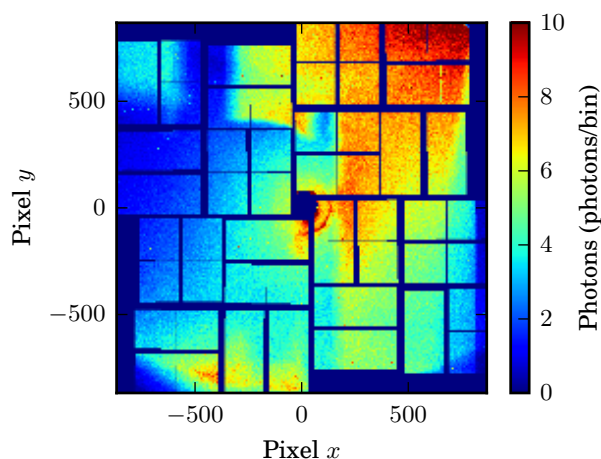


Figure 5.14: Detected photons in the diffraction measurement for an ADU gate of 29-31 ADU, i. e., for a photon energy of 9.5 keV. The highest photon count rate is visible in the upper right corner of the detector, which originates from scattered photons from the beamline.

area under the iodine peaks, i. e., 2.36 times more helium atoms have been detected. With the additional assumption that two ionic iodine fragments are always generated upon interaction with the x-rays, and considering the detection efficiency of 50%, the ratio of helium to molecule is 4.72. Table 2 shows the

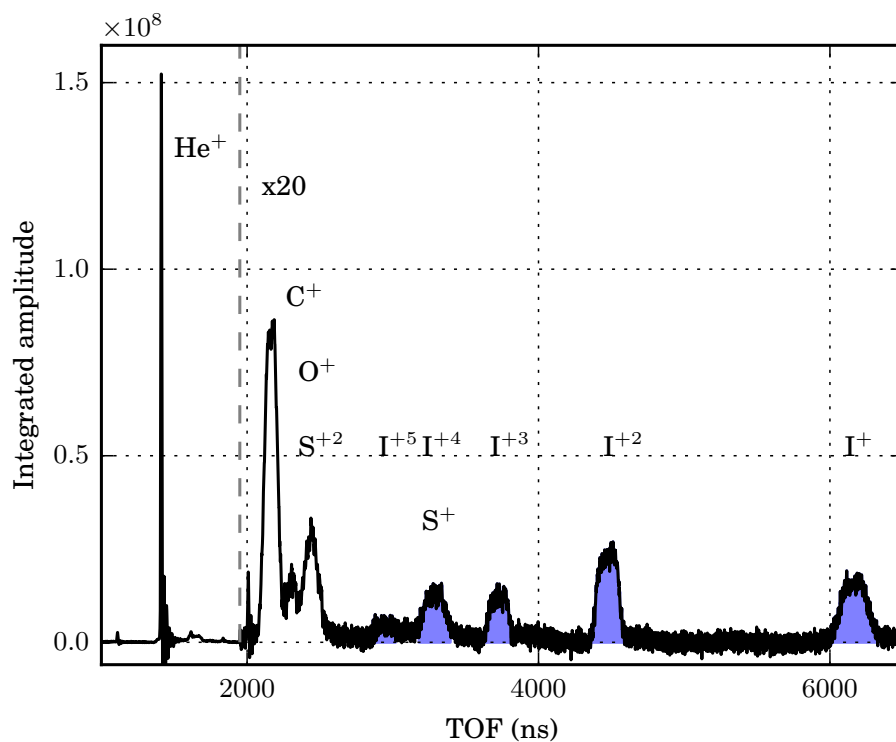


Figure 5.15: Ion TOF spectrum of the molecular beam. For flight times higher than 1950 ns, the recorded signal has been multiplied by a factor of 20.

## 5. X-ray diffractive imaging of controlled molecules

different photoelectric absorption cross sections for the helium and molecular atoms. Assuming that the molecular cross section is equivalent to the sum of its individual atomic cross sections, its total cross section is  $80.360 \cdot 10^{-24} \text{ cm}^2$ , compared to  $0.2306 \cdot 10^{-24} \text{ cm}^2$  for helium. Hence, the probability of ionization of a single molecule is  $\approx 350.000$  times higher. Considering that roughly 4.72 times more helium ions have been detected the helium to molecule ratio in the molecular beam is 1.65 million to 1. This ratio is 20-200 times higher than it was expected to be beforehand and as it is shown in the simulations in Figure 5.4. This estimation suggest that the maximums' origin is due to the background rather than the molecular interference pattern, supported by the statement that the maximum has only been observed in the lower part of the detector. Additionally this estimation can also be used to determine the vapor pressure of the molecule. Due to the good knowledge of the helium pressure in the pulsed valve, the molecule's vapor pressure can be calculate to be 0.05 mbar. This low vapor pressure for 2,5-diiodothiophene above its melting point is highly unlikely and could be explained by the delay between FEL and molecular beam, which has probed a temporally bad position of the molecular beam. Helium is typically a little bit faster than the molecules and thus is more prominent at the front of the pulse. Also a partially clogged valve, which predominantly transported helium to the interaction zone, or simply an empty molecular sample could explain this ratio. During the experiment, a lot of precaution was taken into account to avoid any of these possibilities and hence it is unclear, which, if not all, points are causing the strong deviations from the expected helium to molecule ratio or if the estimation is based on wrong assumptions.

## 5.7 Conclusion and outlook

We have shown that we could retrieve a diffraction signal from the molecular beam despite the high background generated by the beamline as well the used aperture. Whether or not the detected signal from the molecules in the 1D diffraction image is due to the molecules or due to the background from the beamline could not be conclusively answered. We have learned important lessons that show that the field can make great progress in the next generation of FELs. The main challenges for this kind of experiment are the low diffraction signal from the molecules, the resulting slow feedback from the experiment, and the limited time available at a FEL facility. During this experiment 80% of the available time was spent on the reduction of beamline background photons as well as on the reduction of secondary effects such as fluorescence from the iron aperture. A different material for the aperture, like aluminum instead of iron, could have helped to suppress fluorescence photons more efficiently by relying on the energy resolution of the detector to filter the  $K\alpha$  and  $K\beta$  emission lines (which are well below the incident photon energy of 9.5 keV). Additionally, careful selection and placement of beamline apertures could have helped to protect the detector from unwanted background, as it is shown, for instance, by the shadow-area of the VMI electrodes (Figure 5.7). The background from the carrier gas, i. e. helium, can be conceptually suppressed by the use of an electrostatic deflector [25] at the cost of a lower density in the molecular beam. Changing the carrier gas to, for instance, neon is not useful despite the typically lower seeding pressure of 20 bar and the consequent reduction in the number of atoms in the interaction zone. Drawbacks are the reduced

density of the molecular sample due to a slower molecular beam and the increase in the scattering cross section (incoherent and coherent) of the carrier gas ( $\approx$  a factor of 20 and 200 respectively) leading to producing higher background signal.

Beside the challenges presented, diffractive imaging is a highly promising experimental approach to determine molecular structure, and more importantly, to image molecular dynamics like folding, isomerization, or photofragmentation with fs time resolution. The simulations in section 5.3 have shown that under very good experimental conditions enough statistics for a static diffraction image of the molecule could have been recorded within roughly 6 hours of integration time. The repetition rate of the upcoming hard x-ray FELs, e. g., XFEL or LCLS II, is a few hundred to a few thousand times higher compared to the 120 Hz, which were available for the presented experiment. At this high repetition rate it would be possible to record the diffraction image of the molecule within minutes, and thus providing immediate feedback from the experiment. The technology transfer to align molecules at FEL repetition rates [100] is in principle capable of supporting any repetition rate, which is provided by the Ti:Sapphire laser available at the different end stations, given that a few mJ per pulse are available. Additionally, intracavity laser alignment of molecules, allowing for the alignment of molecules at arbitrary repetition rates, is currently under development [147].

To measure the above mentioned molecular dynamics, the upcoming high-repetition rate FELs will play a key-role. In an optical pump-probe experiment only 10-20 % of the molecules in the interaction zone will be typically pumped by a laser; the FEL will probe the structure of all molecules. Thus up to 90 % of the diffraction image will still be due to the static structure of the molecule. In first approximation the integration time has to be 25-100 times longer to see a statistically relevant signal from the triggered dynamics of the molecule. Not taken into account are, for instance, different dissociation channels and different velocity distributions of the dissociation channels, which will further blur the structure. If a ‘well known’ molecular dynamics is the aim of the study, one can in principle beat the above mentioned statement for the SNR and the stated modification of the integration time. Assuming the static diffraction pattern of the molecule shows several minima and maxima on the detector (Figure 5.2), the triggered dynamics could then be probed such that the maxima of the dynamical structure fall into the minima of the static structure, and thus have locally a much lower background. One could measure the different time steps within hours and would thus pave the way toward diffraction imaging of cold, controlled molecules in the gas-phase.

The imaging of small biomolecules under controlled conditions in a cold molecular beam will be the next challenging step. Tryptophan, for instance, is an  $\alpha$ -amino acid with the chemical formula  $C_{11}H_{12}N_2O_2$ . It consists of the chromophore indole and an  $\alpha$ -amino group. It is chosen here exemplarily since both, the indole chromophore and the  $\alpha$ -amino group, were measured in the context of this thesis and are shown in chapter 6, chapter 7 and section 8.2. The coherent scattering cross section of tryptophan is  $63 \cdot 10^{-24} \text{cm}^2$ . For comparison, the coherent scattering cross section of 2,5-diiodothiophene is  $1293 \cdot 10^{-24} \text{cm}^2$ . Thus, the probability of coherently scattering off tryptophan is only 5 % of the probability of scattering off

## 5. X-ray diffractive imaging of controlled molecules

2,5-diiodothiophene. Further, for lighter atoms the ratio of coherent to incoherent scattering cross sections is reduced (Table 2). For tryptophan this ratio is only 1.28 compared to the earlier discussed ratio of 31 for 2,5-diiodothiophene. Thus, even if no background photons from the beamline and the seeding gas are present, more than 40 % of the detected photons originate from incoherently scattered x-ray photons. The shift in energy of the photon due to its elastic scattering (incoherent scattering) cannot be compensated by a high energy resolution detector and subsequent gating on its ADU range since it is typically within the bandwidth of the FEL [148].

A reduction of the photon energy can help in several ways. At a reduced photon energy, the FEL will provide more photons, and the ratio of coherent to incoherent scattering will be much higher. The coherent scattering cross section increase with decreasing photon energy, in contrast to the incoherent scattering, which will be reduced at a lower photon energy. At a photon energy of 4 keV the photons still have a wavelength of 0.31 nm, which will not provide atomic resolution, but can resolve (depending on the molecule) inter-molecular distances.

## 6 X-ray photophysics of indole\*

The following chapter is describing the x-ray photophysics of gas-phase indole upon core-shell ionization. Supplementary informations are given in Appendix B, covering the reconstruction of the molecular beam profile (section B.1), a general explanation of the coincidence spectrum (section B.2), and the calibration measurements for the ion TOF and VMI (section B.3, section B.4), as well as the electron VMI section B.5.

### 6.1 Introduction

Electronic relaxation dynamics, including charge-transfer and charge-migration processes, together with the nuclear fragmentation dynamics after creation of one or several core-shell vacancies, play a crucial role for our understanding of the interaction of x-rays with matter. Because of their element specificity, x-rays can be efficiently employed to induce charge-transfer dynamics at specific and well-defined sites via deep core level ionization of individual atoms inside the molecule. To unravel fundamental relaxation processes, like interatomic coulombic decay (ICD) [80], small molecules and van-der-Waals hydrogen bonded clusters [149, 150] in the gas-phase were widely studied by XUV and (soft) x-ray ionization at various accelerator based facilities like synchrotrons or free electron lasers (FELs). The pioneering experiments on ICD with van-der-Waals bonded Ne clusters were performed at synchrotrons at low intensities below the threshold of photo double ionization for a single Ne site. The availability of FELs with high radiation intensity allowed to study ultrafast charge rearrangement and nuclear dynamics fragmentation subsequent to multiple innershell ionization [53, 54, 151, 152] revealing novel effects such as double or multiple core-hole creation and frustrated x-ray absorption [153–155]. Furthermore, the high temporal resolution of FELs provided access to dynamical studies such as electron transfer and charge migration processes to trace the spatial localization of the charges as a function of time during dissociation [156–160] and isomerization [161] reactions. Coincidence methods, where the momenta of all charged particles are detected for a single event, play a crucial role to understand the complete fragmentation and charge rearrangement dynamics in these experiments. Various techniques were developed during the last years which include Photoion-Photoion Coincidence (PIPICO) [17, 62], Photoelectron-Photoion-Photoion Coincidences (PEPIPICO) [21–23, 58, 59, 61], or Auger-Electron-Photoion-Photoion Coincidences (AEPICO) [60] measurements. An extensive overview of the history and the current state of different coincidence techniques is given in [162]. The accessibility of all momenta allowed in addition to correlate the corresponding electron momenta with the recoil frame of the molecule resulting in Recoil-Frame Photo Angular Distributions (RFPAD) [19, 21–23, 62]. These RFPADs allow in addition to

---

\*This chapter is based on a preliminary version of the manuscript: *X-ray photophysics of indole*, by T. Kierspel, M. Di Fraia, J. Wiese, R. Boll, C. Bomme, D. Rolles, J. Viehhaus, J. Küpper, S. Trippel and others. I contributed to the experimental part by pre-experiments in the laboratory. During the measurement I was responsible for the molecular beam. I did the data analysis and I wrote the chapter supervised by S. Trippel and J. Küpper.

## 6. X-ray photophysics of indole

determine the structure of molecules and molecular dynamics in diffraction from within type of experiments. Furthermore Molecular-Frame Photo Angular Distributions (MFPADs) experiments [16–20], where the molecules are typically aligned, so fixed in space by a strong laser field [35], allow to unravel the dynamics directly in the molecular frame.

Indole is the chromophore of the essential amino acid tryptophan, and as such also part of various proteins and peptides. Indole itself was already in the focus of a variety of different experimental and theoretical studies, ranging from microwave [163, 164] and optical spectroscopy [165, 166], over vibrationally [167] and rotationally resolved electronic spectroscopy [168–172], to photoelectron spectroscopy [173–175]. The lowest electronically excited states of indole are labeled as  $^1L_a$  and  $^1L_b$  (notation after [176]). The  $^1L_a$  state is highly polar and, therefore, its energy is strongly influenced by the polarity of its solvent environment. Already in small clusters like indole-water<sub>1</sub> a shift in the electronic states and their corresponding dipole moments is observed [167, 171, 172, 177, 178]. Tryptophan is used for the same reason in a variety of experiments as an environment marker in proteins [179] (and references therein). The indole-water<sub>1</sub> cluster has a well defined structure: the water is hydrogen bonded to indole at the nitrogen side of the molecule [171]. These clusters are therefore well suited to study the nature of hydrogen bonds, which are of universal importance in chemistry and biochemistry, via site specific core shell ionization.

Before studying the dynamics in clusters it is important to fully understand and characterize the photophysics of the bare indole molecule especially focussing on the site specific ionization at the nitrogen atom. In this study we present the photophysics of gas-phase indole by a single photon ionization primarily at the carbon atomic  $1s$  orbitals as well as by side specific ionization at the nitrogen atom. Photo- and Auger electrons as well as the ionic fragments of indole were detected in coincidence in a double-sided velocity map imaging (VMI) [2–5] spectrometer. Our work provides the basis for fragmentation studies of larger molecules as well as molecular clusters. The experimental setup, described in the next chapter, was chosen such that the photofragmentation of indole and indole-water clusters could be measured. Our findings for the photophysics of indole-water<sub>1</sub> clusters are discussed in chapter 7.

### 6.2 Experimental setup

The experimental setup is shown in Figure 6.1. The part that provides the molecular beam is similar to the one described in [12]. A supersonic expansion of a few mbar of indole and a trace of water molecules seeded in 60 bar of helium was provided by a pulsed Even-Lavie valve [63]. The valve was operated at a repetition rate of 250 Hz, and was heated to a temperature of 110 °C. Due to three-body collisions in the early phase of the expansion indole<sub>m</sub>(H<sub>2</sub>O)<sub>n</sub> clusters are formed. The mixture can be spatially separated using strong inhomogeneous electric fields generated by the electrostatic deflector [9]. From time of flight (TOF) spectra obtained in characterization experiments using a compressed 50 fs laser pulse at 800 nm we estimate a ratio  $R = 4$  of indole molecules to indole<sub>m</sub>(H<sub>2</sub>O)<sub>n</sub> clusters. Due to the difference signature of the fragmentation pattern of indole and indole<sub>m</sub>(H<sub>2</sub>O)<sub>n</sub>, we can estimate a purity of more than 95% for indole on the data presented here. The data obtained from indole<sub>m</sub>(H<sub>2</sub>O)<sub>n</sub> clusters are discussed

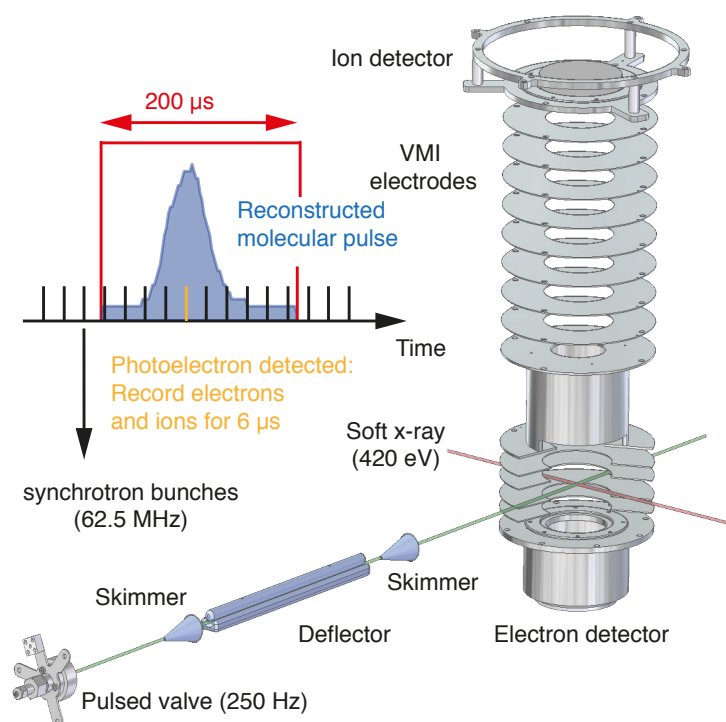


Figure 6.1: Experimental setup showing the pulsed valve, skimmers, deflector, the double-sided VMI with its corresponding delay line detectors to detect electrons and ions in coincidence, and the synchrotron beam which crosses the molecular beam in the center of the VMI. A reconstructed molecular pulse is shown in the top left part. Schematically indicated is the logical gate (red) synchronized to the molecular beam. Multiple synchrotron pulses are crossing the molecular beam without interaction (black vertical bars). A single interaction is indicated by the orange vertical bar.

in chapter 7. The molecular beam apparatus was mounted to the CAMP-CFEL-ASG Multi Purpose-end station [180] which was connected to the synchrotron (Petra III, Variable Polarization Beamline P04 [181], circular polarization ( $> 98\%$ )<sup>†</sup>,  $5 \cdot 10^{13}$  photons/s, 480 bunches, 16 ns bunch period). The molecular beam was crossed by the synchrotron radiation under an angle of 90 degree inside a double sided VMI spectrometer<sup>‡</sup> for simultaneous electron and ion detection. The velocity of the molecular beam caused an TOF dependent VMI offset of the detected ionic fragments due to an extraction of the ions perpendicular to the molecular beam axis. Both, electrons and ions were detected with a hexanode (electrons) and quadranode (ions) delay line detector (DLD, Roentek) respectively. Only two out of three electrodes within the hexanode were working properly.

The pulse duration of the molecular beam in the interaction region was about 60  $\mu\text{s}$  full width at half maximum (FWHM). At the valve repetition rate of 250 Hz this resulted in a duty cycle of 1-2 %. The electronic readout of the detectors was triggered by electrons detected on the electron side of the

<sup>†</sup>At the time of the experiment the only possible polarization

<sup>‡</sup>The VMI images show the 2D-projection of the ions and electrons 3D velocity distribution onto the detector surface in the laboratory frame coordinates.

## 6. X-ray photophysics of indole

spectrometer. In addition a logical gate was used to record data only in a 200  $\mu\text{s}$  time window which was synchronized to the arrival time of the molecular beam in the interaction zone (Figure 6.1). This resulted in a reduction of the background signal created by the high repetition rate of the synchrotron. Once triggered, electrons and ions were recorded for a time of 6  $\mu\text{s}$  and marked as a single event which was tagged with a timestamp (TS). The TS was the relative timing between the trigger of a single event and the starting time of an individual measurement. The corresponding detected electrons/ions were saved in a shot list and could be sorted subsequently according to their temporal position within the 200  $\mu\text{s}$  time window which was calculated by the modulus of  $\text{TS}/4 \text{ ms}$ . A histogram of the modulus time for a single measurement is exemplarily shown in blue in the top left part of Figure 6.1. The envelope represents the temporal molecular profile plus a constant offset. Contributions at the beginning and the end of the indicated temporal gate (red) are due to background events; the rise in the center is due to a higher event rate when the molecular beam is in the interaction zone. The modulus time could be reconstructed to an accuracy of less than 1  $\mu\text{s}$  which was limited by a relative temporal drift within the electronics, but was accurate enough for the conducted measurement. Further shown schematically is the pulse structure of the synchrotron indicated by vertical black lines. The interaction probability of the synchrotron pulses with the background/molecular beam is in the order of 0.005-0.01 %, indicated by the yellow bar. The synchrotron was tuned to a photon energy of 420 eV ( $\lambda = 2.95 \text{ nm}$ ).

### 6.3 Coincidence spectra

The photofragmentation of indole was investigated via a coincidence measurement between the emitted electrons and the corresponding ionic fragments. A background subtracted (PE)PIPICO spectrum [182, 183] of indole, ionized with a single photon at an energy of 420 eV, is shown in Figure 6.2 as a function of the mass to charge ratio of the first and second detected ion,  $m_1/q_1$  and  $m_2/q_2$ , respectively. The map allows to disentangle different fragmentation channels of indole in the case of at least two detected ionic fragments. The background correction was obtained by subtracting the signal outside the molecular pulse from the data recorded inside the molecular pulse with an appropriate weight. If not stated otherwise, no correction is applied to the presented data.

Visible are six main coincidence islands, labeled with 1-6. The coincidence islands 1-3 originate from the fragmentation channels,  $\text{C}_4\text{H}_{4-n} + \text{C}_4\text{NH}_{3-m}$  or  $\text{C}_3\text{NH}_{3-n} + \text{C}_5\text{H}_{4-m}$ ,  $\text{C}_2\text{NH}_{3-m} + \text{C}_6\text{H}_{4-n}$  or  $\text{C}_3\text{H}_{3-m} + \text{C}_5\text{NH}_{4-n}$ , and  $\text{C}_7\text{H}_{5-n} + \text{CNH}_2$  respectively. The indices  $m$  and  $n$  in the formulas account for the loss of hydrogens or protons. The molecular structure of indole (atomic labeling according to [184]) as well as an expanded scale of these coincidence islands is shown by the insets of Figure 6.2. This is visible as different diagonal lines within each of these PIPICO island, corresponding to a spacing of 1 u/e. The sum of the masses of all three islands is equal to the mass of indole, neglecting the loss of hydrogen/protons. The fragmentation patterns show the strongest coincidence upon the emittance of two or three hydrogens/protons in the case of island 1 ( $\text{C}_4\text{H}_{4-n} + \text{C}_4\text{NH}_{3-m}$  or  $\text{C}_3\text{NH}_{3-n} + \text{C}_5\text{H}_{4-m}$ ) and 3 ( $\text{C}_7\text{H}_{5-n} + \text{CNH}_2$ ). PIPICO island 2 ( $\text{C}_2\text{NH}_{3-m} + \text{C}_6\text{H}_{4-n}$  or  $\text{C}_3\text{H}_{3-m} + \text{C}_5\text{NH}_{4-n}$ ) shows only one

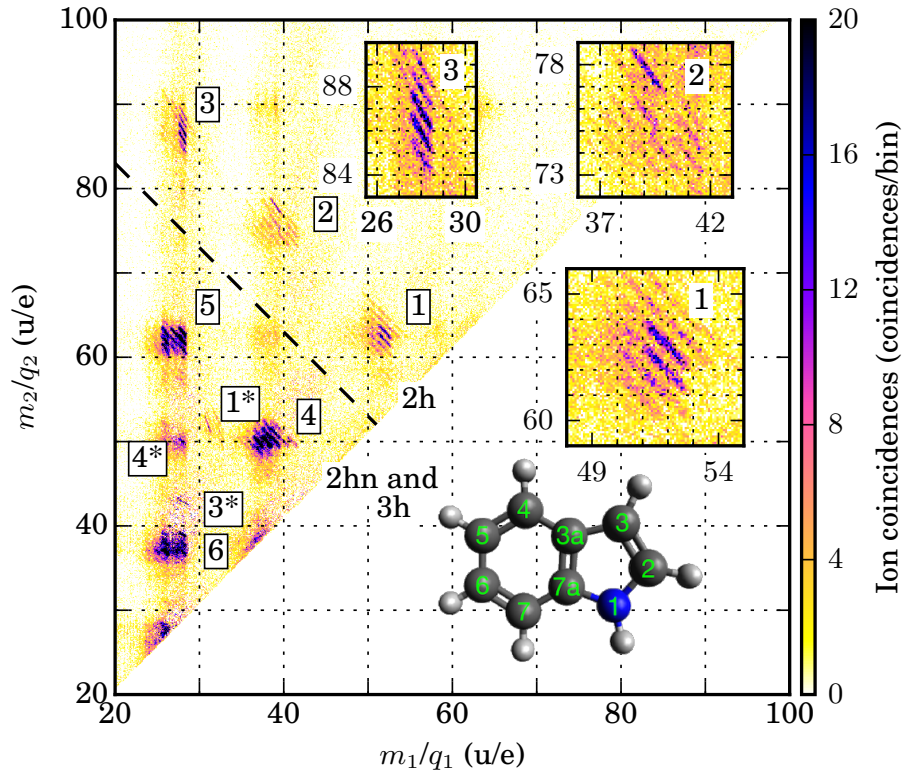


Figure 6.2: PIPICO spectrum of indole following soft x-ray ionization with six main coincidence islands and zooms into coincidence islands 1-3. The inset shows the molecular structure of indole.

dominant coincidence line visible at 39 and 78 u which is attributed to the latter channel. Coincidence island 1-3 have only two ionic fragments, again neglecting the emittance of hydrogens/protons, hence they are also labeled in the following as 2-hole (2h) fragmentation channels.

Coincidence islands 4-6 are due to fragmentation into three or more fragments, i. e., the total mass of the first two detected ions corresponding to a single event do not add up to the atomic mass of the indole monomer. The missing fragments can either be ionic or neutral. The corresponding fragmentation channels are labeled as 3-hole (3h) and 2-hole + neutral (2hn). The neutral fragment of the 2hn fragmentation channels can not be measured directly. Figure 6.3 a)-c) show 2hn coincidence islands; the color code is the same as for Figure 6.2. All three coincidence islands show again diagonal lines separated by 1 mass unit. Figure 6.3 d)-f) and g)-i) show the corresponding 3h fragmentation channels. The coincidence map between the second and third detected ionic fragment is shown in d)-f); the color code is the same as for Figure 6.2. The corresponding mass spectra of the first detected ion is shown in g)-i). For these coincidence events the first detected ion was accepted only if the mass to charge ratio was larger than 5 to suppress random correlations with the carrier gas. Additionally, water and hydronium fragments were not accepted as first detected ion which originate from a strong fragmentation channel of indole-water clusters [185]. The lack of diagonal lines in Figure 6.3 d)-f) is attributed to the momentum conservation of the fragmenting particles. If a fragment has significant momentum, as it is in this case for the first ion, the

## 6. X-ray photophysics of indole

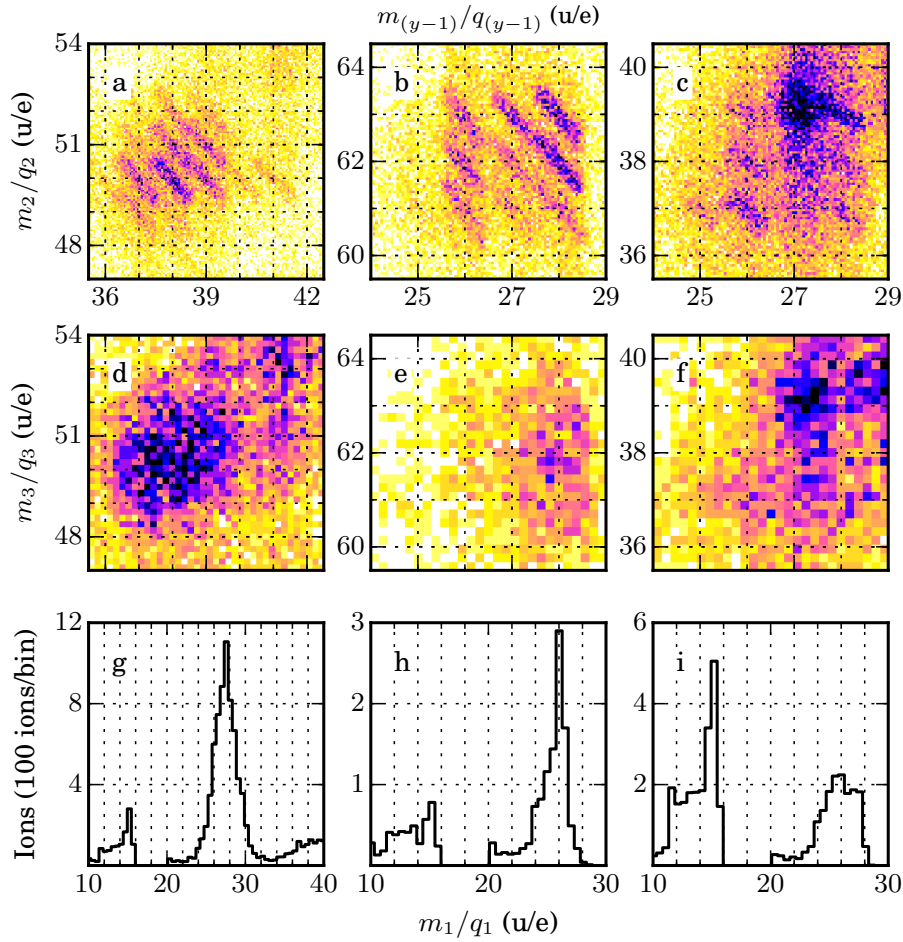


Figure 6.3: a-c: PIPICO islands 4-6 for the first against the second detected ion. d-f: Same PIPICO islands for the second against the third detected ion. g-i: Corresponding  $m/q$  spectrum of the first detected ion in case of a 3h fragmentation. The color code is the same as in Figure 6.2.

momenta of the two other ions are not opposed anymore, leading to a disappearance of the coincidence lines [186]. The ion peak at 15 u/e in Figure 6.3 g-i) is attributed to background ions since it does not obey momentum conservation with the other ions detected in coincidence.

The total mass of the two ionic fragments of PIPICO island 4 (Figure 6.3 a)) is between 86 and 91 u. The mass of the missing fragments ranges between 26 and 31 u which leaves  $2C + xH$  ( $2 \leq x \leq 7$ ) or  $C + N + yH$  ( $0 \leq y \leq 5$ ) as the only possible neutral fragments. The structure of the corresponding 3h fragmentation channel (Figure 6.3 d)) shows an additional enhancement of coincidences in the upper right corner. This is attributed to a background contamination since these ions do not obey momentum conservation. The mass spectrum of the first detected ion for this 3h channel is dominated by ions between 26 and 28 u/e which can be assigned to the ionic fragments  $C_2H_x$  ( $2 \leq x \leq 4$ ) or  $CNH_y$  ( $0 \leq y \leq 2$ ).

PIPICO island 5 (Figure 6.3 b)) consists of three distinct vertical coincidence islands with a mass to charge ratio of 26-28 falling in coincidence with masses of 61-63. The total mass of these ionic fragments is

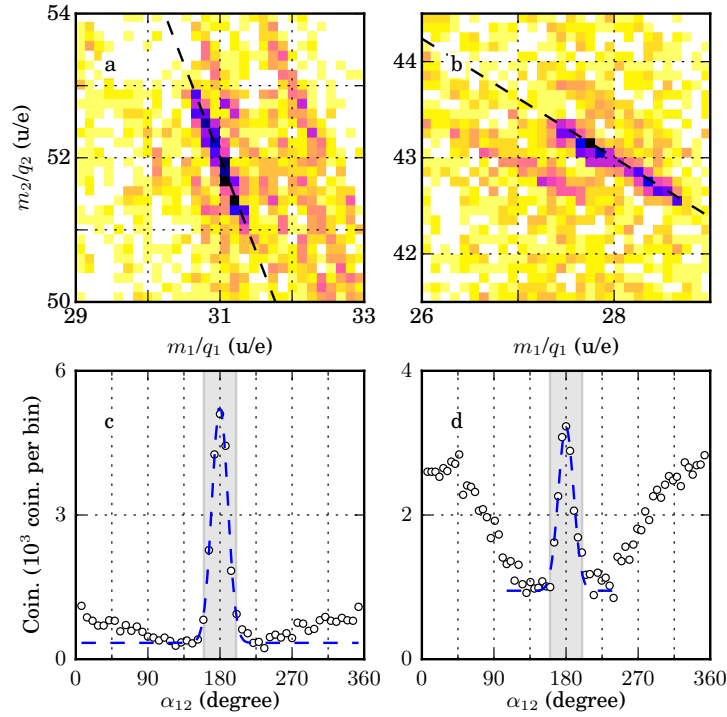


Figure 6.4: a) and b): Highlighted PIPICO islands 1\* (left) and 3\* (right). Dashed black lines show a theoretical linear dependence with slopes corresponding to dicationic first (left) and second (right) detected ions. The color code is the same as in Figure 6.2. c) and d) angle between the velocities  $v_1$  and  $v_2$  for both coincidence islands. The dashed blue lines highlight a Gaussian fit. Gray areas indicate the coincidences accepted for a) and b).

between 87 and 91 u. The mass of the neutral fragment ranges thus from 26 to 30 u.  $2C + xH$  ( $2 \leq x \leq 6$ ) or  $C + N + yH$  ( $0 \leq y \leq 4$ ) are hence the only possible fragments which are similar to the ones for PIPICO island 4. The mass spectrum of the first detected ion (Figure 6.3 h)) shows a strong peak at 26 u showing that only a single ionic fragment is detected in the case of a 3h fragmentation. The structure of the corresponding PIPICO island for the second and third detected ion (Figure 6.3 e)) shows a shift of the coincidence island toward higher masses. The shift in the 3h fragmentation channel can be explained considering the fragmentation possibilities in this channel. The mass of the first detected ion in the 2hn fragmentation channel ((Figure 6.3 b)) is between 26 and 28 u. If both mentioned fragments are ionic (Figure 6.3 h)) the lighter  $C_2H_x$  fragment will always be detected first and its coincidence peak consequently vanished in Figure 6.3 e). PIPICO island 6 is build up of four distinct vertical coincidence islands with ions detected between 25-28 u/e falling in coincidence with ionic fragments between 37-39 u/e. The enhancement of detected coincidences near the ionic fragments of 27 and 39 u/e is due to background contamination since these coincidences do not fulfill momentum conservation. The total mass of the two ionic fragments detected in PIPICO island 6 is between 62 and 67, leaving 50 to 55 u for the neutral fragment(s), i. e.,  $4C + xH$  ( $2 \leq x \leq 7$ ) or  $3C + N + yH$  ( $0 \leq y \leq 5$ ). The 3h coincidence spectrum in

## 6. X-ray photophysics of indole

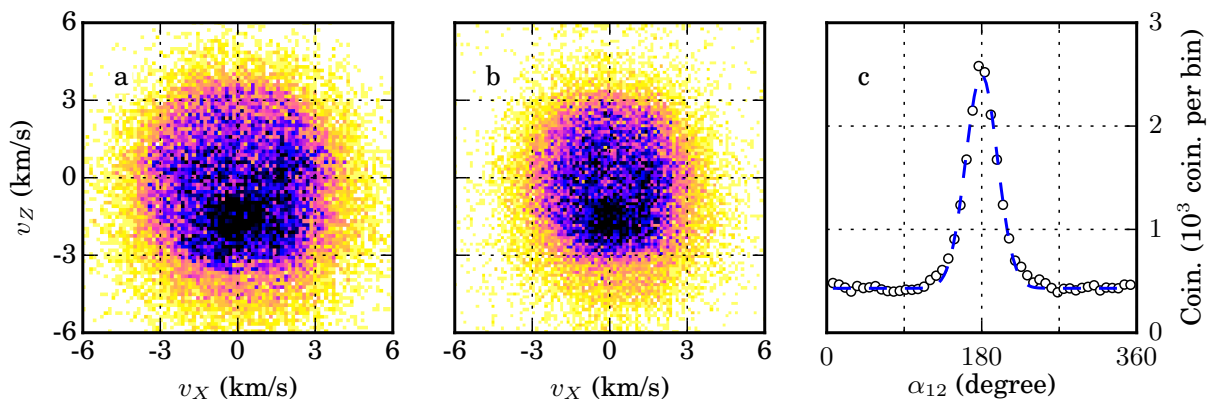


Figure 6.5: a) and b) VMI images of the first and second detected ion contributing to the 2hn fragmentation channel of coincident island 4. The color code is the same as in Figure 6.2 given in the unit of ions (ions/bin). c) Histogram of the angle between the first and the second ion with a Gaussian fit indicated by the dashed blue line.

Figure 6.3 f) is comparable in shape to the 2hn fragmentation channel. The mass spectrum of the first detected ion (Figure 6.3 i)) shows a comparable amount of detected ions between 12-14 u/e ( $\text{CH}_x$ , N) and 26-28 u ( $\text{C}_2\text{H}_x$  or  $\text{CNH}_x$ ). Thus, this channel shows a fragmentation into at least 3 ionic fragments and a, either neutral or ionic, fourth fragment.

Coincidence islands 1\*, 3\*, and 4\* are shown in Figure 6.2 additionally. They are assigned to 3h fragmentation channels of the coincidence island 1, 3, and 4, respectively. The islands 1\* and 3\* are highlighted in Figure 6.4 a) and b); the color code is the same as in Figure 6.2. In both islands a strong coincidence line is visible which is overlaid by a dashed black line. The slope  $s$  of a coincidence line can be used to assign the charge state of the fragments. Typically, the PIPICOs' are shown as a function of the ions TOF, leading to a slope of  $s = -1$  for equally charged fragments [186]. Here, the PIPICOs' axis is converted into mass to charge ratio units to visually assign easier the fragments. Therefore the slope is given by  $-\sqrt{(q_1 m_2)/(q_2 m_1)}$  for the case of a fragmentation into two particles<sup>§</sup>. The dashed black lines show the calculated slopes for the channels  $(\text{C}_4\text{H}_4)^+ + (\text{C}_4\text{N})^{++}$  or  $(\text{C}_3\text{NH}_2)^+ + (\text{C}_5\text{H}_2)^{++}$  in case of island 1\* and the channel  $(\text{CNH}_2)^+ + (\text{C}_7\text{H}_2)^{++}$  for island 3\*, respectively.

Both are in good agreement with the experimental data. Both islands show the strongest coincidence at a total mass of 114 u, as well as a dicationic state of the heavier fragment. For both spectra a filter was applied such that only events which had opposed momenta are displayed. This was especially necessary for Figure 6.4 b) where the PIPICO line is hidden without the filter. The histogram of the angular distribution  $\alpha_{12}$  of all ions without filter is shown in Figure 6.4 c) and d).  $\alpha_{12}$  is defined by the angle between the projected velocity vectors of the first and second detected ion as indicated by the indices. The angle is determined in a mathematical sense starting from the first ion. Both graphs show a maximum at

<sup>§</sup>It is given by  $-\sqrt{(q_2 m_1)/(q_1 m_2)}$  for PIPICOs displayed in the lower right half of the coincidence spectrum.

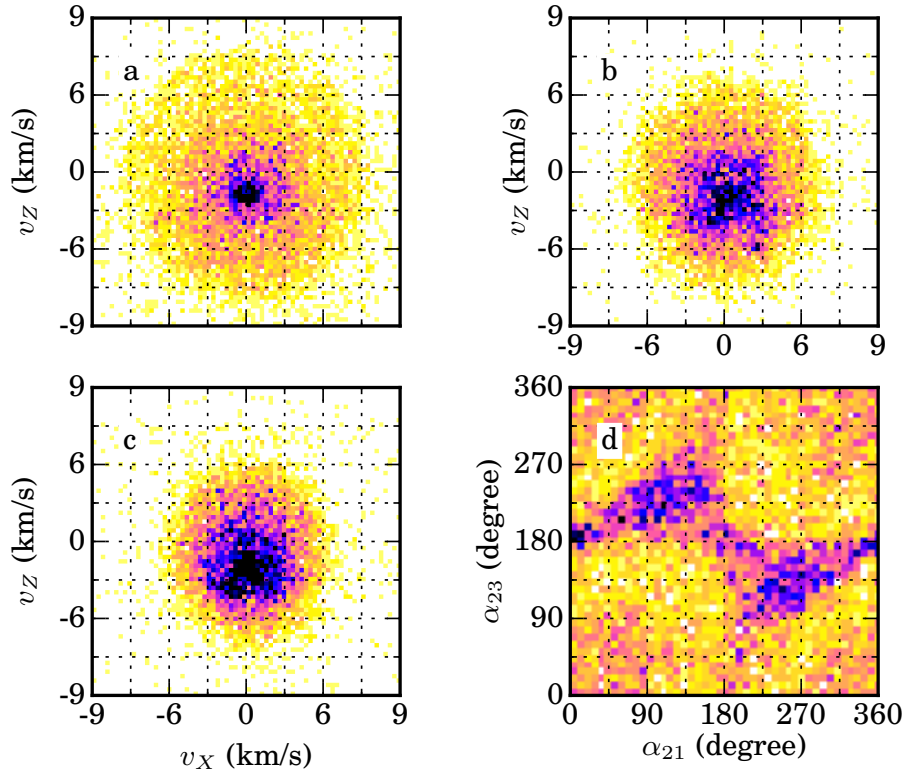


Figure 6.6: a), b) and c) VMI images of the first, second and third detected ion contributing to the 3h fragmentation channel of coincident island 4. d) 2D histogram of the angles between the second and first as well as second and third detected ion. The color code is the same as in Figure 6.2 and for a), b) and c) it is given in the unit of ions (ions/bin).

180 degrees which is expected for an axial recoil of both fragments. The dashed blue line is indicating a Gaussian fit to the data. The RMS of these fits are  $\sigma = 9.8$  and  $\sigma = 9.5$  degrees for  $1^*$  and  $3^*$ , respectively. For the coincidence spectra in Figure 6.4 a) and b) data in the gray area has been used. The width of the grey area is equivalent to  $4\sigma$ . The non-constant offset of the angular distributions is attributed to the molecular beam velocity parallel to the detector surface and the background signal which is centered at the absolute velocity point of origin.

Figure 6.5 and Figure 6.6 show exemplarily VMI images of the coincidence island 4 for the case of a 2hn and a 3h fragmentation channel. The increased number of counts visible in all VMI images at  $v_X = 0$  and  $v_Z \approx -1.5$  is attributed to background from the carrier gas which is falsely detected at that corresponding TOF and does not obey momentum conservation. The VMI images for the two ionic fragments detected in the 2hn fragmentation channel are shown in Figure 6.5 a) and b); the color code is the same as shown in Figure 6.2 given in the unit of ions per bin. The first detected ion shows a slightly higher velocity compared to the second detected ion which is explained by its lower mass and the momentum conservation of the fragmenting particles. Despite the neutral dissociating fragment, the two detected ions do still obey strong axial recoil. This is shown by, for example, the diagonal coincidence lines for island 4 in Figure 6.3.

## 6. X-ray photophysics of indole

A closer insight is given in Figure 6.5 c) by the histogram of the angular relationship between both ionic fragments, where  $\alpha_{12}$  is defined as before. The dashed blue line is indicating a Gaussian fit to the data with an corresponding RMS of  $\sigma = 18.4$ .

VMI images of the 3h fragmentation channel of PIPICO island 4 are shown in Figure 6.6 a)-c) for the first, second and third detected ion; the color code given as the same as in Figure 6.2 in units of ions per bin. The first detected ion shows the highest of all velocities due to its lighter mass and the momentum conservation of the fragmentation process. The angular relationship between all fragments is visible in Figure 6.6 d); the color code is the same as in Figure 6.2. Shown here is the angle  $\alpha_{23}$  plotted against the angle  $\alpha_{21}$ .  $\alpha_{21}$  and  $\alpha_{23}$  are defined as before. Visible is a sand-timer like structure, rotated by approximately  $45^\circ$ . The existence of this structure clearly shows that there is a angular relationship between these fragments. The coincidences outside that structure are due to ions which do not fulfill momentum conservation.

### 6.4 Photoelectron spectrum

Figure 6.7 a) and b) show the electron velocity map in a cartesian and a polar coordinate systems respectively. The labels Q1-Q4 correspond to the four different quadrants of the VMI image. The electrons were detected in coincidence with PIPICO island 1-5, 1\* and 3\* (Figure 6.2). A background correction was applied by accepting only events which obey momentum conservation. Islands 6 was not used due to a high background contamination. The VMI images show four distinct electron velocities at 2.4, 7.1, 9.5, and  $11.2 \cdot 10^6$  m/s which correspond to electron energies of 16, 142, 258, and 358 eV. Additionally, slow electrons are visible in the center of the cartesian VMI image which are assigned to background electrons. The photoelectrons at a velocity of  $v_r = 2.4 \cdot 10^6$  m/s (16 eV) are attributed to localized ionization at the indoles' nitrogen atom from the  $1s$  orbital. The corresponding VMI images show an increased (decreased) signal at  $0^\circ$  and  $180^\circ$  ( $90^\circ$  and  $270^\circ$ ) which is due to ionization from a  $s$ -orbital with circular polarized light polarized in the  $X$ - $Z$  -plane. The angular dependence is best visible in the polar plot of the VMI image. The electrons at an velocity of  $v_r = 7.1 \cdot 10^6$  m/s (143 eV) are assigned to photoelectrons generated by ionization of the indole monomer at a carbon  $1s$  orbital. The anisotropy of the angular distribution is attributed again to the  $s$ -orbital in combination with the circularly polarized synchrotron radiation. Auger electrons are visible at higher electron velocities. The Auger electrons at a velocity of  $9.5 \cdot 10^6$  m/s are due to Auger electrons following the ionization out of a carbon  $1s$  orbital and are isotropically distributed in the laboratory frame. Higher electron velocities are attributed to Auger electrons following ionization at the nitrogen part of the molecule. The electron energy spectrum shown in the bottom graph of Figure 6.7 was obtained from an inverse Abel transformation based on the BASEX algorithm [187]. The inverse Abel transformation was performed by accepting only the second and third quadrant of the electrons VMI image (Q2, Q3, Figure 6.7) due to distortions of the VMI image. These are best visible in the polar plot of Figure 6.7 for Q1. The mean values of the photoelectron energies (*vide supra*) were determined by fitting a Gaussian distribution to the four labeled peaks. The corresponding FWHM is determined to 10, 20, 33, and 31 eV for the nitrogen and carbon  $1s$  as well as Auger electrons. The correspondingly determined  $\beta$

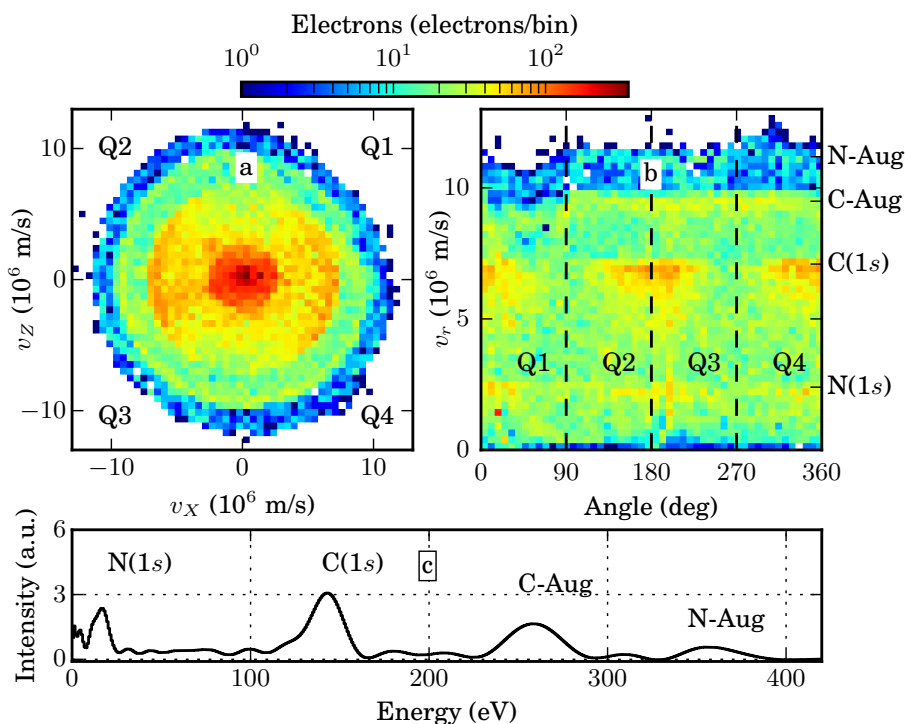


Figure 6.7: Photoelectron VMI image of indole (top) in a cartesian (left) and polar (right) coordinate system. Q1-Q4 indicate the four different quadrants of the VMI image. The photoelectron energy spectrum (inverse Abel transformation of Q2 and Q3) is shown in the lower graph in black.

parameters (anisotropy parameters [67]) are  $-0.6$  ( $0.1$ ),  $-0.8$  ( $0.0$ ),  $-0.1$  ( $0.0$ ), and  $-0.1$  ( $0.1$ ) which were calculated over for the FWHM of the corresponding peak. The numbers in the brackets indicate the determined standard error. Figure 6.8 shows histograms of the electrons velocity spectrum shown in Figure 6.7 sorted into the contributions of the ion fragmentation channels 2h (black), 2hn (red),  $1^* + 3^*$  (blue), and 3h (green). The histograms are normalized to the number of counts and the error bars are given as the statistical error per bin. The connecting lines serve to guide the eye. The spectra for the fragmentation channels 2h and 2hn (black and red) show a similar shape. Both show peaks at energies which were assigned to nitrogen and carbon 1s photoelectrons and Auger electrons. The spectra for the fragmentation channels  $1^* + 3^*$  and 3h (blue and green) again show a similar distribution. Both deviate from the 2h and 2hn electron spectra. The strongest peak of the spectrum is at electron velocities close to the N(1s) photoline. It drops-off quasi continuously toward higher electron velocities, indicating that these fragmentation channels are preferably populated upon side-specific ionization at the indoles' nitrogen atom. For these channels an inverse Abel transformation was not practical due to a low statistics.

## 6.5 Discussion

The photon energy of 420 eV is 10 eV above the atomic nitrogen 1s binding energy, leading to the highest cross section for atomic nitrogen ( $0.6466 \cdot 10^{-22} \text{m}^2$ ), followed by atomic carbon ( $0.4327 \cdot 10^{-22} \text{m}^2$ ) [76].

## 6. X-ray photophysics of indole

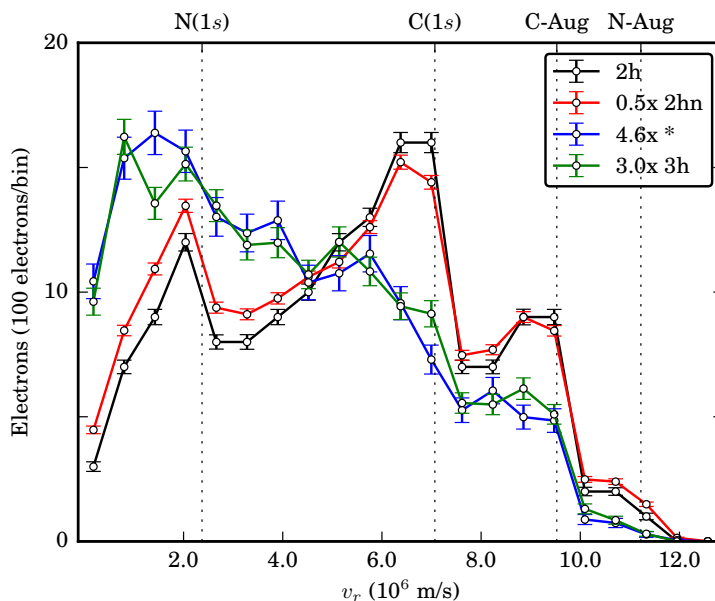


Figure 6.8: Radial plot of the electron VMI image detected in coincidence with the PIPICO islands 1-3 (2h black), 4-5 (2hn, red), 4-5 (3h, green), and 1\* and 3\* (blue). The histograms have been normalized to the number of counts.

In total, the indole monomer has eight carbons and one nitrogen, leading to a probability of 16 % that the complex is locally ionized at the nitrogen  $1s$  assuming that the atomic cross section do not differ significantly from those within the molecule. The photoabsorption cross sections for hydrogen is 3000 times smaller than the nitrogen cross section and is therefore not considered in the following. The PIPICO spectrum shown in Figure 6.2 is highlighting the fragmentation pattern of indole upon single photon core hole ionization from the nitrogen and carbon  $1s$  orbitals. Branching ratios between the main islands from the PIPICO spectrum can be estimated to 27, 60, and 13 % for 2h, 2hn and 3h fragmentation respectively, taking the ion detection efficiency into account. The majority of indole molecules is therefore fragmenting into three heavy fragments.

PIPICO island 3 and 3\* are the only PIPICO islands in which the ionic fragments can be uniquely assigned to the fragments  $C_7H_{5-n} + CNH_2$  of the molecule, if proton and hydrogen transfer processes are neglected. PIPICO island 1 and 2 consist of a superposition of two fragmentation channels. These channels are also not unique in terms of where the fragments are located inside the molecule. Considering, for example, the fragmentation  $C_3NH_{3-n} + C_5H_{4-m}$  of PIPICO island 1. The carbons being part of the nitrogen containing fragment could be due to the carbons (2,3,3a) or (2,3,7a) or (2,7,7a) or (6,7,7a) (see notation in the inset of Figure 6.2). In the case of 2hn and 3h fragmentation channels (islands 4-6 shown in Figure 6.3) the possible combination of ionic fragments is naturally increasing which leads to an even lower probability to uniquely assigning the fragments inside the molecular structure. Exclusions are single coincidence lines like  $C_4H_4 + C_4NH_3$  (PIPICO island 1) whose mass sum is equivalent to the mass of the indole molecule.

A closer assignment of the neutral fragments of PIPICO island 4 and 5 ( $2C + xH$  or  $C + N + yH$ ) is not possible since the neutral fragments cannot be detected. We speculate that the missing masses are intact fragments due to the following reasons. First, the ionic fragments dominantly stay intact in the case of a 3h fragmentation. Second, there is no dominant PIPICO island where only a single carbon is missing.

For the case of the 2h and 2hn fragmentation channels the ions recoil on average at  $180^\circ$  as shown in Figure 6.4 c) and d) and Figure 6.5 c). The width of the angular distribution is dependent on the fragmentation process. Island 1\* and 3\* have a RMS of  $\sigma = 9.8^\circ$  and  $\sigma = 9.5^\circ$ , compared to  $\sigma = 18.4^\circ$  for the 2hn fragmentation channel of PIPICO island 4. The corresponding analysis for the RMS of the PIPICO islands 1-3 (2h) lead to  $\sigma = 12.7^\circ$ . The slightly smaller opening angle observed for island 1\* and 3\* compared to the 2h fragmentation channel can be attributed by the stronger Coulomb repulsion between the ionic fragments leading to a faster dissociation and a more instantaneous mapping of the molecules orientation. The larger opening angle for the 2hn fragmentation channels is ascribed by the momentum transfer to the neutral fragment.

The velocity of the neutral fragment of a 2hn fragmentation can be estimated as described in the following. The momenta of the ionic fragments can be determined from the VMI images. The total momentum of all fragments including electrons and photons has to be zero if energy conversion into internal energies and rotations is neglected. In the case of the 2h fragmentation channels the RMS is broadened by the momentum of the absorbed photon, the emitted electrons, and the emitted protons/hydrogens as these particle momenta were not taken into account. The RMS of a 2hn fragmentation is additionally broadened by the momentum taken up by the neutral fragment. Comparing the RMS distribution between the 2h and 2hn channels provide the information on the momentum taken up by the neutral fragment. A velocity of 0.5 km/s can be assigned to the momentum distribution of the neutral fragment of island 4 assuming a single fragment with a mean mass of 27 u.

The recorded electron velocities spectra show a distortion which is visible in Figure 6.7 b) for electron velocities in the order of  $10 \cdot 10^6$  m/s. The distortions are attributed to a non-perfect setup of the VMI as well as a non-working third electrode which is part of the hexanode DLD. Both limit the reconstruction of the electron energy spectrum shown in Figure 6.7 c).

The mean electron energies are given by 16, 142, 258, and 358 eV for  $N(1s)$ ,  $C(1s)$  photoelectrons, and the corresponding Auger electrons following core-hole ionization at the carbon and nitrogen atoms. The atomic nitrogen and carbons photoelectron energies are 10.1, 135.8 eV [78]. They deviate both by about 6 eV. The observed C-Auger electron energies agree well with the experimentally observed lines in benzene at 243-267 eV [188]. The nitrogen Auger lines agree well with the calculated energies of 356-377 eV [189]. The fitted Gaussian functions allow to determine the relative number of electrons for the specific peaks as they match the spectrum well within the FWHM range of the individual peaks. The fit underestimates the number of events below the mean of the  $N(1s)$  and  $C(1s)$  peak due to the shoulders present in the spectrum. The shoulder at the  $N(1s)$  peak is attributed to the imperfect mapping of the electron velocities as only a single photoelectron energy is present in that energy range. The estimated width of the 8  $C(1s)$

## 6. X-ray photophysics of indole

lines is in the order of 2 eV due to the chemical shift and thus much smaller than the measured RMS of 20 eV. The shoulder is therefore not attributed to the chemical shift of the C(1s) lines. In addition the 0.4 eV bandwidth of the synchrotron radiation can be neglected. The reconstructed beta parameters are -0.6, -0.8, -0.1, and -0.1 for the corresponding electron energies. Beside the N(1s) peak, all determined parameters are within 0.2 of the expectation of a beta parameter of -1 and 0 for photoelectron distributions with  $|J, M\rangle = |1, 1\rangle$  and  $|J, M\rangle = |0, 0\rangle$ . Comparing the relative number of electrons for the N(1s) and C(1s) peak shows a 26.1 % probability for localized ionization at the nitrogen atom. A similar probability of 24.8 % is obtained by comparing the Auger electrons. Both numbers slightly higher than the expected probability of 16 % taking into account the atomic cross sections of C and N.

The 2D projections of the 3D electron velocity distribution are shown in Figure 6.8. The 2h and 2hn fragmentation channels show clearly the four assigned electron energies. The relative peak heights between these 2h and 2hn channels deviate slightly dependent on the photoelectron velocity. For the nitrogen 1s photoelectrons and their corresponding Auger electrons, the 2hn fragmentation channel is stronger than the 2h fragmentation channel. In contrast, for the carbon 1s photoelectrons and their corresponding Auger electrons the 2h fragmentation channel is stronger than the 2hn fragmentation channel. This indicates a higher probability for the 2hn fragmentation channel if the indole monomer is locally ionized at its nitrogen atom. This can be qualitatively explained by considering the ionization state of indole. If indole is locally ionized at the nitrogen atom the molecule has to redistribute  $\approx 410$  eV of energy, compared to  $\approx 284$  eV in the case of a carbon 1s ionization. Thus, a higher fragmentation of the molecule seem to be more likely upon locally ionization of the nitrogen. This statement is additionally confirmed by the electron spectra of the 3h fragmentation channels. They show a relatively higher number of counts for photoelectrons origin from ionization at the nitrogen part of the molecule, and a suppression of the C(1s) photoelectrons.

The presented data can in principle be used to reconstruct recoil-frame photo-angular distributions (RFPAD) which contain information about the molecular structure or possibly the fragmentation process. Photoelectron and Auger electron RFPAD images were reconstructed for the presented data, but the limited amount of electron-ion coincidences (in the order of hundred events) did not show significant asymmetries in the RFPAD distribution.

## 6.6 Conclusion

We have presented the photofragmentation of the indole monomer upon core-shell ionization by soft-x-ray radiation at a photon energy of 420 eV. Both, electrons and ions, have been measured in coincidence via velocity-map imaging. The PIPICO spectrum of indole has been discussed. It was found that the indole monomer was primarily fragmenting into two ionic and a neutral fragment (neglecting the emittance of hydrogens/protons). These fragments consist of at least two bounded carbon atoms if indole was fragmenting in two or three fragments. The ionic fragments recoil on average with an angle of  $180^\circ$  if the fragmentation channel consisted of two ionic fragments or if a third neutral fragment is part of

the fragmentation channel. Fragmentation channels consisting of three ionic fragments also showed a fixed angular relationship. The PIPICO spectrum additionally showed that the unique assignment of a coincidence island to specific atoms within the molecule is rather the exception than the rule. We presented the velocity distribution of selected fragmentation channels and discuss the velocity of a possible neutral fragment.

The electron spectrum showed four electron energies which were assigned to photo- and Auger electrons resulting from side-specific ionization at the indoles' nitrogen as well as ionization at the carbon atoms. The electron spectra have showed that some of the fragmentation channels of indole are primarily correlated to side-specific ionization at the nitrogen part of the molecule. The presented data allowed to measure RFPAD images of indole. Within our low statistics however no significant assymetries in the RFPAD distribution were found.

Our work provides the basis for fragmentation studies of larger molecules as well as molecular clusters. Comparison of the found fragmentation channels and dissociation energies will allow to study the role of solvents on the photophysics of indole upon site specific x-ray ionization.



## 7 X-ray photophysics of indole-water clusters

The following chapter is describing the photophysics of indole(H<sub>2</sub>O) upon core-shell ionization by soft x-ray radiation. The experiment was conducted along with the experiment described in chapter 6. Thus, the experimental setup is the same, and a more detailed description is given in section 6.2. The supplementary informations are given in Appendix B, covering the reconstruction of the molecular beam profile (section B.1), a general explanation of an ion-coincidence spectrum (section B.2), and the calibration measurements for the ion TOF and VMI (section B.3,section B.4), as well as the electron VMI (section B.5). This chapter starts with a motivation and short description of the experimental setup (section 7.2), followed by a comparison of the ion coincidence spectrum (section 7.3) and the recorded electron spectrum (section 7.4). It is closing with the discussion (section 7.5) and a summary including outlook (section 7.6).

### 7.1 Introduction

Properties of atoms and molecules are strongly dependent on their environment. Hydrogen bonds are of universal importance in chemistry and biochemistry and it is, therefore, of great interest to bridge the gap between single isolated molecules and molecules in solvation. Indole (C<sub>8</sub>H<sub>7</sub>N) is the chromophore of the amino acid tryptophan. Indole and tryptophan have been intensively studied by a variety of experiments (see section 6.1). This experiment is a follow-up experiment to the experiment presented in chapter 6, and is focussing on the photofragmentation of indole(H<sub>2</sub>O) clusters upon localized ionization at the indole-part of the molecule. The structure of indole(H<sub>2</sub>O) is already well known [171, 178], the water is hydrogen-bonded to the nitrogen part of the indole as it is shown by the inset of Figure 7.2 [190]. The indole(H<sub>2</sub>O) cluster can be spatially separated from the other species in the molecular beam, such as indole or higher clusters like indole(H<sub>2</sub>O)<sub>2</sub> [12]. The well known structure and the purification of the indole(H<sub>2</sub>O) in the molecular beam make indole(H<sub>2</sub>O) a good candidate to study hydrogen bonding. Further, the localized ionization by the soft x-ray radiation leads to a well known starting point for the study of the photophysics of indole(H<sub>2</sub>O). The aim of the study is to focus on the photofragmentation of indole(H<sub>2</sub>O), and to learn about the influence of the hydrogen-bonded water on the fragmentation of indole by comparison to the photofragmentation of the isolated indole monomer (chapter 6). Therefore, indole(H<sub>2</sub>O) is ionized at its (atomic) carbon 1s orbitals, or site-specific ionization at the nitrogen 1s orbital. VMI spectra of electrons and ions were recorded in coincidence. A coincidence map allowed to disentangle the different fragmentation channels, and the VMI images allowed to get a deeper insight into the fragmentation process.

## 7. X-ray photophysics of indole-water clusters

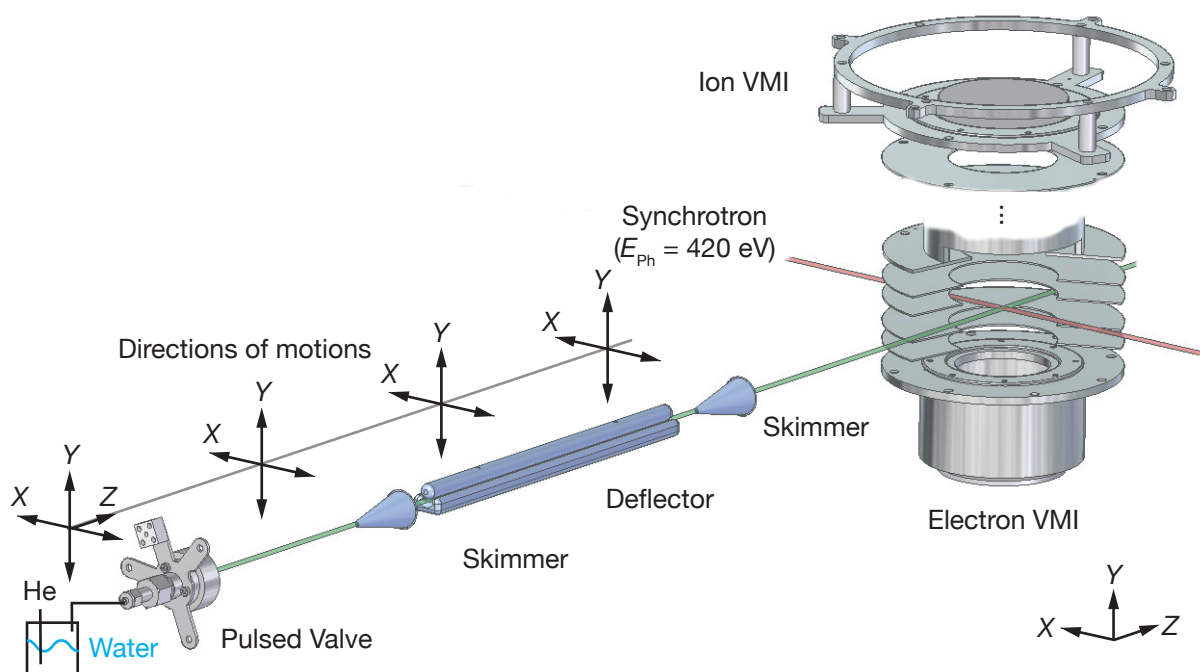


Figure 7.1: Experimental setup showing the water reservoir, pulsed valve, two skimmers, the deflector, and the electron and ion detector as well as the optical axis of the synchrotron (red). The valve was movable in all directions, both skimmers and the deflector were movable in  $X$  and  $Y$  directions. In that way different spatial positions within the molecular beam could be probed to select the desired molecular species.

### 7.2 Experimental setup

The experimental setup is shown in Figure 7.1 and is the same as shown in section 6.2, extended by the water reservoir and the motion directions of the movable parts of the experimental setup. In short, the seeding gas (60 bar helium) was bubbled through a water reservoir, which was connected to the pulsed valve [63]. The valve contained the sample reservoir filled with indole, and was heated to a temperature of 110 °C. The mixture of indole, water, and seeding gas was expanded into vacuum at a repetition rate of 250 Hz. During the early phase of the supersonic expansion 3-body collisions occur, which lead to the formation of indole<sub>m</sub>(H<sub>2</sub>O)<sub>n</sub> clusters. Clusters and the water monomer contributed approximately 20 % to the molecular species present in the molecular beam. Considering only the clusters, indole(H<sub>2</sub>O) clusters had the highest population, the remaining 80 % of the molecular species were due to the indole-monomer. The molecular beam was singly skimmed before it was transmitted through the deflector. The deflector consists of two closely spaced electrodes, which were used to generate a strongly inhomogeneous electric field to spatially separate the different molecular species [12] according to their effective dipole moment to mass ratio. The species-dependent deflection allowed to spatially separate indole<sub>1</sub>(H<sub>2</sub>O)<sub>1</sub> clusters from the other species because it has the highest effective dipole moment to mass ratio. The molecular beam was probed by the synchrotron in the center of the double-sided VMI. All the components of the molecular

beam could be moved such that it was possible to probe the different positions within the molecular beam. The photon energy of the synchrotron was tuned to 420 eV\*, which is 10 eV higher than the binding energy of the 1s electrons of atomic nitrogen [78]. The electron/ion detection system consisted of a double-sided VMI to measure electrons and ions in coincidence. Each VMI was equipped with a MCP and a hexanode/quadanode delay-line detector (DLD, Roentek) for the electron/ion side. Once an electron was detected, the ions were recorded for a time of 6  $\mu$ s. The detected electron(s) and ions were written down in a shot-list and marked as a single event. A more detailed description of the setup is given in section 6.2, and the calibrations used for the presented data are given in Appendix B.

### 7.3 Ion coincidence spectra

The photofragmentation of indole-water was investigated via a coincidence measurement between the detected electrons and ions subsequent to core-shell ionization at the indole-part of the cluster. The coincidence spectrum of two ions can be plotted in a so-called Photoion-Photoion Coincidence (PIPICO) map (section B.2). This is shown in Figure 7.2 for the first ( $m_1/q_1$ ) and second ( $m_2/q_2$ ) detected ion of all events. The PIPICO map has been corrected for the background by the same method as described for Figure 6.2. The color scheme is given in coincidences per bin, and the insets show the molecular structure of indole(H<sub>2</sub>O) [171, 178, 190], and a deflection profile of the molecular beam. The coincidence spectrum shows a sum of all recorded coincidence spectra at various spatial positions in the molecular beam. Highlighted are three areas by the blue square, and the red and green triangle. These are assigned to fragmentation channels from indole(H<sub>2</sub>O), indole, and other clusters, respectively. Within the area of the other clusters the summed mass of  $m_1/q_1$  and  $m_2/q_2$  is bigger than 135 u/e, i. e., they are heavier than the indole(H<sub>2</sub>O) cluster. Thus they must originate from bigger clusters. The red triangle highlights the fragmentation signature of indole, which is in detail described in section 6.3.

The blue area is assigned to fragmentation channels from indole(H<sub>2</sub>O), and is highlighted again in Figure 7.3. This assignment of the blue area to indole(H<sub>2</sub>O) was done for the following reasons. At first, the first detected ion has a mass to charge ratio 18 and 19 u/e, which can be assigned to the fragments H<sub>2</sub>O<sup>+</sup> and H<sub>3</sub>O<sup>+</sup>. These channels are absent in the PIPICO of the indole-monomer (section 6.3). Further, the deflection profile, which is shown in the inset of Figure 7.2, and discussed in the next paragraph, supports the assignment of the blue area to indole(H<sub>2</sub>O) since it is much stronger deflected than, for example, the higher clusters.

The deflection profile was recorded by moving the molecular beam (pulsed valve, skimmers and deflector) over a distance of 3 mm in the *Y*-direction, which is equal to a scan of the vertical molecular beam profile [12]. This has been done for an applied voltage difference of zero and 25 kV at the deflector electrodes. The undeflected beam profile (0 V) is visible as a black line connecting the individual measurement points (circles). The deflection profiles (25 kV) for indole, indole-water and higher-order clusters are highlighted

---

\*Petra III, Variable Polarization Beamline P04 [181], circular polarization (> 98%). At the time of the experiment the only possible polarization.

## 7. X-ray photophysics of indole-water clusters

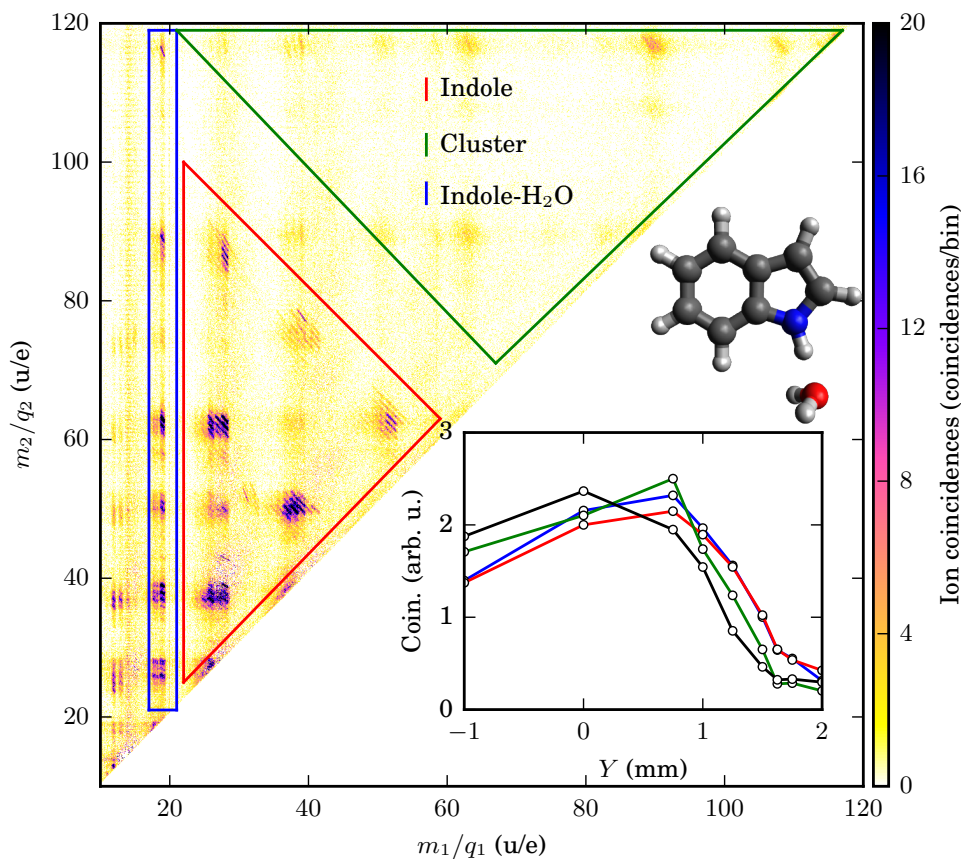


Figure 7.2: Coincidence spectra between the mass to charge ratio of the first ( $m_1/q_1$ ) and second detected ion ( $m_2/q_2$ ) per event. The insets show the molecular structure of indole-water [171, 178, 190] as well as the deflection profile extracted from the PIPICO map. The PIPICO map shows a sum of all coincidence spectra recorded at the different spatial positions of the molecular beam and the color scheme is given in coincidences per bin.

by their corresponding color scheme. For each species the (background corrected) counts within the major coincidence islands were integrated. The undeflected beam profile shows a normalized sum of all integrated coincidence islands (indole, indole( $H_2O$ ), and cluster) for the case where the deflector was switched off. The deflection profile for the different species are normalized to their individual undeflected beam profiles. Additionally, each measurement has been normalized to the integration time to compensate for the different recording times at each spatial position. It can be seen that indole and indole( $H_2O$ ) are stronger deflected than the clusters due to their higher effective dipole moment to mass ratio [12]. Though, in contrast to [12], indole shows a similar deflection profile to indole( $H_2O$ ).

The coincidence islands of indole( $H_2O$ ) are highlighted in Figure 7.3; the color scheme is the same as in Figure 7.2. The  $x$  and  $y$ -axes have been reversed such that the first (second) detected ion is now displayed on the  $y$ -axis ( $x$ -axis). In all coincidence islands the hydronium fragmentation channel ( $m_1/q_1 = 19$ ) is

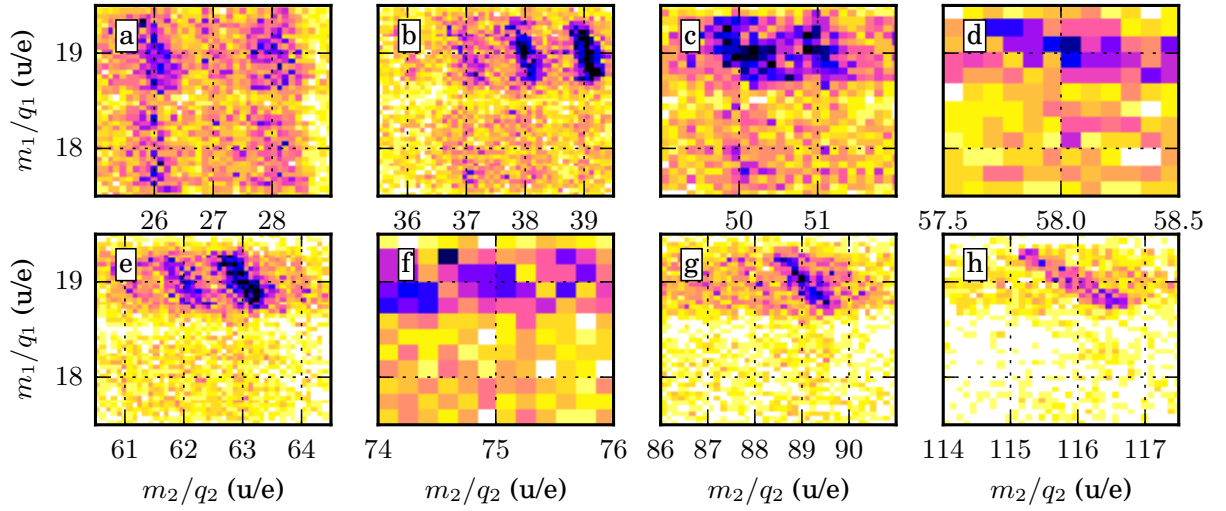


Figure 7.3: Highlighted coincidence islands of indole-water (blue square in Figure 7.2) for the first and second ion detected. The color scheme is the same as given in Figure 7.2

dominant compared to the  $\text{H}_2\text{O}^+$  ( $m_1/q_1 = 18$ ) fragmentation channel. In Figure 7.3 e-h) a coincidences between  $\text{H}_2\text{O}^+$  and the indole-fragments is not visible. This is only due to the given color scale and the given binning of the PIPICO map. They are similar to the  $\text{H}_3\text{O}^+$  fragmentation channels but simply have a much lower population. Therefore those channels are not highlighted separately. Most coincidence islands show an increased detection in the form of lines, which are signatures of an axial recoil of the detected ionic fragments [186]. The second detected ions in Figure 7.3 a)-c) and e)-g) have all been detected in the photofragmentation of the indole monomer (section 6.3). This is also clearly visible in Figure 7.2 by comparing the second detected ion of indole and indole( $\text{H}_2\text{O}$ ). Additional channels are given by Figure 7.3 d) and h). The latter one is a coincidence between  $\text{H}_3\text{O}^+$  and the  $(\text{indole-H})^+$ , i. e., the ion of the indole monomer, which donated a hydrogen/proton to the hydrogen-bonded water. Figure 7.3 d) shows in principle the same channel, but this time singly charged  $\text{H}_3\text{O}^+$  is in coincidence with doubly-charged  $(\text{indole-H})$ , given thus in the mass to charge ratio 58 u/e instead of 116 u/e.

A coincidence map between the second and third detected ion is show in Figure 7.4 for which the first detected ion was selected between 17.5 to 19.5 u/e, i. e.,  $\text{H}_2\text{O}^+$  and  $\text{H}_3\text{O}^+$ . Visible is the coincidence structure of indole and higher clusters, highlighted by the red and green triangles as shown as well in Figure 7.2. The existence of the indole fragmentation pattern confirms the findings in Figure 7.3 that  $\text{H}_2\text{O}^+$  and  $\text{H}_3\text{O}^+$  are always found in coincidence with a fragment of indole. Also, it shows that there is a probability of triple-ionization of the indole( $\text{H}_2\text{O}$ ) cluster, where one charge is found on the hydrogen-bonded water and two charges are left on the indole. Latter one is leading to a similar fragmentation process of the indole-part compared to the indole monomer shown in Figure 6.2. The inset is highlighting the washed out PIPICO island structure. The earlier mentioned diagonal lines within the PIPICO are not

## 7. X-ray photophysics of indole-water clusters

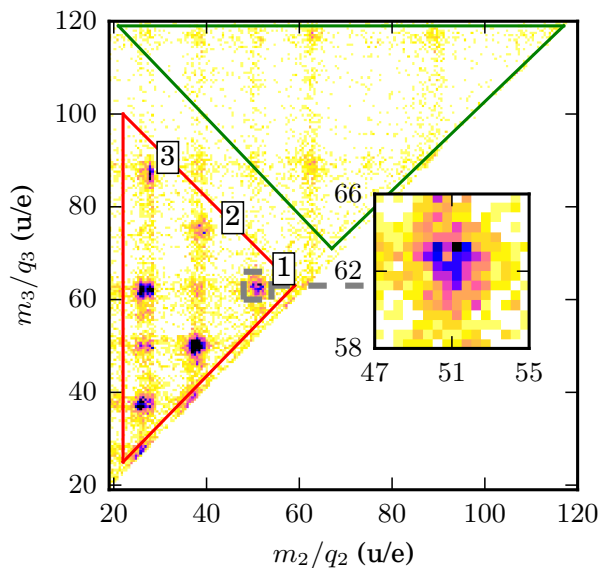


Figure 7.4: PIPICO spectrum of the second and third detected ion. In order to produce this figure, a gate was set for the mass to charge ratio of the first ion such that it was between 17.5 and 19.5 u/e, i. e.,  $\text{H}_2\text{O}^+$  and  $\text{H}_3\text{O}^+$ . The red and green triangles are the same as shown in Figure 7.2 and are corresponding to the indole and cluster fragmentation patterns. The inset highlights a coincidence island of the indole part. The labels 1-3 highlight PIPICO islands where  $m_1/q_1 + m_2/q_2$  is equal to the mass of the indole monomer, if proton loss is neglected.

present anymore, which is a common feature of a 3-body break up where all fragments carry significant momentum. The labels 1-3 highlight PIPICO islands where  $m_1/q_1 + m_2/q_2$  is equal to the mass of the indole monomer if proton loss is neglected. The labeling of these islands is in accordance with the labels given in chapter 6. In addition to the pure indole coincidences, there are also heavier fragments, which are in coincidence with  $\text{H}_2\text{O}^+$  and  $\text{H}_3\text{O}^+$ . This shows that the deflection profile shown in Figure 7.2 is underestimating the deflection in indole( $\text{H}_2\text{O}$ ), due to the contributions of these ions to the assigned blue area.

The visible diagonal lines in Figure 7.3 and the washed-out structure shown in Figure 7.4 seem to be contradicting results because if all fragments carry significant momentum, all coincidence lines should be invisible. The contradiction can be explained by the existence of several fragmentation channels. In one case, the indole monomer is singly ionized and recoils from singly ionized  $\text{H}_2\text{O}^+$  and  $\text{H}_3\text{O}^+$ , which gives rise to the diagonal lines visible in Figure 7.3. Since only one hole is located at the indole part of the molecule it will not be shown in a coincidence spectrum between the second and third detected ion. In the second case, two holes are located on the indole fragment and  $\text{H}_2\text{O}^+$  and  $\text{H}_3\text{O}^+$  are singly ionized. In that case, the diagonal lines are washed out for all ions, which expressed itself in Figure 7.3 as an even distributed background feature. This hypothesis is supported by the VMI images of  $\text{H}_2\text{O}^+$  and  $\text{H}_3\text{O}^+$  shown in Figure 7.5. The color scheme for the VMI images is the same as shown in Figure 7.2,

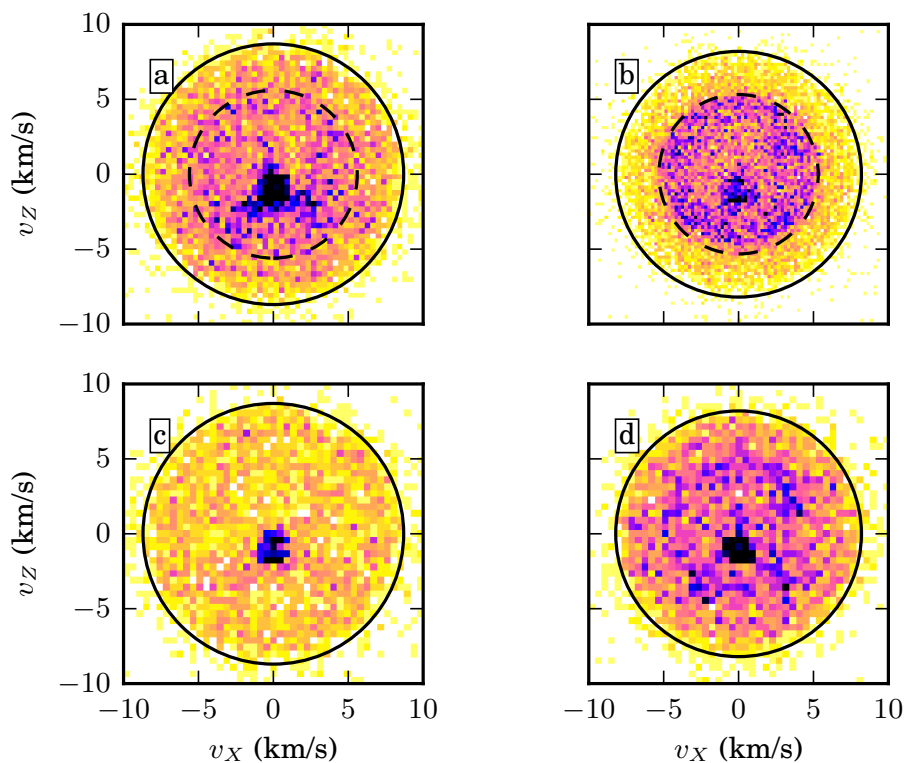


Figure 7.5: VMI images of ionized water (left) and hydronium (right). The top (bottom) row shows the cases where one (two) ions were detected in addition to the water/hydronium ion. The dashed (solid) circle shows the maximum velocity for particles for a detection one (two) ions. Due to limited detection efficiency both channels are visible in the upper row.

but given in a unit of ions per bin. In all VMI images an increased number of counts is visible at  $v_X = 0$  and  $v_Z \approx -1.5$  km/s, which is attributed to background from the carrier gas falsely detected at that corresponding mass to charge ratio. The VMI images of  $\text{H}_2\text{O}^+$  are shown in Figure 7.5 for the case of a) one and c) two additionally detected ionic fragments. The circles shown in a) represent two different velocity channels observed in radial plots of the ion VMI spectrum. The inner velocity channel is assigned to the case where only one hole is located on the fragmenting indole. The faster channel is assigned to the case where two holes are located on the indole part of the molecule, but only one ion was detected due to the limited detection efficiency. This is supported by the velocity distribution shown in Figure 7.5 c), where two additional ions were detected, which do have the same velocity as the faster channel in Figure 7.5 a). The same situation accounts for the VMI images of  $\text{H}_3\text{O}^+$ , which are shown in Figure 7.5 for the case of one (b)) and two (d)) additionally detected ionic fragments. b) also shows two velocity channels where the inner one is much more prominent. The faster channel in b) has the same velocity as the channel presented in d), which is also explained by the limited detection efficiency<sup>†</sup>.

<sup>†</sup>These VMI images have been used to determine the detection efficiency. Therefore, the amount of ions detected in Figure 7.5 b) from the faster channel, i. e., at radial velocities between  $\approx 6$ -8 km/s, was compared to the number of detected ions in Figure 7.5 d) for the same velocity. It showed that the detection efficiency was slightly higher than 50 %

## 7.4 Electrons

Figure 7.6 shows the electron VMI spectrum detected in coincidence with the ionic fragments of indole( $\text{H}_2\text{O}$ ). The electrons were gated such that the highlighted coincidence islands shown in Figure 7.3 were accepted as events. Further, for the channels where two ionic fragments have been detected in addition to  $\text{H}_2\text{O}^+/\text{H}_3\text{O}^+$ , only the main coincidence islands within the area of the indole monomer (Figure 7.4) have been accepted. Figure 7.6 a) and b) show the same electron VMI spectrum in a cartesian (a)) and polar (b)) coordinate system. The different quadrants in the cartesian VMI spectrum are labeled as Q1-Q4, and are displayed again in the polar spectrum. The electron VMI spectrum shows four main velocity channels at velocities of 2.3, 7.1, 9.6, and  $11.3 \cdot 10^6$  m/s, corresponding to electron energies of 14.8, 141.7, 260.7 and 364.9 eV. These are assigned to the photoelectrons originating from localized ionization at the (atomic) nitrogen and carbon  $1s$  orbitals, as well as Auger electrons following carbon ( $\text{C}_{\text{Aug}}$ ) and nitrogen ( $\text{N}_{\text{Aug}}$ ) ionization respectively. The radial anisotropy in the photoelectrons, which is best visible for the  $\text{C}(1s)$  electrons in Figure 7.6, is due to the ionization from a  $s$ -orbital with circular polarized light; the Auger electrons are isotropically distributed in the laboratory frame. In addition to the four detected photoelectron energies, slow electrons in the center of the VMI are detected. These are best visible for Figure 7.6 a) and are assigned to background electrons.

Figure 7.6 c) shows the inverse Abel transformation of the electrons VMI spectrum. The Abel transformation was performed based on the BASEX algorithm [187]. The black electron energy spectrum shows the electrons detected in coincidence with indole( $\text{H}_2\text{O}$ ), reconstructed from the second and third quadrant of the electron VMI images. These quadrants were chosen because the electron VMI spectrum in these quadrants is less distorted than, for instance, in Q1 (Figure 7.6 b)). The energy spectrum is overlaid by the dashed red line, showing the electron energy spectrum of the indole monomer retrieved from the same quadrants (Figure 6.7). Both spectra are comparable and show the four measured electron energies. The electrons detected in coincidence with indole( $\text{H}_2\text{O}$ ) show a higher offset value for energies below the  $\text{C}(1s)$ . This is attributed to a relatively higher background signal due to a lower density in the molecular beam for indole( $\text{H}_2\text{O}$ ) compared to indole. The energies of the peaks have been assigned by Gaussian fits including an offset value evaluated in the vicinity of the peak. The area of the fits is proportional to the number of electrons per electron energy. By comparing the photoelectrons and Auger electrons separately, a contribution of 22.8 % and 16 % was attributed to localized ionization at the nitrogen part of the molecule. The corresponding  $\beta$  parameters (anisotropy parameters [67]) were determined by the mean value at the full-width at half maximum (FWHM) of the fitted Gaussian distribution and are determined to be -0.44(0.08), -0.77(0.01), 0.03 (0.03), and -0.31 (0.02) for the  $\text{N}(1s)$ ,  $\text{C}(1s)$ , C-Aug and N-Aug respectively. The values in the brackets show the standard error of the  $\beta$  parameter.

Figure 7.7 shows a comparison of the photoelectrons in coincidence with one (black) or two holes (red) detected on the indole-part of the molecule. The spectra are given as a histogram of the electrons radial velocity  $v_r$ . The connection lines between the point serve to guide the eye. The ion gating was applied

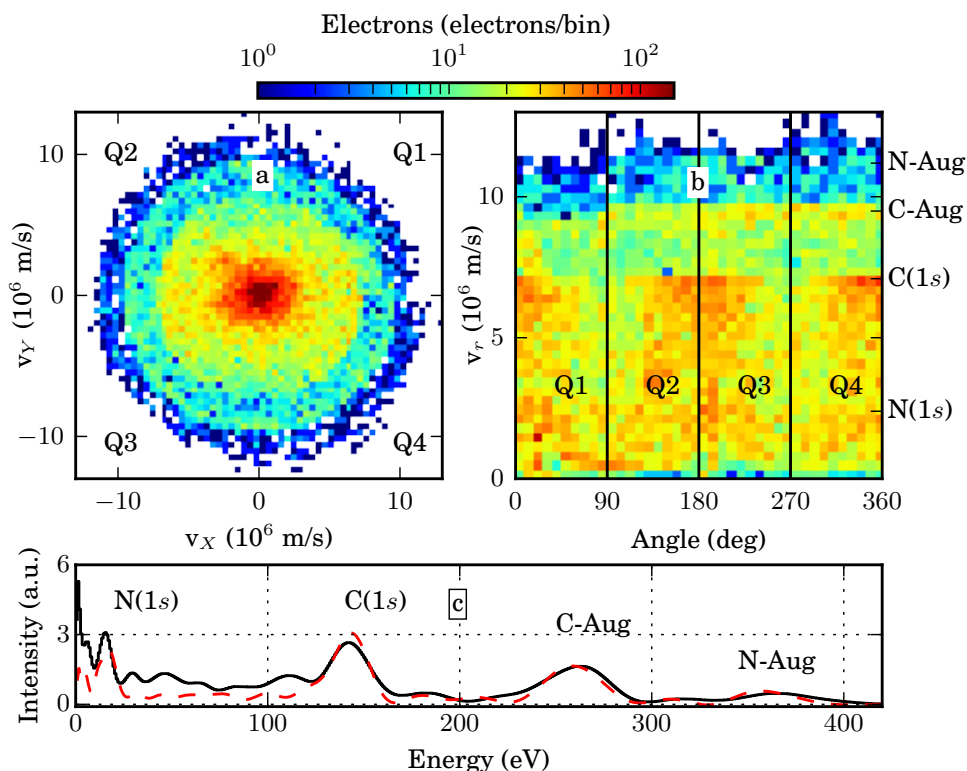


Figure 7.6: a) and b) VMI images in a cartesian and polar coordinate system for the electrons detected in coincidence with the ionic fragments of indole( $\text{H}_2\text{O}$ ). Q1-Q4 show the different quadrants of the VMI image. c) The black curve shows the electron energy spectrum of indole-water calculated by an inverse Abel transformation based on the BASEX algorithm [187] for the quadrants Q2 and Q3. The red dashed line shows the energy spectrum obtained from the indole monomer (Figure 6.7) for comparison.

in the same way as for Figure 7.6. Additionally, for the case of two detected ions ( $\text{H}_2\text{O}^+/\text{H}_3\text{O}^+$  and one ionic fragment of indole), the coincidences have been gated on the angular relationship between the ionic fragments (as described in the following) to suppress the influence from the faster three-ion channel ( $\text{H}_2\text{O}^+/\text{H}_3\text{O}^+$  and two ionic fragments of indole, Figure 7.5). The VMI images of the ionic fragments allow one to determine the relative angle between two detected ions. If indole( $\text{H}_2\text{O}$ ) fragments into two ionic species, the ions must be detected on opposite directions in the VMI, i. e., their 3D velocity vectors and their measured 2D projection must point in opposite directions to fulfill momentum conservation. If a third fragment is part of the fragmentation process (neutral or ionic), the momentum sum between all fragments must be zero, which leads to non-axial recoil between the fragments if all ions have some momenta. For the case of indole (Figure 6.5) it was shown that the velocity vectors for two ions are still pointing to a high degree in opposite directions if the third fragment is neutral. This is also the case for indole( $\text{H}_2\text{O}$ ). This was utilized to suppress the influence of the three-ion channel, by accepting only ionic fragments whose velocity vectors were detected between an angle of  $170^\circ$ - $190^\circ$ .

The 2-ion channel shows an increase in detected electrons at radial velocities corresponding to the nitrogen

## 7. X-ray photophysics of indole-water clusters

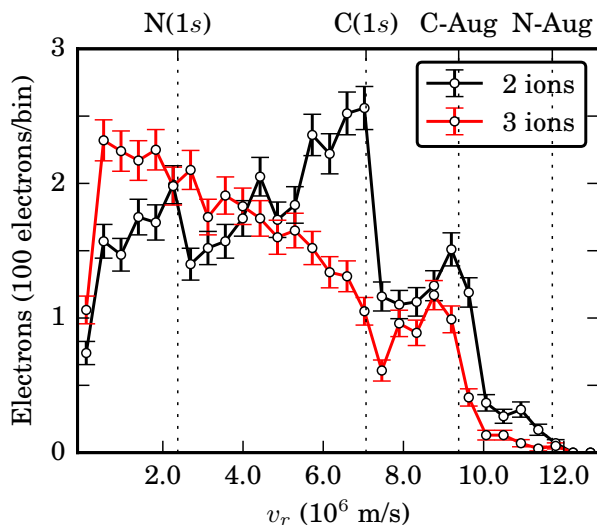


Figure 7.7: Comparison of the electrons radial velocity distribution detected in coincidence with two ( $\text{H}_2\text{O}^+/\text{H}_3\text{O}^+$  and one ionic fragment of indole) and three ( $\text{H}_2\text{O}^+/\text{H}_2\text{O}^+$  and two ionic fragments of indole) ionic fragments of indole( $\text{H}_2\text{O}$ ).

photoelectrons and the carbon photoelectrons as well as Auger electrons. The nitrogen Auger electrons are suppressed, which is attributed to the distortion of the electron VMI which is best visible in Figure 7.6 b). The 3-ion channel shows the most prominent peak at radial velocities attributed to nitrogen photoelectrons, and a suppression of photoelectrons from the carbon 1s orbital compared to the 2-ion channel.

### 7.5 Discussion

The coincidence spectrum presented in Figure 7.3 gives an overview of the fragmentation pattern of indole (red triangle), indole( $\text{H}_2\text{O}$ ) (blue square), and higher clusters (green triangle) for two detected ions. The higher clusters could be assigned by their mass sum  $m_1/q_1 + m_2/q_2$ , which is already bigger than the total mass of indole( $\text{H}_2\text{O}$ ). The red triangle is assigned to the fragmentation pattern of indole, as discussed in chapter 6. Additionally, in Figure 7.4 it was shown that also fragments from indole( $\text{H}_2\text{O}$ ) contribute to this area in the coincidence spectrum. The blue square has been assigned to the fragmentation pattern of indole( $\text{H}_2\text{O}$ ). Also here, it was shown that fragmentations from higher clusters do partly contribute to that assigned area (Figure 7.4). The deflection profile extracted from the PIPICO spectrum showed that bigger clusters were less deflected than indole and indole( $\text{H}_2\text{O}$ ). Indole( $\text{H}_2\text{O}$ ) does not show a stronger deflection than indole [12]. On the other hand, the deflection profile of indole( $\text{H}_2\text{O}$ ) is underestimated due to the contribution of higher clusters, and the deflection of indole could be overestimated due to the contribution from indole( $\text{H}_2\text{O}$ ). Though, the contribution from higher clusters in the indole area is unknown.

The fragmentation of indole( $\text{H}_2\text{O}$ ) showed a charge and mass transfer to the hydrogen bonded water.

The ratio between  $\text{H}_2\text{O}^+$  and  $\text{H}_3\text{O}^+$  is  $\approx 1:2$ , if the ion detection efficiency is taken into account. The formation of  $\text{H}_2\text{O}^+$  and  $\text{H}_3\text{O}^+$  could be triggered by, for instance, relaxation via interatomic coulombic decay (ICD) [80], electron-transfer mediated decay (ETMD) [82], or proton transfer mediated charge separation (PTM-CS) [191] of the highly excited indole( $\text{H}_2\text{O}$ ) subsequent to core-shell ionization. Also, secondary ionization of the water by the photoelectron cannot be excluded.

Both fragmentation channels ( $\text{H}_2\text{O}^+$  and  $\text{H}_3\text{O}^+$ ) could be separated further by the presence of one or two holes on the indole-part of the cluster. The  $\text{H}_2\text{O}^+$  fragmentation channels were detected in 60 % of the cases with two ionic fragments of indole, compared to 50 % detection in the case of a  $\text{H}_3\text{O}^+$  fragmentation channel. For the indole monomer, the probability to create three ionic fragments is 13 %, and is thus much lower than for indole( $\text{H}_2\text{O}$ ). If two holes were present on the indole part of the molecule, the coincidence pattern of the indole was comparable to the indole-monomer, but the branching ratios between the channels not. In Figure 7.4 the islands 1-3 have branching ratio of 45 %, 27 %, and 28 %, compared to nearly equal populations for the indole monomer.

VMI images presented in Figure 7.5 showed that the presence of one or two holes on the indole lead to two different velocity channels for  $\text{H}_2\text{O}^+$  and  $\text{H}_3\text{O}^+$ , which can be explained by a stronger Coulomb repulsion of the fragmenting particles for the two holes located on indole.

The VMI images of the electrons have been recorded in coincidence with ionic fragments. The electron energy spectrum for indole( $\text{H}_2\text{O}$ ) is comparable to the electron energy spectrum of indole at the given resolution. Nitrogen photo- and Auger electrons showed a contribution of 22.8 % and 16 % compared to the ones detected for carbon. Taking the atomic cross section for the given photon energy into account ( $\text{N} = 0.6466 \cdot 10^{-22} \text{m}^2$ ,  $\text{C} = 0.4327 \cdot 10^{-22} \text{m}^2$ ,  $\text{O} = 0.06023 \cdot 10^{-22} \text{m}^2$ ) [76], and neglecting the contribution from the proton, the probabilities are 15.5 %, 83 %, and 1.5 % for localized ionization at the nitrogen, carbon and oxygen, respectively. This discrepancy could be either explained by the non-perfect reconstruction of the electron energy spectrum, or by alternative fragmentation channels of indole( $\text{H}_2\text{O}$ ), which, on the other hand, have not yet been observed in the data. The photoelectrons from the oxygen  $2s$  orbital would be expected at a photon energy 378.4 eV ( $11.5 \cdot 10^6$  m/s) [78] and are not observed. These electrons are strongly overlapping with the nitrogen Auger electrons and hence could be hidden in the signal due to their low contribution to the overall spectrum.

In Figure 7.7 it was shown that two holes on the indole-part of the cluster are primarily populated upon localized ionization at the nitrogen end of the molecule. This has also been observed for the indole-monomer in chapter 6, where three ionic fragments were primarily observed upon site-specific ionization at the nitrogen end of the molecule.

## 7.6 Summary and outlook

This chapter presented the photophysics of indole( $\text{H}_2\text{O}$ ) upon core-shell ionization primarily at the indole-part of the cluster. VMI spectra of electrons and ions have been recorded in coincidence, and the fragmentation pattern was displayed in a coincidence map. It was shown that a dominant relaxation

## 7. X-ray photophysics of indole-water clusters

process of indole(H<sub>2</sub>O) is a charge and mass transfer to the hydrogen-bonded water. The fragmentation pattern of the indole-part of the molecule was comparable to the fragmentation of the indole-monomer. Differences were found in the relative population of the fragmentation channels. The VMI images of H<sub>2</sub>O<sup>+</sup> and H<sub>3</sub>O<sup>+</sup> showed two velocity channels, which were assigned to the existence of one or two holes created on the indole-part of the molecule.

The photoelectron spectrum of indole(H<sub>2</sub>O) was, at the given quality, comparable to the photoelectron spectrum of the indole monomer. The photoelectron spectra revealed in both cases, that fragmentation channels, which resulted in three ionic fragments, were primarily populated upon site-specific ionization. The disentanglement of the different relaxation mechanisms, which lead to the charge-, and mass transfer to the hydrogen-bonded water, will be part of future studies. Possible candidates are, e. g., interatomic coulombic decay (ICD) [80], electron-transfer mediated decay (ETMD) [82], proton transfer mediated charge separation (PTM-CSs) [191], or also electron impact ionization of the water molecule by photo- or Auger electrons emitted from the indole part of the molecule. The distance dependence of these processes make indole(H<sub>2</sub>O) a very suitable system to study these processes, because indole(H<sub>2</sub>O) can be neutrally dissociated upon absorption of a single UV photon. The VMI spectra of H<sub>2</sub>O<sup>+</sup> and H<sub>3</sub>O<sup>+</sup>, and the relative populations of the different channels, are most likely very sensitive probes dependent on the distance between indole and water subsequent to UV absorption, as the H<sub>2</sub>O<sup>+</sup> and H<sub>3</sub>O<sup>+</sup> velocity depends on the Coulomb repulsion between the fragments, and therefore on their distance. Additional information on the relaxation process could be provided by high-resolution Auger electron spectroscopy.

## 8 Applications of HHG photon sources

The following chapter is separated into two parts. The first part is based on the publication [192] and shows an experiment, which was utilizing XUV radiation to measure the photophysics of iodomethane upon localized ionization within the molecule. The XUV radiation was generated by a laboratory based high-harmonic (HHG) source. The experiment was aiming at the demonstration of a HHG source as additional photon source along with accelerator based facilities, to measure the photophysics of gas-phase molecules upon inner-shell ionization. The second part of the chapter is focussing on the conformer separation of glycine in a cold-molecular beam with the aim to perform an (HHG-based) attosecond pump-probe experiment with a conformer selected sample to study conformer-dependent charge migration [193]. Simulations are conducted to show how well the different conformers possibly can be separated in an experiment. Additionally, the generation of a cold molecular beam of glycine is discussed.

### 8.1 HHG source for coincidence ion imaging of gas-phase molecules\*

Unraveling and controlling chemical dynamics requires techniques to image structural changes of molecules with femtosecond temporal and picometer spatial resolution. Ultrashort-pulse x-ray free-electron lasers have significantly advanced the field by enabling advanced pump-probe schemes. There is an increasing interest in using table-top photon sources enabled by high-harmonic generation of ultrashort-pulse lasers for such studies. We present a novel high-harmonic source driven by a 100 kHz fiber laser system, which delivers  $10^{11}$  photons/s in a single 1.3 eV bandwidth harmonic at 68.6 eV. The combination of record-high photon flux and high repetition rate paves the way for time-resolved studies of the dissociation dynamics of inner-shell ionized molecules in a coincidence detection scheme. First coincidence measurements on  $\text{CH}_3\text{I}$  are shown and it is outlined how the anticipated advancement of fiber laser technology and improved sample delivery will, in the next step, allow pump-probe studies of ultrafast molecular dynamics with table-top XUV-photon sources. These table-top sources can provide significantly higher repetition rates than the currently operating free-electron lasers and they offer very high temporal resolution due to the intrinsically small timing jitter between pump and probe pulses.

---

\*This chapter is based on the paper *High-repetition-rate and high-photon-flux 70 eV high-harmonic source for coincidence ion imaging of gas-phase molecules* J. Rothhardt, S. Hädrich, Y. Shamir, M. Tschernajew, R. Klas, A. Hoffmann, G.K. Tadesse, A. Klenke, T. Gottschall, T. Eidam, J. Limpert, A. Tünnermann, R. Boll, C. Bomme, H. Dachraoui, B. Erk, M. Di Fraia, D. Horke, T. Kierspel, T. Mullins, A. Przystawik, E. Savelyev, J. Wiese, T. Laarmann, J. Küpper, D. Rolles, *Optics Express* **24**, 16 (2016).

I contributed to the measurements and I was doing the data analysis for the part shown in subsection 8.1.6 and subsection 8.1.7, which was focussing on the coincidence measurement of iodomethane and the photon flux estimation.

## 8. Applications of HHG photon sources

### 8.1.1 Introduction

The availability of ultrashort-pulse short-wavelength photon sources is an essential prerequisite to enable studies of matter on atomic (picometer) length and (femtosecond) timescales. As such, they constitute an indispensable tool for modern science, which is reflected by the growing number of free-electron lasers (FELs) that are operating or being constructed at the moment [194–199]. These sources allow to address many of the fundamental questions in areas as diverse as physics, chemistry, biology, material science and medicine [200, 201]. Here, we will concentrate on ultrafast molecular dynamics imaging experiments [18, 25, 160] that aim, e.g., at tracing initial charge-transfer processes in space and time [157, 160], which can be considered as a fundamental process in many photochemical reactions. Understanding these processes has the potential to control, manipulate, and steer the reaction in a desired channel using ultrafast light. A particularly powerful method for such studies is the coincident momentum imaging technique [133], which yields multi-dimensional data sets that can provide kinematically complete, channel-resolved, and highly differential measurements that contain a wealth of information, and, which allow studies in the molecular reference frame [160]. However, it imposes the restriction of less than one ionization event per X-ray pulse in the probed sample, on average, to unambiguously correlate the ionization fragments stemming from the same molecule. Therefore, the acquisition of sufficient statistics is only feasible with high-repetition-rate pump-probe sources, ideally with a multi-kHz repetition rate, which is beyond the capabilities of the current FEL setups. Moreover, the x-ray pulses must be synchronized to optical pump pulses with femtosecond precision, which is hindered by the long beam paths through the FEL machines and the intrinsic arrival time jitter [202]. Nevertheless, pump-probe timing jitter at FELs has steadily been improved and sub 10 fs timing jitter has already been demonstrated by a measure-and-sort method recently [203]. Complementary table-top sources, realized *via* HHG of ultrashort-pulse lasers, have attracted significant attention with a growing user community over the last years, since they are compact and highly accessible. The process of HHG itself has been known for several decades already, but the repetition rate of the sources has been mostly limited to the low kHz regime, which is dictated by the employed laser technology [204–208]. However, there is a strong demand for high repetition rate sources not only for coincidence experiments, but also for many applications, e.g. in surface science [209, 210] or atomic [211] and molecular [212] physics. The development of new high repetition rate HHG sources has seen rapid progress enabled by recent advances in high average power femtosecond laser technology [213–219]. In that regard, fiber lasers in combination with nonlinear compression have played a pivotal role, since these enabled high average power ultrashort pulse laser sources [220, 221]. Additionally, the investigation of phase-matching aspects during the frequency up-conversion for such rather low pulse energy lasers has finally led to efficient HHG using fiber lasers [222, 223]. As a consequence, this approach produced a maximum photon flux of more than  $10^{13}$  photons/s (100  $\mu$ W of average power) in the XUV at 600 kHz repetition rate [224], or  $>10^9$  photons/s in the soft X-ray region at 100 kHz [225]. The repetition rate of these sources can even be pushed up to 10 MHz, still with  $10^{13}$  photons/s [226], rendering novel applications in solid state and molecular physics

possible with fiber-laser-based HHG sources.

In this contribution, we present coincidence experiments for iodomethane ( $\text{CH}_3\text{I}$ ) that were conducted with 68.6 eV photons from a laser-based 50/100 kHz repetition rate source. The XUV source was enabled by a state-of-the-art chirped-pulse-amplification fiber-laser system that incorporates coherent combination of two main amplifier channels to achieve 1 mJ, 300 fs pulses with 50/100 W of average power at a central wavelength of 1030 nm. Subsequent spectral broadening in an argon-filled hollow-core fiber followed by temporal compression via chirped mirrors supplied 0.6 mJ pulses with a duration of 35 fs. A part of this pulse energy (up to 100  $\mu\text{J}$ ) can be used for optical pumping of the molecular sample ( $\text{CH}_3\text{I}$ ) while the remainder is used for high-harmonic generation. Particular optimization of the photon flux of the 57th harmonic yielded up to  $6.8 \cdot 10^{10}$  photons/s at a repetition rate of 50 kHz. This is not only the highest achieved value in this spectral range, but it also allowed for the first successful demonstration of a coincidence measurement on inner-shell ionized gas-phase molecules performed with table-top sources. Previous coincidence experiments with HHG sources have been limited to valence ionization [227–233] and only a few, non-coincident atomic inner-shell ionization experiments have been performed with HHG sources to date [234–236]. Important aspects for future pump-probe experiments, such as finding the temporal overlap between the pump and the probe pulses, increasing the density of the molecular beam, and advances in laser technology to further increase the photon flux will be discussed, providing evidence that time-resolved coincidence experiments on inner-shell ionized gas-phase molecules with high-order harmonic sources are in reach. Since HHG sources can also provide attosecond pulses at high repetition rates [237], such experiments are expected to access molecular dynamics at shortest timescales in the future.

### 8.1.2 High-repetition-rate and high-photon-flux XUV source

The realization of a long-term-stable high-repetition-rate source of high harmonics inherently requires a suitable high average power laser system. Here, a fiber chirped pulse amplifier was used that was operated with two coherently combined main amplifier channels and that is described in subsection 8.1.3. The pulses emerging from this laser were subsequently compressed in time utilizing a gas-filled hollow-core fiber and chirped mirrors, as outlined in subsection 8.1.4. After the compression step, high harmonics were generated in an argon gas jet with the generation process being particularly optimized for a photon energy of 68.6 eV. The experimental characterization of the XUV source and details on selecting the harmonic and focusing it onto the molecular target are described in subsection 8.1.5.

### 8.1.3 Coherently combined femtosecond fiber chirped pulse amplifier

The fiber chirped pulse amplification (FCPA) system is sketched in Figure 8.1. Its design is similar to the laser system reported in [238], but incorporates only two instead of four main amplifier channels. The frontend is a home-built femtosecond fiber oscillator that operates at 19 MHz repetition rate and 1030 nm central wavelength with a spectral bandwidth of  $\sim 10$  nm (FWHM). It is directly spliced to a first

## 8. Applications of HHG photon sources

fiber-integrated pre-amplifier, which increases the average power to 130 mW. Subsequently, the pulses are stretched to  $\sim 1.5$  ns in duration by means of a dielectric grating based stretcher and then sent into a spatial-light-modulator-based pulse shaper, which is used to compensate the residual linear and nonlinear spectral phase for almost perfect pulse compression. The signal after this device is coupled to another cascade of fiber-integrated pre-amplifiers that also include two acousto-optical modulators, which are used to reduce the repetition rate to 1 MHz and then to the final value of 50 kHz or 100 kHz for the present experiment; this yields a pulse energy of 0.5  $\mu$ J. This amplifier chain is followed by a first large pitch fiber (LPF) with a mode field diameter of 55  $\mu$ m, which delivers 20  $\mu$ J of pulse energy for seeding of the main amplifiers. As shown in Figure 8.1 this signal is equally split into two spatial replicas by a polarizing beam splitter cube and each of the beams is sent to a large pitch fiber amplifier with 80  $\mu$ m mode-field diameter. Before entering the main amplifiers, the linearly polarized signals are circularly polarized with a quarter wave plate (QWP) to reduce the impact of nonlinearity [239]. After amplification and traversing another QWP each channel delivers 750  $\mu$ J pulses with linear polarization, and recombination is done with a thin film polarizer (TFP). After recombination a small portion of the beam ( $<1\%$ ) is sent to a

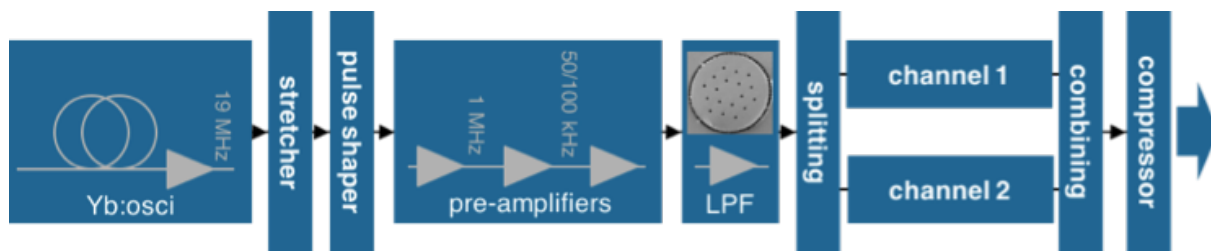


Figure 8.1: Experimental setup of the coherently combined fiber chirped pulse amplification system (CC-FCPA).

Hänsch-Couillaud detector, that analyzes the polarization state of the recombined beam and uses this to generate an error signal. This is fed-back to a piezo-driven mirror within the pre-amplifier section of the laser system that adjusts the temporal delay between the two channels [217, 238]. Finally, the beam is compressed to 300 fs duration in a dielectric grating based compressor. The compressed pulse energy is 1 mJ, corresponding to an average power of 50 W (100 W) at 50 kHz (100 kHz) repetition rate. Due to the use of fiber amplifiers the spatial beam quality is excellent as verified by  $M^2 < 1.4$  measurements in previous experiments [240, 241].

### 8.1.4 Nonlinear compression

As outlined in subsection 8.1.3, the pulses emerging from the coherently combined-fiber chirped-pulse-amplification system (CC-FCPA) are 300 fs in duration, which is too long for efficient high harmonic generation [206]. For that reason a nonlinear compression (NC) setup has been implemented that closely

follows the design presented in [221, 224]. A schematic setup of this NC stage together with the pump-probe splitting is shown in Figure 8.2. The 1 mJ, 300fs pulses are coupled into an argon-filled ( $\sim 4.5$  bar)

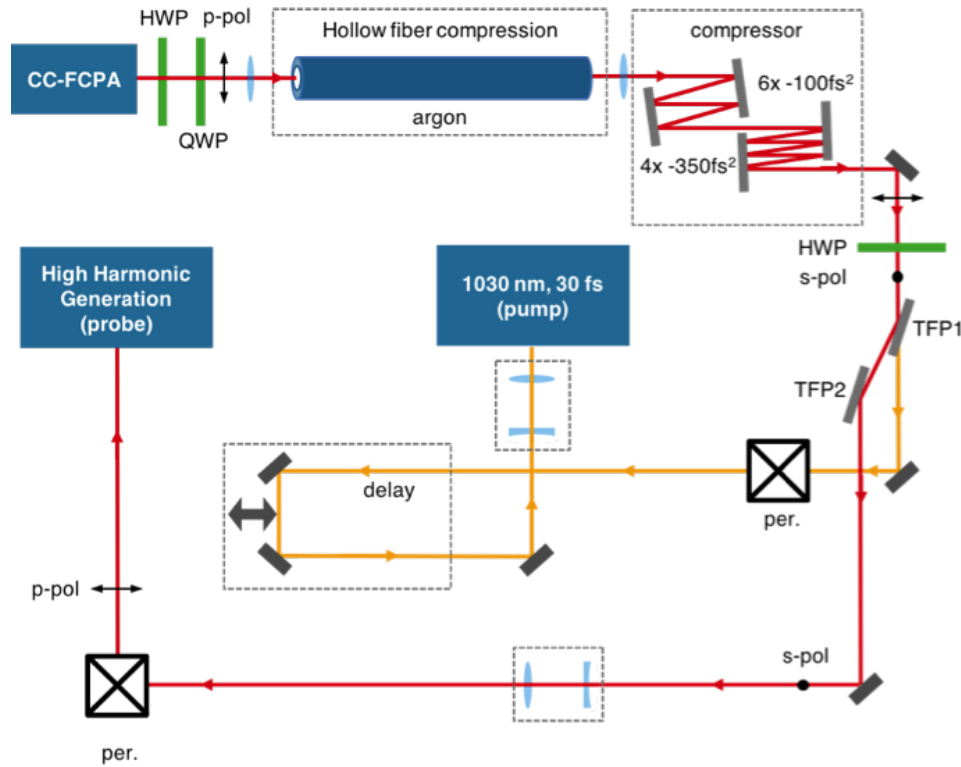


Figure 8.2: Experimental setup of the nonlinear compression stage and the pump and probe generation. As mentioned in the text p-polarization refers to parallel and s-polarization to perpendicular polarization with respect to the surface of the optical table. (HWP-half-wave plate, QWP-quarter-wave plate, TFP-thin film polarizers, per.-periscope)

hollow-core fiber with an inner diameter of 250  $\mu\text{m}$  and a length of 1 m. Propagation in this waveguide leads to self-phase modulation resulting in spectral broadening. The imposed chirp is removed by a chirped mirror compressor with a group delay dispersion (GDD) of  $-2000$  fs<sup>2</sup> leading to 35 fs pulses. The pulse energy after the compressor is still as high as 0.6 mJ corresponding to an average power of 30 W (60 W) at 50 kHz (100 kHz) repetition rate. The polarization used for the NC stage is parallel to the optical table, which is ensured by a combination of a quarter and half-wave plate located before the hollow-core fiber. In the following, we will refer to p-polarization (s-polarization) if the polarization is parallel (perpendicular) to the surface of the optical table. A measurement of the polarization revealed less than 1% of content in the perpendicular polarization state after the chirped mirror compressor. This linearly polarized light is sent through another half-wave plate (HWP) and then impinges on a chicane

## 8. Applications of HHG photon sources

of two thin film polarizers (TFP), which are used to split part of the beam by rotating the polarization with the HWP (Figure 8.2). The transmitted part with an energy of up to 100  $\mu\text{J}$ , which is p-polarized, is sent through a delay line and can then be used as a pump pulse, initiating electronic and nuclear dynamics in small molecular quantum systems. Although in the present experiment no time-dependent molecular-dynamics were observed, robust methodologies for finding temporal overlap were established as preparatory work, see supplementary online material for details. The main part of the beam with 0.5 mJ of pulse energy and s-polarization is reflected off the TFPs, traverses another telescope to enlarge the spatial beam diameter, is sent up on a periscope rotating back to p-polarization and then enters the high harmonic generation chamber. The latter will be described in the following subsection 8.1.5 and provides the XUV-probe beam at 68.6 eV used in present experiments.

### 8.1.5 High photon flux source at 68.6 eV

Using the 0.5 mJ, 35 fs pulses, which are available after splitting the pump beam (subsection 8.1.4), a high harmonic source has been realized that is particularly optimized for operation at 68.6 eV. This photon energy was chosen since it allows photo-ionizing the iodine 4*d* inner-shell electron in the  $\text{CH}_3\text{I}$  molecule. The experimental setup of the HHG source, including the selection of a single harmonic and the steering

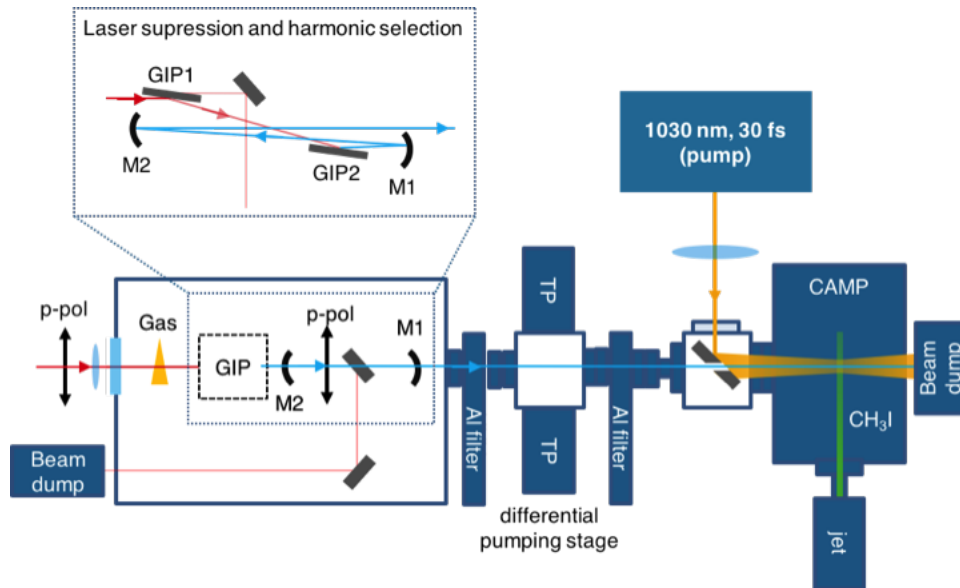


Figure 8.3: Top view on the experimental setup used for high harmonic generation. The inset shows a more detailed side-view of the separation of the harmonics from the fundamental driving laser, selection of a single harmonic and focusing of the harmonic into the experiment. (GIP-grazing incidence plates, M1/2-XUV mirrors at 68.6 eV, TP-turbo pumps, CAMP- CFEL-ASG Multi Purpose end station [180])

to the experimental chamber, is shown in Figure 8.3. The pulses are sent into a vacuum chamber and are focused into an argon gas jet, which produced from a thin round orifice with 150  $\mu\text{m}$  inner diameter. Using a  $f = 300$  mm focusing lens leads to a focal spot size ( $1/e^2$ -intensity) of  $\sim 90$   $\mu\text{m}$  and an intensity of  $> 2 \cdot 10^{14}$   $\text{W}/\text{cm}^2$ . The generated high harmonics and the laser co-propagate and impinge on a chicane of two grazing incidence plates (GIP) [242]. The latter are XUV-grade  $\text{SiO}_2$  substrates that are anti-reflection coated for 930-1130 nm (s-polarization) used under  $82^\circ$  angle of incidence. As shown in the detailed view in Figure 8.3, the two GIPs are used such that the XUV and infrared are s-polarized with respect to the plane of incidence. Therefore, the XUV beam is changed in height, but maintains p-polarization with respect to the optical table and the detector normal (see subsection 8.1.6). The reflectance of the top layer of  $\text{SiO}_2$  is calculated to be 63 % (40 % after two reflections) of the 68.6 eV photon pulses, whereas the reflection of the infrared laser is reduced to 10 % by the AR coating. Consequently, the IR laser is suppressed to 1 % after two reflections, which is important to prevent subsequent aluminum filters for complete reduction of NIR light from damage. In a first experimental campaign, a thorough characterization of the high harmonic generation source was performed. For that purpose, the XUV beam after the second reflection of the GIP was sent through two aluminum filters with a thickness of 200 nm each, which were used to further suppress the 1030 nm driving laser and to attenuate the XUV in order to prevent saturation of the following detector. A spatial-spectral analysis of the harmonics was done with a flat-field grating spectrometer with an attached XUV CCD camera. The experimental conditions, i. e., intensity, gas jet position relative to the focus, and the gas pressure were optimized so as to maximize the signal of H57 at  $\sim 68.6$  eV. Figure 8.4(a) shows the spatial-spectral distribution of the harmonic signal between 55 eV and 75 eV at optimum conditions (7 bar backing pressure). Under these conditions, spatially well-defined harmonics were generated with nearly Gaussian-like profiles [Figure 8.4(a) right side]. Integration along the spatial direction yields the harmonic spectrum as shown by the blue curve in Figure 8.4(b), which can then be used to obtain the number of photons per second by accounting for the detection efficiency as described in [224]. Furthermore, absorption on the 90 cm beam path to the detector has been taken into account. The rather high background pressure of  $4 \cdot 10^{-1}$  mbar in the chamber results in a transmission of only  $T = 30$  % at 68.6 eV. Note that additional corrections due to clipping of the XUV beam at the detector, which is obvious in Figure 8.4(a), and at the diffraction grating are taken into account for estimation of the photon flux. The corrected spectrum is displayed in Figure 8.4 (b) (red curve). The resulting photon flux for the highest harmonic orders is obtained by additional spectral integration across each individual harmonic line and summarized in Table 4. It should be noted that this is a rather conservative analysis and resulting in a minimum value for the achieved photon flux for the measured harmonics. It yields  $6.8 \cdot 10^{10}$  photons/s for harmonic 57 at 68.6 eV, which constitutes at least an order of magnitude higher photon flux than previously reported in this spectral region [243, 244]. However, the transmission of the Al filters, the diffraction efficiency of the grating and the detection efficiency of the XUV CCD tend to degrade with time due to surface contamination. Hence, the real photon flux might have been even higher than estimated above. As described below, an

## 8. Applications of HHG photon sources

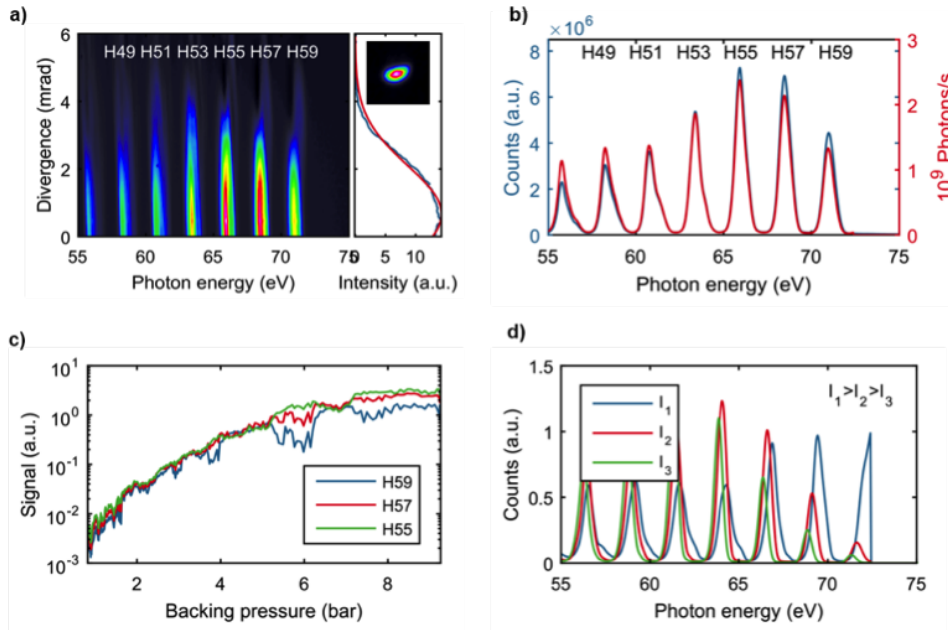


Figure 8.4: Characterization of the high harmonic source. (a) Measured spatio-spectral distribution of the harmonics at the optimal generation conditions (7 bar backing pressure). The HHG signal has been analyzed with an imaging spectrometer (flat-field grating) that allows observation of the divergence for each individual harmonic. The right part of (a) shows the lineout (blue) and a Gaussian fit (red) of H57 at 68.6 eV. The inset shows the focus of the XUV beam at 68.6 eV. (b) Integration along the spatial (divergence) axis leads to the harmonics spectrum (blue). When accounting for the detection efficiency and background absorption in the chamber a calibrated spectrum (red curve) can be obtained. (c) Harmonic signal of H55, H57 and H59 vs. backing pressure. A saturation of the signals is reached at pressures above 7 bar. (d) The harmonics can be slightly shifted by varying the intensity of the input laser. Three spectra for three different intensities are plotted.

Table 4: Number of photons per second generated in harmonic 47 to 59 measured by the grating spectrometer. The laser was operated at 50 kHz repetition rate.

Harmonic	47	49	51	53	55	57	59
Photon energy	56.6	59.0	61.4	63.8	66.2	68.6	71.0
Photons/s ( $10^{10}$ )	5.0	6.4	7.9	7.9	7.8	6.8	4.0

independent measurement of the photon flux utilizing photoionization within a neon flooded experimental chamber yields about  $2 \cdot 10^{11}$  photons/s for H57. The values shown here are obtained at a repetition

rate of 50 kHz, while part of the experiments subsection 8.1.6 has also been conducted with a repetition rate of 100 kHz. Note that all other laser parameters such as pulse energy, pulse duration and focal spot diameter remain unchanged. Hence, the XUV photon flux is expected to increase linearly with the laser repetition rate [224] and  $>10^{11}$  photons/s could be generated in a single harmonic at 68.6 eV with the presented system at 100 kHz.

Due to the use of grazing incidence reflections, the XUV beam still contains a broad spectrum of harmonics after the GIPs. Selection of a single harmonic (H57) is done by two XUV mirrors that additionally are used for collimation and re-focusing (Figure 8.3). Both are designed for reflection of 68.6 +/- 0.5 eV ( $R = 0.5$ ), while the first mirror ( $f = 300$  mm) collimates the XUV beam and the second one ( $f = 1200$  mm) focuses the XUV pulses onto the molecular beam of  $\text{CH}_3\text{I}$  (Figure 8.3). The latter is located in the CAMP end station. The inset of (Figure 8.4)(a) shows a nice and clean XUV focal spot with a diameter of  $\sim 120$   $\mu\text{m}$  ( $1/e^2$ -intensity). Fine tuning of the photon energy of the harmonic so as to match the mirror reflection curve was possible by adapting the intensity of the driving laser. Three harmonic spectra for different driving laser intensities are shown in Figure 8.4(d). The HHG chamber was separated from CAMP via a differential pumping unit (Figure 8.3) and a sealed aluminum filter with 200 nm thickness that was placed just in front of the differential pumping unit. This way, the pressure in CAMP stayed below  $10^{-9}$  mbar, while the pressure was  $4 \cdot 10^{-1}$  mbar in the HHG chamber when the gas jet was operated. As shown in Figure 8.3, the XUV (probe) beam was focused into CAMP through a holey mirror while the infrared pump was reflected of the same device with a focusing lens placed outside of the chamber. The temporal delay was controlled by an additional delay line within the pump arm (see Figure 8.2). Note that the employed 200 nm thick aluminum filter suppressed the average power of the HHG-driving IR beam to  $<0.3$  mW for the coincidence experiment.

### 8.1.6 Coincidence detection of $\text{CH}_3\text{I}$ ionization fragments

The coincidence experiment was performed in the CAMP instrument [180], a mobile multi-purpose experimental station that was previously used, e. g., for electron and ion imaging experiments at the LCLS and FLASH free-electron lasers [17, 18, 20, 25, 157, 158] and for electron-ion and ion-ion coincidence experiments at the PETRA III synchrotron radiation source at DESY [245]. The current setup consists of a doubly skimmed supersonic molecular beam (nozzle diameter: 30  $\mu\text{m}$ , skimmer diameters: 200 and 400  $\mu\text{m}$ , distance nozzle to interaction region: roughly 70 cm) and a double-sided velocity map imaging (VMI) spectrometer equipped with two microchannel plate (MCP) detectors with position-sensitive delay-line anodes (Roentdek DLD80 for the ions and HEX80 for the electrons), as shown in Figure 8.5. The HHG and/or NIR beams intersected with the molecular beam inside the VMI spectrometer, where a constant, inhomogeneous electric field guided the electrons and ions created by the interaction of the photons with the target molecules onto the position-sensitive detectors. Typical flight times of the ionic fragments were on the order of 0.5 to 7  $\mu\text{s}$ , while the electron time of flight was on the order of a few ns. The MCP and position signals were recorded with a multi-hit time-to-digital converter (TDC) that was triggered

## 8. Applications of HHG photon sources

by the detection of an electron, and the data was stored event by event in a list-mode format that allowed retrieving coincidences between the detected particles. With this detection scheme, it is possible to record electron-ion coincidence data with up to MHz-repetition sources as long as the average time between ionization events is considerably larger than the TDC acquisition window (for a 10  $\mu\text{s}$  window, this corresponds to an ionization rate of 100 kHz). Here, we only recorded events where at least one electron and one ion was detected, which resulted in a typical event rate of about 900 Hz. For the data in Figure 8.6(b), only those events were considered where two ionic fragments were detected in coincidence with a photo- or Auger electron. This represents the most stringent coincident requirement one would typically impose in such coincidence experiments and further reduced the count rate by more than a factor of two. From the time of flight and the hit positions of the ions, the three-dimensional ion momenta can be calculated, while the time of flight of the electrons is too short for a meaningful 3-D momentum reconstruction such that only 2-D projections of the electron momentum distributions were measured. For cylindrically symmetric electron distributions it is possible to retrieve the 3-D distributions through inversion algorithms [246, 247].

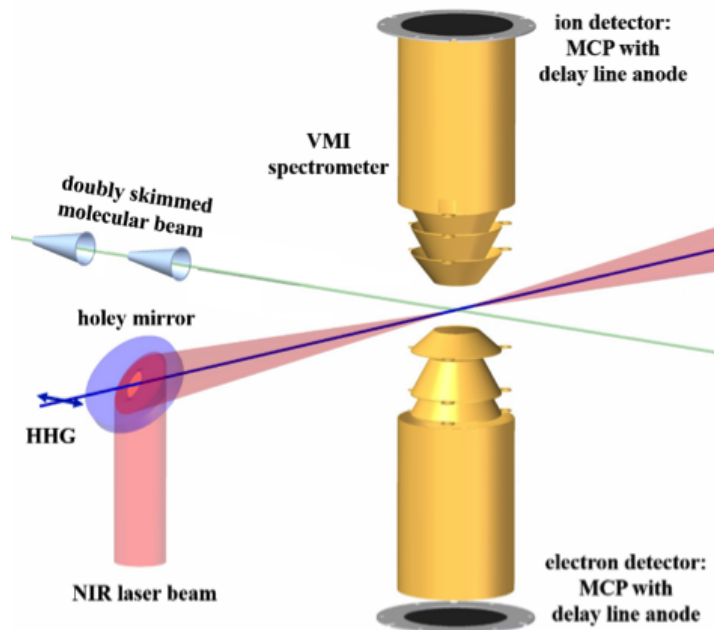


Figure 8.5: Schematics of the coincidence apparatus with a supersonic molecular beam and a double-sided velocity map imaging (VMI) spectrometer with MCP delay-line detectors for time- and position resolved coincident electron and ion detection.

In the experiment described here, we recorded electron-ion-ion coincidence data for the photoionization of  $\text{CH}_3\text{I}$  molecules by photons from the HHG pulses. We chose  $\text{CH}_3\text{I}$  as a target for this proof-of-principle

experiment since it is a prototypical polyatomic molecule whose UV- and NIR-induced dissociation and ionization as well as XUV-induced inner-shell ionization are well-studied [157, 158, 248]. In particular, we have recently investigated charge transfer dynamics in  $\text{CH}_3\text{I}$  after inner-shell ionization in pump-probe experiments at the LCLS and FLASH free-electron lasers [157, 158] and it is of enormous interest to perform similar experiments with a significantly improved temporal resolution, e.g., on the order of some 10 fs.

At a photon energy of 68.6 eV, as chosen in the present experiment, the cross sections for both, valence and inner-shell ionization, are roughly equal [248]. Thus, the  $\text{CH}_3\text{I}$  molecules can either be valence ionized, resulting predominantly in singly charged  $\text{CH}_3\text{I}^+$  ions, or a  $\text{I}(4d)$  inner-shell electron can be removed, which leads to a doubly or triply charged final state after the inner-shell vacancy relaxes via Auger decay. The majority of these doubly or triply charged cations then break up into charged fragments as seen in the ion time-of-flight mass spectrum shown in Figure 8.6(a). A plot of the ion-ion coincidences between  $\text{CH}_x^+$  ( $x = 0, 1, 2, 3$ ) fragments and  $\text{I}^+$  fragments is shown in Figure 8.6(b). Due to momentum conservation, these coincidence events, which resulted from a (quasi-) two-body fragmentation—the neutral or charged  $\text{H}^+$  fragments that may also be emitted carry very little momentum due to their light mass—can be clearly identified by diagonal lines in the photoion-photoion coincidence (PIPICO) spectrum. The corresponding detector images for  $\text{I}^+$ ,  $\text{CH}_x^+$ , and  $\text{CH}_3\text{I}^+$  are shown in Figure 8.7. Combining the time-of-flight information with the ion hit positions, the three-dimensional momentum of each fragment can be calculated and one can determine the total kinetic energy release and three-dimensional angular distributions as well as angular correlations between fragments, which, for the present data, agree with our previous measurements on  $\text{CH}_3\text{I}$  using synchrotron radiation [245]. Note that the results shown here were obtained from a single, continuous, 20-hour long measurement during which the laser system, the high harmonic generation, and the coincidence apparatus were operated constantly and without interruption. This reliability and long-term stability is an important prerequisite for coincidence measurements such as the one presented here and, in particular, also for future time-resolved experiments.

In order to demonstrate spatial and temporal overlap between the NIR-pump pulses and the XUV-probe pulses, we removed the Al filter in front of the differential pumping section such as the NIR drive-laser beam from the HHG chamber, which traveled collinear with the XUV pulses, could reach the interaction region inside the CAMP chamber. Using a small Ce-doped YAG crystal that could be driven into the interaction region on an xyz-manipulator and that could be viewed on a CCD camera through a long-distance microscope, we first spatially overlapped the two NIR beams. Then we used a fast photodiode that was also mounted on the xyz-manipulator to overlap the two laser pulses to within a few tens of picoseconds. Finally, we scanned the delay stage in the pump arm until we observed interference fringes on the Ce:YAG screen due to interferometric autocorrelation between the two NIR pulses, as shown by the short movie that we recorded with the pnCCD camera attached to the microscope (see Visualization 1). Thus, technically pump-probe experiments on femtosecond timescales would be feasible with the presented setup.

## 8. Applications of HHG photon sources

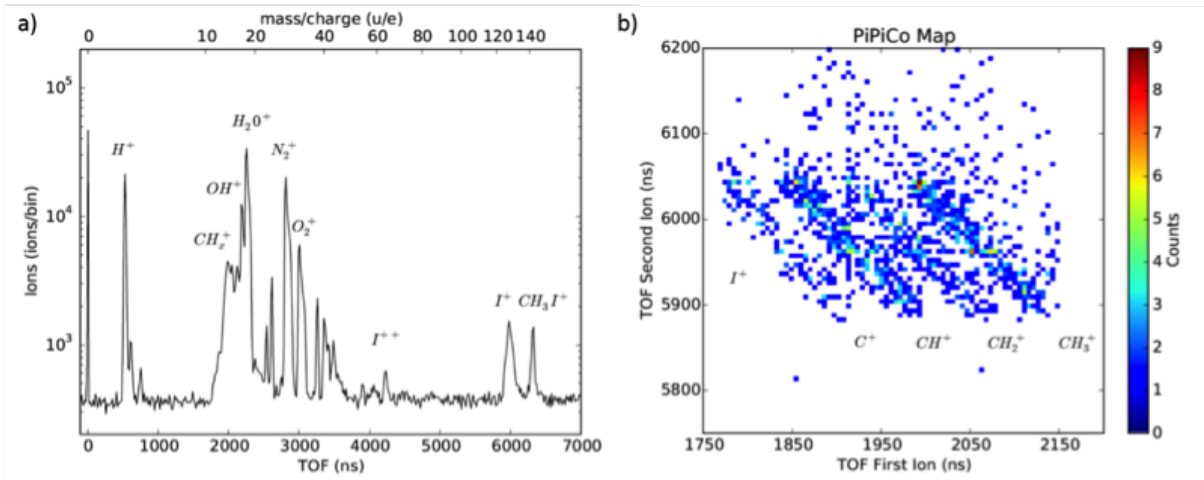


Figure 8.6: (a) Ion time-of-flight mass spectrum of  $\text{CH}_3\text{I}$  recorded at 68.6 eV photon energy. The  $\text{CH}_3\text{I}^+$  parent ion as well as several ionic fragments can be seen along with several ions resulting from the ionization of the residual background gas in the chamber. (b) Ion-ion coincidence spectrum of  $\text{CH}_3\text{I}$  zoomed in on the region containing the coincidences between  $\text{CH}_x^+$  ( $x = 0, 1, 2, 3$ ) and  $\text{I}^+$  fragments. For the data shown in panel (b), only those events were considered where two ionic fragments were detected in coincidence with a photo- or Auger electron, which results in a quite low coincidence count rate of less than one coincidence even per second in the selected coincidence channel; see text for details.

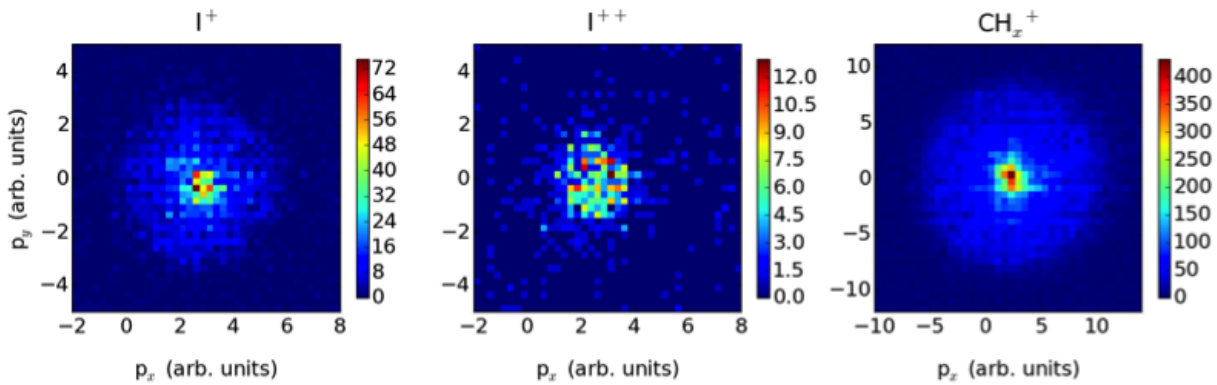


Figure 8.7: Two-dimensional ion momentum distributions (ion detector images) for three distinct ionic fragments of  $\text{CH}_3\text{I}$ : (a)  $\text{I}^+$ , (b)  $\text{CH}_x^+$ , and (c)  $\text{CH}_3\text{I}^+$ .

### 8.1.7 Photon flux estimate

In order to obtain an experimental estimate of the actual XUV photon flux in the CAMP chamber, we leaked  $5.4 \cdot 10^{-6}$  mbar of neon (as measured by a hot cathode ion gauge, taking into account the appropriate correction factor) into the vacuum chamber through a needle valve and measured the count

rate of  $\text{Ne}^+$  ions with our VMI spectrometer described above. Using the formula

$$I = \phi\sigma D\delta L \quad (17)$$

where  $I = 2500$  Hz is the  $\text{Ne}^+$  ion count rate,  $\phi$  is the photon flux,  $\sigma = 6.1$  Mbarn is the Ne photoionization cross section at 69 eV [249] (which we consider to be constant over the bandwidth of the XUV pulses),  $D = 0.5$  is the detector efficiency,  $\delta = 1.3 \cdot 10^{11} \text{ cm}^{-3}$  is the target density, and  $L = 2.0$  cm the interaction length inside the spectrometer, we can calculate the photon flux to be  $\phi = 3.2 \cdot 10^9$  photons/s. Note that the uncertainties connected to the ion gauge reading, the exact detector efficiency, and the effective interaction length that is imaged by the spectrometer, result in an uncertainty of about a factor of two for the absolute photon flux. When taking into account the estimated losses that occur on the path into the CAMP chamber (EUV mirror reflectivity  $(R = 0.5)^2 = 0.25$ ; transmission of the aluminum filter of 0.5 and of the grazing incidence plates of 0.4; transmission through the HHG chamber due to absorption because of the high background pressure of 0.3), we estimate a photon flux of about  $2 \cdot 10^{11}$  photons/s that was generated by the HHG source. This even exceeds the photon flux measured with a grating spectrometer as described in subsection 8.1.5.

### 8.1.8 Conclusion and outlook

In conclusion, we demonstrated coincidence experiments on gas phase-molecules after inner-shell ionization with a table-top high harmonic source. This XUV source, based on a femtosecond fiber laser system, provides a record high photon flux ( $> 4 \cdot 10^{10}$  photons/s per harmonic) up to 71 eV at up to 100 kHz repetition rate. The unprecedented combination of high photon flux, high repetition rate, and long term stability enables photon-hungry experiments such as photoionization of gas-phase molecules with coincidence detection of the fragments. We have performed molecular physics experiments with continuous experimental runs up to 20 hours. Electron-ion-ion coincidence data were recorded for the photoionization of  $\text{CH}_3\text{I}$  molecules excited by HHG pulses at a photon energy of 68.6 eV. This first data is promising and indicates that pump-probe experiments with such table-top sources are in reach. Since the pump pulse and the XUV pulse are generated by the same laser and are, thus, inherently synchronized, it is technologically possible to control their relative timing with sub-fs precision as demonstrated by attosecond pump-probe beamlines in many laboratories worldwide [250]. Note that a 600 kHz repetition rate attosecond source has already been demonstrated [237], and laser technology is currently progressing towards much higher average power for few-cycle driving lasers [225, 251].

However, for real pump-probe experiments, the count rate of the presented experiment has to be increased by about two orders of magnitude. We expect to obtain at least an order of magnitude higher sample density with a more compact molecular beam design that greatly reduces the distance between nozzle and interaction region. The anticipated reduction in electron energy resolution due to space charge effects is far less critical compared to the significant improvement in count rate, which would allow for pump-probe scans with reasonable measurement times (few-hours). Furthermore, the experiments presented in this

## 8. Applications of HHG photon sources

manuscript have been performed with 25 W (50 W) of average power. Since more than 500 W of average power have been demonstrated from a femtosecond fiber laser already [217] an order of magnitude higher photon flux is expected to be available soon.

Finally, the combination of both improvements will enable ultrafast time-resolved imaging of charge transfer processes with unprecedented time resolution on timescales, which are hard to be accessed by today's FEL facilities.

### 8.2 Toward charge migration in conformer-selected molecular samples

Within the last decade the development of ultrashort laser pulses, and the growing interest in theoretical physics to model electronic states of molecules and their correlation, opened the field of so-called attosecond physics, with the idea of driving that field toward attosecond chemistry. The following, very basic introduction into this field of science, is based on the review article [252] and references therein.

An attosecond is  $10^{-18}$  s and is generally considered as the timescale in which it is possible to observe fast electron dynamics. The first experiment, which was exploring ultrafast charge migration, was [253] where neutral peptides of neutral amino acids were locally ionized on the C-terminal end, and the ion yield related to the N-terminal end of the molecule was probed. The results were interpreted as charge migration in ions. The term *charge migration* is used to describe purely electron correlated driven electronic motions, fully decoupled and independent on the nuclear degrees of freedom. Contrary, and often mixed, is the term *charge transfer* where the charge dynamics does depend on the nuclear coordinates and involves dissipation of the electronic energy.

Charge migration can be triggered by coupling of electronic states within a molecule. This can be achieved by ionization from delocalized orbitals of the molecule if the energy spacing between two electronic states is smaller than the band-width of the laser. If the ionization process is additionally fast enough such that rearrangement of the electronic structure during the course of ionization is negligible (prompt ionization), these electronic states can be coherently coupled. The observation and understanding of the evolution of this coherently coupled hole states, with also a possible aim of steering chemical reactions, is one principle goal attosecond chemistry.

Experimentally, the observation of charge migration in a pump-probe experimental scheme is challenging. To observe fast motion the laser pulses have to be sufficiently short, which results in a broad spectrum of the laser pulse [254]. This spectral broadening leads to a higher probability of ionizing from more than only the desired states to couple. Additionally, if the desired initially populated states are not the highest occupied molecular orbitals (HOMO), but orbitals lower in energy, the laser pulses have always sufficient energy to ionize higher lying orbitals. Thus, the molecular sample should have only few homo orbitals in energy close by, with a big energy gap to the lower lying ones. Such conditions are also found in the indole molecule [255].

Electron dynamics on ultrafast timescales have already been observed in the amino acid phenylalanine [256–258]. In [257] phenylalanine was evaporated "from a thin metallic foil heated by a continuous wave (CW)

laser” before the dynamics were pumped by an XUV pulse (pulse duration sub-300 as) and probed by an IR laser pulse with a pulse duration of 4 fs. Due to the simple evaporation method, the retrieved signal was averaged over the different conformers—in total 6 with relevant population under the experimental conditions—though theoretical predictions show conformer-dependent electron dynamics.

We propose an experiment to probe charge migration in a conformer-selected, cold molecular sample of glycine ( $\text{C}_2\text{H}_5\text{NO}_2$ ). Glycine is of particular interest because it is the smallest amino acid and a building block of almost all proteins. It is thus of considerably importance for biology and chemistry. Its observation in interstellar clouds [259], as well as its recent detection in the coma of a comet [260], has had, and will have, profound impact onto the new field of astrobiology and -biochemistry. Furthermore, glycine is a particularly good candidate to study charge migration since theoretical predictions of the most abundant conformers suggest strong conformer-dependent charge migration with timescales of the hole motion, which also vary strongly as a function of the prepared state of the pump pulse [193].

Further, the deflection profile of glycine can be used to address the question whether or not there exists the IV conformer of glycine (conformer notation according to [261]), which has so far been predicted by theory [261, 262] but could not yet been conclusively detected in experiments. This lack of detection could be explained by an interconversion (IC) of this conformer into the first conformer during the course of the free jet expansion [263], leading to a shift of the overall population.

### 8.2.1 Simulations: Stark curves and deflection profile

Table 5 shows the rotational constants and dipole moments for the first four conformers of glycine, which are required to calculate the energies and Stark shifts of the rovibronic molecular states (section 2.2). The corresponding Stark curves were calculated [70] up to a rotational state of  $J = 40$ , with an electric field strength resolution of 1 kV/cm, and are shown in Figure 8.8 for the lowest rovibronic quantum states. The Stark curves for conformer I and II/III and IV are shown in the left and right graph respectively. The Stark energies are given in  $\text{cm}^{-1}$  in dependence of the electric field strength  $\epsilon$ . Standing out here is conformer II (black), which shows the most prominent Stark shift followed by conformer IV, III and I, which do have a comparable shift in energy. The simulations of the deflection profiles—shown in Figure 8.9 and discussed in the corresponding paragraph—were done with an in-house developed particle tracing software, which has already been used to simulate the deflection profiles in [11, 12]. The experimental setup, i. e., the dimensions of the setup, skimmer sizes and deflector type, were taken from [12]. For the simulated deflection profiles a molecular beam velocity of 1800 m/s and a molecular beam temperature of 1 K was assumed. Both are typically achieved under experimental conditions when the molecules are seeded in helium. At this temperature, quantum states up to  $J = 6$  are populated, where ”populated” means that they contribute to more than 1 % to the overall population. The populations of the different conformers in the molecular beam were taken from [262] and are shown in Table 6 in the left and middle column for ’no IC’ and ’IC’ of the fourth conformer (*vide supra*). These populations are derived from the

## 8. Applications of HHG photon sources

Table 5: Rotational constants and dipole moments for the first four conformers of glycine (I and II [264], III and IV [262, 265])

Conf.	A (MHz)	B (MHz)	C (MHz)	$\mu_A$ (D)	$\mu_B$ (D)	$\mu_C$ (D)
I	10.34	3.876	2.912	0.911	0.697	0.00
II	10.13	4.072	3.007	5.372	0.93	0.00
III	9.72	3.979	2.987	-0.156	1.691	-0.077
IV	10.26	3.971	2.962	-0.006	-1.552	1.436

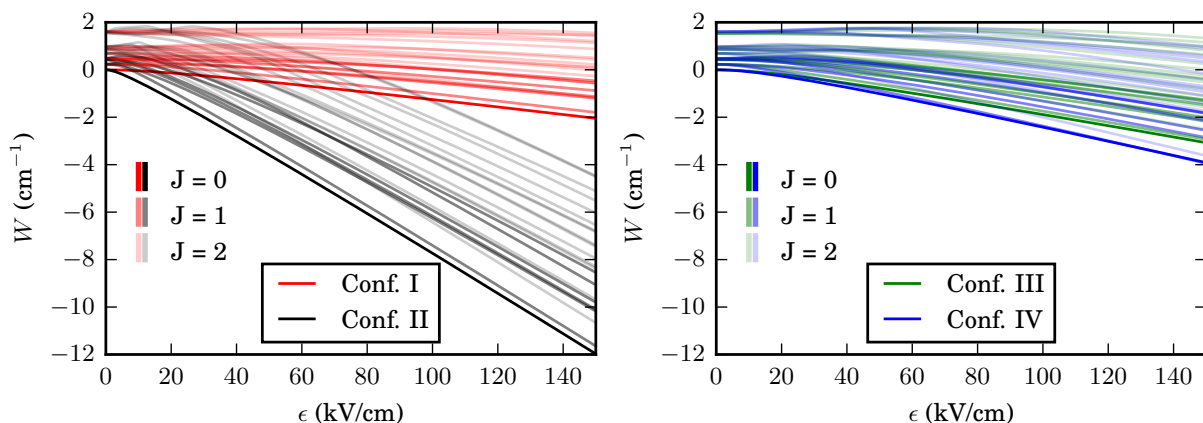


Figure 8.8: Left (right): Stark-energies for the lowest rovibronic quantum states of the first and second (third and fourth) conformer of glycine as a function of the electric field strength.

simulations for a temperature of 385 K. Experimental determined populations [266] at this temperature are shown in the right column of Table 6 simply for completeness.

Figure 8.9 shows smoothed simulated deflection profiles for a voltage of  $\pm 4$  kV (top) and  $\pm 14$  kV (bottom) applied at the deflector electrodes. The different populations of the conformers for IC and no IC of the fourth conformer are shown in the left and right graph respectively. The individual deflection profiles of the different conformers are highlighted by their corresponding color visible in the legend in the upper right graph. For comparison, an undeflected deflection profile is shown by the dashed black line. At an applied voltage of  $\pm 4$  kV, conformer II is already strongly deflected and fully separated from the other conformers at a position of  $Y > 1.5$  mm. All other conformers experience a much weaker deflection. At an applied voltage of  $\pm 14$  kV, the second conformer experience such a strong deflection that it collides with the deflector rod and thus, on the scale of these simulations, is fully discriminated. Conformer IV experiences the second strongest deflection, followed by conformer III and I. At  $Y > 2.5$  conformer III

Table 6: Population of the first four conformers of glycine in percent for a temperature of 385 K. Experimental determined populations as well as calculations with and without interconversion of the fourth conformer are shown [262, 263, 266]

Conf.	Calc. without IC in %	Calc. with IC in %	Exp. in %
I	60.2(4)	74.9(4)	77(8)
II	12.1(1)	12.1(1)	10(2)
III	13.0(1)	13.0(1)	13(2)
IV	14.7(1)	–	–

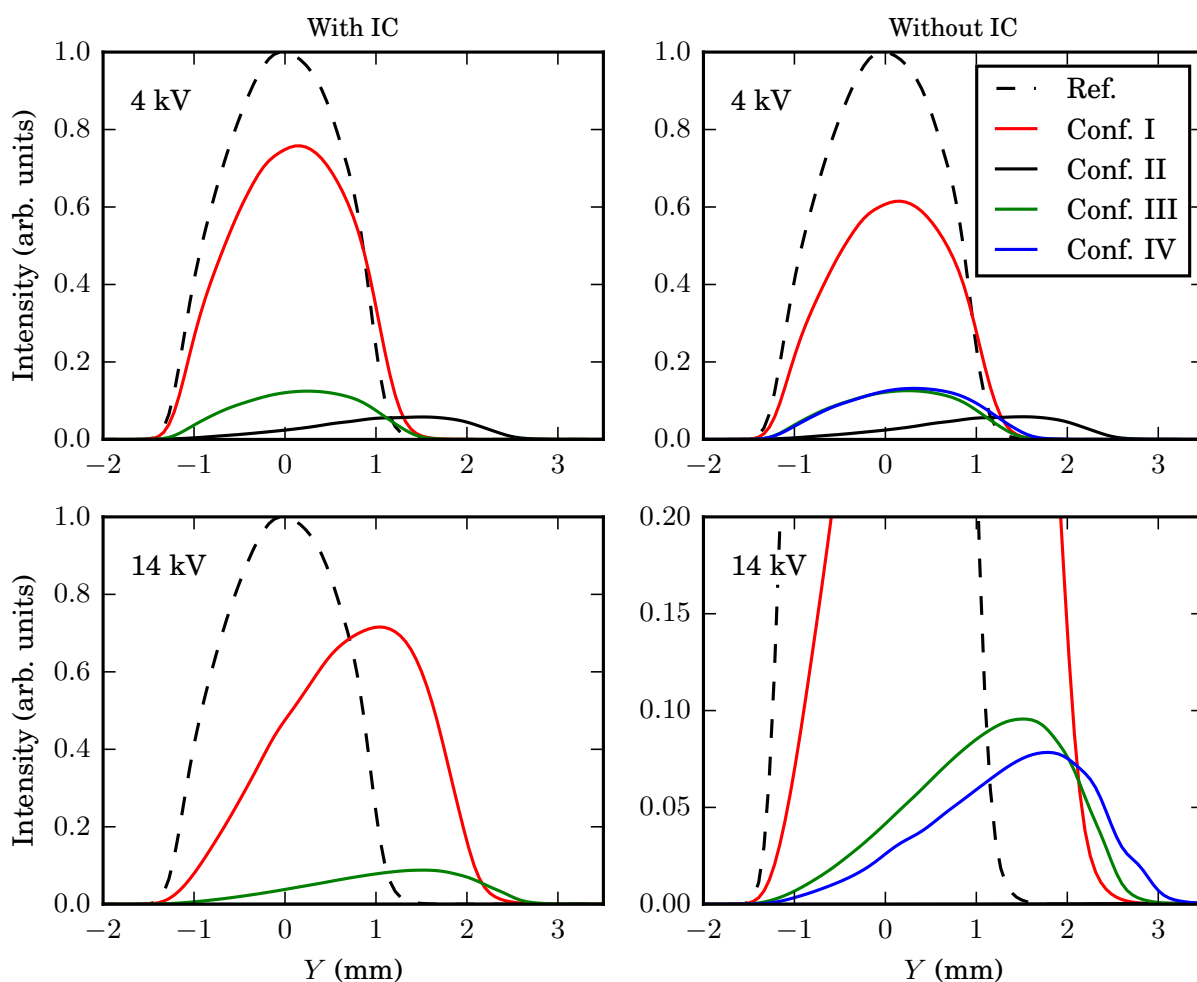


Figure 8.9: Simulated deflection profiles for the first four conformers of glycine. Top/bottom deviate by the voltage applied to the deflector electrodes, and left/right shows deviate by the non-existence/existence of the fourth conformer.

## 8. Applications of HHG photon sources

and IV are separated from conformer I. Though the separation is not very strong, experimentally it would be possible to probe at this position both conformers, and reduce thus strongly the influence of the first conformer. Depending on the IC-factor, conformer I can be purified to  $>90\%$  (with IC) or  $>82\%$  (without IC) at a position between  $-1 < Y < 1$ .

### 8.2.2 Experiment

The experimental section can be separated into two parts, i. e., in the evaporation of glycine within a pulsed valve [63] and two alternative evaporation techniques, namely laser desorption (LD) and laser-induced acoustic desorption (LIAD) source. For the first part, the experimental setup was similar to section 6.2, deviating only by the detection scheme, which was replaced by a time-of-flight mass spectrometer similar to the one described in section 3.2. The molecules were seeded in 50-80 bar helium and the temperature of the pulsed valve was varied between 110 and 170° C. Additional care was taken to the thermal insulation of the pulsed valve such that the temperature gradient between the tip and the back of the valve (where the sample reservoir was located) was not bigger than 20° C. The molecular beam was probed by a fs-laser pulse at pulse energies varying from 50-250  $\mu\text{J}$ . The pulse duration was  $< 40$  fs (FWHM for an Gaussian temporal profile), and the laser pulse was focused with a 50 cm focussing lens. The recorded ion-mass

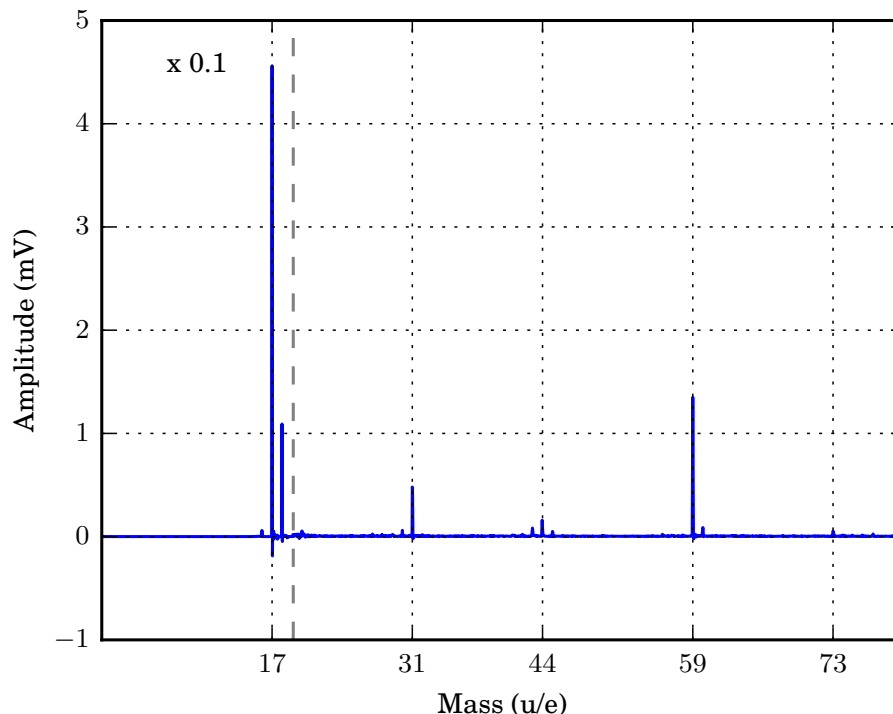


Figure 8.10: Mass spectrum of glycine by thermal evaporation within a pulsed valve [63]. The spectrum below a mass of 19 u has been scaled by 0.1.

spectra for the different experimental conditions looked similar. Exemplarily, a single mass spectrum is shown in Figure 8.10. The spectrum has been recorded at a valve temperature of 155 ° C, with a backing pressure of 50 bar helium, and a laser pulse energy of 150  $\mu$ J. The amplitude in left part of the spectrum ( $< 19$  u) was divided by a factor of 10. The spectrum is dominated by a peak at a mass of 17 u, e. g.  $\text{OH}^+$ , followed by singly ionized water at mass of 18 u. Smaller ion signals can be seen at masses of, for example, 59, 31 and 44 u. A very small signal is visible at a mass of 73 u, which is close to the parent ion of glycine (75 u). The lack of parent ion and the very low count rate for ions above a mass of 19 u rose the question whether or not intact glycine molecules do reach the interaction zone, and whether they are destroyed in the former case by the fs-laser probe. Within the CMI-group (<https://www.controlled-molecule-imaging.org>) alternative approaches to promote labile molecules into the gas-phase are currently under development by graduate students. Nicole Teschmit is developing a LD supersonic-expansion source similar to [64], and a LIAD source is being developed by Zhipeng Huang, which is similar to [65, 267]. Both experimental setups were used to measure TOF-mass spectra of glycine. In the former case, the molecules were desorbed in front of a pulsed valve, which used argon as carrier gas to transport the desorbed molecules into the spectrometer. In the latter case, the molecules were placed on a modified repeller electrode of the TOF spectrometer. The molecules have been probed by a fs-laser (*vide supra*) at a pulse energy of 170  $\mu$ J

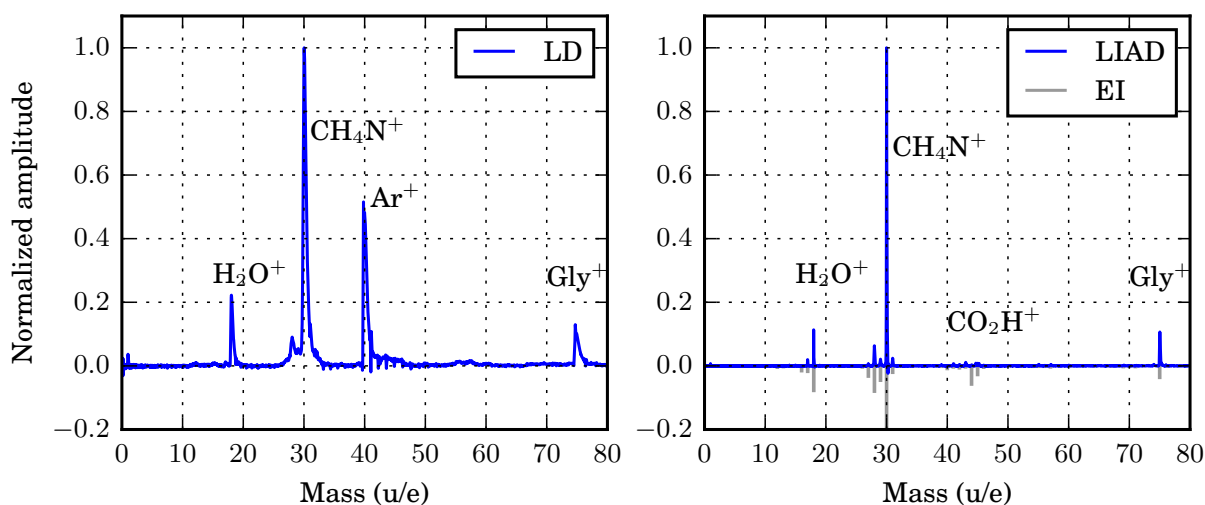


Figure 8.11: TOF mass spectra of glycine. Left (right): Glycine has been evaporated using a LD supersonic-expansion source (LIAD). The spectra have been normalized and a spectrum of glycine recorded via electron impact (EI) ionization is shown for comparison [268].

and their (normalized) recorded mass-spectra are shown in the left and right graph of Figure 8.11. Both spectra show a similar structure with a dominant peak at 30 u, corresponding to a fragmentation of glycine into an ionic  $\text{CH}_4\text{N}$  fragment and a neutral carboxyl group. The emission of hydrogens from that ionic

## 8. Applications of HHG photon sources

fragment can lead to the small peaks visible at 27-29 u. The parent ion of glycine as well as ionic water is visible in all cases. For comparison, a mass spectrum of glycine obtained from [268] and recorded via electron impact (EI) ionization is shown in the right graph. Its amplitude is reversed and has been normalized to -1. This spectrum looks comparable to the one acquired by LD and LIAD beside the more prominent peak at 45 u, which is assigned to an ionic carboxyl group. <sup>†</sup>

### 8.2.3 Conclusion and outlook

The simulated deflection profiles in Figure 8.9 show that a conformer separation in glycine is possible. Specifically, the second conformer of glycine is much stronger deflected than the other conformers and should thus be ‘easily’ separated from the other conformers, even under non-perfect experimental conditions. Conformer I, III and IV do have similar deflection profiles and, therefore, it will be challenging to get a full separation of the latter ones under these experimental conditions. Though, deflection profiles at different applied voltages, and possible conformer-dependent fragments in the TOF spectrum, could help to disentangle the contribution of the individual conformers in the deflection profile, which could allow to make statements about the existence/non-existence of the fourth conformer. Conformer I has the highest population and can be purified to a high degree.

In the experimental section mass spectra for different evaporation methods have been compared. It can be concluded that an evaporation within the pulsed valve leads to a fragmentation of the molecules. LD and LIAD are promising approaches to evaporate glycine. The LD-approach additionally showed that a subsequent cooling of the molecules with a seeding gas does not harm the molecules. Both approaches are designed such that they can be combined with the deflector, providing thus the potential to measure a deflection profile of glycine, i. e., providing a conformer separated molecular beam.

---

<sup>†</sup>Mass-spectra recorded from glycine via XUV photon ionization do show a similar mass-spectrum [269]

## 9 Summary

The presented experiments covered the control of cold gas-phase molecules, x-ray diffractive imaging of such controlled gas-phase molecules, and the x-ray photophysics and charge-rearrangement processes of gas-phase molecules and molecular clusters. All experiments were designed such that they provided, next to their results, a foundation for future experiments to study ultrafast structural changes or charge-rearrangement processes by making use of x-ray free-electron lasers.

### 9.1 Sample preparation

The control of cold gas-phase molecules was covering the spatial separation of different species, such as isomers or molecular clusters, to provide a strongly purified molecular sample as a starting point for an experiment. In chapter 3 the spatial separation of the *trans* and *cis* conformer of 3-fluorophenol was demonstrated. 3-fluorophenol is a prototypical large molecule, where the conformers differ by the orientation of their OH functional group. The conformers have a relative abundance of 2:1 (*trans:cis*) in the molecular beam, and the *trans* conformer has the higher permanent dipole moment. It was demonstrated that both conformers could be purified to more than 90 %, and providing thus a strongly purified molecular sample to study isomerization dynamics. 3-fluorophenol was chosen such that isomerization dynamics can be studied by molecular-frame photo angular distribution (MFPAD) measurements of aligned gas-phase molecules at a free electron lasers (FELs).

Simulations of the spatial separation of four different conformers of the smallest amino acid glycine were presented in section 8.2. It was shown that the second conformer of glycine could be fully separated from the other conformers. Additionally, it was shown that the first conformer can be purified to more than 90 %. The conformer separation of glycine is here in particular aiming at the study of conformer-dependent charge migration, triggered by the creation of coherently coupled hole-states in the molecular sample.

The spatial separation of the indole(H<sub>2</sub>O) clusters from the indole monomer and other species present in the molecular beam [12] was utilized in chapter 7. The experiment was aiming at the study of the x-ray photophysics of the micro-solvated indole(H<sub>2</sub>O), where the spatial separation was an important factor for the right interpretation of the data.

In addition to the separation of different conformers in the gas-phase, control of the molecules was achieved by laser-alignment to gain control about the orientation of the molecules in space. Alignment is necessary, or can be highly advantageous, for experiments aiming at the study of molecular frame dependent properties such as MFPAD measurements, or x-ray diffraction experiments, which aim at the structure determination small molecular samples in the gas-phase. In chapter 4 a general approach is presented to strongly align gas-phase molecules at the full FEL repetition rate by utilizing an in-house Ti:Sapphire laser system. Therefore, the compressor of the Ti:Sapphire laser system was bypassed, and the

## 9. Summary

direct output of the regenerative amplifier was used to strongly 3D align 2,5-diiodothiophene molecules. It was shown that the achieved alignment of  $\langle \cos^2 \theta_{2D} \rangle = 0.85$  was limited by the warm molecular beam rather than by the alignment laser pulse. Further, it was explained that the same laser system could be used as a pump or probe laser in an ultrafast pump-probe experiment, and providing thus direct an intrinsic synchronization between the alignment and the pump or probe laser.

### 9.2 X-ray diffractive imaging

Strongly aligned 2,5-diiodothiophene molecules were probed by hard x-ray photons to measure their structure via x-ray diffraction (chapter 5). X-ray diffraction is a highly promising approach to image the intrinsic structural changes of gas-phase molecules on ultrafast timescales. The alignment of the molecular sample does have the advantage that, providing the molecules are perfectly aligned (or more generally oriented), the diffraction pattern is equal to the diffraction pattern of the single molecule, which allows for the reconstruction of bond-length and bond-angles of the molecule. The simulations showed the feasibility to record 1D as well as 2D diffraction patterns of controlled gas-phase molecules within 6 hours at the free-electron laser LCLS, if the molecules are probed at the full FEL repetition rate, and if the background signal from the beamline is negligible. In the experimental section evidence for a 1D diffraction pattern was presented, which, on the other hand, could not be confirmed by the 2D diffraction pattern. Also, it was shown that the background signal from the beamline as well fluorescence background signal induced by the FEL at an aperture, could be partially suppressed by making use of the ADU signature in the x-ray camera. The experiment also showed that the upcoming high-repetition rate FELs like XFEL or LCLS 2 are highly promising photon sources to image structural changes in controlled gas-phase molecules via x-ray diffraction.

### 9.3 X-ray photophysics and coincident measurements

The x-ray photophysics of indole and indole water have been presented in chapter 6 and chapter 7. In both cases, the indole molecule was core-shell ionized at the carbons as well as site-specific ionized at its nitrogen atom by soft x-ray radiation. Electrons and ions have been recorded in coincidence. The photofragmentation of indole showed that the indole monomer is primarily fragmenting into three fragments, with two of them being ionic, and one being neutral. The recorded electron spectra showed that some of the detected fragmentation channels were primarily populated upon site-specific ionization at the nitrogen atom. The photofragmentation of indole(H<sub>2</sub>O) showed two main dissociation channels in which charge and mass transfer to the hydrogen-bonded water was observed. It was shown that both channels were accompanied by one or two holes located on the indole-site of the molecular cluster. In both cases, the indole part of the molecule showed a similar fragmentation pattern compared to the indole monomer. The indole(H<sub>2</sub>O) cluster is a highly promising sample to learn about the photofragmentation and ultrafast relaxation processes like intermolecular Coulombic decay (ICD) or electron-transfer mediated

decay (ETMD) in hydrogen-bonded systems. FELs provide the required time resolution and, if a neutral dissociation is triggered in the indole(H<sub>2</sub>O) system via a fs-UV laser pulse, these processes can be studied with fs time resolution.

In addition to the photophysics studied at accelerator based facility, a laboratory based high harmonic generation (HHG) source was used to study the photophysics of iodomethane upon site-specific ionization. The HHG source was operating at a repetition rate up to 100 kHz, thereby generating more than 10<sup>10</sup> photons/s per harmonic at a photon energy of up to 71 eV. It was possible to demonstrate that even photon-hungry experiments such as photoionization of gas-phase molecules with coincidence detection of the fragments could be performed with an HHG source. This experiment was conducted to demonstrate the potential use of a laboratory based photon source as an alternative to accelerator based facilities.



## 10 Conclusion and outlook

Complementary experiments for imaging structure and molecular dynamics of controlled gas-phase molecules have been presented. It was argued and demonstrated, that the control of gas-phase molecules is often highly advantageous or simply necessary for various kinds of experiments.

Control was gained by laser alignment of an isotropically oriented ensemble of cold gas-phase molecules, or by spatial separation of different species, e. g., conformers or molecular cluster, present in the molecular beam. A high degree of alignment of a molecular ensemble is crucial for x-ray diffraction experiments, because it increases locally the signal to noise ratio on the detector, and it allows to reconstruct the structure of a single molecules, including bond-angles and atomic distances. The deflection profile of indole and indole(H<sub>2</sub>O) was crucial for the disentanglement the photofragmentation pattern of both species, and its separation from bigger clusters. Further, the spatial separation of the *cis* and *trans* conformer of 3-fluorophenol was demonstrated, providing an ideal sample for the study of isomerization dynamics.

Different imaging techniques such as diffractive imaging or velocity map imaging were used for structure determination, or the study of the photofragmentation of isolated gas-phase molecules and cluster. The structure of strongly-aligned molecules was measured via hard x-ray diffractive imaging. Evidence for a 1D diffraction image has been presented, which could not be confirmed by the 2D diffraction image. Background photons could be partially suppressed by making use of the ADU signature in the x-ray camera. Electron-ion coincidence measurements have been used to study the photofragmentation of indole and indole(H<sub>2</sub>O) upon localized core-shell ionization. Charge and mass transfer to the hydrogen-bonded water was observed. The indole-part of the cluster was fragmenting in a similar way to the indole monomer, though the population of the fragmentation channels differed.

The combination of the different presented experiments, or the extension of the experiments toward the measurement of ultrafast dynamics, is feasible in various ways in a pump-probe experiment. Isomerization dynamics of 3-fluorophenol could be measured at an FEL with a conformer-selected molecular beam, aligned at full FEL repetition rate, and probed by x-ray diffraction or molecular-frame photoelectron angular distribution. Indole(H<sub>2</sub>O) can be used to study charge transfer and relaxation processes like interatomic coulombic decay (ICD), electron-transfer mediated decay (ETMD), or proton transfer mediated charge separation (PTM-CS), by neutral dissociation of the cluster, and subsequent ionization at the indole or water part of the cluster by localized ionization.

Coincidence measurements, which were performed at a high-repetition rate HHG source, showed the potential use of laboratory based photon sources to perform pump-probe coincidence measurements by making use of the XUV photons localized ionization in the sample. Laboratory based HHG sources allow for long-term measurements, under typically more stable environments than provided at accelerator-based facilities. The upcoming high repetition rate FELs like the European XFEL or LCLS II are promising photon sources to measure intrinsic dynamics of molecules with various imaging techniques such as x-ray diffraction, MFPAD, RFPAD, or Coulomb exploding imaging.



## Bibliography

- [1] Wiley W and McLaren I 1955 *Rev. Sci. Instrum.* **26** 1150–1157
- [2] Eppink A T J B and Parker D H 1997 *Rev. Sci. Instrum.* **68** 3477–3484 URL <http://link.aip.org/link/?RSI/68/3477/1>
- [3] Ashfold M N R, Nahler N H, Orr-Ewing A J, Vieuxmaire O P J, Toomes R L, Kitsopoulos T N, Garcia I A, Chestakov D A, Wu S M and Parker D H 2006 *Phys. Chem. Chem. Phys.* **8** 26–53 URL <http://pubs.rsc.org/en/content/articlelanding/2006/cp/b509304j>
- [4] Chichinin A I, Gericke K H, Kauczok S and Maul C 2009 *Int. Rev. Phys. Chem.* **28** 607–680 URL <http://www.tandfonline.com/doi/abs/10.1080/01442350903235045>
- [5] Stei M, von Vangerow J, Otto R, Kelkar A H, Carrascosa E, Best T and Wester R 2013 *J. Chem. Phys.* **138** 214201
- [6] Zewail A H 2000 *Pure & Appl. Chem.* **72** 2219–2231 URL <http://www.degruyter.com/view/j/pac.2000.72.issue-12/pac200072122219/pac200072122219.xml>
- [7] Scoles G 1988 *Atomic and Molecular Beam Methods* (Oxford University Press)
- [8] Rizzo T R, Park Y D, Peteanu L and Levy D H 1985 *J. Chem. Phys.* **83** 4819–4820
- [9] Chang Y P, Horke D A, Trippel S and Küpper J 2015 *Int. Rev. Phys. Chem.* **34**(4) 557–590 (*Preprint* 1505.05632) URL <http://dx.doi.org/10.1080/0144235X.2015.1077838>
- [10] Filsinger F, Küpper J, Meijer G, Hansen J L, Maurer J, Nielsen J H, Holmegaard L and Stapelfeldt H 2009 *Angew. Chem. Int. Ed.* **48** 6900–6902 URL <http://onlinelibrary.wiley.com/doi/10.1002/anie.200902650/abstract>
- [11] Kierspel T, Horke D A, Chang Y P and Küpper J 2014 *Chem. Phys. Lett.* **591** 130–132 ISSN 0009-2614 (*Preprint* 1312.4417) URL <http://www.sciencedirect.com/science/article/pii/S0009261413014000>
- [12] Trippel S, Chang Y P, Stern S, Mullins T, Holmegaard L and Küpper J 2012 *Phys. Rev. A* **86** 033202 (*Preprint* 1208.4935) URL <http://pra.aps.org/abstract/PRA/v86/i3/e033202>
- [13] Horke D A, Trippel S, Chang Y P, Stern S, Mullins T, Kierspel T and Küpper J 2014 *J. Vis. Exp.* (83) e51137 URL <http://www.jove.com/video/51137/spatial-separation-of-molecular-conformers-and-clusters>
- [14] Gerlach W and Stern O 1922 *Z. Phys.* **9** 349–352 URL <http://dx.doi.org/10.1007/BF01326983>
- [15] Holmegaard L, Hansen J L, Kalhøj L, Kragh S L, Stapelfeldt H, Filsinger F, Küpper J, Meijer G, Dimitrovski D, Abu-samaha M, Martiny C P J and Madsen L B 2010 *Nat. Phys.* **6** 428 (*Preprint* 1003.4634) URL <https://www.nature.com/articles/nphys1666>
- [16] Krasniqi F, Najjari B, Strüder L, Rolles D, Voitkiv A and Ullrich J 2010 *Phys. Rev. A* **81** 033411
- [17] Boll R, Rouzée A, Adolph M, Anielski D, Aquila A, Bari S, Bomme C, Bostedt C, Bozek J D, Chapman H N, Christensen L, Coffee R, Coppola N, De S, Decleva P, Epp S W, Erk B, Filsinger F, Foucar L, Gorkhover T, Gumprecht L, Hömke A, Holmegaard L, Johnsson P, Kienitz J S, Kierspel T, Krasniqi F, Kühnel K U, Maurer J, Messerschmidt M, Moshhammer R, Müller N L M, Rudek B, Savelyev E, Schlichting I, Schmidt C, Scholz F, Schorb S, Schulz J, Seltmann J, Stener M, Stern S, Techert S, Thøgersen J, Trippel S, Viefhaus J, Vrakking M, Stapelfeldt H, Küpper J, Ullrich J, Rudenko A and Rolles D 2014 *Faraday Disc.* **171** 57–80 (*Preprint* 1407.7782)
- [18] Boll R, Anielski D, Bostedt C, Bozek J D, Christensen L, Coffee R, De S, Decleva P, Epp S W, Erk B,

## Bibliography

- Foucar L, Krasniqi F, Küpper J, Rouzée A, Rudek B, Rudenko A, Schorb S, Stapelfeldt H, Stener M, Stern S, Techert S, Trippel S, Vrakking M J J, Ullrich J and Rolles D 2013 *Phys. Rev. A* **88** 061402(R)
- [19] Toffoli D, Lucchese R R, Lebeck M, Houver J C and Doweck D 2007 *J. Chem. Phys.* **126** 054307 URL <http://scitation.aip.org/content/aip/journal/jcp/126/5/10.1063/1.2432124>
- [20] Rolles D, Boll R, Adolph M, Aquila A, Bostedt C, Bozek J, Chapman H, Coffee R, Coppola N, Declava P, Delmas T, Epp S, Erk B, Filsinger F, Foucar L, Gumprecht L, Hömke A, Gorkhover T, Holmegaard L, Johnsson P, Kaiser C, Krasniqi F, Kühnel K U, Maurer J, Messerschmidt M, Moshhammer R, Quevedo W, Rajkovic I, Rouzée A, Rudek B, Schlichting I, Schmidt C, Schorb S, Schröter C D, Schulz J, Stapelfeldt H, Stener M, Stern S, Techert S, Thøgersen J, Vrakking M J J, Rudenko A, Küpper J and Ullrich J 2014 *J. Phys. B* **47** 124035
- [21] Bomme C, Guillemin R, Marin T, Journal L, Marchenko T, Doweck D, Trcera N, Pilette B, Avila A, Ringuenet H, Kushawaha R K and Simon M 2013 *Rev. Sci. Instrum.* **84** 103104 URL <http://scitation.aip.org/content/aip/journal/rsi/84/10/10.1063/1.4824194>
- [22] Guillemin R, Bomme C, Marin T, Journal L, Marchenko T, Kushawaha R K, Trcera N, Piancastelli M N and Simon M 2011 *Phys. Rev. A* **84** 063425 URL <http://link.aps.org/doi/10.1103/PhysRevA.84.063425>
- [23] Doweck D, Haouas A, Guillemin R, Elkharrat C, Houver J C, Li W B, Catoire F, Journal L, Simon M and Lucchese R R 2009 *Eur. Phys. J. Special Topics* **169** 85–93 URL <http://link.springer.com/article/10.1140/epjst/e2009-00977-8>
- [24] Stern S 2013 *Controlled Molecules for X-ray Diffraction Experiments at Free-Electron Lasers* Dissertation Universität Hamburg Hamburg, Germany URL <http://www-library.desy.de/cgi-bin/showprep.pl?desy-thesis-13-054>
- [25] Küpper J, Stern S, Holmegaard L, Filsinger F, Rouzée A, Rudenko A, Johnsson P, Martin A V, Adolph M, Aquila A, Bajt S, Barty A, Bostedt C, Bozek J, Caleman C, Coffee R, Coppola N, Delmas T, Epp S, Erk B, Foucar L, Gorkhover T, Gumprecht L, Hartmann A, Hartmann R, Hauser G, Holl P, Hömke A, Kimmel N, Krasniqi F, Kühnel K U, Maurer J, Messerschmidt M, Moshhammer R, Reich C, Rudek B, Santra R, Schlichting I, Schmidt C, Schorb S, Schulz J, Soltau H, Spence J C H, Starodub D, Strüder L, Thøgersen J, Vrakking M J J, Weidenspointner G, White T A, Wunderer C, Meijer G, Ullrich J, Stapelfeldt H, Rolles D and Chapman H N 2014 *Phys. Rev. Lett.* **112** 083002 (*Preprint* 1307.4577)
- [26] Stern S, Holmegaard L, Filsinger F, Rouzée A, Rudenko A, Johnsson P, Martin A V, Barty A, Bostedt C, Bozek J D, Coffee R N, Epp S, Erk B, Foucar L, Hartmann R, Kimmel N, Kühnel K U, Maurer J, Messerschmidt M, Rudek B, Starodub D G, Thøgersen J, Weidenspointner G, White T A, Stapelfeldt H, Rolles D, Chapman H N and Küpper J 2014 *Faraday Disc.* **171** 393 (*Preprint* 1403.2553)
- [27] Barty A, Küpper J and Chapman H N 2013 *Annu. Rev. Phys. Chem.* **64** 415–435 URL <http://dx.doi.org/10.1146/annurev-physchem-032511-143708>
- [28] Filsinger F, Meijer G, Stapelfeldt H, Chapman H and Küpper J 2011 *Phys. Chem. Chem. Phys.* **13** 2076–2087 (*Preprint* 1009.0871)
- [29] Müller N L M 2016 *Electron diffraction and controlled molecules* Dissertation Universität Hamburg Hamburg, Germany
- [30] Yang J, Beck J, Uiterwaal C J and Centurion M 2015 *Nat. Commun.* **6** 8172
- [31] Yang J, Guehr M, Vecchione T, Robinson M S, Li R, Hartmann N, Shen X, Coffee R, Corbett J, Fry A, Gaffney

- K, Gorkhover T, Hast C, Jobe K, Makasyuk I, Reid A, Robinson J, Vetter S, Wang F, Weathersby S, Yoneda C, Centurion M and Wang X 2016 *Nat. Commun.* **7** 11232 URL <http://dx.doi.org/10.1038/ncomms11232>
- [32] Hensley C J, Yang J and Centurion M 2012 *Phys. Rev. Lett.* **109** 133202
- [33] Loesch H J and Remscheid A 1990 *J. Chem. Phys.* **93** 4779
- [34] Friedrich B and Herschbach D R 1991 *Z. Phys. D* **18** 153–161 URL <http://dx.doi.org/10.1007/BF01437441>
- [35] Stapelfeldt H and Seideman T 2003 *Rev. Mod. Phys.* **75** 543–557 URL <http://link.aps.org/abstract/RMP/v75/p543>
- [36] Friedrich B and Herschbach D 1995 *Phys. Rev. Lett.* **74** 4623–4626
- [37] Ortigoso J, Rodriguez M, Gupta M and Friedrich B 1999 *J. Chem. Phys.* **110** 3870–3875 URL <http://link.aip.org/link/?JCP/110/3870/1>
- [38] Holmegaard L, Nielsen J H, Nevo I, Stapelfeldt H, Filsinger F, Küpper J and Meijer G 2009 *Phys. Rev. Lett.* **102**(2) 023001 (*Preprint* 0810.2307) URL <http://dx.doi.org/10.1103/PhysRevLett.102.023001>
- [39] Friedrich B and Herschbach D 1999 *J. Chem. Phys.* **111** 6157
- [40] Abbe E 1873 *Arch. Mikrosk. Anat.* **9** 413–418 ISSN 0176-7364 URL <http://dx.doi.org/10.1007/BF02956173>
- [41] Röntgen W C 1898 *Annalen der Physik* **300** 12–17 ISSN 1521-3889 URL <http://dx.doi.org/10.1002/andp.18983000103>
- [42] Attwood D 2000 *Soft x-rays and extreme ultraviolet radiation: principles and applications* (University of California, Berkeley: Cambridge University Press) ISBN 0521652146
- [43] Als-Nielsen J and McMorrow D 2001 *Elements of Modern X-ray Physics* (Chichester, West Sussex, United Kingdom: John Wiley & Sons) ISBN 978-0-471-49858-2
- [44] Santra R 2009 *J. Phys. B* **42** 023001 URL <http://iopscience.iop.org/article/10.1088/0953-4075/42/2/023001>
- [45] Lonsdale K 1929 *Proc. Royal Soc. London A* **123** 494–515 ISSN 0950-1207
- [46] Watson J and Crick F 1953 *Nature* **171** 737–738 URL <http://dx.doi.org/10.1038/171737a0>
- [47] Anderson A C 2003 *Chemistry & Biology* **10** 787–797 URL <http://linkinghub.elsevier.com/retrieve/pii/S1074552103001947>
- [48] Ramakrishnan V 2010 *Angew. Chem. Int. Ed.* **49** 4355–4380 URL <http://onlinelibrary.wiley.com/doi/10.1002/anie.201001436/full>
- [49] Neutze R, Wouts R, van der Spoel D, Weckert E and Hajdu J 2000 *Nature* **406** 752–757 URL <http://dx.doi.org/10.1038/35021099>
- [50] Chapman H N, Fromme P, Barty A, White T A, Kirian R A, Aquila A, Hunter M S, Schulz J, Deponte D P, Weierstall U, Doak R B, Maia F R N C, Martin A V, Schlichting I, Lomb L, Coppola N, Shoeman R L, Epp S W, Hartmann R, Rolles D, Rudenko A, Foucar L, Kimmel N, Weidenspointner G, Holl P, Liang M, Barthelmeß M, Caleman C, Boutet S, Bogan M J, Krzywinski J, Bostedt C, Bajt S, Gumprecht L, Rudek B, Erk B, Schmidt C, Hömke A, Reich C, Pietschner D, Strüder L, Hauser G, Gorke H, Ullrich J, Herrmann S, Schaller G, Schopper F, Soltau H, Kühnel K U, Messerschmidt M, Bozek J D, Hau-Riege S P, Frank M, Hampton C Y, Sierra R G, Starodub D, Williams G J, Hajdu J, Timneanu N, Seibert M M, Andreasson J, Rocker A, Jönsson O, Svenda M, Stern S, Nass K, Andritschke R, Schröter C D, Krasniqi F, Bott M, Schmidt K E, Wang X, Grotjohann I, Holton J M, Barends T R M, Neutze R, Marchesini S, Fromme R, Schorb S, Rupp D, Adolph M, Gorkhover T, Andersson I, Hirsemann H, Potdevin G, Graafsma H, Nilsson B and Spence J C H

## Bibliography

- 2011 *Nature* **470** 73 URL <http://www.nature.com/nature/journal/v470/n7332/full/nature09750.html>
- [51] Minitti M P, Budarz J M, Kirrander A, Robinson J S, Ratner D, Lane T J, Zhu D, Glownia J M, Kozina M, Lemke H T, Sikorski M, Feng Y, Nelson S, Saita K, Stankus B, Northey T, Hastings J B and Weber P M 2015 *Phys. Rev. Lett.* **114** 255501 URL <http://link.aps.org/doi/10.1103/PhysRevLett.114.255501>
- [52] Glownia J M, Cryan J, Andreasson J, Belkacem A, Berrah N, Blaga C I, Bostedt C, Bozek J, DiMauro L F, Fang L, Frisch J, Gessner O, Guehr M, Hajdu J, Hertlein M P, Hoener M, Huang G, Kornilov O, Marangos J P, March A M, McFarland B K, Merdji H, Petrovic V S, Raman C, Ray D, Reis D A, Trigo M, White J L, White W, Wilcox R, Young L, Coffee R N and Bucksbaum P H 2010 *Opt. Exp.* **18** 17620–17630
- [53] Erk B, Rolles D, Foucar L, Rudek B, Epp S W, Cryle M, Bostedt C, Schorb S, Bozek J, Rouzee A, Hundertmark A, Marchenko T, Simon M, Filsinger F, Christensen L, De S, Trippel S, Kupper J, Stapelfeldt H, Wada S, Ueda K, Swiggers M, Messerschmidt M, Schroter C D, Moshhammer R, Schlichting I, Ullrich J and Rudenko A 2013 *J. Phys. B* **46** 164031 URL [http://iopscience.iop.org/0953-4075/46/16/164031/pdf/0953-4075\\_46\\_16\\_164031.pdf](http://iopscience.iop.org/0953-4075/46/16/164031/pdf/0953-4075_46_16_164031.pdf)
- [54] Erk B, Rolles D, Foucar L, Rudek B, Epp S W, Cryle M, Bostedt C, Schorb S, Bozek J, Rouzee A, Hundertmark A, Marchenko T, Simon M, Filsinger F, Christensen L, De S, Trippel S, Küpper J, Stapelfeldt H, Wada S, Ueda K, Swiggers M, Messerschmidt M, Schroter C D, Moshhammer R, Schlichting I, Ullrich J and Rudenko A 2013 *Phys. Rev. Lett.* **110** 053003 URL <http://prl.aps.org/abstract/PRL/v110/i5/e053003>
- [55] McFarland B K, Farrell J P, Miyabe S, Tarantelli F, Aguilar A, Berrah N, Bostedt C, Bozek J D, Bucksbaum P H, Castagna J C, Coffee R N, Cryan J P, Fang L, Feifel R, Gaffney K J, Glownia J M, Martinez T J, Mucke M, Murphy B, Natan A, Osipov T, Petrovic V S, Schorb S, Schultz T, Spector L S, Swiggers M, Tenney I, Wang S, White J L, White W and Gühr M 2014 *Nat. Commun.* **5** 4235 URL <http://www.nature.com/doi/10.1038/ncomms5235>
- [56] Gessner O and Gühr M 2016 *Acct. Chem. Res.* **49** 138–145 URL <http://pubs.acs.org/doi/abs/10.1021/acs.accounts.5b00361>
- [57] Sanchez-Gonzalez A, Barillot T R, Squibb R J, Kolorenč P, Agåker M, Averbukh V, Bearpark M J, Bostedt C, Bozek J D, Bruce S, Montero S C, Coffee R N, Cooper B, Cryan J P, Dong M, Eland J H D, Fang L, Fukuzawa H, Guehr M, Ilchen M, Johnsson A S, Liekhus-S C, Marinelli A, Maxwell T, Motomura K, Mucke M, Natan A, Osipov T, Östlin C, Pernpointner M, Petrovic V S, Robb M A, Sâthe C, Simpson E R, Underwood J G, Vacher M, Walke D J, Wolf T J A, Zhaunerchyk V, Rubensson J E, Berrah N, Bucksbaum P H, Ueda K, Feifel R, Frasinski L J and Marangos J P 2015 *J. Phys. B* **48** 234004 URL <http://iopscience.iop.org/article/10.1088/0953-4075/48/23/234004>
- [58] Levola H, Itala E, Schlesier K, Kooser K, Laine S, Laksman J, Ha D T, Rachlew E, Tarkanovskaja M, Tanzer K and Kukk E 2015 *Phys. Rev. A* **92** 063409 URL <http://link.aps.org/doi/10.1103/PhysRevA.92.063409>
- [59] Kukk E, Ha D T, Wang Y, Piekarski D G, Diaz-Tendero S, Kooser K, Itala E, Levola H, Alcamí M, Rachlew E and Martín F 2015 *Phys. Rev. A* **91** 043417 URL <http://link.aps.org/doi/10.1103/PhysRevA.91.043417>
- [60] Ha D T, Wang Y, Alcamí M, Itaelae E, Kooser K, Urpeainen S, Huels M A, Kukk E and Martín F 2014 *J. Phys. Chem. A* **118** 1374–1383 URL <http://eutils.ncbi.nlm.nih.gov/entrez/eutils/elink.fcgi?dbfrom=pubmed&id=24517120&retmode=ref&cmd=prlinks>
- [61] Ha D T, Huels M A, Huttula M, Urpelainen S and Kukk E 2011 *Phys. Rev. A* **84** 033419 URL <http://link.aps.org/doi/10.1103/PhysRevA.84.033419>

- [62] Sugishima A, Nagaya K, Iwayama H, Yao M, Adachi J, Kimura Y, Yamazaki M and Yagishita A 2009 *J. Chem. Phys.* **131** 114309 URL <http://scitation.aip.org/content/aip/journal/jcp/131/11/10.1063/1.3224117>
- [63] Even U, Jortner J, Noy D, Lavie N and Cossart-Magos N 2000 *J. Chem. Phys.* **112** 8068–8071 URL <http://dx.doi.org/10.1063/1.481405>
- [64] Meijer G, de Vries M S, Hunziker H E and Wendt H R 1990 *Appl. Phys. B* **51** 395–403 ISSN 1432-0649 URL <http://dx.doi.org/10.1007/BF00329101>
- [65] Lindner B and Seydel U 1985 *Anal. Chem.* **57** 895–899 URL <http://pubs.acs.org/doi/abs/10.1021/ac00281a027>
- [66] Gordy W and Cook R L 1984 *Microwave Molecular Spectra* 3rd ed (New York, NY, USA: John Wiley & Sons)
- [67] Zare R N 1988 *Angular Momentum* (New York, NY, USA: John Wiley & Sons) ISBN 0471858927
- [68] Bunker P R and Jensen P 2005 *Fundamentals of Molecular Symmetry* Series in Chemical Physics (Bristol, UK: Institute of Physics Publishing)
- [69] Demtröder W 2003 *Molekülphysik, Theoretische Grundlagen und experimentelle Methoden* (Oldenbourg Verlag München Wien)
- [70] Chang Y P, Filsinger F, Sartakov B and Küpper J 2014 *Comp. Phys. Comm.* **185** 339–49 (*Preprint* 1308.4076) URL <http://www.sciencedirect.com/science/article/pii/S0010465513003019>
- [71] Stark J and Wendt G 1914 *Ann. Phys.* **348** 983–990 ISSN 1521-3889 URL <http://dx.doi.org/10.1002/andp.19143480703>
- [72] Kienitz J S, Trippel S, Mullins T, Długolecki K, González-Férez R and Küpper J 2016 *Chem. Phys. Chem.* **17** 3740–3746 (*Preprint* 1607.05615) URL <http://dx.doi.org/10.1002/cphc.201600710>
- [73] Horke D A, Chang Y P, Długolecki K and Küpper J 2014 *Angew. Chem. Int. Ed.* **53** 11965–11968 (*Preprint* 1407.2056) URL <http://onlinelibrary.wiley.com/doi/10.1002/anie.201405986/abstract>
- [74] Bulthuis J, Möller J and Loesch H J 1997 *J. Phys. Chem. A* **101** 7684–7690
- [75] Friedrich B and Herschbach D 1995 *J. Phys. Chem.* **99** 15686
- [76] 2017 Elettra Web Page atomic Calculation of Photoionization Cross-Sections and Asymmetry Parameters URL <https://vuo.elettra.eu/services/elements/WebElements.html>
- [77] Berger M J, Hubbell J H, Seltzer S M, Chang J, Coursey J S, Sukumar R, Zucker D S and Olsen K 2010 XCOM: Photon Cross Sections Database available at <http://physics.nist.gov/xcom>, National Institute of Standards and Technology, Gaithersburg, MD URL <http://physics.nist.gov/xcom>
- [78] Thompson A, Lindau I, Attwood D, Liu Y, Gullikson E, Pianetta P, Howells M, Robinson A, Kim K J, Scofield J, Kirz J, Underwood J, Kortright J, Williams G and Winick H 2009 *X-Ray Data Booklet* (Center for X-Ray Optics and Advanced Light Source, Lawrence Berkeley National Laboratory, Berkeley, CA) URL <http://xdb.lbl.gov/>
- [79] Burhop 1952 *The Auger Effect and Other Radiationless Transitions* (Cambridge University Press) ISBN 9781107641105
- [80] Cederbaum L S, Zobeley J and Tarantelli F 1997 *Phys. Rev. Lett.* **79** 4778–4781 URL <https://doi.org/10.1103/PhysRevLett.79.4778>
- [81] Zobeley J, Cederbaum L S and Tarantelli F 1998 *J. Chem. Phys.* **108** 9737–9750 URL <http://scitation.aip.org/content/aip/journal/jcp/108/11/10.1063/1.478110>

## Bibliography

- [aip.org/content/aip/journal/jcp/108/23/10.1063/1.476448](http://aip.org/content/aip/journal/jcp/108/23/10.1063/1.476448)
- [82] Zobeley J, Santra R and Cederbaum L S 2001 *J. Chem. Phys.* **115** 5076–5088 URL <https://doi.org/10.1063/1.1395555>
- [83] Rupp B 2009 *Biomolecular Crystallography: Principles, Practice, and Application to Structural Biology* 1st ed (270 Madison Avenue, New York NY 10016, USA: Garland Science, Taylor & Francis Group)
- [84] Waasmaier D and Kirfel A 1995 *Acta Cryst. A* **51** 416–431 URL <http://dx.doi.org/10.1107/S0108767394013292>
- [85] Henke B, Gullikson E and Davis J 1993 *Atomic Data and Nuclear Data Tables* **54** 181–342 ISSN 0092-640X URL <http://www.sciencedirect.com/science/article/pii/S0092640X83710132>
- [86] Klein O and Nishina Y 1929 *Z. Phys.* **52** 853–868 URL <http://link.springer.com/article/10.1007/BF01366453>
- [87] Hubbell J H, Veigle W J, Briggs E A, Brown R T, Cromer D T and Howerton R J 1975 *J. Phys. Chem. Ref. Data* **4** 471–538 URL <http://scitation.aip.org/content/aip/journal/jpcrd/4/3/10.1063/1.555523>
- [88] Sciaini G and Miller R J D 2011 *Rep. Prog. Phys.* **74** 096101 URL <http://iopscience.iop.org/0034-4885/74/9/096101/>
- [89] Chang Y P, Dhugołęcki K, Küpper J, Rösch D, Wild D and Willitsch S 2013 *Science* **342** 98–101 ISSN 0036-8075 (*Preprint* 1308.6538) URL <http://dx.doi.org/10.1126/science.1242271>
- [90] Ghafur O, Rouzee A, Gijsbertsen A, Siu W K, Stolte S and Vrakking M J J 2009 *Nat. Phys.* **5** 289–293
- [91] Filsinger F, Erlekam U, von Helden G, Küpper J and Meijer G 2008 *Phys. Rev. Lett.* **100**(13) 133003 (*Preprint* 0802.2795) URL <http://dx.doi.org/10.1103/PhysRevLett.100.133003>
- [92] Reuss J 1988 State Selection by Nonoptical Methods *Atomic and molecular beam methods* vol 1 ed Scoles G (New York, NY, USA: Oxford University Press) chap 11, pp 276–292 ISBN 0195042808
- [93] Filsinger F, Küpper J, Meijer G, Holmegaard L, Nielsen J H, Nevo I, Hansen J L and Stapelfeldt H 2009 *J. Chem. Phys.* **131** 064309 (*Preprint* 0903.5413) URL <http://scitation.aip.org/content/aip/journal/jcp/131/6/10.1063/1.3194287>
- [94] Putzke S, Filsinger F, Haak H, Küpper J and Meijer G 2011 *Phys. Chem. Chem. Phys.* **13** 18962 (*Preprint* 1103.5080)
- [95] Jaman A I, Nandi R N and Ghosh D K 1981 *J. Mol. Spec.* **86** 269–274 URL <http://linkinghub.elsevier.com/retrieve/pii/0022285281902794>
- [96] Dutta A and Jaman A I 1985 *Pramana – J. Phys.* **24** 499–502 URL <http://link.springer.com/10.1007/BF02894850>
- [97] Nevo I, Holmegaard L, Nielsen J H, Hansen J L, Stapelfeldt H, Filsinger F, Meijer G and Küpper J 2009 *Phys. Chem. Chem. Phys.* **11** 9912–9918 (*Preprint* 0906.2971)
- [98] Fujimaki E, Fujii A, Ebata T and Mikami N 1999 *J. Chem. Phys.* **110** 4238–4247
- [99] Manocha A S, Carlson G L and Fateley W G 1973 *J. Phys. Chem.* **77** 2094–2098 URL <http://pubs.acs.org/doi/abs/10.1021/j100636a013>
- [100] Kierspel T, Wiese J, Mullins T, Robinson J, Aquila A, Barty A, Bean R, Boll R, Boutet S, Bucksbaum P, Chapman H N, Christensen L, Fry A, Hunter M, Koglin J E, Liang M, Mariani V, Morgan A, Natan A, Petrovic V, Rolles D, Rudenko A, Schnorr K, Stapelfeldt H, Stern S, Thøgersen J, Yoon C H, Wang F, Trippel S and Küpper J 2015 *J. Phys. B* **48** 204002 (*Preprint* 1506.03650)

- [101] Meckel M, Comtois D, Zeidler D, Staudte A, Pavičić D, Bandulet H C, Pépin H, Kieffer J C, Dörner R, Villeneuve D M and Corkum P B 2008 *Science* **320** 1478–1482 ISSN 0036-8075 URL <http://science.sciencemag.org/content/320/5882/1478>
- [102] Itatani J, Levesque J, Zeidler D, Niikura H, Pépin H, Kieffer J C, Corkum P B and Villeneuve D M 2004 *Nature* **432** 867–871
- [103] Wörner H J, Bertrand J B, Kartashov D V, Corkum P B and Villeneuve D M 2010 *Nature* **466** 604–607
- [104] Zuo T, Bandrauk A D and Corkum P B 1996 *Chem. Phys. Lett.* **259** 313–320
- [105] Blaga C I, Xu J, DiChiara A D, Sistrunk E, Zhang K, Agostini P, Miller T A, DiMauro L F and Lin C D 2012 *Nature* **483** 194–197 URL <https://www.nature.com/articles/nature10820>
- [106] Stern S, Chapman H and Küpper J 2015 *J. Phys. B* In preparation for special issue on "science at free-electron lasers"
- [107] Block P A, Bohac E J and Miller R E 1992 *Phys. Rev. Lett.* **68** 1303–1306
- [108] Normand D, Lompre L and Cornaggia C 1992 *J. Phys. B* **25** 497–503
- [109] Rosca-Pruna F and Vrakking M J J 2001 *Phys. Rev. Lett.* **87** 153902 URL <http://prola.aps.org/abstract/PRL/v87/i15/e153902>
- [110] Sakai H, Safvan C P, Larsen J J, Hilligsøe K M, Hald K and Stapelfeldt H 1999 *J. Chem. Phys.* **110** 10235–10238 URL <http://link.aip.org/link/?JCP/110/10235/1>
- [111] Larsen J J, Hald K, Bjerre N, Stapelfeldt H and Seideman T 2000 *Phys. Rev. Lett.* **85** 2470–2473
- [112] Lee K F, Villeneuve D M, Corkum P B, Stolow A and Underwood J G 2006 *Phys. Rev. Lett.* **97** 173001 URL <http://link.aps.org/abstract/PRL/v97/e173001>
- [113] Ren X, Makhija V and Kumarappan V 2014 *Phys. Rev. Lett.* **112** 173602
- [114] Tanji H, Minemoto S and Sakai H 2005 *Phys. Rev. A* **72** 063401
- [115] Pabst S, Ho P J and Santra R 2010 *Phys. Rev. A* **81** 043425 URL <http://pra.aps.org/abstract/PRA/v81/i4/e043425>
- [116] Kumarappan V, Bisgaard C Z, Viftrup S S, Holmegaard L and Stapelfeldt H 2006 *J. Chem. Phys.* **125** 194309
- [117] Torres R, de Nalda R and Marangos J P 2005 *Phys. Rev. A* **72** 023420
- [118] Owschimikow N, Schmidt B and Schwentner N 2011 *Phys. Chem. Chem. Phys.* **13**(19) 8671–8680
- [119] Trippel S, Mullins T, Müller N L M, Kienitz J S, Długołęcki K and Küpper J 2013 *Mol. Phys.* **111** 1738 (*Preprint* 1301.1826) URL <http://dx.doi.org/10.1080/00268976.2013.780334>
- [120] Trippel S, Mullins T, Müller N L M, Kienitz J S, Omiste J J, Stapelfeldt H, González-Férez R and Küpper J 2014 *Phys. Rev. A* **89** 051401(R) (*Preprint* 1401.6897) URL <https://journals.aps.org/pr/abstract/10.1103/PhysRevA.89.051401>
- [121] Boutet S and Williams G 2010 *New J. Phys.* **12** 035024
- [122] Liang M, Williams G J, Messerschmidt M, Seibert M M, Montanez P A, Hayes M, Milathianaki D, Aquila A, Hunter M S, Koglin J E *et al.* 2015 *J. Synchrotron Rad.* **22** 514–519
- [123] Johnsson P, Rouzée A, Siu W, Huismans Y, Lepine F, Marchenko T, Dusterer S, Tavella F, Stojanovic N, Azima A, Treusch R, Kling M F and Vrakking M J J 2009 *J. Phys. B* **42** 134017 URL <http://www.iop.org/EJ/abstract/0953-4075/42/13/134017/>
- [124] Cryan J P, Glowia J M, Andreasson J, Belkacem A, Berrah N, Blaga C I, Bostedt C, Bozek J, Buth C,

## Bibliography

- DiMauro L F, Fang L, Gessner O, Guehr M, Hajdu J, Hertlein M P, Hoener M, Kornilov O, Marangos J P, March A M, McFarland B K, Merdji H, Petrovic V S, Raman C, Ray D, Reis D, Tarantelli F, Trigo M, White J L, White W, Young L, Bucksbaum P H and Coffee R N 2010 *Phys. Rev. Lett.* **105** 083004
- [125] Barty A, Kirian R A, Maia F R N C, Hantke M, Yoon C H, White T A and Chapman H 2014 *J. Appl. Crystallogr.* **47** 1118–1131
- [126] Kella D, Algranati M, Feldman H, Heber O, Kovner H, Malkin E, Miklazky E, Naaman R, Zajfman D, Zajfman J and Vager Z 1993 *Nucl. Instrum. Meth. A* **329** 440–452 ISSN 0168-9002
- [127] Chang B Y, Hoetzlein R C, Mueller J A, D G J and Houston P L 1998 *Rev. Sci. Instrum.* **69**(4) 1665–1670
- [128] Berger M, Hubbell J, Seltzer S, Chang J, Coursey J, Sukumar R, Zucker D and Olsen K 2010 *XCOM: Photon Cross Section Database (version 1.5)* URL <http://physics.nist.gov/xcom>
- [129] Larsen J J, Sakai H, Safvan C P, Wendt-Larsen I and Stapelfeldt H 1999 *J. Chem. Phys.* **111** 7774
- [130] Hansen J L, Omiste J J, Nielsen J H, Pentlechner D, Küpper J, González-Férez R and Stapelfeldt H 2013 *J. Chem. Phys.* **139** 234313 (*Preprint* 1308.1216)
- [131] Luria K, Christen W and Even U 2011 *J. Phys. Chem. A* **115** 7362–7367 URL <http://dx.doi.org/10.1021/jp201342u>
- [132] Spence J C H, Schmidt K, Wu J S, Hembree G, Weierstall U, Doak R B and Fromme P 2005 *Acta Cryst. A* **61** 237–245 URL <http://dx.doi.org/10.1107/S0108767305002710>
- [133] Ullrich J, Moshhammer R, Dorn A, Dörner R, Schmidt L P H and Schmidt-Böcking H 2003 *Rep. Prog. Phys.* **66** 1463–1545 URL <http://stacks.iop.org/0034-4885/66/1463>
- [134] Hart P, Boutet S, Carini G, Dubrovin M, Duda B, Fritz D, Haller G, Herbst R, Herrmann S, Kenney C, Kurita N, Lemke H, Messerschmidt M, Nordby M, Pines J, Schafer D, Swift M, Weaver M, Williams G, Zhu D, Van Bakel N and Morse J 2012 *Proc. SPIE* **8504** 85040C–85040C–11 URL <http://journals.iucr.org/j/issues/2014/03/00/he5638/he5638.pdf>
- [135] Glowia J M, Natan A, Cryan J P, Hartsock R, Kozina M, Minitti M P, Nelson S, Robinson J, Sato T, van Driel T, Welch G, Weninger C, Zhi D and Bucksbaum P H 2016 *Phys. Rev. Lett.* **117** 153003 (*Preprint* 1608.03039)
- [136] Loh N T D and Elser V 2009 *Phys. Rev. E* **80**(2) 026705 URL <http://link.aps.org/doi/10.1103/PhysRevE.80.026705>
- [137] Loh N D 2014 *Phil. Trans. R. Soc. B* **369** 20130328–20130328 URL <http://rstb.royalsocietypublishing.org/cgi/doi/10.1098/rstb.2013.0328>
- [138] Ayyer K, Geloni G, Kocharyan V, Saldin E, Serkez S, Yefanov O and Zagorodnov I 2015 *Struct. Dyn.* **2** 041702 URL <http://scitation.aip.org/content/aca/journal/sdy/2/4/10.1063/1.4919301>
- [139] Yefanov O M and Vartanyants I A 2013 *J. Phys. B* **46** 164013 URL <http://stacks.iop.org/0953-4075/46/i=16/a=164013>
- [140] Yefanov O, Gati C, Bourenkov G, Kirian R A, White T A, Spence J C H, Chapman H N and Barty A 2014 *Phil. Trans. R. Soc. B* **369** 20130333–20130333 URL <http://rstb.royalsocietypublishing.org/cgi/doi/10.1098/rstb.2013.0333>
- [141] Müller N L M, Trippel S, Dhugolecki K and Küpper J 2015 *J. Phys. B* **48** 244001 (*Preprint* 1507.02530)
- [142] Siwick B J, Dwyer J R, Jordan R E and Miller R J D 2002 *J. Appl. Phys.* **92** 1643–1648
- [143] Dantus M, Scott B K, Williamson J C and Zewail A H 1994 *J. Chem. Phys.* **98** 2782–2796 URL [http:](http://)

- [//pubs.acs.org/doi/pdf/10.1021/j100062a011](http://pubs.acs.org/doi/pdf/10.1021/j100062a011)
- [144] Manz S, Casandruc A, Zhang D, Zhong Y, Loch R A, Marx A, Hasegawa T, Liu L C, Bayesteh S, Delsim-Hashemi H, Hoffmann M, Felber M, Hachmann M, Mayet F, Hirscht J, Keskin S, Hada M, Epp S W, Flöttmann K and Miller R J D 2015 *Faraday Disc.* **177** 467–491
- [145] Weathersby S P, Brown G, Centurion M, Chase T F, Coffee R, Corbett J, Eichner J P, Frisch J C, Fry A R, Gühr M, Hartmann N, Hast C, Hettel R, Jobe R K, Jongewaard E N, Lewandowski J R, Li R K, Lindenberg A M, Makasyuk I, May J E, McCormick D, Nguyen M N, Reid A H, Shen X, Sokolowski-Tinten K, Vecchione T, Vetter S L, Wu J, Yang J, Dürr H A and Wang X J 2015 *Rev. Sci. Instrum.* **86** 073702 URL <http://scitation.aip.org/content/aip/journal/rsi/86/7/10.1063/1.4926994>
- [146] Morgan A, Ayyer K, Barty A, Küpper J, Chapman H and et al A likelihood model for photon finding to be published
- [147] Deppe B, Huber G, Kränkel C and Küpper J 2015 *Opt. Exp.* **23** 28491 (*Preprint* 1508.03489)
- [148] Slowik J M, Son S K, Dixit G, Jurek Z and Santra R 2014 *New J. Phys.* **16** 073042 URL <http://stacks.iop.org/1367-2630/16/i=7/a=073042?key=crossref.2c232c97241e69fdf774cf23f17b54da>
- [149] Marburger S, Kugeler O, Hergenbahn U and Möller T 2003 *Phys. Rev. Lett.* **90** 203401 URL <http://link.aps.org/doi/10.1103/PhysRevLett.90.203401>
- [150] Jahnke T, Sann H, Havermeier T, Kreidi K, Stuck C, Meckel M, Schöffler M, Neumann N, Wallauer R, Voss S, Czasch A, Jagutzki O, Malakzadeh A, Afaneh F, Weber T, Schmidt-Böcking H and Dörner R 2010 *Nat. Phys.* **6** 139–142 URL <http://www.nature.com/doi/10.1038/nphys1498>
- [151] Mertens K, Gerken N, Klumpp S, Braune M and Martins M 2016 *J. Mod. Opt.* **63** 383–389 URL <http://www.tandfonline.com/doi/full/10.1080/09500340.2015.1046521>
- [152] Motomura K, Kukk E, Fukuzawa H, Wada S i, Nagaya K, Ohmura S, Mondal S, Tachibanai T, Ito Y, Koga R, Sakai T, Matsunami K, Rudenko A, Nicolas C, Liu X J, Miron C, Zhang Y, Jiang Y, Chen J, Anand M, Kim D E, Tono K, Yabashi M, Yao M and Ueda K 2015 *J. Phys. Chem. Lett.* **6** 2944–2949 URL <http://pubs.acs.org/doi/abs/10.1021/acs.jpcclett.5b01205>
- [153] Young L, Kanter E P, Kraessig B, Li Y, March A M, Pratt S T, Santra R, Southworth S H, Rohringer N, DiMauro L F, Doumy G, Roedig C A, Berrah N, Fang L, Hoener M, Bucksbaum P H, Cryan J P, Ghimire S, Glowina J M, Reis D A, Bozek J D, Bostedt C and Messerschmidt M 2010 *Nature* **466** 56 URL <http://dx.doi.org/10.1038/nature09177>
- [154] Hoener M, Fang L, Kornilov O, Geßner O, Pratt S T, Gühr M, Kanter E P, Blaga C, Bostedt C, Bozek J D, Bucksbaum P H, Buth C, Chen M, Coffee R, Cryan J, DiMauro L, Glowina M, Hosler E, Kukk E, Leone S R, McFarland B, Messerschmidt M, Murphy B, Petrovic V, Rolles D and Berrah N 2010 *Phys. Rev. Lett.* **104** 253002 URL <http://link.aps.org/doi/10.1103/PhysRevLett.104.253002>
- [155] Schorb S, Rupp D, Swiggers M L, Coffee R N, Messerschmidt M, Williams G, Bozek J D, Wada S i, Kornilov O, Möller T and Bostedt C 2012 *Phys. Rev. Lett.* **108** 233401 URL <http://link.aps.org/doi/10.1103/PhysRevLett.108.233401>
- [156] Schnorr K, Senftleben A, Schmid G, Rudenko A, Kurka M, Meyer K, Foucar L, Kuebel M, Kling M F, Jiang Y H, Duesterer S, Treusch R, Schroeter C D, Ullrich J, Pfeifer T and Moshhammer R 2014 *Faraday Discuss.* **171** 41–56 URL <http://xlink.rsc.org/?DOI=C4FD00031E>
- [157] Erk B, Boll R, Trippel S, Anielski D, Foucar L, Rudek B, Epp S W, Coffee R, Carron S, Schorb S, Ferguson

## Bibliography

- K R, Swiggers M, Bozek J D, Simon M, Marchenko T, Küpper J, Schlichting I, Ullrich J, Bostedt C, Rolles D and Rudenko A 2014 *Science* **345** 288–291
- [158] Boll R, Erk B, Coffee R, Trippel S, Kierspel T, Bomme C, Bozek J D, Burkett M, Carron S, Ferguson K R, Foucar L, Küpper J, Marchenko T, Miron C, Patanen M, Osipov T, Schorb S, Simon M, Swiggers M, Techert S, Ueda K, Bostedt C, Rolles D and Rudenko A 2016 *Struct. Dyn.* **3** 043207 URL <http://scitation.aip.org/content/aca/journal/sdy/3/4/10.1063/1.4944344>
- [159] Rudenko A, Jiang Y H, Kurka M, Kühnel K U, Foucar L, Herrwerth O, Lezius M, Kling M F, Schroter C D, Moshhammer R and Ullrich J 2010 *Journal Of Physics B-Atomic Molecular And Optical Physics* **43** 194004 URL <http://iopscience.iop.org/article/10.1088/0953-4075/43/19/194004>
- [160] Rudenko A and Rolles D 2015 *J. Electron. Spectrosc. Relat. Phenom.* **204** 228–236 URL <http://linkinghub.elsevier.com/retrieve/pii/S0368204815001553>
- [161] Liekhus-Schmaltz C E, Tenney I, Osipov T, Sanchez-Gonzalez A, Berrah N, Boll R, Bomme C, Bostedt C, Bozek J D, Carron S, Coffee R, Devin J, Erk B, Ferguson K R, Field R W, Foucar L, Frasiniski L J, Glowonia J M, Gühr M, Kamalov A, Krzywinski J, Li H, Marangos J P, Martinez T J, McFarland B K, Miyabe S, Murphy B, Natan A, Rolles D, Rudenko A, Siano M, Simpson E R, Spector L, Swiggers M, Walke D, Wang S, Weber T, Bucksbaum P H and Petrovic V S 2015 *Nat. Commun.* **6** 8199 URL <http://www.nature.com/ncomms/2015/150910/ncomms9199/full/ncomms9199.html>
- [162] Arion T and Hergenbahn U 2015 *J. Electron. Spectrosc. Relat. Phenom.* **200** 222–231 URL <http://linkinghub.elsevier.com/retrieve/pii/S0368204815001310>
- [163] Suenram R D, Lovas F J and Fraser G T 1988 *J. Mol. Spec.* **127** 472–480 URL [https://doi.org/10.1016/0022-2852\(88\)90135-X](https://doi.org/10.1016/0022-2852(88)90135-X)
- [164] Caminati W and Di Bernardo S 1990 *J. Mol. Struct.* **240** 253 ISSN 0022-2860 URL [https://doi.org/10.1016/0022-2860\(90\)80514-K](https://doi.org/10.1016/0022-2860(90)80514-K)
- [165] Philips L A and Levy D H 1986 *J. Chem. Phys.* **85** 1327–1332 URL <https://doi.org/10.1063/1.451219>
- [166] Berden G, Meerts W L and Jalviste E 1995 *J. Chem. Phys.* **103** 9596–9606 URL <https://doi.org/10.1063/1.469974>
- [167] Short K W and Callis P R 1998 *J. Chem. Phys.* **108** 10189 URL <https://doi.org/10.1063/1.476478>
- [168] Hager J and Wallace S C 1983 *J. Phys. Chem.* **87** 2121–2127 URL <https://doi.org/10.1021/j100235a019>
- [169] Brand C, Küpper J, Pratt D W, Meerts W L, Krügler D, Tatchen J and Schmitt M 2010 *Phys. Chem. Chem. Phys.* **12** 4968 URL <http://dx.doi.org/10.1039/C001776K>
- [170] Küpper J, Pratt D W, Meerts L, Brand C, Tatchen J and Schmitt M 2010 *Phys. Chem. Chem. Phys.* **12** 4980–4988 URL <http://dx.doi.org/10.1039/C001778G>
- [171] Korter T M, Pratt D W and Küpper J 1998 *J. Phys. Chem. A* **102** 7211–7216 URL <http://dx.doi.org/10.1021/jp982456x>
- [172] Kang C, Korter T M and Pratt D W 2005 *J. Chem. Phys.* **122** 174301 URL <https://doi.org/10.1063/1.1883635>
- [173] Livingstone R, Schalk O, Boguslavskiy A E, Wu G, Therese Bergendahl L, Stolow A, Paterson M J and Townsend D 2011 *J. Chem. Phys.* **135** 194307 URL <https://doi.org/10.1063/1.3659231>
- [174] Chrostowska A, Xu S, Mazière A, Boknevitc K, Li B, Abbey E R, Dargelos A, Graciaa A and Liu S Y 2014 *J. Am. Chem. Soc.* **136** 11813–11820 URL <http://pubs.acs.org/doi/abs/10.1021/ja5063899>

- [175] Godfrey T J, Yu H, Biddle M S and Ullrich S 2015 *Phys. Chem. Chem. Phys.* **17** 25197–25209 URL <http://dx.doi.org/10.1039/C5CP02975A>
- [176] Platt J R 1949 *J. Chem. Phys.* **17** 484–495
- [177] Sobolewski A L, Domcke W, Dedonder-Lardeux C and Jouvet C 2002 *Phys. Chem. Chem. Phys.* **4** 1093–1100
- [178] Blanco S, Lopez J, Alonso J, Ottaviani P and Caminati W 2003 *J. Chem. Phys.* **119** 880–886
- [179] Vivian J T and Callis P R 2001 *Biophys J* **80** 2093–2109
- [180] Strüder L, Epp S, Rolles D, Hartmann R, Holl P, Lutz G, Soltau H, Eckart R, Reich C, Heinzinger K, Thamm C, Rudenko A, Krasniqi F, Kühnel K, Bauer C, Schroeter C D, Moshhammer R, Techert S, Miessner D, Porro M, Haelker O, Meidinger N, Kimmel N, Andritschke R, Schopper F, Weidenspointner G, Ziegler A, Pietschner D, Herrmann S, Pietsch U, Walenta A, Leitenberger W, Bostedt C, Moeller T, Rupp D, Adolph M, Graafsma H, Hirsemann H, Gaertner K, Richter R, Foucar L, Shoeman R L, Schlichting I and Ullrich J 2010 *Nucl. Instrum. Meth. A* **614** 483–496
- [181] Viehhaus J, Scholz F, Deinert S, Glaser L, Ilchen M, Seltmann J, Walter P and Siewert F 2013 *Nucl. Instrum. Meth. A* **710** 151–154 URL <http://www.sciencedirect.com/science/article/pii/S0168900212012831>
- [182] Eland J, Wort F S and Royds R N 1986 *J. Electron. Spectrosc. Relat. Phenom.* **41** 297–309 URL <http://linkinghub.elsevier.com/retrieve/pii/0368204886850101>
- [183] Frasiniski L J, Stankiewicz M, Randall K J, Hatherly P A and Codling K 1986 *J. Phys. B* **19** L819–L824
- [184] Moss G P 1998 *Pure Appl. Chem.* **70** 143–216 URL <http://dx.doi.org/10.1351/pac199870010143>
- [185] Kierspel T, Trippel S, Küpper J *et al.* 2017 *In preparation*
- [186] Eland J H D 1987 *Mol. Phys.* **61** 725–745 URL <http://www.tandfonline.com/doi/abs/10.1080/00268978700101421>
- [187] Dribinski V, Ossadtchi A, Mandelshtam V A and Reisler H 2002 *Rev. Sci. Instrum.* **73** 2634 ISSN 00346748 URL <http://scitation.aip.org/content/aip/journal/rsi/73/7/10.1063/1.1482156>
- [188] Tarantelli F, Sgamellotti A, Cederbaum L S and Schirmer J 1987 *J. Chem. Phys.* **86** 2201–2206 URL <http://scitation.aip.org/content/aip/journal/jcp/86/4/10.1063/1.452118>
- [189] Thompson M, Hewitt P A and Wooliscroft D S 1976 *Anal. Chem.* **48** 1336–1340 URL <http://pubs.acs.org/doi/abs/10.1021/ac50003a020>
- [190] Hanwell M D, Curtis D E, Lonie D C, Vandermeersch T, Zurek E and Hutchison G R 2012 *Journal of Cheminformatics* **4** 17 URL <http://jcheminf.springeropen.com/articles/10.1186/1758-2946-4-17>
- [191] Slavíček P, Kryzhevoi N V, Aziz E F and Winter B 2016 *The Journal of Physical Chemistry Letters* **7** 234–243 URL <http://pubs.acs.org/doi/10.1021/acs.jpcllett.5b02665>
- [192] Rothhardt J, Hädrich S, Shamir Y, Tschernajew M, Klas R, Hoffmann A, Tadesse G K, Klenke A, Gottschall T, Eidam T, Limpert J, Tünnermann A, Boll R, Bomme C, Dachraoui H, Erk B, Di Fraia M, Horke D A, Kierspel T, Mullins T, Przystawik A, Savelyev E, Wiese J, Laarmann T, Küpper J and Rolles D 2016 *Optics Express* **24** 18133–18147 URL <http://www.osapublishing.org/viewmedia.cfm?uri=oe-24-16-18133&seq=0>
- [193] Kuleff A I and Cederbaum L S 2007 *Chem. Phys.* **338** 320–328 URL <http://www.sciencedirect.com/science/article/pii/S0301010407001413>
- [194] Shintake T, Tanaka H, Hara T, Tanaka T, Togawa K, Yabashi M, Otake Y, Asano Y, Bizen T, Fukui T, Goto S, Higashiya A, Hirono T, Hosoda N, Inagaki T, Inoue S, Ishii M, Kim Y, Kimura H, Kitamura M,

## Bibliography

- Kobayashi T, Maesaka H, Masuda T, Matsui S, Matsushita T, Marechal X, Nagasono M, Ohashi H, Ohata T, Ohshima T, Onoe K, Shirasawa K, Takagi T, Takahashi S, Takeuchi M, Tamasaku K, Tanaka R, Tanaka Y, Tanikawa T, Togashi T, Wu S, Yamashita A, Yanagida K, Zhang C, Kitamura H and Ishikawa T 2008 *Nat. Photon.* **2** 555–559 URL <http://www.nature.com/doifinder/10.1038/nphoton.2008.134>
- [195] Feldhaus J 2010 *J. Phys. B* **43** 194002 URL <http://stacks.iop.org/0953-4075/43/i=19/a=194002?key=crossref.f9eae7a79a592c26663ab12544e864d5>
- [196] Emma P, Akre R, Arthur J, Bionta R, Bostedt C, Bozek J, Brachmann A, Bucksbaum P, Coffee R, Decker F J, Ding Y, Dowell D, Edstrom S, Fisher A, Frisch J, Gilevich S, Hastings J, Hays G, Hering P, Huang Z, Iverson R, Loos H, Messerschmidt M, Miahnahri A, Moeller S, Nuhn H D, Pile G, Ratner D, Rzepiela J, Schultz D, Smith T, Stefan P, Tompkins H, Turner J, Welch J, White W, Wu J, Yocky G and Galayda J 2010 *Nat. Photon.* **4** 641–647 URL <http://www.nature.com/nphoton/journal/vaop/ncurrent/abs/nphoton.2010.176.html>
- [197] Ishikawa T, Aoyagi H, Asaka T, Asano Y, Azumi N, Bizen T, Ego H, Fukami K, Fukui T, Furukawa Y, Goto S, Hanaki H, Hara T, Hasegawa T, Hatsui T, Higashiya A, Hirono T, Hosoda N, Ishii M, Inagaki T, Inubushi Y, Itoga T, Joti Y, Kago M, Kameshima T, Kimura H, Kirihara Y, Kiyomichi A, Kobayashi T, Kondo C, Kudo T, Maesaka H, Marechal X M, Masuda T, Matsubara S, Matsumoto T, Matsushita T, Matsui S, Nagasono M, Nariyama N, Ohashi H, Ohata T, Ohshima T, Ono S, Otake Y, Saji C, Sakurai T, Sato T, Sawada K, Seike T, Shirasawa K, Sugimoto T, Suzuki S, Takahashi S, Takebe H, Takeshita K, Tamasaku K, Tanaka H, Tanaka R, Tanaka T, Togashi T, Togawa K, Tokuhisa A, Tomizawa H, Tono K, Wu S, Yabashi M, Yamaga M, Yamashita A, Yanagida K, Zhang C, Shintake T, Kitamura H and Kumagai N 2012 *Nat. Photon.* **6** 540–544 ISSN 1749-4885 URL <http://dx.doi.org/10.1038/nphoton.2012.141>
- [198] Abela R, Witte K, Schwarz A, Redlin H, Eckoldt H J, Hartrott M, Floettmann K, Fajardo M, Katalev V, Schilcher T, Tiedtke K, Baehr J, Singer W, Sombrowski E, Casalbuoni S, Hajdu J, Schneider J, Dipirro G, Kim J W, Brinkmann R, Racky B, Chen J, Nienhaus A, Chapman H, Lierl H, Gadwinkel E, Gerth C, Robinson I, Choroba S, Maslov M, Wenndorff R, Pagani C, Tallents G, Grabosch H J, Jaeschke E, Paparella R, Seller P, Piot P, Tsakov I, Kraemer D, Winter A, Sachwitz M, Cianchi A, Weddig H, Sandner W, Schroer C, Nunez T, Castro P, Napoly O, Kong Q, Simrock S, Gensch U, Thom H, Bratos S, Altucci C, Dobson B, Masciovecchio C, Quack H, Kienberger R, Wendt M, Chergui M, Grimm O, Plech A, Obier F, Schmidt B, Sytchev V, Rossbach J, Kozlov O, Kuhlmann M, Senf F, Wolf A, Vogel J, Prenting J, Stephan F, Syresin E, Sertore D, Decking W, Baboi N, Vogel E, Juha L, Brandt A, Collet E, Filipov Y, Vartanians I, Marangos J, Golubeva N, Smith R, Techert S, Fateev A, Wulff M, Haenisch L, Huening M, Honkimäki V, Treusch R, Ihee H, Prat S, Petrosyan B, Prat E, Tolan M, Honkavaara K, Tsakanov V, Ramert D, Ilday F Ö, Schulte-Schrepping H, Moeller W D, Schuch R, Shabunov A, Sellmann D, Wark J S, Schäfer J, Stulle F, Nicolosi P, Castellano M, Trines D, Fominykh B, Ross M, Kim Y, McCormick D, Tschentscher T, Toral F, Sytchev K, Reschke D, Anfinrud P, Will I, Toleikis S, Schlarb H, Brück H, Monaco L, Ploenjes E, Johnson S, Schmueser P, Aghababayan A, Krause B, Han J H, Tesch N, Klose K, Feldhaus J, Nagl M, Staack M, Ischebeck R, Kocharyan V, Vuilleumier R, French M, Wittenburg K, Grübel G, Riemann S, Froehlich L, Wochner P, Dehler M, García-Tabarés L, Seidel M, Celik S, Lilje L, David C, Edwards H, Gel'mukhanov F, Poletto L, Bostedt C, Wabnitz H, Bressler C, Delsim-Hashemi H, Kapitzka H, Kostin D, Bohnet I, Lange R, Richter D, Matheisen A, Kook W, Zambolin P, Griogoryan B, Hahn U, Wohlenberg T, Miltchev V, Schmitz M, Petrosyan L, Schreiber S, Havlicek J, Roensch J, Saldin E, Gareta J J, Matzen O, Schrader S, Catani L,

- Kammering R, Jablonka M, Lipka D, Ullrich F R, Blome C, Petersen B, Goerler M, Krasilnikov M, Loehl F, Jensen J P, Proch D, Laich H, Balandin V, Tischer M, Charalambidis D, Garvey T, Luong M, Rybnikov V, Minty M, Sinn H, Cavalleri A, Variola A, Möller T, Weiland T, Pöplau G, Becker J, Yurkov M, Zeitoun P, Bandelmann R, Pflueger J, Wanzenberg R, Larsson M, Steffen B, Lindenberg A, Riley D, Rehlich K, Remde H, Michelato P, Hacker K, Krzywinski J, Pugachov D, Lee R W, Graeff W, Schneidmiller E, Noelle D, Bolzmann A, Faatz B, Carneiro J P, Kolleye M, Meyners N, Gutt C, Weise H, Duesterer S, Petrov A, Kaerntner F, Altarelli M, May H J, Brovko O, Schlott V, Ayvazyan V, Neubauer G, Frisch J, Kube G, van Rienen U, Zagorodnov I, Sorokin A A, Clausen M, Bozhko Y, Stephenson B, Graafsma H, Maquet A, Zolotov A, Schloesser M, Sekutowicz J, Matyushevskiy E, Koerfer M, Howells M R, Dohlus M, McNulty I, Oppelt A, Rosmej F, Khodyachykh S, Wichmann R, Amatuni G, Wojtkiewicz J, Meulen P, Eckhardt A, Limberg T, Mildner N, Krebs O, Reiningger R, Koehler W, Hensler O, Staykov L, Schotte F, Jensch K, Ziemann V, Springate E, Keil B, Audebert P, Pedersen H B, Danared H, Magne C, Leuschner A, Beutner B, Follath R, Zapfe K, Hott T, Ludwig K and Richter M 2006 *XFEL: The European X-Ray Free-Electron Laser - Technical Design Report* (DESY) ISBN 978-3-935702-17-1 URL <https://bib-pubdb1.desy.de/record/77248#>
- [199] Schoenlein R W 2015 New science opportunities enabled by lcls-ii x-ray lasers URL [https://portal.slac.stanford.edu/sites/lcls\\_public/Lists/Publications/DispForm.aspx?ID=1004&ContentTypeId=0x0100D2D2C16F06384A44A845B10E6FC226F600DC7CB9184F2FB34484887A99919A7390](https://portal.slac.stanford.edu/sites/lcls_public/Lists/Publications/DispForm.aspx?ID=1004&ContentTypeId=0x0100D2D2C16F06384A44A845B10E6FC226F600DC7CB9184F2FB34484887A99919A7390)
- [200] McNeil B W J and Thompson N R 2010 *Nat. Photon.* **4** 814–821 ISSN 1749-4885 URL <http://dx.doi.org/10.1038/nphoton.2010.239>
- [201] Bilderback D H, Elleaume P and Weckert E 2005 *J. Phys. B* **38** S773–S797 URL <http://stacks.iop.org/0953-4075/38/i=9/a=022?key=crossref.fff50e96d91376df49e03a0a29977070>
- [202] Schulz S, Grguraš I, Behrens C, Bromberger H, Costello J T, Czwalinna M K, Felber M, Hoffmann M C, Ilchen M, Liu H Y, Mazza T, Meyer M, Pfeiffer S, Prędko P, Schefer S, Schmidt C, Wegner U, Schlarb H and Cavalieri A L 2015 *Nat. Commun.* **6** 5938 URL <http://www.nature.com/doifinder/10.1038/ncomms6938>
- [203] Harmand M, Coffee R, Bionta M R, Chollet M, French D, Zhu D, Fritz D M, Lemke H T, Medvedev N, Ziaja B, Toleikis S and Cammarata M 2013 *Nat. Photon.* **7** 215–218 ISSN 1749-4885 URL <http://dx.doi.org/10.1038/nphoton.2013.11>
- [204] Ferray M, L’Huillier A, Li X F, Lompre L A, Mainfray G and Manus C 1988 *J. Phys. B* **21** L31–L35 URL <http://stacks.iop.org/0953-4075/21/L31>
- [205] McPherson A, Gibson G, Jara H, Johann U and Luk T S 1987 *J. Opt. Soc. Am. B* **4** 595–601 URL <http://www.opticsinfobase.org/abstract.cfm?URI=josab-4-4-595>
- [206] Popmintchev T, Chen M C, Arpin P, Murnane M M and Kapteyn H C 2010 *Nat. Photon.* **4** 822–832 URL <http://www.nature.com/doifinder/10.1038/nphoton.2010.256>
- [207] L’Huillier A, Descamps D, Johansson A, Norin J, Mauritsson J and Wahlstrom C G 2003 *Eur. Phys. J. D* **26** 91–98 URL <http://www.springerlink.com/openurl.asp?genre=article&id=doi:10.1140/epjd/e2003-00072-2>
- [208] Schultze M, Wirth A, Grguras I, Uiberacker M, Uphues T, Verhoef A J, Gagnon J, Hofstetter M, Kleineberg U, Goulielmakis E and Krausz F 2011 *J. Electron. Spectrosc. Relat. Phenom.* **184** 68–77 URL <http://linkinghub.elsevier.com/retrieve/pii/S0368204811000090>
- [209] Sudmeyer T, Marchese S V, Hashimoto S, Baer C R E, Gingras G, Witzel B and Keller U 2008 *Nat. Photon.*

## Bibliography

- 2 599–604 URL <http://www.nature.com/doifinder/10.1038/nphoton.2008.194>
- [210] Mathias S, Bauer M, Aeschlimann M, Miaja-Avila L, Kapteyn H C and Murnane M M 2010 Time-resolved photoelectron spectroscopy at surfaces using femtosecond xuv pulses *Dynamics at Solid State Surfaces and Interfaces* (Weinheim, Germany: Wiley-VCH Verlag GmbH & Co. KGaA) pp 499–535 URL <http://doi.wiley.com/10.1002/9783527633418.ch21>
- [211] Rothhardt J, Hädrich S, Demmler S, Krebs M, Winters D F A, Kühl T, Stöhlker T, Limpert J and Tünnermann A 2015 *Phys. Scr.* **T166** 014030 URL <http://iopscience.iop.org/article/10.1088/0031-8949/2015/T166/014030/pdf>
- [212] Kling M F and Vrakking M J J 2008 *Annu. Rev. Phys. Chem.* **59** 463–492 URL <http://eutils.ncbi.nlm.nih.gov/entrez/eutils/elink.fcgi?dbfrom=pubmed&id=18031218&retmode=ref&cmd=prlinks>
- [213] Russbueldt P, Mans T, Weitenberg J, Hoffmann H D and Poprawe R 2010 *Opt. Lett.* **35** 4169–4171 URL <http://ol.osa.org/abstract.cfm?URI=ol-35-24-4169>
- [214] Saraceno C J, Emaury F, Heckl O H, Baer C R E, Hoffmann M, Schriber C, Golling M, Südmeyer T and Keller U 2012 *Opt. Exp.* **20** 23535–23541
- [215] Schulz M, Riedel R, Willner A, Düsterer S, Prandolini M J, Feldhaus J, Faatz B, Rossbach J, Drescher M and Tavella F 2012 *Opt. Exp.* **20** 5038–5043 URL <http://www.opticsexpress.org/abstract.cfm?URI=oe-20-5-5038>
- [216] Eidam T, Hanf S, Seise E, Andersen T V, Gabler T, Wirth C, Schreiber T, Limpert J and Tünnermann A 2010 *Opt. Lett.* **35** 94–96 URL <http://ol.osa.org/abstract.cfm?URI=ol-35-2-94>
- [217] Klenke A, Breitkopf S, Kienel M, Gottschall T, Eidam T, Hädrich S, Rothhardt J, Limpert J and Tünnermann A 2013 *Opt. Lett.* **38** 2283–2285 URL <http://ol.osa.org/abstract.cfm?URI=ol-38-13-2283>
- [218] Emaury F, Saraceno C J, Debord B, Ghosh D, Diebold A, Gèrôme F, Südmeyer T, Benabid F and Keller U 2014 *Opt. Lett.* **39** 6843–6846 URL <http://ol.osa.org/abstract.cfm?URI=ol-39-24-6843>
- [219] Negel J P, Loescher A, Voss A, Bauer D, Sutter D, Killi A, Ahmed M A and Graf T 2015 *Opt. Exp.* **23** 21064–21077 URL <https://www.osapublishing.org/abstract.cfm?URI=oe-23-16-21064>
- [220] Rothhardt J, Hädrich S, Carstens H, Herrick N, Demmler S, Limpert J and Tünnermann A 2011 *Opt. Lett.* **36** 4605–4607 URL <http://ol.osa.org/abstract.cfm?URI=ol-36-23-4605>
- [221] Hädrich S, Klenke A, Hoffmann A, Eidam T, Gottschall T, Rothhardt J, Limpert J and Tünnermann A 2013 *Opt. Lett.* **38** 3866–3869 URL <http://ol.osa.org/abstract.cfm?URI=ol-38-19-3866>
- [222] Heyl C M, Güdde J, L’Huillier A and Höfer U 2012 *Journal of Physics B: Atomic, Molecular and Optical Physics* **45** 074020 URL <http://stacks.iop.org/0953-4075/45/i=7/a=074020>
- [223] Rothhardt J, Krebs M, Hädrich S, Demmler S, Limpert J and Tünnermann A 2014 *New J. Phys.* **16** 033022 URL <http://stacks.iop.org/1367-2630/16/i=3/a=033022>
- [224] Hädrich S, Klenke A, Rothhardt J, Krebs M, Hoffmann A, Pronin O, Pervak V, Limpert J and Tünnermann A 2014 *Nat. Photon.* **8** 779–783 URL <http://www.nature.com/doifinder/10.1038/nphoton.2014.214>
- [225] Rothhardt J, Hädrich S, Klenke A, Demmler S, Hoffmann A, Gottschall T, Eidam T, Krebs M, Limpert J and Tünnermann A 2014 *Opt. Lett.* **39** 5224–5227 URL <http://ol.osa.org/abstract.cfm?URI=ol-39-17-5224>
- [226] Hädrich S, Krebs M, Hoffmann A, Klenke A, Rothhardt J, Limpert J and Tünnermann A 2015 *Light: Science & Applications* **4** e320 URL <http://www.nature.com/doifinder/10.1038/lsa.2015.93>
- [227] Gagnon E, Ranitovic P, Tong X M, Cocke C L, Murnane M M, Kapteyn H C and Sandhu A S 2007 *Science*

- 317** 1374–1378 URL <http://www.sciencemag.org/cgi/doi/10.1126/science.1144920>
- [228] Sandhu A S, Gagnon E, Santra R, Sharma V, Li W, Ho P, Ranitovic P, Cocke C L, Murnane M M and Kapteyn H C 2008 *Science* **322** 1081–1085 URL <http://www.sciencemag.org/cgi/doi/10.1126/science.1164498>
- [229] Cao W, De S, Singh K P, Chen S, Schöffler M S, Alnaser A S, Bocharova I A, Laurent G, Ray D, Zherebtsov S, Kling M F, Ben-Itzhak I, Litvinyuk I V, Belkacem A, Osipov T, Rescigno T and Cocke C L 2010 *Phys. Rev. A* **82**(4) 043410 URL <http://link.aps.org/doi/10.1103/PhysRevA.82.043410>
- [230] Zhou X, Ranitovic P, Hogle C W, Eland J H D, Kapteyn H C and Murnane M M 2012 *Nat. Phys.* **8** 232–237 URL <http://www.nature.com/doi/10.1038/nphys2211>
- [231] Ranitovic P, Hogle C W, Rivière P, Palacios A, Tong X M, Toshima N, González-Castrillo A, Martín L, Martín F, Murnane M M and Kapteyn H 2014 *Proceedings of the National Academy of Sciences of the United States of America* **111** 912–917 URL <http://www.pnas.org/cgi/doi/10.1073/pnas.1321999111>
- [232] Fischer A, Sperl A, Cörlin P, Schönwald M, Rietz H, Palacios A, González-Castrillo A, Martín F, Pfeifer T, Ullrich J, Senftleben A and Moshhammer R 2013 *Phys. Rev. Lett.* **110** 213002 URL <http://link.aps.org/doi/10.1103/PhysRevLett.110.213002>
- [233] Mansson E P, Guenot D, Arnold C L, Kroon D, Kasper S, Dahlstrom J M, Lindroth E, Kheifets A S, L’Huillier A, Sorensen S L and Gisselbrecht M 2014 *Nat. Phys.* **10** 207–211 URL <http://www.nature.com/doi/10.1038/nphys2880>
- [234] Drescher M, Hentschel M, Kienberger R, Uiberacker M, Yakovlev V, Scrinzi A, Westerwalbesloh T, Kleineberg U, Heinzmann U and Krausz F 2002 *Nature* **419** 803–807 URL <http://www.nature.com/doi/10.1038/nature01143>
- [235] Uiberacker M, Uphues T, Schultze M, Verhoef A J, Yakovlev V, Kling M F, Rauschenberger J, Kabachnik N M, Schröder H, Lezius M, Kompa K L, Müller H G, Vrakking M J J, Hendel S, Kleineberg U, Heinzmann U, Drescher M and Krausz F 2007 *Nature* **446** 627–632 URL <http://www.nature.com/doi/10.1038/nature05648>
- [236] Uphues T, Schultze M, Kling M F, Uiberacker M, Hendel S, Heinzmann U, Kabachnik N M and Drescher M 2008 *New J. Phys.* **10** 025009 URL <http://stacks.iop.org/1367-2630/10/i=2/a=025009>
- [237] Krebs M, Hädrich S, Demmler S, Rothhardt J, Zair A, Chipperfield L, Limpert J and Tünnermann A 2013 *Nat. Photon.* **7** 555–559 URL <http://www.nature.com/doi/10.1038/nphoton.2013.131>
- [238] Klenke A, Hädrich S, Eidam T, Rothhardt J, Kienel M, Demmler S, Gottschall T, Limpert J and Tünnermann A 2014 *Opt. Lett.* **39** 6875–6878 URL <http://ol.osa.org/abstract.cfm?URI=ol-39-24-6875>
- [239] Schimpf D N, Eidam T, Seise E, Hädrich S, Limpert J and Tünnermann A 2009 *Opt. Exp.* **17** 18774–18781 URL <http://www.opticsexpress.org/abstract.cfm?URI=oe-17-21-18774>
- [240] Stutzki F, Jansen F, Eidam T, Steinmetz A, Jauregui C, Limpert J and Tünnermann A 2011 *Opt. Lett.* **36** 689–691 URL <http://ol.osa.org/abstract.cfm?URI=ol-36-5-689>
- [241] Limpert J, Stutzki F, Jansen F, Otto H J, Eidam T, Jauregui C and Tünnermann A 2012 *Light: Science & Applications* **1** e8 URL <http://www.nature.com/doi/10.1038/lsa.2012.8>
- [242] Pronin O, Pervak V, Fill E, Rauschenberger J, Krausz F and Apolonski A 2011 *Opt. Exp.* **19** 10232–10240 URL <http://www.opticsexpress.org/abstract.cfm?URI=oe-19-11-10232>
- [243] Zhang X, Lytle A L, Popmintchev T, Zhou X, Kapteyn H C, Murnane M M and Cohen O 2007 *Nat. Phys.* **3** 270–275 URL <http://www.nature.com/doi/10.1038/nphys541>

## Bibliography

- [244] Ding C, Xiong W, Fan T, Hickstein D D, Popmintchev T, Zhang X, Walls M, Murnane M M and Kapteyn H C 2014 *Opt. Exp.* **22** 6194–6202 URL <http://www.opticsexpress.org/abstract.cfm?URI=oe-22-5-6194>
- [245] Bomme C *et al.* 2018 No title to be published
- [246] Vrakking M J J 2001 *Rev. Sci. Instrum.* **72** 4084–4089 URL <http://scitation.aip.org/content/aip/journal/rsi/72/11/10.1063/1.1406923>
- [247] García G, Nahon L and Powis I 2004 *Rev. Sci. Instrum.* **75** 4989–4996 URL [http://rsi.aip.org/resource/1/rsinak/v75/i11/p4989\\_s1](http://rsi.aip.org/resource/1/rsinak/v75/i11/p4989_s1)
- [248] Holland D M P, Powis I, Öhrwall G, Karlsson L and von Niessen W 2006 *Chem. Phys.* **326** 535–550 URL <http://linkinghub.elsevier.com/retrieve/pii/S0301010406001595>
- [249] Samson J A R and Stolte W C 2002 *J. Electron. Spectrosc. Relat. Phenom.* **123** 265–276 URL <http://linkinghub.elsevier.com/retrieve/pii/S0368204802000269>
- [250] Frank F, Arrell C, Witting T, Okell W A, McKenna J, Robinson J S, Haworth C A, Austin D, Teng H, Walmsley I A, Marangos J P and Tisch J W G 2012 *Rev. Sci. Instrum.* **83** 071101 URL <http://scitation.aip.org/content/aip/journal/rsi/83/7/10.1063/1.4731658>
- [251] Hädrich S, Rothhardt J, Demmler S, Tschernajew M, Hoffmann A, Krebs M, Liem A, de Vries O, Plötner M, Fabian S, Schreiber T, Limpert J and Tünnermann A 2016 *Appl. Opt.* **55** 1636–1640 URL <http://ao.osa.org/abstract.cfm?URI=ao-55-7-1636>
- [252] Lépine F, Ivanov M Y and Vrakking M J J 2014 *Nat. Photon.* **8** 195–204 URL <http://www.nature.com/doi/10.1038/nphoton.2014.25>
- [253] Weinkauff R, Schanen P, Yang D, Soukara S and Schlag E W 1995 *J. Phys. Chem.* **99** 11255–11265 URL <http://pubs.acs.org/doi/abs/10.1021/j100028a029>
- [254] Heisenberg W 1927 *Z. Phys.* **43** 172–198 URL <http://link.springer.com/article/10.1007/BF01397280>
- [255] Popova-Gorelova D, Küpper J and Santra R 2016 *Phys. Rev. A* **94** 013412 URL <https://doi.org/10.1103/PhysRevA.94.013412>
- [256] Belshaw L, Calegari F, Duffy M J, Trabattoni A, Poletto L, Nisoli M and Greenwood J B 2012 *J. Phys. Chem. Lett.* **3** 3751–3754 URL <http://pubs.acs.org/doi/abs/10.1021/jz3016028>
- [257] Calegari F, Ayuso D, Trabattoni A, Belshaw L, De Camillis S, Anumula S, Frassetto F, Poletto L, Palacios A, Decleva P, Greenwood J B, Martín F and Nisoli M 2014 *Science* **346** 336–339
- [258] Calegari F, Ayuso D, Trabattoni A, Belshaw L, De Camillis S, Frassetto F, Poletto L, Palacios A, Decleva P, Greenwood J B, Martín F and Nisoli M 2015 *IEEE Journal of Selected Topics in Quantum Electronics* **21** 1–12 URL <http://ieeexplore.ieee.org/document/7078880/>
- [259] Kuan Y J, Charnley S B and Huang H C 2003 *Astrophys. J.* **593** 848–867 URL <http://iopscience.iop.org/article/10.1086/375637/meta>
- [260] Altwegg K, Balsiger H, Bar-Nun A, Berthelier J J, Bieler A, Bochsler P, Briois C, Calmonte U, Combi M R, Cottin H, De Keyser J, Dhoooghe F, Fiethe B, Fuselier S A, Gasc S, Gombosi T I, Hansen K C, Haessig M, Jäckel A, Kopp E, Korth A, Le Roy L, Mall U, Marty B, Mousis O, Owen T, Rème H, Rubin M, Sémon T, Tzou C Y, Hunter Waite J and Wurz P 2016 *Science advances* **2** e1600285 URL <http://advances.sciencemag.org/content/2/5/e1600285.abstract>
- [261] Hu C H, Shen M and Schaefer H F 1993 *Journal Of The American Chemical Society* **115** 2923–2929 URL <http://pubs.acs.org/doi/abs/10.1021/ja00060a046>

- [262] Miller T F and Clary D C 2004 *Physical Chemistry Chemical Physics* **6** 2563–2571
- [263] Miller III T F, Clary D C and Meijer A J H M 2005 *The Journal of Chemical Physics* **122** 244323 URL <http://scitation.aip.org/content/aip/journal/jcp/122/24/10.1063/1.1927527>
- [264] Lovas F J, KAWASHIMA Y, Grabow J U, Suenram R D, Fraser G T and HIROTA E 1995 *Astrophys. J.* **455** L201 URL <http://stacks.iop.org/1538-4357/455/i=2/a=L201>
- [265] Meijer A J H M 2013 *private communication*
- [266] Ivanov A Y, Sheina G and Blagoi Y P 1998 *Spectrochimica Acta Part A* **55** 219–228 URL <http://linkinghub.elsevier.com/retrieve/pii/S1386142598002881>
- [267] Calvert C R, Belshaw L, Duffy M J, Kelly O, King R B, Smyth A G, Kelly T J, Costello J T, Timson D J, Bryan W A, Kierspel T, Rice P, Turcu I C E, Cacho C M, Springate E, Williams I D and Greenwood J B 2012 *Phys. Chem. Chem. Phys.* **14** 6289–6297 URL <http://dx.doi.org/10.1039/c2cp23840c>
- [268] Linstrom P J and Mallard W G (eds) 2017 *NIST Chemistry WebBook, NIST Standard Reference Database Number 69* (Gaithersburg MD, 20899: National Institute of Standards and Technology) URL <http://webbook.nist.gov>
- [269] Lago A F, Coutinho L H, Marinho R R T, Naves de Brito A and de Souza G G B 2004 *Chemical Physics* **307** 9–14 URL <http://linkinghub.elsevier.com/retrieve/pii/S0301010404003465>



## A Supplementary information chapter 5

### A.1 Molecular properties of 2,5-diiodothiophene

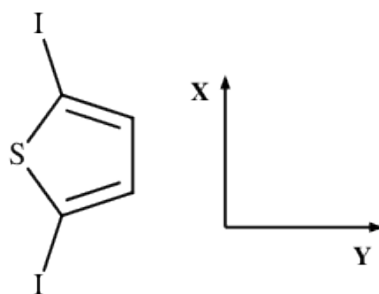


Figure A.1: Structure of 2,5-diiodothiophene

Table 7: Atomic positions of 2,5-diiodothiophene

Atom	$x$ ( $10^{-10}$ m)	$y$ ( $10^{-10}$ m)	$z$ ( $10^{-10}$ m)
I	-3.27	0.12	0
I	3.27	0.12	0
H	-1.34	-2.61	0
C	-1.25	-0.42	0
C	-0.72	-1.70	0
S	0	0.81	0
C	0.72	-1.70	0
C	1.25	-0.42	0
H	1.34	-2.61	0

Table 8: Principle moments of inertia and principal components of polarizability

Component	$I_{ii}$ / ( $\text{\AA}^2$ )	$\alpha_{ii}$ / ( $e^2 a_0^2 / E_h$ )
$I_{xx}$	111	198
$I_{yy}$	2770	118
$I_{zz}$	2880	85

## A.2 Diffractive imaging – ADU gate optimization

The determination of the ADU gates shown in Figure 5.9 was done based on a signal to noise estimation. Therefore, the recorded diffraction measurements (signal) and background measurement 1 (labeling according to Table 3) were compared. The background measurement 1 was scaled such that it contains the same number of FEL shots as the signal measurement; background measurements 2 and 3 were not taken into account since they do also have contributions from the helium and molecular diffraction pattern. The signal measurement contains thus signal from the helium, molecules and background from the beamline as well as fluorescence photons. The background measurement contains only background photons from the beamline and fluorescence photons.

Next, the number of photons detected within a certain ADU gate width have been integrated for both, the signal and background measurements. By subtracting the number of photons within the background measurement from the number of photons within the signal measurements results in the amount of detected signal photons within that certain ADU gate width. Comparing the background subtracted signal photons to the number of background photons provides an estimation of the signal-to-noise ratio (SNR). This has been conducted for an (quasi arbitrary) chosen ADU gate width of 5 and 10 ADU. Shifting the ADU gate over the full given ADU range allows to find an optimum ADU gate width and position. This is shown in Figure A.2 and also explained again on two examples.

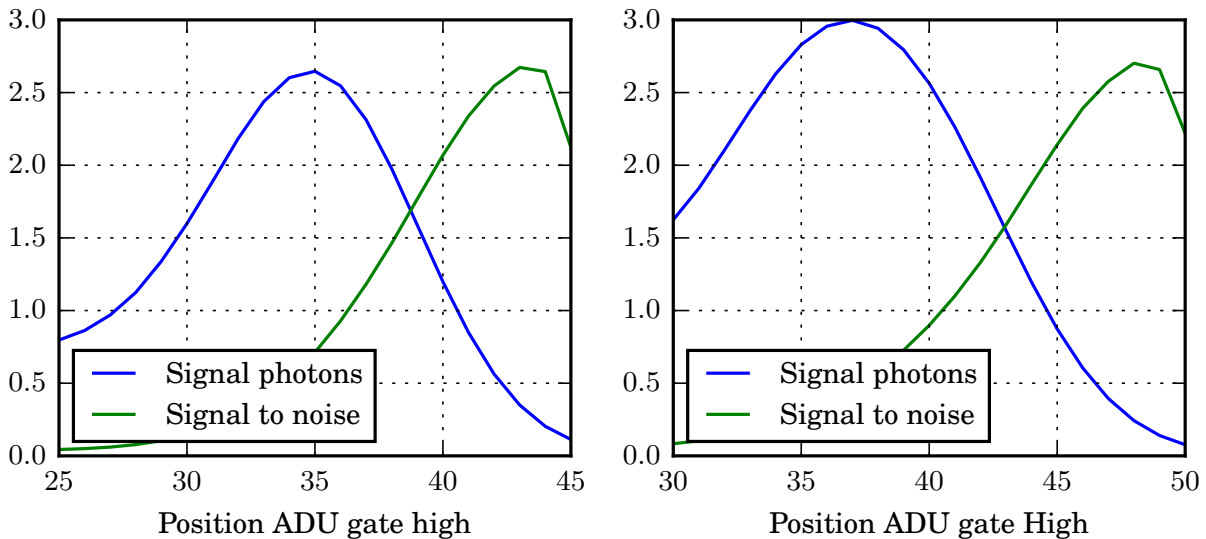


Figure A.2: Signal to noise ratio and total counts in the diffraction pattern for a ADU gate width of 5 (left) and 10 (right). The x-value shows the ADU upper value of the gate. The signal photons are given in  $2 \cdot 10^6$  and  $3 \cdot 10^6$  photons per ADU gate width.

In both plots of Figure A.2 the SNR (green) and the total number of diffracted photons (blue) is given for the two different gate width of 5 (left) and 10 (right) ADU. The  $x$ -axis represents the location of the

upper gate position in ADU, i. e., if  $x$  is 25, the ADU gate used to integrate the photons is between 20-25 ADU for an ADU gate width of 5, and from 15-25 ADU for a ADU gate width of 10. Next, if  $x$  is 26, the chosen ADU gate ranges are 21-26 ADU and 16-26 ADU, and so on. The ADU value for the 9.5 keV signal photons was 30 ADU. For both plots shown in Figure A.2 the lower ADU gate position was chosen between 20 and 40 ADU, leading to the displayed range of 25-45 ADU (30-50 ADU) for a chosen gate width of 5 ADU (10 ADU).

Both graphs show at their maximum number of detected signal photons an SNR is below 1, meaning that more background photons than signal photons have been detected. Contrary, the number of detected photons decreases dramatically at a higher SNR value. Thus intermediate values have been used in the analysis in section 5.5. The chosen gates shown in Figure 5.4 where a) 35-45 ADU, 2) 36-41, and 3) 31-41. At this gate positions the SNR ratios are 2.1, 2.3, and 1.1 and the total number of diffracted photons in the signal gate are 2.6, 1.7 and 6.8 million photons.



## B Supplementary information chapter 6 and 7

### B.1 Molecular beam reconstruction

To reconstruct the temporal molecular beam profile, the recorded events had to be sorted based on their timestamp (TS). The TS for each event was recorded with respect to the beginning of an individual measurement. Therefore, the TS does not directly provide the information at which relative time within the logical set time window of 200  $\mu\text{s}$  (Figure 6.1) a certain event has been occurred. The reconstruction of the relative time  $t_{rel}$  can be done by

$$t_{rel} = TS - \frac{\text{int}(TS \cdot f_{Valve})}{f_{Valve}}, \quad (18)$$

where  $\text{int}$  is the integer value of the numerator, and  $f_{Valve}$  the frequency of the pulsed valve. The numerator of the fraction can be interpreted as the pulse counter. If, for example, the recorded event has a TS of 2.0001 seconds, the numerator in Equation 18 is 500,025, and its integer value is 500. This means, that the event has been recorded at the five-hundredth molecular pulse after the measurement has been started. Dividing the integer value by the repetition rate of the valve gives a value of 2 seconds, i. e., the starting time of the logical set time window. The difference between the TS and the starting time of the 200  $\mu\text{s}$  long time window results in the relative time for a certain event. Thus,  $t_{rel}$  should always be between 0 and 200  $\mu\text{s}$ .

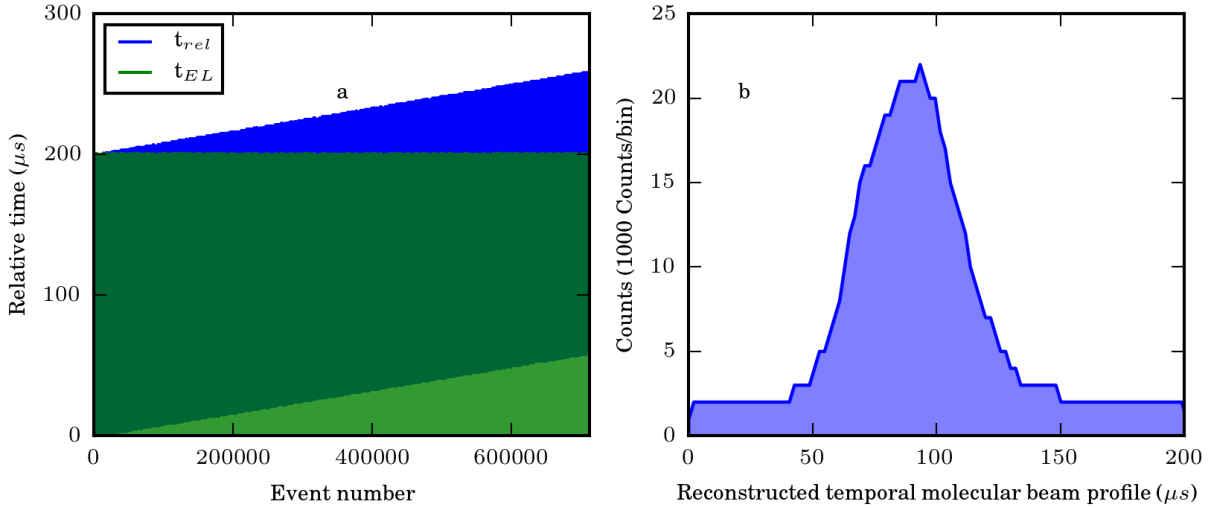


Figure B.1: a) Reconstructed relative timing and b) reconstructed molecular beam profile based on  $t_{EL}$

The reconstruction of  $t_{rel}$  based on the TS of one randomly selected measurement is shown in Figure B.1 a). The y-axis shows the time difference between the beginning of the logical set time window and the time of the event within that window, and the x-axis shows the individual event number. Due to the

## B. Supplementary information chapter 6 and 7

high number of events only the envelope of the reconstructed time is visible. Clearly visible is that the blue graph has a relative time width of approximately 200  $\mu\text{s}$  and expresses a linear, positive slope. This can be explained by a timing drift between the pulse driver for the pulsed valve and the time-to-digital converter (TDC). The green curve shows the same events corrected by a linear function

$$t_{EL} = t_{rel} - c \cdot EN, \quad (19)$$

where  $c$  is a constant and  $EN$  is the event number. It can be seen that the reconstructed time is now between a relative time of 0 and 200  $\mu\text{s}$ , i. e., the chosen time window. The constant  $c$  was dependent on the individual measurement due to, for instance, a higher event rate per second which resulted in a different delay in the TDC unit. An algorithm was used to find for each measurement the constant by variation of that constant until the difference between the minimum and maximum of the reconstructed time was minimized. The difference between the maximum and minimum time of  $t_{EL}$  was smaller than 200  $\pm$  1  $\mu\text{s}$  for each measurement, which is accurate enough for the current experiment. The reconstructed pulse structure is shown in Figure B.1 b), where the counts are given in counts per bin. The counts at the beginning and at the end of the histogram with a constant value of approximately 2000 counts per bin are background. The increased signal in the center of the image is due to an increased detection of ions while the molecular beam is present in the interaction zone. From this reconstruction a pulse duration of 45  $\mu\text{s}$  FWHM is derived. The pulse duration varied depending on the spatial position in the deflected molecular beam.

## B.2 Coincidence spectrum (PIPICO)

An ion coincidence spectrum, as it is shown for instance in Figure 6.2, can be used to disentangle the different fragmentation channels of a molecule. Requirements are the detection of two or more ionic fragments from a single molecule, as well as (ideally) a maximum of one event per TOF spectrum. Latter one is important for high repetition rate photon sources like synchrotrons, where the photon pulse separation is typically in the order of ns, while the measurement of a TOF spectrum is typically in the order of  $\mu\text{s}$ . Figure B.2 shows exemplarily a Coulomb exploding indole molecule for the three different orientations a), b) and c). In this example the fragments 1 and 2 are ionic and are extracted toward the detector, located in the upper part of Figure B.2. Fragment 2 is heavier than fragment 1 and will thus always be detected as second ion. The TOF of the fragments will vary slightly depending on the orientation of the molecule with respect to the detector. In a) fragment 1 will have an initial momentum  $p_1$  in the opposite direction of the extracting field leading to a longer TOF compared to case b) and c). On the other side, fragment 2, whose momentum  $p_2$  is in the direction of the extracting field, will have a shorter TOF compared to case b) and c). Averaging over all different orientations of the molecule leads to a diagonal line in the PIPICO spectrum as it is indicated in the right part of Figure B.2. The slope and shape of a coincidence line is dependent on the charge state of the fragments as well as the angle between their momentum vectors. A detailed description of the difference can be found for instance in [186] and

references therein.

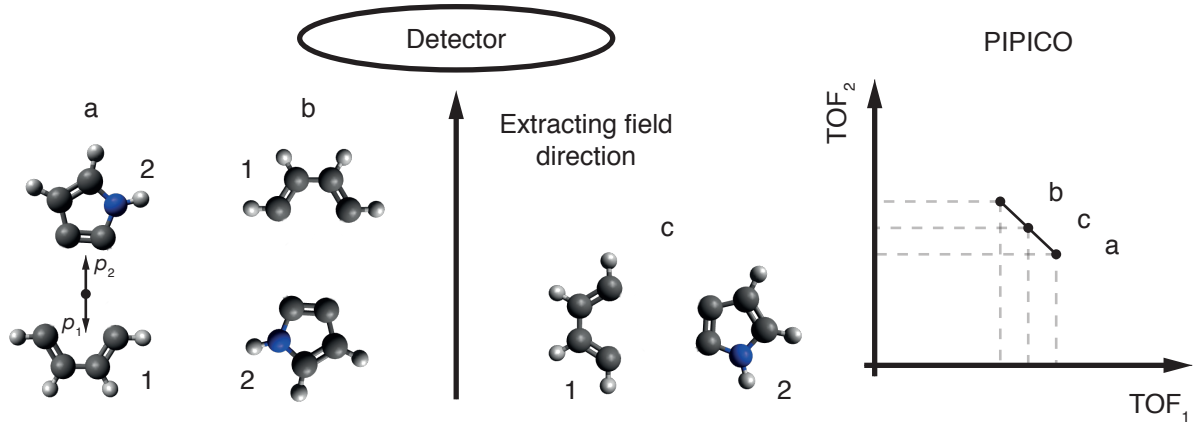


Figure B.2: Schematic drawing of a Coulomb exploding indole molecule for the three different orientations a), b), and c) and their indicated PIPICO spectrum.

### B.3 Mass spectrum calibration

Figure B.3 shows a background subtracted TOF spectrum of the first four detected ions of indole, indole-water and higher clusters upon single photon ionization at a photon energy of 420 eV. The background subtraction was done by averaging the background measured before and after the molecular pulse (Figure B.1) was crossed by the synchrotron radiation in the interaction zone. Below a TOF of 1  $\mu$ s the spectrum was scaled by 0.05 to provide a better overview of the whole spectrum. The calibration was done by selecting the central parts of the helium and indole peak, which correspond to a mass of 4 and 117 u, and are located at a TOF of 791.25 and 4386.96 ns. The TOF offset can be calculated by

$$\text{offset} = \left( \sqrt{\frac{m_{\text{He}}}{m_{\text{Ind}}}} \cdot \text{TOF}_{\text{Ind}} - \text{TOF}_{\text{He}} \right) \cdot \left( \sqrt{\frac{m_{\text{He}}}{m_{\text{Ind}}}} - 1 \right)^{-1} \quad (20)$$

which is -24.41 ns for the given parameters. The corresponding mass spectrum  $\text{mass}(\text{TOF})$  can be calculated by

$$\text{mass}(\text{TOF}) = m_{\text{He}} \cdot \left( \frac{\text{TOF} - \text{offset}}{\text{TOF}_{\text{He}} - \text{offset}} \right)^2. \quad (21)$$

The top scale of Figure B.3 shows the calculated mass spectrum given in units of u/e.

### B.4 Ion VMI calibration

Velocity map imaging (VMI) is used to measure the velocity distribution of ionic species of, e. g., molecules in space. Once the molecules interact with ionization radiation they can fragment. These fragments will

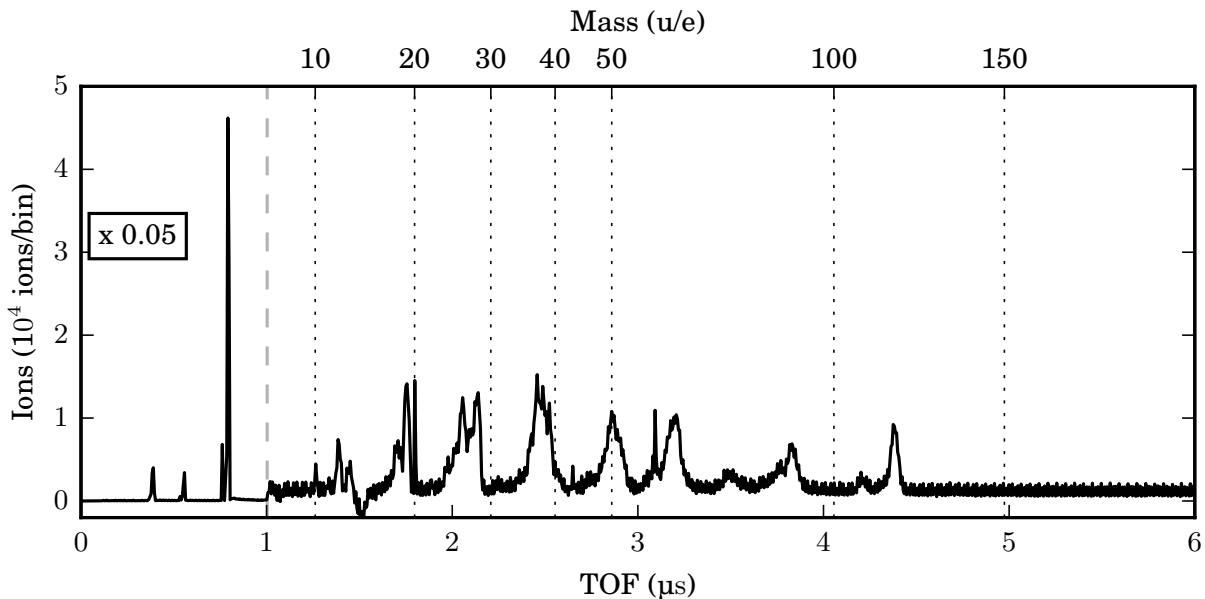


Figure B.3: Background subtracted TOF spectrum of indole, indole-water and higher clusters. The top scale shows the corresponding mass spectrum.

have a certain 3D momentum distribution in space. For ionic fragments, the 3D velocity distribution can be measured by a projection of this velocity distribution onto a 2D detector surface [2–5]. The position of the ions on the detector can be described by

$$\text{position} = M \cdot \text{TOF} \cdot (\mathbf{v}_{\text{beam}} + \mathbf{v}_{\text{ion}}) + \text{offset}, \quad (22)$$

where  $M$  is the magnification factor of the VMI, TOF is corresponding to the time of flight of a certain fragment and is proportional to  $\sqrt{\text{mass}}$  of the fragment,  $\mathbf{v}_{\text{beam}}$  is the initial velocity of the molecules with respect to the detector frame,  $\mathbf{v}_{\text{ion}}$  is the velocity of the ions which they obey upon fragmentation, and the offset is the shift of the VMI image of an ionic fragment with zero velocity with respect to an arbitrary position on the detector, typically chosen as the center of the detector. The experimental setup in Figure 6.1 illustrates that the molecular beam direction is in the plane of the detector. Thus, the individual VMI spectra for single masses will have a TOF dependent shift of their mean position on the detector. The presented data were corrected for this shift as it is described in the following. Figure B.4 a) shows a TOF spectra of the first detected ion. Highlighted is a single peak between 4.3 and 4.4 μs which is corresponding to the mass of 117 u, i. e., the parent ion of indole. The corresponding VMI image is shown in Figure B.4 b); the center of the detector is at  $X = 0$  and  $Z = 0$ . Visible are two different VMI distributions indicated by the two circles. The upper circle originates from indole ions which have at

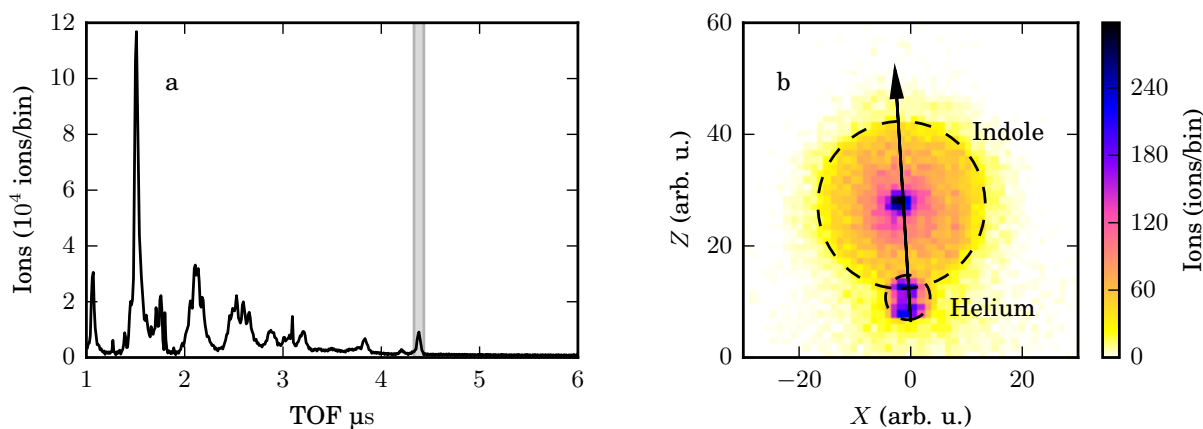


Figure B.4: a) TOF spectra of the first detected ion. Highlighted in gray is the parent ion of indole. b) VMI image of the parent ion of indole with the different contributions from background and indole molecules. The arrow is indicating the axis of the molecular beam direction.

least two velocity channels; <sup>‡</sup> the lower circle originates from helium ions which are falsely detected at this TOF. The center of gravity of both points (center of the indicated circles) is equivalent to the product of the TOF of the ions and the velocity vector of the molecular beam in the detector frame. The connection between both centers is indicated by the arrow and represents this product which is, in principle, enough information to determine this product for all masses. Though, a more accurate determination is required. Due to the helium contamination only a few specific ions, namely helium, water, hydronium and dicationic indole, could be used to determine the molecular beam axis.

Additionally, one can use coincidences between ionic fragments to determine the product. From the PIPICO spectrum shown in Figure 6.2 specific coincidence lines have been chosen. A single coincidence line, i. e., a single dissociation channel, can be used to get in total three points for the determination. These of the two individual ions detected in coincidence can be used to determine their specific central VMI position (*vide supra*). Additionally, under the assumption that these ionic fragments do recoil in opposite directions with parallel momentum vectors, the coincidence can be used to determine a third point which is as well located on the molecular beam axis. This is schematically shown in Figure B.5 where  $\mathbf{v}_1$  ( $\mathbf{v}_2$ ) is the velocity of the first (second) detected ion and  $\text{TOF}_1$  ( $\text{TOF}_2$ ) is the offset corrected TOF of this fragment. The product of TOF and  $\mathbf{v}_{\text{beam}}$  is again indicated by the arrow. The velocity vectors  $\mathbf{v}_1$  and  $\mathbf{v}_2$  are parallel due to the recoil in opposite directions, and the VMI images are indicated by the gray circles. Due to momentum conservation of the fragmenting molecule  $\mathbf{v}_2$  will always be smaller than  $\mathbf{v}_1$

<sup>‡</sup>The slow ions visible in the center are due to slow ions which could origin from monomeric indole which relaxes via emission of a photon subsequent to ionization. The faster ions are assigned to fragmentation of, e. g., indole-indole clusters which experience Coulomb explosion after ionization

B. Supplementary information chapter 6 and 7

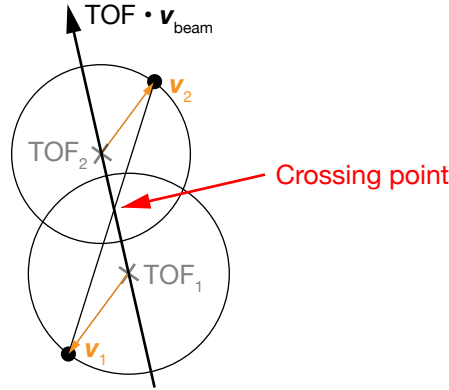


Figure B.5: Illustration of the reconstruction of the crossing point which is used as additional point to determine the product of TOF and  $\mathbf{v}_{\text{beam}}$ .

since it has a higher TOF, i. e., higher mass. The linear connection between both fragments crosses the molecular beam vector always at the same point, no matter where the ions from the molecular fragment are detected in the VMI. The crossing point (CP) can be determined from the ions position and TOF via

$$\text{CP}(X, Z) = \text{Ion}_1(X, Z) + \left(1 + \frac{\text{TOF}_1}{\text{TOF}_2}\right)^{-1} \cdot (\text{Ion}_2(X, Z) - \text{Ion}_1(X, Z)), \quad (23)$$

where  $\text{Ion}_1(X, Z)$  and  $\text{Ion}_2(X, Z)$  are the positions of the ions in the units of the detector, and TOF is the offset corrected TOF of the ions determined as described in section B.3. The time of flight corresponding to the crossing point  $\text{TOF}_{\text{CP}}$  can be calculated by

$$\text{TOF}_{\text{CP}} = \frac{\text{TOF}_1^2 + \text{TOF}_2^2}{\text{TOF}_1 + \text{TOF}_2}. \quad (24)$$

The determined centers of the different TOF-specific VMI distributions, as well as the determined CPs, are shown in Figure B.6 a) in red and blue respectively. The position  $X$  and  $Z$  is given in the detector units; the error bars show the determined standard error. Note that the  $X$  and  $Z$ -axis do have different scales, leading to a visually larger error in the  $X$ -direction. However, both error are comparable in numbers. The gray line shows a linear fit to the data points corresponding to the product of  $\mathbf{v}_{\text{beam}} \cdot \text{TOF}$ , and has a slope of -15.7 and a zero-crossing at 1.75  $X$ . The center of gravity of the indole monomer (as shown in Figure B.4 b)) is highlighted by the oval. The scaling of the TOF axis, and the determination of the zero point, i. e., the point on the axis for  $\text{TOF} = 0$  ( $X_0$  and  $Z_0$ ), was determined in the following way: The TOF-dependent VMI centers as well as CPs (Figure B.6 a)) were projected in a right-angle onto the determined product of  $\mathbf{v}_{\text{beam}} \cdot \text{TOF}$ . These points serve as a calibration for the TOF scale by the individual TOF of the VMI centers as well as the determined TOF for the CPs (Equation 24). The zero

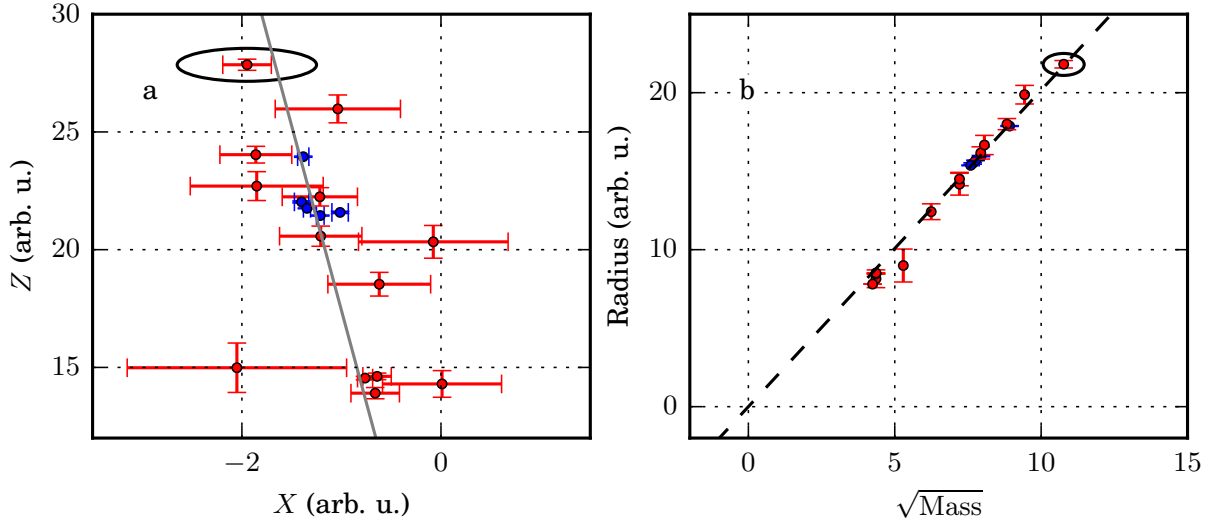


Figure B.6: a) Overview of the determined points located on the velocity vector  $\mathbf{v}_{\text{beam}}$ . The red data points are determined from the TOF-dependent VMI distributions, the blue points correspond to CPs (Equation 24), and the gray line shows the linear fit of  $\mathbf{v}_{\text{beam}} \cdot \text{TOF}$ . b) Determination of the VMI positions for a TOF = 0. The ellipse is highlighting the TOF-dependent center of the VMI for ionic indole shown in Figure B.4

point was placed at a random position on the fitted line below the smallest determined TOF. The distance between the zero point and the projected data can now be plotted against the TOF of the individual points as it is shown in Figure B.6 b), where the red and blue points correspond again to the TOF dependent VMI centers and CPs. The error bars were determined from Figure B.6 a) by considering the  $X$ - and  $Z$  contributions on the projection, and the point corresponding to ionic indole is again highlighted by the circle. If the zero position is at the appropriate location, the fitted line should cross the axis's origin since at a distance of 0 from the zero point the TOF is corresponding to zero. Thus, the zero point was varied till the intercept was minimized. The corresponding zero point is  $X_0 = -0.077$  and  $Z_0 = 6.121$ .

## B.5 Electron VMI calibration

The electron VMI calibration has been done by photoelectrons originating from neon and helium ionized at various photon energies. Figure B.7 a) shows exemplarily the sum of two spectra of neon ionized at 960 and 980 eV, resulting in photoelectrons with an energy of 89.9 and 109.8 eV (neon  $1s = 870.2$  eV [78]). The corresponding radial integration (1D spectrum) is shown in the histogram in Figure B.7 c). The diagonal lines in the VMI spectrum are caused by the hexanode where only two out of three electrodes were working properly. Figure B.7 b) shows the inverse Abel transformation of Figure B.7 a) which was

## B. Supplementary information chapter 6 and 7

calculated based on the BASEX algorithm [187]; the corresponding 1D spectrum is shown in the histogram in Figure B.7 d). The 1D spectra obtained from the inverse Abel transformation were used as basis for a Gaussian fit to determine the mean radius for a certain photoelectron velocity.

Additionally to neon, helium photoelectrons have been measured for ionization energies of 310 and 420 eV, which correspond to a photoelectron energies of 285.4 and 395.4 eV. Figure B.8 shows the four determined radii for the four measured photoelectron velocities. The red and orange crosses correspond here to the measurement points for neon and helium respectively. The  $x$ -axis represents the radius in detector units, the  $y$ -axis displays the velocity of the photoelectrons. The black circle is indicating the center of the VMI images and the black graph is indicating a polynomial fit to the data which resulted in a slope of 0.9948, crossing the origin at 0.

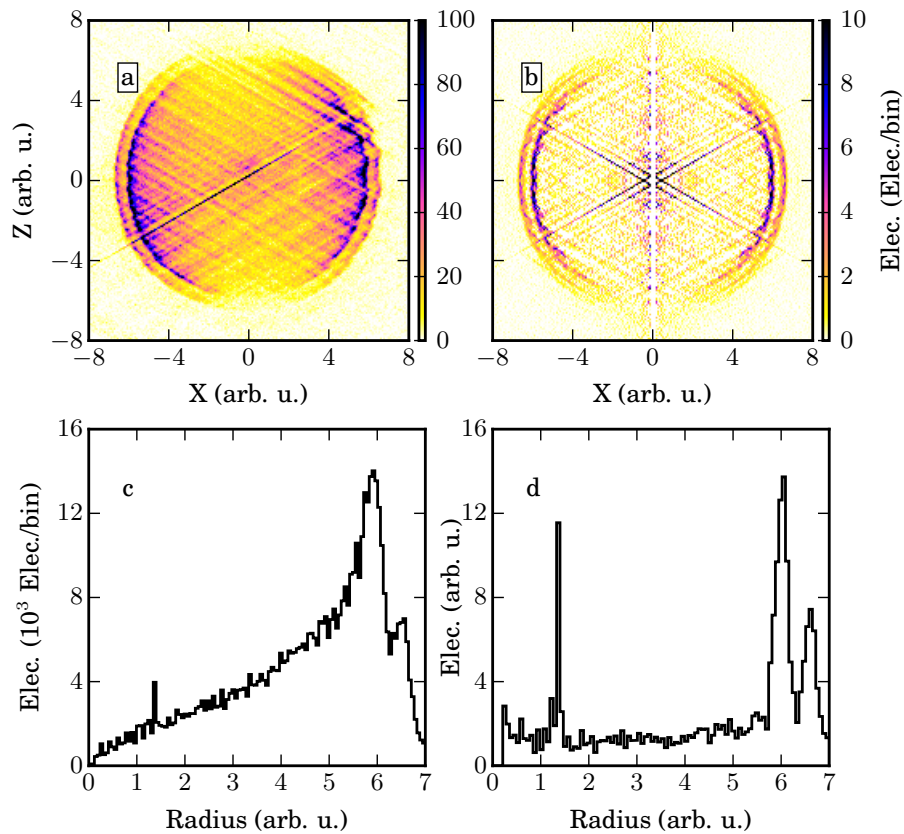


Figure B.7: a) Sum of two photoelectron spectra for neon ionized at a photonenergy of 960 and 980 eV. The corresponding 1D spectrum is shown in c). b) shows the inverse Abel transformation of a) based on the BASEX algorithm [187]. d) shows the 1D energy spectrum of b).

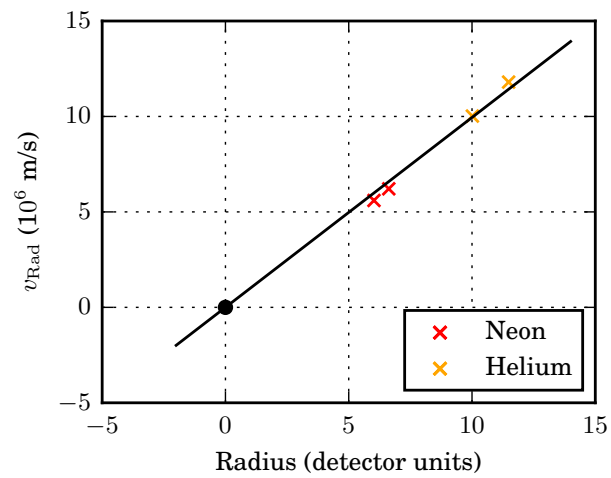


Figure B.8: Electron velocity as a function of the distance to the origin of the VMI images. Neon and helium is indicating the radii determined for the two different electron velocities of both atomic species. The origin is labeled by the black circle and the black line shows a fit to the determined data points.



## Acknowledgment

At first I would like to thank my group leader and Doktorvater Jochen Küpper for being my Doktorvater, for the great experiments whom I was allowed to participate, for his continuously open ear for private as well as work related discussions, his continuous advise, and of course for given me the chance to conduct the PhD in his group.

I would like to thank Oriol Vendrell for being the second examiner, and, despite the distance he has currently to Hamburg, also to thank him for being part of my PhD defense committee.

Further, I would like to thank Henry Chapman, Oliver Mücke, the other members of my PhD defense committee, and Caren Hagner, leader of my PhD defense committee, for not hesitating to join the committee, and therefore also to accompany me by my last steps as a PhD student.

I would like to thank Sebastian Trippel for his great supervision of the indole and indole-water experiments. Despite the time consuming work he had always an open ear, was giving always good advises, and was always listen to counter-arguments(!)...until he found a good reason why that beautiful counter-argument is not a good argument anymore!

I would like to thank Andrew Morgan for his awesome python skills, which he was willing to share with me, and his continuous support in the data analysis of the x-ray diffraction experiment. Not to mention countless discussions about everything one can imaging accompanied by a nice cold beer.

I would like to thank Daniel Horke and Yuan-Pin Chang. Both of them had the drawback of conducting the first experiment with me. I was at the time a so-called laser person with no real experience in molecular physics. They were at the front-end of my question marathon but were patient enough to keep me alive. Along the same line I would like to thank Stephan Stern whom was my predecessor, and whom was really patient with me, explained me everything necessary to conduct an experiment with his machine, which I finally took over. I hope you appreciate that I kept that baby alive!

I would like to thank Mr. Mullins for being Mr. Mullins! Typically we were working together on beamtimes, which were not always successful but at least we had fun! Not to mention here also his continuous support and open ear.

Nele Müller and Jens Kienitz! A special thanks for the good time we had all the years, for all the fruitful work related discussions, for all the good time after work! Without you the time would have been different, Kölle Alaaf!

Joss Wiese, you smart guy! Thanks very much also to you for all your help and the great time!

Nicole Teschmit, another person whom won my heart! Thanks very much for ur help, discussions, continuous smile, and the good time outside work!

My dear Italian friends Michele Di Fraia and Andrea Maria Trabattoni, my dear Scottish friend Ruth Livingstone, one beamtime, several beers, thanks for the good time! Grazie mille! Thank ye uncolly! And the google-translated go raibh maith agat!

Karol Długolecki and Lars Gumprecht! I think without you the machine would have been fallen apparat,

and modifications as well as technical drawings were on a level I do not dare to imagine. Thanks very much to both of you!

Barbora Vagovič and Irmtraud Kleine, the glue of the group! Thanks very much for helping me and the group to keep everything in order!

My dear PhD co-fighters Salah Awel, Helen Bieker, Bastian Deppe, Zhipeng Huang, Evangelos Karamatskos, Nils Roth and Linda Thesing. My dear CMI co-workers Wilhelm Frisch, Daniel Gusa, Pau Gonzalez-Caminal, Igor Rubinsky, Xiaoyan Sun, Lena Worbs, Lu Wu, ..., my dear CMI colleagues and former colleagues! We did not have too much work-related overlap during the time my PhD, but we still had enough to giggle during, and off-time work! I really enjoyed being part of the group thanks to all of you! From our collaborators I would like to explicitly mention the "CAMP-crew" headed by Daniel Rolles, and consisting (at this time) of Denis Anielski, Sadia Bari, Rebecca Boll, Cédric Bomme, Benjamin Erk, and Evgeny Savelyev. Thank you very much for all the nice experiments, the support, the discussions, and also the nice time off-work!

I would like to thank the Coherent Imaging Team headed by Henry Chapman, including Valerio Mariani and Holger Fleckenstein. All of you were always really helpful, and also did not hesitate to borrow me/us stuff for various experiments.

I would like to thank the people and groups around the beamlines where we have conducted the experiments, namely the Variable Polarization Beamline P04 at Petra III headed by Jens Viefhaus, the CXI Beamline at the LCLS headed by Sebastien Boutet, and the fiber and waveguide lasers group at the Friedrich-Schiller-Universität Jena headed by Jens Limpert.

I would like to thank my colleagues and friends of the CFEL and DESY, including Frederike Ahr, Jonathan Correa, Hauke Höppner, Yannis La-Place, Francesca Moglia, and many more. All of you made it possible that I really enjoyed my time as a PhD student!

Finally, I would like to thank my girlfriend for being so patient with me, and my parents and friends from Bergisch Gladbach for supporting me all the time in Hamburg!

Peace, love, and rock 'n' roll!

## List of Publications

1. *Charge transfer in dissociating iodomethane and fluoromethane molecules ionized by intense femtosecond X-ray pulses*  
R. Boll, B. Erk, R. Coffee, S. Trippel, T. Kierspel, C. Bomme, J. Bozek, M. Burkett, S. Carron, K. Ferguson, L. Foucar, J. Küpper, T. Marchenko, C. Miron, M. Patanen, T. Osipov, S. Schorb, M. Simon, M. Swiggers, S. Techert, K. Ueda, C. Bostedt, D. Rolles, A. Rudenko  
*Structural Dynamics*, **3**, 4 (2016)
2. *High-repetition-rate and high-photon-flux 70 eV high-harmonic source for coincidence ion imaging of gas-phase molecules*  
J. Rothhardt, S. Hädrich, Y. Shamir, M. Tschernajew, R. Klas, A. Hoffmann, G.K. Tadesse, A. Klenke, T. Gottschall, T. Eidam, J. Limpert, A. Tünnemann, R. Boll, C. Bomme, H. Dachraoui, B. Erk, M. Di Fraia, D. Horke, T. Kierspel, T. Mullins, A. Przystawik, E. Savelyev, J. Wiese, T. Laarmann, J. Küpper, D. Rolles,  
*Optics Express* **24**, 16 (2016).
3. *Strongly aligned gas-phase molecules at free-electron lasers*  
T. Kierspel, J. Wiese, T. Mullins, J. Robinson, A. Aquila, A. Barty, R. Bean, R. Boll, S. Boutet, P. Bucksbaum, H. Chapman, L. Christensen, A. Fry, M. Hunter, J. Koglin, M. Liang, V. Mariani, A. Morgan, A. Natan, V. Petrovic, D. Rolles, A. Rudenko, K. Schnorr, H. Stapelfeldt, S. Stern, J. Thøgersen, C. Yoon, F. Wang, S. Trippel, J. Küpper  
*Journal Of Physics B-Atomic Molecular And Optical Physics* **48**, 204002 (2015).
4. *Imaging Molecular Structure through Femtosecond Photoelectron Diffraction on Aligned and Oriented Gas-Phase Molecules*  
R. Boll, A. Rouzee, M. Adolph, D. Anielski, A. Aquila, S. Bari, C. Bomme, C. Bostedt, J. D. Bozek, H. N. Chapman, L. Christensen, R. Coffee, N. Coppola, S. De, P. Decleva, S. W. Epp, B. Erk, F. Filsinger, L. Foucar, T. Gorkhover, L. Gumprecht, A. Hömke, L. Holmegaard, P. Johnsson, J. S. Kienitz, T. Kierspel, F. Krasniqi, K.-U. Kühnel, J. Maurer, M. Messerschmidt, R. Moshhammer, N. L. M. Müller, B. Rudek, E. Savelyev, I. Schlichting, C. Schmidt, F. Scholz, S. Schorb, J. Schulz, J. Seltmann, M. Stener, S. Stern, S. Techert, J. Thøgersen, S. Trippel, J. Viefhaus, M. Vrakking, H. Stapelfeldt, J. Küpper, J. Ullrich, A. Rudenko and D. Rolles  
*Faraday discussions* **171**, 57 - 80 (2014)
5. *Spatial Separation of Molecular Conformers and Clusters*  
D. A. Horke, S. Trippel, Y.-P. Chang, S. Stern, T. Mullins, T. Kierspel, and J. Küpper  
*J. Vis. Exp.* **83**, e51137 (2014)
6. *Spatially separated polar samples of the cis and trans conformers of 3-fluorophenol*  
T. Kierspel, D. Horke, Y.-P. Chang, and J. Küpper  
*Chemical Physics Letters* **591**, 130–132 (2014).